STUDIES IN CLAY CHEMISTRY

ARVIND-PAL SINGH MANDAIR

Doctor of Philosophy

THE UNIVERSITY OF ASTON IN BIRMINGHAM

DECEMBER 1988

To

Mum, Dad, Navdeep and Navroop,

and

the beloved memory of my Grandparents

੧ ਓ ਸਤਿਗੁਰ ਪ੍ਰਸਾਦਿ ॥

The One, The Infinite
Realised by the Grace of the True Guru

ਜੇ ਸਉ ਚੜਹਿ ਦਿਵਾਣਿ
ਸੂਰਜ ਚੜਹਿ ਹਜਾਰ॥
ਏਤੇ ਚਾਨਣ ਹੋਦਿਆਂ
ਗੁਰ ਬਿਨੁ ਘੋਰ ਅੰਧਾਰ॥
—ਮਃ੨-ਵਾਰ ਆਸਾ

Were a hundred moons to rise and a thousand suns to mount the sky,
Even in the midst of such light there would be appalling darkness without the Guru (spiritual guide)

M:2 - Var Asa

ਪੜਿਆ ਮੂਰਖੁ ਆਖੀਐ
ਜਿ ਲਬੁ ਲੋਭੁ ਅਹੰਕਾਰ॥
ਮਃ ੧ - ਮਾਝ ਕੀ ਵਾਰ

Count that scholar a fool,
Who harbours ego, greed and lust.

M:1 - Majh di Var

Acknowledgements

I should like to express my debt of sincere gratitude to my academic supervisor, Professor W R McWhinnie, for his guidance, invaluable advice and constant encouragement throughout my period as a research student. I am especially grateful to Professor McWhinnie (and the Royal Society of Chemistry, Midlands Division) for giving me the opportunity to present some of our work at the Dalton Symposium (Birmingham University 21.4.88).

I am grateful to Dr Parisa Monsef-Mirzai for many useful discussions and helpful advice. Thanks are due to Mike Perry for his help in obtaining NMR spectra. I also wish to thank the technical staff in the Department of Chemistry for their assistance in my work. I wish to express thanks to my colleagues in NL11 for their company, and to Mushtaq Ali for his help in a number of matters (NKD! thanks for help with the x-ray tables).

Many thanks are due to Christine Jukes for her patience in producing the manuscript.

I am grateful to Barry Saye, Dr David Apperly and Dr Race Young (NMR Department, University of Durham) for valuable advice in practical solid-state NMR.

I gratefully acknowledge the time off given to me by Akzo to complete the thesis.

Last but not least, I want to say a special thank you to my family and to relatives in Hoshiarpur for constant moral support during the last three years.

LIST OF CONTENTS

Chapter Two - Charge Transfer Interactions in Smectite Clays

Chapter Three - A Study of Redox Catalysts Immobilised on Clay Modified Electrodes

LIST OF TABLES

LIST OF ILLUSTRATIONS

CHAPTER ONE

1.1 PREAMBLE

Clays are formed by natural geological processes and the constituents of the clay depend on the minerals present at the time of formation and the effects of subsequent weathering and ageing. The term clay can be used to describe a wide range of products and many systems of classification exist. In most cases the system is very much orientated towards application. For our purposes it is convenient to begin by saying that a clay is a 'hydrous silicate of aluminium, magnesium or iron.' It is also worth bearing in mind that clay particles in the dispersed state are generally less than two microns whereas non-clay particles are somewhat larger.

Clays were first shown to be composed of crystalline materials in the early 1920's by Hadding and Rinne,[5] who were the first to apply X-ray diffraction analyses to the study of clays. By the late 1920's evidence for the crystalline nature of clays was beginning to accumulate largely due to the work of Ross and Hendricks. In 1930 Linus Pauling published his X-ray diffraction results for a number of silicate systems including micas, talc, pyrophyllite, chlorite and kaolinite. Pauling found that although these minerals had widely differing chemical compositions the dimension of their unit cell in the plane of cleavage was similar, which led him to conclude that they had a layer structure composed of sheets of silica and either gibbsite or brucite. This laid the foundations for a scheme of classification. The crystallinity and structures of the main groups of layer silicates had been established by 1940 and subsequent efforts were directed to the elucidation of the partial order and disorder in these systems.

1.1.1 The Structure of Silicates [1 3 2]

Clays are members of the silicate family which has as its common structural unit, the SiO_4 tetrahedron

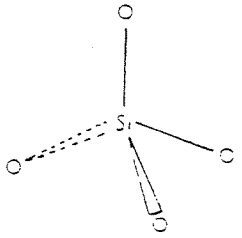

Fig. 1.1 Spatial Representation of the SiO_4 Tetrahedron

This silicate building unit extends in three dimensions, therefore depending on how collections of these tetrahedra are linked together, a polymeric lattice can be built up on one, two or three dimensions. Where $(SiO_4)^{4-}$ units exist separately in so called 'island structures' [2] are formed composed of discrete SiO_4^{4-} units linked to each other only through other cations which may be in three, four, eight or twelve coordination with oxygen. Minerals in this category are called orthosilicates.

When two or more silica tetrahedra are linked together by sharing one common corner and introducing a Si-O-Si linkage, isolated group structures are formed. the remaining 3 oxygens attached to each silicon must receive their extra valency from external cations. Such units have the chemical composition $(Si_2O_7)^{6-}$. Other silicates within this group are known which contain more complicated groupings. For example three, four or six-unit ring structures having the respective compositions $(Si_3O_9)^{6-}$ and $(Si_4O_{12})^{8-}$ and $(Si_6O_{18})^{12-}$ may be formed as show in Fig. 1.2.

Chain structures are formed when two oxygen atoms of every SiO_4 tetrahedron are joined to others and the resulting structure is capable of indefinite extension in the form of parallel chains. Single complete chains have the general formula $(SiO_3)^{2-}$ and are exemplified by pyroxenes. As each chain can be linked to other similar chains through the external cations, the structure is capable of extension in three dimensions. Related chain structures which have two identical parallel chains and a chemical composition of $n(Si_4O_{11})^{6-}$ are known as amphiboles.

When three oxygens of each SiO_4 tetrahedra are linked with adjacent units, a continuous sheet structure results. Only one oxygen of each group is not fully satisfied electrically and requires to be linked with external cations. The sheet of silicon-oxygen atoms is capable of indefinite extensions in two dimensions at right angles. The silica units are arranged in the form of hexagonal rings and the sheet is constructed of such symmetrical rings surrounded by six similar ones, each of which share two corners. Definite layers of these sheets are formed which are stacked one above the other. The bonds between each layer are

STRUCTURAL FORMS OF SILICATES

NO BRIGDING OXYGENS (0.BO)

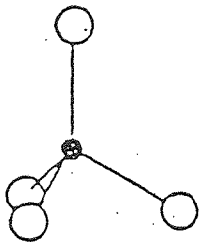

$(SiO_4)^{4-}$

ONE BRIDGING OXYGEN (I.BO)

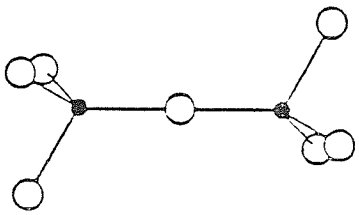

$(Si_2O_7)^{6-}$

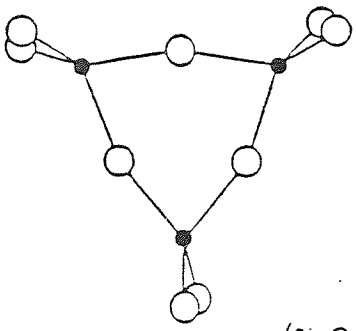

$(Si_3O_9)^{6-}$

TWO BRIDGING OXYGENS (B.O.)

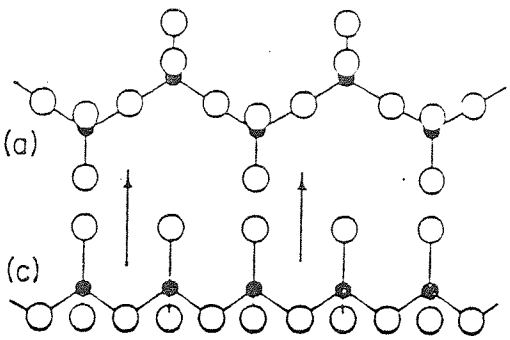

THREE BONDING OXYGENS (3 B.O.)

SHEET STRUCTURES
e.g. CLAY MINERALS

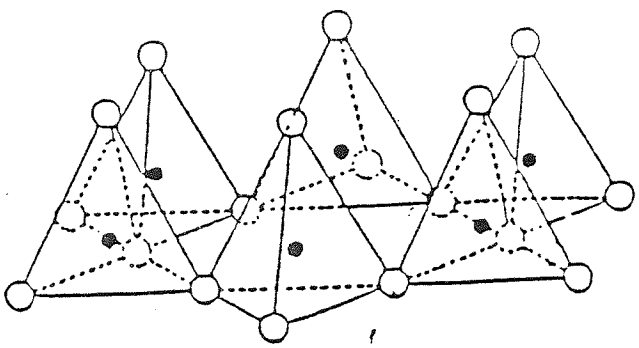

FOUR BRIDGING OXYGENS (4 B.O.)

FRAMEWORK STRUCTURES
e.g ZEOLITES, FELDSPARS

FIG 1-2

Table 1.1

Location of Any Isomorphous Substitution	Trioctahedral Minerals	Dioctahedral Minerals
Prototype (no substitutions)	Talc	Pyrophyllite
Practically all in the octahedral layer	Hectorite	Montmorillonite
Predominantly in the tetrahedral layer	Vermiculite	Beidellite

	meq/100g clay
Kaolinite	3-15
Halloysite	5-40
Montmorillonite	80-150
Vermiculite	100-150
Hectorite	40-70
Chlorite	10-40

relatively weak. Sheet structures can be simple where layers of tetrahedral silica are linked to cations of one type with a specific coordination, or they may be complex with substitutions of many types. Clay minerals constitute an important group within sheet or layered silicates and consist of well defined subgroups.

1.1.2 Structural Principles of Clay Minerals [2,4]

The principal building elements of the clay minerals are two-dimensional arrays of SiO_4 tetrahedra and two-dimensional arrays of aluminium or magnesium - oxygen - hydroxyl octahedra. Such sheets or layers of tetrahedra and octahedra are superimposed in different ways within most clays. In the tetrahedral silica layers the Si atoms are coordinated with four oxygen atoms. The atoms are located on the four corners of a regular tetrahedron with silicon at the centre (Fig. 1.3). Within the layer three out of the four oxygens of one tetrahedron are shared by neighbouring tetrahedra. The fourth oxygen atom of each tetrahedron is pointed downward and is termed as the apical oxygen.

In the Al-, Mg-O-OH sheets, the Al or Mg atoms are coordinated with six oxygen atoms or OH groups which are located around the Al or Mg atom with their centres on the six corners of a regular octahedron. The sharing of oxygen atoms by neighbouring octahedra results in a sheet as shown in Fig. 1.3. The oxygen atoms and the hydroxyl groups lie in two parallel planes with Al or Mg atoms between these planes. The oxygen atoms and hydroxyl groups form a hexagonally close-packed system, and the layer is termed as the octahedral layer (or sheet).

As the tetrahedral and octahedral sheets have almost analagous symmetry and identical dimensions, this allows sharing of the oxygen atoms between these sheets. The apical oxygens protruding from the tetrahedral sheet is shared by the octahedral sheet.

At this stage an important distinction can be made. If the sharing of atoms occurs between one tetrahedral silica and one octrahedral (alumina or magnesia)

layer this gives rise to two-layer minerals. In the three layer minerals, one octahedral sheet is sandwiched; it shares oxygens with two silica sheets, one on each side. The combination of an octahedral sheet and one or two tetrahedral sheets is called a unit layer. Most clay minerals consist of such unit layers stacked parallel to each other. Within each layer a certain unit of structure repeats itself in a lateral dimension. This repeating structure is called the 'unit cell'. The atomic arrangements in a typical unit cell for a two layer clay mineral (or 1:1) such as kaolinite, and a three layer (or 2:1) clay mineral such as pyrophillite is shown in Fig. 1.4.

The distance between a certain plane in the unit layer and the corresponding plane in the next unit layer is called the 001 basal or c spacing. The determination of this repeat distance by XRD enables one to distinguish between two-layer clays where d_{001} = 7.1 to 7.2Å and three layer clays where d_{001} = 9.2Å.

The two crystal lattices depicted in Fig.1.4 are those of talc and pyrophyllite. Both are ideal electroneutral lattices and occur in nature. The neutral three layer structure represents that of pyrophyllite where two out of three possible octahedral positions are occupied by trivalent Al^{3+}. Due to this two-thirds occupancy of the available octahedral sites pyrophyllite is termed a dioctahedral mineral. Talc on the other hand is a trioctahedral mineral, since all of the available octahedral positions in the octahedral layer are filled by divalent Mg atoms.

Both talc and pyrophyllite consist of stacks of the above unit layers held together by van der Waals forces which are comparatively weak compared to the forces holding the atoms together within the unit cells. Cleavage parallel to the layers is easy and hence these minerals occur in flakes. Structurally, although not in origin, pyrophyllite and talc are the parent structures of the smectite group of minerals. Smectite minerals can be derived from the ideal parent structures by introducing random atomic substitutions in the lattices.

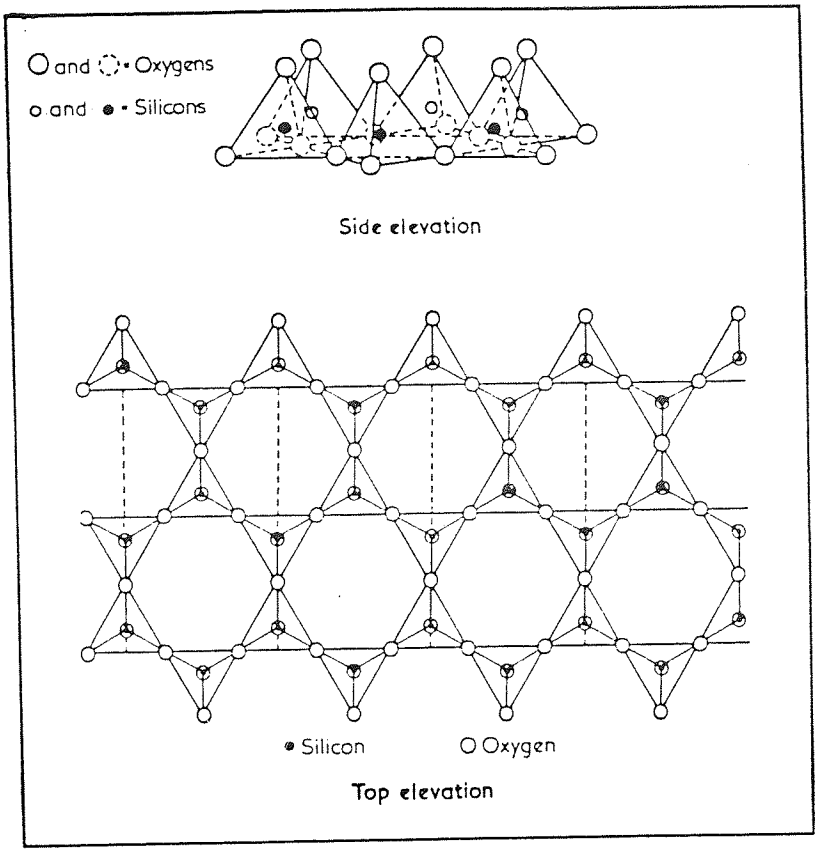

Fig. 1.3 The Structure of the Ideal Silica Layer of Layer Lattice Silicates

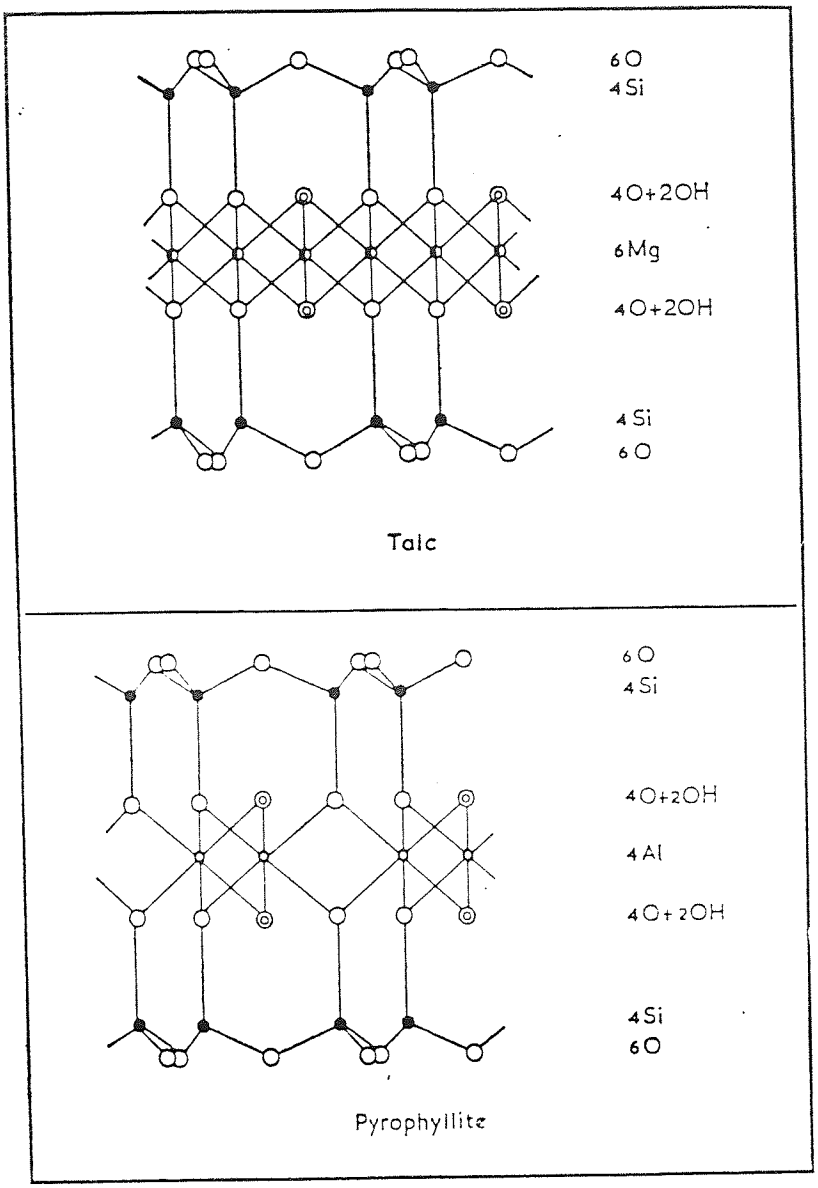

Fig. 1.4 The Side Elevation Structures of Talc and Pyrophillite

1.1.3 The Smectite Minerals [1,2,4]

The smectite group consists of a number of members, the most important ones being montmorillonite and hectorite. Their structures are derived from pyrophyllite and talc respectively by substitution of certain atoms for other atoms. Both talc and pyrophyllite have balanced charges within the lattice and the net lattice charge is zero. Hence they have non-expanding lattices and are unable to imbibe polar molecules. The smectite clays on the other hand have net negative charges in their lattice structures and this facilitates the uptake of polar molecules. Therefore, smectites are also known as 'expanding lattice' or 'swelling clays'.

With regard to montmorillonite and hectorite the net negative lattice charge results because of a charge imbalance in the lattice. Such a charge inbalance could result from:

(a) A substitution in the tetrahedral layer of a lower valent metal eg Al^{3+} for Si^{4+}.

(b) A substitution in the octahedral layer of a lower-valent metal eg Al^{3+} for Mg^{2+}.

(c) Different minerals contain structural differences such that F^- ions may be replaced by OH^- ions.

A convenient classification is that minerals shown in table 1.1 are related to pyrophyllite and talc by isomorphous substitutions of type (a) and (b).

The excess negative charge in smectite clays can be compensated by absorption on the layer surfaces of cations which are too large to be accommodated within the lattice interior. In the presence of water the compensating cations on the clay surface may be readily exchanged with other cations in solution; hence they are called 'exchangeable cations'. The total amount of these cations may be determined analytically and when expressed in milliequivalents per 100g of dry clay, it is called the cations exchange capacity (CEC) or the base exchange

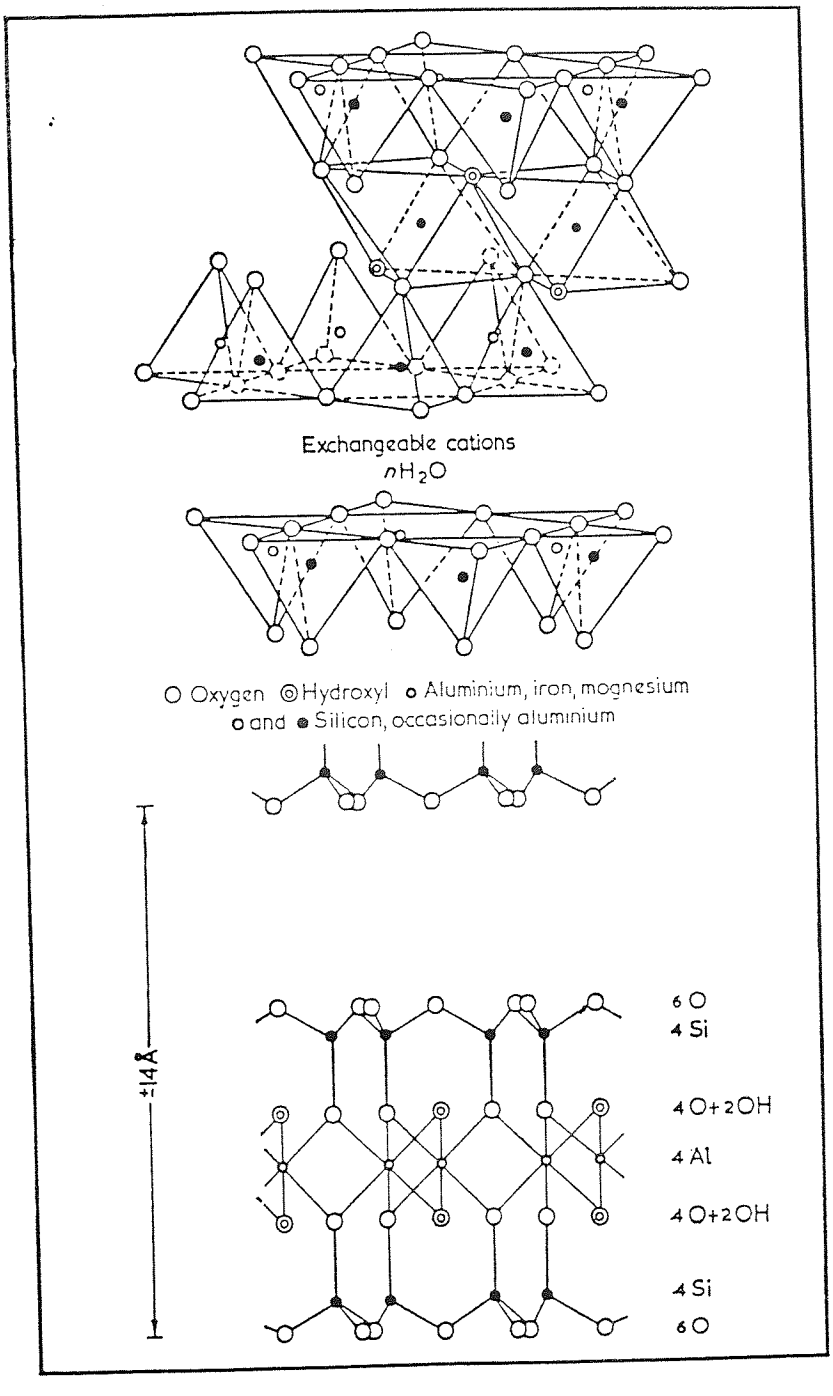

Fig. 1.5 Diagrammatic Structure of Montmorillonite

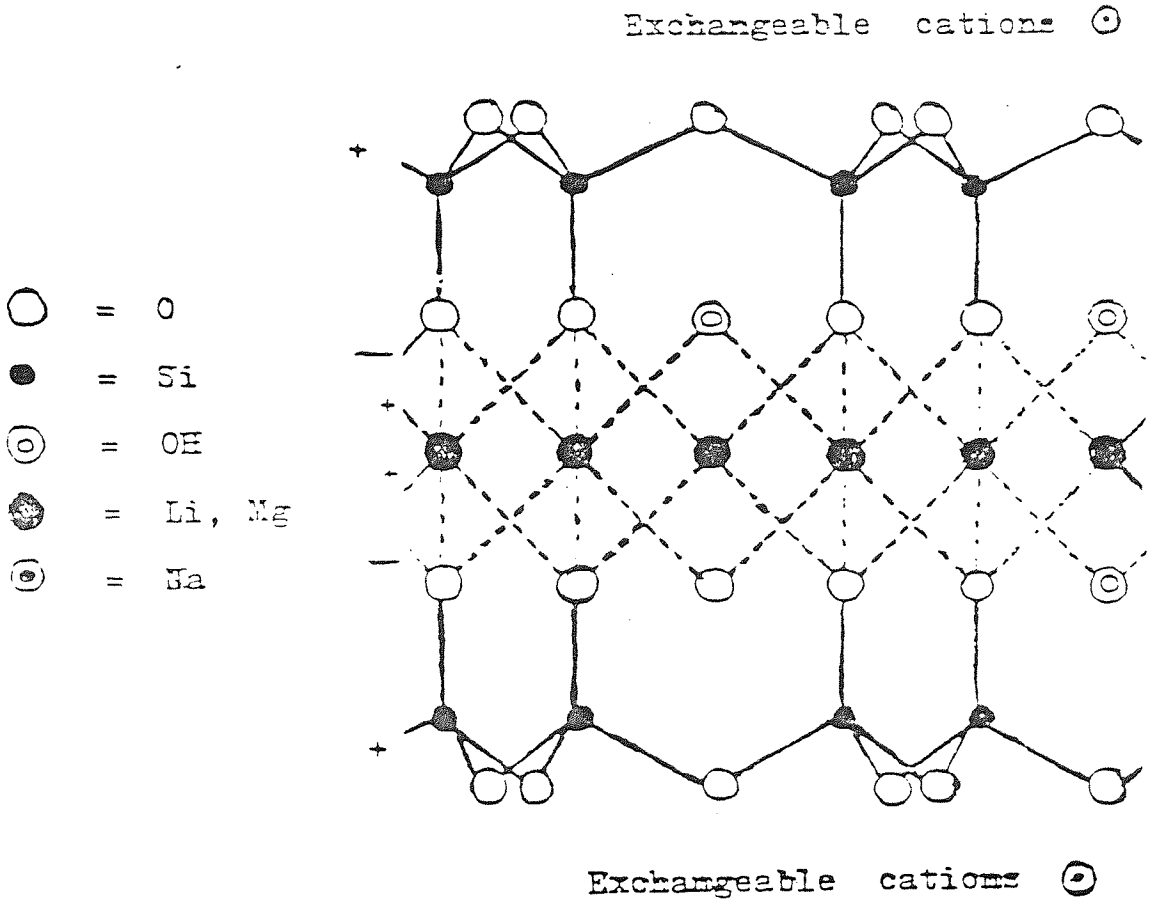

Fig. 1.6 The Side Elevation Structure of Hectorite

capacity (BEC) of the clay.

Unlike the kaolinite minerals, the montmorillonite group have only weak van der Waals attraction between unit layers due to tetrahedral sheets being positioned adjacent to other tetrahedral sheets. Hence interlayer expansion becomes easier, and polar organic molecules as well as inorganic cations can be sorbed onto the internal surfaces. Thus apparently two types of exchange site exist: (1) those within the interlayer region of the clay responsible for 80% of the exchange capacity in montmorillonite, (2) those on the external surface due to compensation of excess negative charge resulting from broken bonds.

The presence of the interlayer cations causes an increase in basal spacing of montmorillonites as compated with pyrophyllite although the difference is smaller than the six of the compensating cation due to its partial withdrawal into the holes of the tetrahedral sheet.

A basal spacing of 9.8Å is typical of a sodium saturated montmorillonite, although unlike kaolinite, this cannot be taken as the value consistently found for montmorillonite samples in general. Hydrated sodium-montmorillonite has a basal spacing of 12.5Å and calcium-montmorillonite has a value of 14.4Å. Hence the c-spacing is characteristic of the species sorbed in the interlayer region. Organic molecules may also be absorbed by montmorillonite showing consequent shifts in the c-spacing eg absorbed glycerol exhibits a c-spacing of 17.7Å.

Of the dioctahedral smectites, montmorillonite, beidellite and nontronite form the end-members and a complete set of solid solution exists between them. Montmorillonite has 0.33 of the octahedral aluminium atoms replaced by magnesium per unit formula so requiring 0.33 sodium ions to compensate for the excess negative lattice charge.

MONTMORILLONITE

$$Na_{0.33}\ |\ (Al_{1.67}\ Mg_{0.33})\ Si_4\ O_{10}(OH)_2 \quad <------> \quad Na_{0.33}\ |\ (Fe^{3+}{}_{1.67}\ Mg^{2+}{}_{0.33})\ Si_4\ O_{10}\ (OH)_2$$

NONTRONITE

BEIDELLITE

$$Na_{0.33}\ |\ Al_{2.22}(Al,Si_3)\ O_{10}\ (OH)_2 \quad <------> \quad Na_{0.33}\ |\ (Fe^{3+}{}_{2.22})\ (Al_1\ Si_3)\ O_{10}\ (OH)_2$$

There is also a series of minerals of the trioctahedral type with two end members represented by the formulae:

$$Na_{0.33}\ |\ (Mg^{2+}{}_{2.67}\ Li^{1+}{}_{0.33})\ Si_4\ O_{10}\ (F, OH)_2$$

HECTORITE

$$Mg_3{}^{2+}\quad (Al_{0.33}Si_{3.67})O_{10}(OH)_2)$$

SAPONITE

Apparently there is a complete range of solid solutions between the two extremes. Hectorite has 0.33 of its octahderal magnesium atoms replaced by lithium, per unit formula, which then necessitates the admission of 0.33 sodium ions to compensate for the negative lattice charge.

1.2 INTERCALATION AND ION-EXCHANGE

Ion exchange which refers to the replacement of ions within a structure from for example an aqueous solution, and intercalation, which refers to the insertion of extra ions, atoms or larger molecules into the structure of a solid, are important properties that are not exclusive to clay minerals. The same properties have been observed and studied in different materials such as TaS_2, zeolites and graphite. Clearly in order for such compounds to undergo one of the

above reactions, they must possess certain structural features in common with clay minerals, the most important of which is a degree of structural openness which permits foreign atoms or molecules to readily diffuse in and out of the crystal. For example in the case of graphite and TaS_2 intercalation compounds, the host crystals possess a layer structure where the layers are pushed apart as foreign atoms or ions penetrate the interlayer space. In the ß - aluminium structure open layers also exist which permit the easy migration of Na^+ ions. Zeolite molecular sieves possess three-dimensional aluminosilicate framework structures which contain networks of interconnecting cages and tunnels. They normally contain hydrated cations which may be readily exchanged by other cations using suitable ion-exchange procedure. The structural properties of clays are such that they allow both ion-exchange and intercalation reactions to occur.

1.2.1 Ion Exchange in Smectite Clays

The phenomenon of ion-exchange has significance in aspects of clay technology as diverse as agriculture, petroleum engineering, soil mechanics, organo-clays and radioactive waste disposal. The smectite minerals have the property of sorbing certain ions and retaining them in an exchangeable state. The exchange reaction is stoichiometric, the exchangeable ions being held around the outside of the clay structural unit. This property of ion-exchange is measured in terms of milliequivalents per gram and is called the cation exchange capacity (C.E.C)[1]. It is one of fundamental importance in the investigation of these materials because the nature of the exchangeable ion may influence substantially the physical properties of the materials[4].

A range of C.E.Cs exist for different clay minerals. There is no single C.E.C value that is characteristic of a given group of clay minerals and hence a range of capacities is given[1].

	meq/100g clay
Kaolinite	3 - 15
Halloysite	5 - 40
Montmorillonite	80 - 150
Vermiculite	100 - 150
Hectorite	40 - 70
Chlorite	10 - 40

There are three main causes of the C.E.C of minerals:

(1) Broken bonds around the edges of the clay platelets give rise to unsatisfied charges which can be balanced by adsorbed cations. The number of broken bonds (and hence C.E.C) increases with a decrease in particle size. In kaolinite, broken bonds are the major cause of exchange capacity.

(2) Substitutions within the lattice of trivalent aluminium for quadrivalent silicon in the tetrahedral sheet, and of ions of lower valence particularly magnesium for trivalent aluminium in the octahedral sheet may result in unbalanced charges within the platelets. In montmorillonite and vermiculite substitutions within the lattice cause 80% of the total C.E.C.

(3) The hydrogen atoms of exposed hydroxyls may be replaced by a cation which would be exchangeable. Depending on the actual cause of ion-exchange within certain clays, the exchangeable cations can either be held around the edges of the flakes as in kaolinite (broken bonds) or on the basal surfaces of the platelet (isomorphous lattice substitution).

1.2.2 Factors Affecting the Rate of Ion Exchange

The rate of ion exchange varies with the clay mineral, the concentration of the cations and the nature and concentration of the anions. Generally the reaction for kaolinite is most rapid, almost instantaneous. It is much slower for smectites. Apparently exchange on the edges of particles as in kaolinite can

take place quickly by penetration between montmorillonite takes much longer.

Particle size has a pronounced effect on kaolinite type minerals where broken bonds are the major cause of C.E.C but has a much less pronounced effect on smectites. A slight increase in C.E.C is noticed however, but this is probably due to broken bonds on the edges of clay platelets.

Temperature has a varied effect on the C.E.C. The exchange capacity of montmorillonite is reduced on heating but the reduction is not uniform and varies with the cation present. For non-expanding clays the available data indicates a gradual reduction in C.E.C with increasing temperature.

The replaceablility of cations is of great importance and a large amount of work has been devoted to the subject. Replaceability is not completely understood but it is know that it is controlled by a considerable number of factors. Increased concentration of the replacing cation causes an increase in the exchange rate since cation exchange is a stoichiometric reaction and the laws of mass action would hold. Jenny et al[134] have shown that the case of release of an ion depends not only on the nature of the complimentary ions filling the remainder of the exchange positions. It has been shown that as the amount of exchangeable Ca^{2+} ions on the clay mineral is reduced, the Ca^{2+} ion becomes more difficult to release. Na^{+}, however, becomes easier to release as the degree of saturation with Na^{+} ions becomes less. Other factors which influence the replaceability of cations are the valence of the ion, ie the higher the valence of a cation the more difficult it is to replace when already on the clay, and the nature of the clay mineral itself.

1.2.3 Theories of Cation Exchange in Clays

Numerous attempts have been made to develop a theory of cation exchange which would permit the quantitative expression of exchange data by an equation. The two general approaches that have been taken are based on (i) thermodynamic equilibria of exchange reactions (ii) kinetic considerations.

The thermodynamic approach has been better documented than the kinetic approach. Jenner[183], and Vageler and Wotersdorf derived empirical equations connected with adsorption isotherms. The general basis of these theories is Freundlich's adsorption equation or certain modifications of it. Thermodynamic arguments involving a more or less crude approximation have led to various mass action equations by Kerr[1], Vaneslow and Rothmund[1]. More recently Laudelout[6] has considered the thermodynamic argument in a wider sense and has derived equations in terms of the modern theories of electrolytes including such factors as chemical potentials, activities of ions and selectivity coefficients. Since it well documented Laudelout's work and the thermodynamic approach will not be considered further.

An understanding of the kinetics of ion-exchange has applications in two general areas; (i) it helps to elucidate the nature of the various ion transport mechanisms which contribute to the overall exchange rate and (ii) numerical perameters such as rate constants, mass transfer and diffusion coefficients derived from a rate investigation are of value in process control.

Kinetic theories of ion-exchange have been presented by Vageler and Woldersdorf,[136], Gapor and Jenny[133]. Vageler and Woldersdorf attempted to apply Langmuir's adsorption theory to the formation of two complexes formed by the adsorption of each kind of exchangeable ion. It was assumed that the rate of each adsorption is proportional to the concentration of the liquid phase of the ion being adsorbed and to the number of ions of the colloidal surface. These two theories are apparently based on the assumption that adsorption is a simple process involving a monomolecular layer on the clay surface. Ions are present in the system either in an adsorbed state or completely free. Neither of these two theories is entirely consistent with the concept of the diffuse double layer.

However, Jenny's theory represents the ions as present in a diffuse double layer. Each ion required to neutralise the charge on the particle is oscillating in an oscillation cell adjacent to a charged area on the clay particle surface. Other ions from the added electrolyte may enter the oscillation cell or may remain in the external phase.

It is now recognised[135] that the time dependent coupling of mass and charge transfer which epitomises the ion-exchange situation is extremely complex and it can be solved only by the use of computer techniques employing a sophisticated model. In the case of certain clay minerals, however, the use of much simpler models has furthered the understanding of the fundamentals within a specific range of experimental conditions.

1.2.4 Diffusion Kinetics[135]

The fact that the overall rate-controlling mechanism of ion-exchange was one of diffusion, was realised through experiment. Kunin and Myers showed that the ion-exchange rate depended on factors such as particle size, concentration and the degree of exchange which indicated diffusion rather than chemical reaction to be the rate determining step. Boyd first proved that the most fundamental mechanism of ion-exchange was one of several types of diffusion including film and particle diffusion. Film diffusion is the corrective transport of ions within the external solution. although this is not considered to play an important rate determining role, since efficient mixing should ensure a zero concentration gradient. Particle diffusion is applied to the case where diffusion or transport within the exchanging clay mineral is the rate-determining step. The quantitative aspects of this diffusion are more complex than in aqueous electrolytes since the whole internal phase is not available as a diffusion medium. A large fraction of the interior is occupied by the silicate clay structure which gives rise to a steric barrier to diffusion. The idealised case of particle diffusion is normally considered by the applications of Fick's first and second laws of diffusion.

However the boundary conditions and theoretical requirements necessary for correct application of Fick's laws imply that the mathematical relationships for film and particle diffusion kinetics are valid only for isotopic exchange. In real situations though, the interdiffusion of different ions, selectivity and the changing composition of the two phases results in non-constant interdiffusion kinetics. A further complicating factor is that different counter-ions possess different mobilities. Therefore during the counter diffusion process a diffusion

potential (electric filed gradient) is established which accelerates the slower moving ion whilst retarding the the faster ones. Thus superimposed on the ordinary diffusion mechanism is the coupling action of the diffusion potential which is effective in preserving the macroscopic flux and charge balance. Hence the quantitative treatment of particle diffusion is more advanced than that of film diffusion.

Various workers have used variations of the kinetic concept to bring about an enhancement of ion-exchange in a range of materials including zeolites and soils. Normally, the more commonly employed methods of bringing about ion-exchange are convective methods including the use of various types of stirring and shaking apparatus. Certain workers have examined the possibility of ultrasonic irradiation to bring about an enhancement of the ion-exchange mechanism, assuming that the mechanism was controlled by particle diffusion kinetics rather than thermodynamic factors. For example, Olmstead[137] described a method of dispersing soil by ultrasonic waves produced by a piezo-electric quartz crystal driven by a 1500W vacuum tube oscillator. It was found that the percentage of colloidal material extracted from solution was the same as that secured by an abrasive/shaking method. More recently Kiezel et al used ultrasound to effect ion-exchange in molecular sieves. These workers found that the Na^+ to Ca^{2+} exchange rate in 13x zeolites was considerably increased by application of a 800 Hz ultrasonic field. The application of ultrasound to ion-exchange in clay minerals is as yet largely unexplored although its possible success would be determined mainly by the nature of the mineral itself.

1.3 SOME IMPORTANT PROPERTIES OF SMECTITE CLAYS [4,139]

1.3.1 Adsorption[139]

Montmorillonites and hectorites have a very high adsorptive capacity for water and other polar molecules because of the high surface area of each clay platelet, all of which is available for adsorption, even in agglomerate (ie stacked) particles. The principal driving force for adsorption is the electrostatic attraction between the dipole of the polar molecule and the charge

of the exchangeable cation. The magnitude of the cation dipole attraction will depend on the dipole size and the cation's effective charge (which in turn depends on the valency, size, extent of hydration/solvation etc). A further contribution to adsorption particularly with large organic molecules, is that of van der Waal's attraction between the adsorbed molecule and the clay surface. The following methods may be used for measuring surface area:

(i) Air permeability: This measures only the outside surface of clay particles, so varies with particle size distribution.

(ii) Nitrogen adsorption: Under the conditions employed (high vacuum, low temperature) penetration into the particle occurs with adsorption on domain outer surfaces, and is not dependant on particle size.

(iii) Polar molecules: (H_2O, glycols). These can penetrate between stacked platelets and so measure the total surface area. The mechanisms of adsorption processes have been reviewed by Mortland.

1.3.2 Swelling

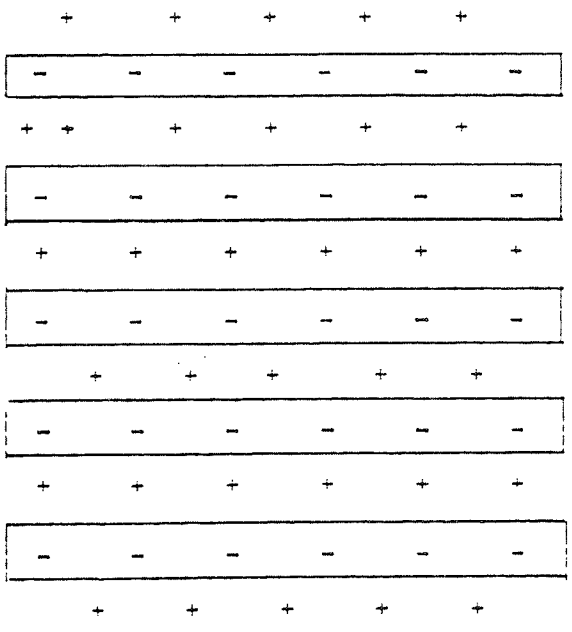

Fig. 1.7 Stacking of Clay Platelets in a Clay Particle/ Domain

Each mechanism is considered in turn.

1.4.1 Organic Complexes Formed by Cationic Exchange

Organic cations will be absorbed at clay mineral surfaces by ion exchange with cations neutralising the negative charges responsible for the cation exchange capacity of the mineral:

$$RNH_3^+ + M^+ \text{-Clay} == RNH_3^+ \text{-Clay} + M^+$$

where RNH_3^+ is some organic cation and M+ another species of cation. Many organic cations are positively charged because of protonation of amine groups as in the case of alkyl amines and amino acids . Other compounds such as urea and amides are protonated on the oxygen of the carbonyl group. Certain properties of organic cations differentiate them from metal ions also influence their adsorption on or displacement from clay surfaces. These properties are: (i) The ionic property is usually pH dependant. (ii) Other forces such as hydrogen bonding, ion-dipole and physical forces influence adsorption to the clay surface. Their relative importance depends on the molecular group, nature of the functional groups present and configuration of the molecule. (iii) the interaction of the inorganic ion with water may be of crucial importance in its interrelations with the clay surface and exchangeable metal ions residing there.

1.4.2 Protonation of Organic Bases

Many compounds may become cationic after adsorption at the clay surface through protonation. The sources for the protons for such a reaction are (i) exchangeable proton occupying cation exchange sites (ii) water association with metal cations at the exchange sites, or (iii) proton transfer from another cationic species already at the clay surface. The existence of an organic compound in an ionic form obviously depends on the acidity or proton donating power of the clay surface.

1.4 SOME RELEVANT CLAY ORGANIC INTERACTIONS

The scientific study of complexes formed by clays and organic substances was inititiated in the 1930's. Experiments involving simple organic chemicals and pure bentonite clay soon made it clear that the exchangeable inorganic cations could be replaced by pure organic cations,[6] and that uncharged polar compounds could enter the interlayer space without cations being released. Developments coincided with the rapidly increasing use of x-ray diffraction in clay minerals research. The most obvious manifestation of the introduction of organic molecules into the interlayer space of clays is a modification of the basal spacing of the mineral.

As a result of chemical and x-ray studies, mechanisms of the interaction of absorbed molecules and the clay surfaces were postulated. Other spectroscopic studies using special techniques of sample preparation have led to major breakthroughs in the investiagation of clay organic complexes. Infra-red (IR) spectra provide valueable information on molecular orientation in ther interlayer space and on mechanisms of interaction with the silicate surface, with the interlayer cations, with residual water and also between the molecules themselves. In contrast with XRD, IR spectroscopy deals directly with molecular orientations and does not require the existence of long-range ordering. Ultraviolet and visible, nuclear magnetic resonance, electron spin resonance and other techniques are now widely used to provide complementary information on bonding, kinetics of adsorption and the nature of the reaction occurring at clay surfaces.[142]

Clay organic interactions are multivariable reactions involving the silicate layers, the inorganic cations, water and the organic molecules. The study of clay-organic interactions is inevitably linked to intercalation chemistry or to put the term in its present context, 'the interlayer adsorption of molecules' which is one of the most active fields of chemisty today. The intercalation of organic molecules with some aromatic character is thought to proceed mainly by one of four mechanisms.[5] These mechanisms are cation exchange with positively charged molecules, protonation with organic bases, complexation with interlayer transition metal (or other) cations and charge-transfer with the clay lattice.

Addition of an electrolyte affects the equilibrium cation distribution. The increased total cation concentration in solution tends to compress the ion atmosphere towards the clay platelet surfaces. Hence at any point A some distance from the clay surface, a compression of the ion atmosphere results in more cations between A and the surface. If all the exchangeable cations are between A and the platelet, then the charge felt by A due to the platelet is zero. As the ion atmosphere becomes more diffuse, increasingly less insulation by cations means that A is increasingly affected by the negative charges within the platelet.

In a dispersion, two clay platelets which approach each other present a net negative charge with respect to each other when their ion atmospheres overlap, and they are subject to a face-to-face repulsion. However, at the edges there are positive charges, which are attracted to the negative face charge, if the edge is within the ion atmosphere. If a dispersion of Na-montmorillonite in distilled water is prepared, there is no gel formation since the ion atmosphere is very diffuse and the dominant effect is strong face-to-face repulsion which keeps the platelets well separated. If a small amount of electrolyte is added to this, the ion atmosphere is compressed, face-to-face repulsion decreases and the platelets approach each other close enough to allow face to edge cohesion, resulting in a rigid gel.

A dispersion can be peptised (ie treated so that it does not form a gel structure)by neutralising the positive platelet edge charges with an anion that is held strongly at the edge. An example is TSPP which ionizes to produce a complexing anion in solution which sits on the platelet edges and ties up positive charges.

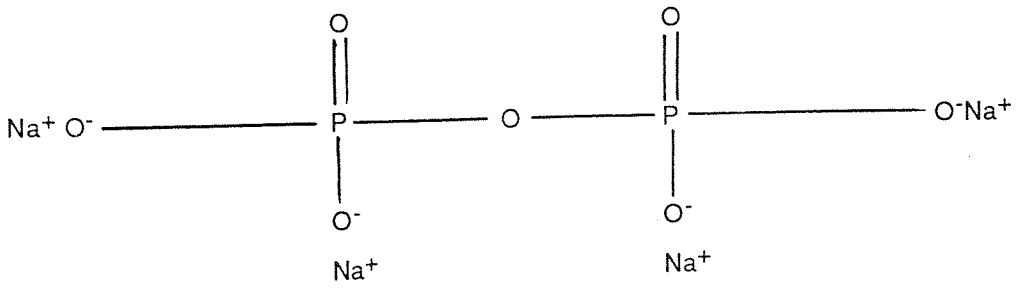

T.S.P.P: Tetrasodium Pyrophosphate

Fig. 1.7 represents stacked clay platelets in a dried clay particle; if this is exposed to an environment of polar molecules, then cation-dipole attraction will result in adsorption of the polar molecules on all the clay platelet surfaces ie it will be intercalated. If the interlayer separation if insufficient to accommodate the adsorbed molecules, then if the driving force for adsorption is strong enough, the platelets will be pushed further apart in order to create sufficient interlayer space for the adsorption/intercalation. This effect is known as swelling of the clay, since the particle size increases as more solvent is taken up. The extent of swelling depends upon the strength of adsorption, which in turn depends upon the nature of the cation, and the polar molecule. As the clay platelets are stacked regularly, they diffract x-rays and therefore x-ray diffraction study can be used to quantitatively monitor any small changes in the regular spacing of the clay layers.

1.3.3 Gelation of Solvents

A colloidal clay dispersion in certain conditions is thixotropic ie when stirred it is a free-flowing liquid, but otherwise it forms a rigid, structured gel.

A completely dispersed clay sample is a colloidal solution of individual clay platelets. In a solvent medium the exchangeable cations have a tendency to diffuse away into the bulk of the solution. Opposing this is their electrostatic attraction to the negatively charged sites within the clay lattice. The result is an equilibrium when an ion atmosphere exists around the clay platelets.

Fig. 1.8

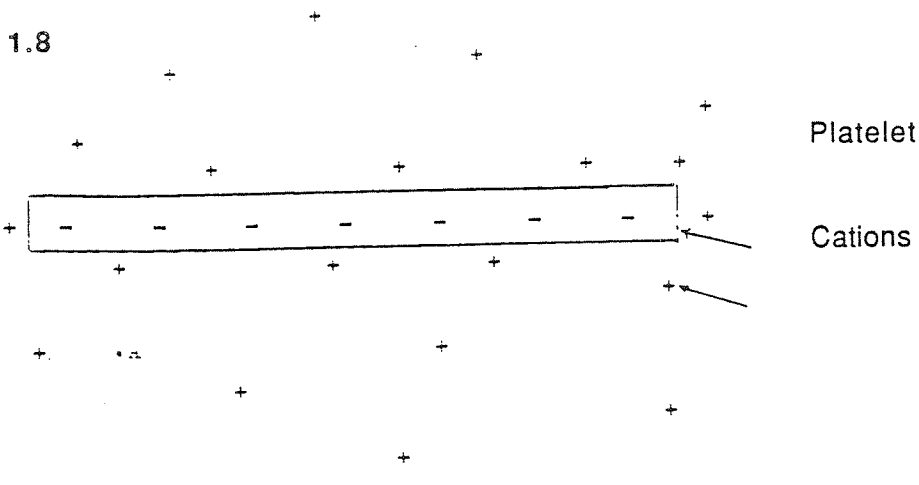

RNH_2 + H^+-clay ---> RNH_3^+ clay

base (acid) (salt)

Another process for protonation of organic molecules is by proton donation from water at the clay mineral surface. When water is associated with metal cations hydrolysis of th complex produces more of less H^+ depending on the metal ion involved. The more electronegative the metal ion, the more acidic will be the complex with water. Thus aqueous solutions of Al^{3+} are quite acidic while those of Na^+ are much less so. The hydrolysis of the hydrated metal cations is described as:

$$[M\ (H_2O)_x]^{+n} \rightleftharpoons [MOH\ (H_2O)_{x-2}]^{+n-2} + H^+$$

Acid Conjugate base

Where M is the metal cation involved.

The overall reaction involved when an organic molecule is protonated by such a process is:

$$M\ (H_2O)_x^{+n} + B \rightleftharpoons [MOH\ (H_2O)_{x-1}]^{+n-1} + BH^+$$

Where M is the exchangeable metal cation and B is the base in question.

1.4.3 Complexation of Interlayer Metal Ions

a) Non-transition Metal Ions

The nature of complexes formed by ethanol and acetone with cations of the most highly electropositive non-transition metals in the interlayer region of smectites has been investigated in detail by Bissada et al[143]. Their results have shown that interlayer separations are conditioned by the number of molecules adsorbed per exchangeable cation, which in turn depends on the interlayer cation present. Thus two molecules exist per K^+ ion and three molecules per Na^+ ion. For the

divalent cations Ca^{2+} and Ba^{2+} molecule/cation rations are 8-10 for complexes with 17Å basal spacing (two-layer complexes) and 4-5 when more stable 13-14Å complexes are formed.

b) Transition Metal Ions

Crystal field and molecular orbital theories afford explanations for the stronger bond energies in coordination complexes with the transition metal ions, and for the fact that no straight forward relationship exists between bond energy and ionic charge and radius. They also afford an explanation for ligand exchange reactions where water ligands are replaced by organic molecules.

Smectites saturated with transition metal ions form coordination complexes with many organic substances. At pH values where cation exchange reactions do not occur, complexes are also readily formed from aqueous solutions, for example with purines, amino acids, ethylenediamine and fulvic acids.[5]

The preparation and properties of smectite complexes with coordination compounds of transition metal ions and 2,2' - bipydridine have been extensively studied in recent years. Traynor et al[145] studied the ion-exchange and intercalation reactions of hectorite with tris-bypyridyl metal complexes. They managed to show that the binding of tris-bipyridyl metal complexes of the type $[M(bpy)_3]^{2+}$ ($M=Fe^{2+}$, Cu^{2+}, Ru^{2+}) to hectorite surfaces occurred by (i) replacement of Na^+ ions in the native mineral by cation exchange up to its cation exchange capacity and (ii) intercalation of excess salt beyond the exchange capacity. Intercalation reactions were found to be dependent on the nature of the counter-anion: SO_4^{2-},Br^->ClO_4^->Cl^-.

Abdo et al[122] studied the structure of $[Ru(bpy)_3]^{2+}$ and $[Cr(bpy)_3]^{3+}$ adsorbed in the interlayer region of of hectorite using IR and X-ray photoelectron (XPS) spectroscopy. Their interests in these compounds is due to the fact that they are used as sensitizers for the photodecomposition of water into H_2 and O_2. When these compounds are adsorbed in the interlayer space of smectites, both their reactivity and photophysical properties are different from the same properties in

homogenous solution. Also these properties depend on the water content of the clay. Thus the emission quantum yields of $[Ru(bpy)_3]^{2+}$ adsorbed on hectorite can reach values between 2 and 100 times higher than those observed in aqueous solution.

Other complexes have been obtained in recent years with Cu^{2+} or Ag^{+} saturated smectites and aromatic compounds that do not contain functional groups with basic or polar substituents capable of acting as electron donors for coordination with the exchangeable metal ions. Coordination compounds via donation of π electrons are well known. The prototype compound, dibenzene chromium $[(C_6H_6)_2Cr]$ is formed by direct interaction of the aromatic hydrocarbon with the metal halide in the presence of an appropriate reducing agent, halogen acceptor and a Friedel-Crafts activator. The cationic form $[(C_6H_6)_2Cr]^{+}$ is formed by hydrolysis of the reaction mixture with acid. It is therefore to be expected that π coordination compounds may also be formed in the interlayer region of smectites, although some of the compounds so formed have no counter part in reactions taking place in solution media. For example Cu^{2+} ions form π coordination compounds with arenes in montmorillonite[146] but not in homogeneous solution. The clay must be a stabilizing factor in preserving the complexes since aromatic compound-metal complexes commonly decompose when exposed to air.

1.4.4 Charge-transfer Interactions

The charge transfer mechanism as a means for interlayer adsorption is the least documented of the clay organic interactions. It has long been known that many aromatic amines convert to their coloured derivatives when brought into contact with clays. In these colour reactions of clays, both Lewis and Bronsted acidites are involved. Adsorption of the organic molecules is controlled by electron transfer and by cation exchange processes occurring at both the edge and the basal surfaces of the clay crystals. The colour reaction of benzidine with layer silicates is perhaps the best known and most widely studied system.

The conversion of the colourless neutral diamine (A) to its blue derivative is added to certain clays has been reported by several workers.[5] The agreed transformation involves electron transfer from the diamine to the mineral yielding the blue monovalent radical-cation. The stability and blue colour of this species are thought to arise from conjugation of the unpaired $2p_z$ electron from nitrogen to the π electron system of the aromatic ring. When the pH of the system falls below 2, it can accept a proton on the lone pair of electrons of the nitrogen atom giving the yellow radical cation.

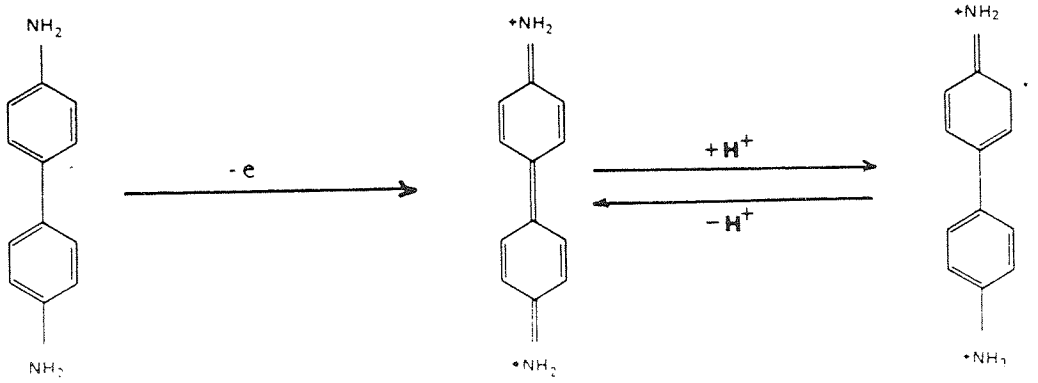

Clourless uncharged base | Blue monovalent radical-cation | Yellow divalent radical-cation

Fig. 1.9 An Illustration of the Influence of Clays and pH on the Transformation of Benzidine into its Radical-cation Forms (after Theng)[5].

Solomon et al[147] demonstrated that by using a range of clays each clay produced a blue colour of varying intensity when brought into contact with a saturated aqueous solution of benzidine hydrochloride, with the exception of talc. Montmorillonites previously treated with sodium hexametaphosphate which specifically adsorbs on the edge surface of the clay crystals, showed a decrease in activity whereas kaolinite and pyrophyllite similarly treated, failed to react. Solomon et al were able to show that octahedrally coordinated aluminium at exposed crystal edges of the clays were capable of accepting electrons from benzidine molecules ie acting on Lewis acids. Clays containing ferric ions also

underwent similar reactions ie Fe^{3+} accepting electrons and being reduced to Fe^{2+}.

In a particularly elegant study Tennakoon and Thomas[21] studied the surface and intercalate chemistry of monmorillonites using benzidine. They presented direct ^{57}Fe - Mossbauer spectroscopic evidence for the involvement of lattice-substituted iron(III)as an electron accepting site within the clays following intercalation of the clay by benzidine which resulted in the production of benzidine radical cations. The oxidation mechanism evidently involved electron transfer from adsorbed benzidine to structural ironIII in the octahedral layer of montmorillonites to form the mono-valent radical cation. Dehydration of the clay inevitably shifts the equilibrium in favour of the quinoidal yellow divalent cation. McBride et al[148] found that although oxidation of benzidine on smectites with structural iron III is rapid, slow oxidation occurs in the presence of O_2 on smectites with no significant Fe^{3+} content. Benzidine adsorption initially occurs via ion-exchange as the protonated mono- and divalent ions, but intercalation of benzidene in excess of the cation-exchange capacity can also occur on smectites.

In a recent study using the methylated derivative of benzidine, 3,3',5,5'-tetramethyl benzidine (TMB), McBride[149] examined the surface reactions of the TMB on hectorite such as adsorption and oxidation by applying x-ray diffraction, UV-vis, ESR and IR spectroscopy. McBride found that the molecule was adsorbed by cation exchange at low adsorption levels and oxidised to the yellow monomeric radical cation. At higher adsorption levels intercalation of TMB occurred in greater amounts than the cation exchange capacity of hectorite, and the π-π charge transfer complex (blue) becomes more evident.

Wudl and coworkers[11] were among the first to synthesize a new class of highly conducting, highly anisotropic charge-transfer complexes consisting of stacks of strong electron donors and acceptors. The best known examples of such a charge-transfer complex is the TTF-TCNQ system, where TTF (tetrathiafulvalene) is a strong electron donor and TCNQ (tetracyanoquinodimethane) is a strong electron acceptor. Torrance et al[10] succeeded in synthesising and characterising charge-transfer complexes where either TTF or TCNQ were added to a variety of metal ions to form metal-TTF or

metal TCNQ linear chain complexes. Son and Maeda[15] extended Torrance's ideas to clay chemistry and reported the first synthesis of a Cu-TNCQ complex within the interlayer region of montmorillonite. The resultant CuII - TCNQ complex was shown to be of the charge-transfer type and evidence was provided for the interaction between CuII ion and the -C≡N group of the TCNQ molecule.

Van Damme[24] and coworkers recently reported the intercalation of TTF into smectite clays. Using XRD, IR and UV-VIS spectroscopy they were able to show that intercalation proceeded via a charge transfer mechanism since the intercalated species were most probably TTF^+ cations. These species were found to be perpendicular to the clay sheets. However these workers were not able to provide any direct evidence for a transferal of charge from TTF to the clay lattice. Their conclusion were based mainly on the UV-visible absoprtion and infra-red data for hectorite-TTF films.

1.5 CLAY INTERCALATED METAL COMPLEX CATALYSTS

Recent advances in the intercalation chemistry of smectite clays have rekindled interest in these minerals as catalyst supports for metal complex catalysts. Although the immobilisation of complex catalysts in clays makes it possible to conduct solution-like reactions in the solid state and to minimise many of the technical and economic barriers associated with the use of homogenous solution catlysts, the advantages of catalyst intercalation go beyond mere immobilization. By modifying the chemical and physical forces acting on interlayer reactants one can often improve catalytic specificity relative to homogenous solution.

Metal complex catalysts intercalated in smectites are accessible for reaction under ambient conditions, provided that the interlayers are swollen to permit rapid diffusion of reagents. A solution-like environment exists when the interlayers are highly expanded by a large number of molecular layers of solvent. However, the gel like nature of such highly swollen phases makes them highly resistant to fluid flow and therefore unsuitable as heterogenous catalysts. For an intercalated clay molecular catalyst to be useful, the interlayers must be

mobile under intermediate degrees of swelling where the intercalate retains the mechanical properties of a genuine solid.

Pinnavaia[22], Stone and Fripiat[142] have independently used ESR and NMR experiments along with quasi-elastic neutron scattering studies to provide incisive information on the interlayer dynamics of clay intercalates. A general picture of the interlayer environment has emerged form these studies. At low degrees of interlayer solvation, the solvated exchange cations adopt oriented positions on the interlamellar surfaces. Though oriented, the solvated cations are in a dynamic state and undergo anisotropic rotations about specific molecular axes. Uncoordinated water molecules between the solvated cations are capable of translational diffusion within and between the 'cages' defined by the solvated cations and the silicate layers. Restricted motions and prefered orientations also have been observed for intercalated organic species.[150]

Clementz et al[151] and McBride et al found that hydrated Cu^{2+} ions in clay interlayers are highly oriented when solvated by one to three molecular layers of water. However, swelling the layers to 12Å with more water results in rapid tumbling and dynamic Jahn-Teller distortion of the hydrated Cu^{2+} ion. Quantitative estimates of the tumbling Mn^{2+} and VO^{2+} ions under comparable swelling conditions show their correlation times to be only 30 - 50℥. Larger than those observed for the same ions in dilute aqueous solution. It is this labile nature of solvated smectite clay interlayers at intermediate degrees of swelling which make possible their use as intercalation catlysts under mild reaction conditions. A number of different types of reactions have been catalysed by metal complexes in clays including the hydrogenation and isomerisation of alkenes and alkynes. Some examples are briefly given below.

Pinnavaia et al[152] found that di-rhodium acetate cations intercalated in hectorite react with triphenyl phosphine from methanol solution to form intercalated $Rh(PPH_3)n^+$ species

$$\underline{\overline{Rh_2(OAc)^{x+}}}_{4-x} \quad \underline{PPh_3} \xrightarrow[Me\ OH]{} \underline{\overline{2Rh(PPh_3)_n^+}}$$

where x=1 or 2, n=2 or 3 and the horizontal lines represent the silicate sheets.

$Rh)PPh_3)_n^+$ cations are catalyst precursors for the hydrogenation of alkenes and alkynes. Under the reaction conditions employed, the hydrogen uptake rate is lower for the intercalated catalyst than for the homogenous catalyst. However, the intercalated catalyst greatly reduces the extent of 1-hexene to 2-hexene isomerisation which accompanies hydrogenation. In this catalytic system, the reaction mechanism involves the formation of the metal dihydride and monohydride intermediates which are in protonic equilibrium:

$$\underline{\overline{Rh\ (PPh_3)_2}}^+ \xrightarrow{H_2} \underline{\overline{RhH_2(PPh_3)_2}}^+ \rightleftharpoons \underline{\overline{RhH(PPh_3)_2}} + H^+$$

Recently, Giannelis and Pinnavaia reported the intercalation of cationic metal cluster carbonyl complexes of the types $Ru_3(CO)_3(P\text{-}P^+)_3$, $H_4Ru(CO)_8(P\text{-}P^+)_4$ $Os_3(CO)_{11}(P\text{-}P^+)$ where $P\text{-}P^+$ is the phosphonium and phosphine ligand $Ph_2P(CH_2)_2P^+Ph_2(CH_2Ph)$.[153] Ion-exchange reactions of Na^+ -hectorite in aqueous suspension with solutions of the cationic clusters in acetone resulted in the formation of cluster clay intercalation compounds with d_{001} spacings in the range 22 - 27Å and gallery heights of 12.5 - 17.5Å. This was the first known example of a catalytically active metal cluster intercalated complex. The metal clusters complexes were found to be catalytically active for the isomerisation of hex-1-ene.

Monsef-Mirzai[154] and McWhinnie presented new results relating to copper(II) complexes supported on smectite clays together with details of an attempt to utilise the interlayer water of the clay species as an aqueous phase in phase transfer catalysis. The possible use of clay supported copper(II) dimers containing oxygen bridges and nitrogen heterocyclic ligands to catalyse ring opening reactions of phenols were investigated. The use of montmorillonite supported phase transfer catalysts such as the benzyltri-n-butyl ammonium ion was shown. Such catalysts were found to be effective for some organic and organometallic reactions and the advantages offered were greater ease of phase separation after the reaction, together with shorter reaction times.

Following on from the phase transfer catalysis work, Davison and McWhinnie[117]

have recently reported the synthesis of a trisbipyridyl cobalt III complex in the interlayer region of hectorite. This particular clay supported metal complex redox catalyst was found to efficiently catalyse the conversion of nitrobenzene to aniline, and more importantly offered the practical advantages of reuseability ease of work up and storage. The redox catalysis was effected both chemically ($NaBH_4$) and electrochemically (on a platinum electrode).

1.6 PILLARED CLAYS

Interlayer reactions in ordinary metal ion-exchange forms of smectite clays at high temperatures (>200°C) are precluded by the dehydration and collapse of the interlayer region. The limitations imposed by interlayer collapse have recently been circumvented by the intercalation of thermally stable, robust cations which act as molecular props or pillars in keeping the silicate layers separated in the absence of a swelling solvent. As illustrated in Fig.1.9 various types of cation have been use as pillaring agents including alkylammonium ions, bicyclic amine cations, metal chelate complexes, and polynuclear hydroxy metal cations.[8]

The concept of pillaring smectite clays was first demonstrated by Barrer and McLeod[155] when they utilised tetraalkylammonium ions to induce interlayer porosity in montmorillonite. Although Barrer further developed the chemistry of alkyl-ammonium clays, and even demonstrated their selective adsorption properties, the idea of pillaring clays to achieve porous networks seems to have been over shadowed by the rapid advances being made in the synthesis and applications of zeolites. However, there is renewed interest in pillared clays because it is now realised that the pore sizes can be designed to be larger than those of faujasitic zeolites. By varying the size of the pillar and/or the spacing between pillars, one has the potential of adjusting the pore size to suit a certain application. Thus pillared clays now offer new possibilities for catalysis of larger molecules such as those found in residual crude oils.

Among the pillaring agents illustrated in Fig.1.10 the alkylammonium and bicyclic amine cations decompose above 250°C and the metal chelates degrade below 450°C.

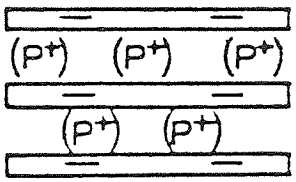

Fig. 1.9 Schematic Respresentation of a Pillared Clay

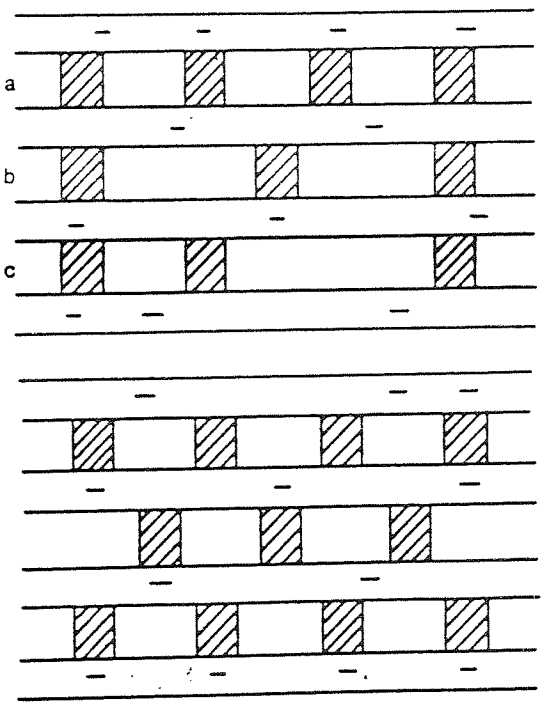

Fig. 1.10 (A) Irregular (B) Regular Distribution of Pillaring Cations in Clay Interlayers

However, at least two polynuclear hydroxycations are know to afford pillared phases which are stable above 500°C. Brindley and Sempels[157] and Yamanaka and Brindley[156] were the first to report that hydroxyl aluminium and -zirconium cations formed by hydrolysis over a specific range of OH^-/M^{n+} values yielded thermally stable clays with a surface area in the range 200 - 500m^2g^{-1} and interlayer free spacings of approximately 9Å. Using similar methods of preparation Lahar et al[158], and Vaughan and Lussier[159] independantly prepared analogous pillared phases containing hydroxy aluminium ions.

The hydroxyl-zirconium pillars are Zr_4 oligomer of the type $Zr_4(OH)_{16-x}$. Although Al_6 oligocations have been proposed as the intercalated species in the hydroxy-aluminium system, the structrue of the pillaring cations is almost certainly an Al_{13} oligomer related to the known cation $Al_{13}O_4(OH)_{24}^{7+}$ as suggested by Vaughan and Lussier[159]. A recent evaluation of ^{27}Al NMR and potentiometric data by Bottero et al[160] for hydrolysed solutions of Al^{3+} indicate $Al_{13}O_4(OH)_{28}^{3+}$ to be the dominant species present in the solution at the OH^-/Al^{3+} ratios used to prepare hydroxy aluminium pillared clays. Also, the interlayer free spacing (~9.5Å) of smectites intercalated with hydroxy-aluminium is consistent with the expected size of an Al_{13} oligomer.

The remarkable thermal stability of the Zr_4 and Al_{13} pillared smectites has been attributed to the formation of metal oxide clusters upon dehydroxylation of the hydroxy cations at elevated temperatures. In the case of Al_{13}-montmorillonite the overall interlayer reaction may be written:

$$Al_{13}O_4(OH)_{28+n}^{(3-n)+} \xrightarrow{-H_2O} 6.5\ Al_2O_3 + (3-n)H^+$$

Where the alumina is in the form of small clusters. Little is presently known regarding the structrue of the clusters or the location of the protons in the intercalate.

Shabtai, Lussier and Vaughan independantly disclosed the molecular sieving and acid catalytic properties of clays pillared by hydroxyl metal ions. For example Al_{13}- and Zr_4- montmorillonite when utilised as petroleum cracking catalysts give gasoline octane ratings comparable to zeolite catalysts, along with enhanced light cycle oil yields.

Al_{13}- montmorillonite is reported to adsorb molecules as large as mesitylene, but not methyl mesitylene, which have kinetic diameters of 7.6 and 8.0Å respectively. The highly selective molecular sieving properties of clays pillared by hydroxy metal cation requires a regular distribution of pillars and pores in the interlayer region. However it is known that the layer charge distribution in smectite clays is highly irregular[161], with the layer charge varying by as much as a factor of two from interlayer to interlayer. Thus one should expect pillared clays to exhibit a range of pore sizes, particularly for those intercalates containing hydrolytically stable pillaring agents such as $M(chel)_3^{n+}$, where ion exchange is the sole driving force for intercalation. With polynuclear hydroxy metal pillars however, the ions fill each interlayer region to essentially the same population density, regardless of the layer charge. In this latter case, the pillar spacing is decided by the radius of the hydrated cations, and the charge on the cations is regulated by the extent of hydrolysis, which is dependent on layer charge.

Although polynuclear hydroxy metal ions formed by hydrolysis in aqueous solution can yield pillared clays with interlayer free spacings in the range 5-20Å, the number of metals which can form suitable oligomeric species is limited. New approaches to the pillaring of smectite clays are being developed which promise to extend the number of pillaring species. It has been possible for example, to intercalate montmorillonite with silicic acid by hydrolysis of silicon acetyl acetonate in the interlayer region:[162]

$$Si\ (ac\ ac)_3^+ \xrightarrow[-H_{(ac\ ac)}]{H_2O} Si(OH)_4 + H^+$$

The silicic acid-clay complex exhibits an interlayer free spacing of 3Å and a nitrogen surface area of ca, $200m^2g^{-1}$. Also, a related approach involving hydrolysis and oxidation of metal cluster cations such as $Nb_6Cl_{12}^{2+}$ and $Ta_6Cl_{12}^{2+}$ affords clays pillared by small clusters of metal oxide approximately 10Å in diameter and stable up to 400°C.[6]

$$Nb_6\,Cl_{12}^{2+} \xrightarrow[-H_2,-HCl]{H_2O} 3Nb_2O_5 + 2H^+$$

A new addition to the literature on pillared clays is the synthesis of a new family of chromia pillared clays[163]. Although several polyoxycation exchange forms of smectite clays have been synthesized only a few such as the alumina and zirconia derivates noted in the above discussion, exhibit d_{001} spacings of around 18Å and gallery heights of ≈ 8.7Å, sufficient for facile intracrystalline catalysis. Clays pillared by catalytically useful transition metal oxides such as those of Nill, Cr and Fe typically exhibit chlorite-like spacings of ≈ 14.5Å when dehydrated above 250°C. The chromia pillared clays represented the first examples of novel intercalates in which the intracrystalline pillaring agent itself is the catalytic species. Pinnavaia et al reported intercalates with d_{001} spacings near 27Å. The intercalated Cr is expressed as $[Cr(OH)_{3-q}]^{q+}$ where q is the apparent net charge per chromium atom.

Fripiat et al[77] recently reported on a high resolution ^{27}Al and ^{29}Si solid-state magic-angle spinning NMR study of Al_{13} intercalated pillared clays. ^{27}Al and ^{29}Si represent a powerful new technique to the elucidation of catalytic processes in silicate structures. A great deal of literature has already been published on the catalytic properties of zeolites investigated by new NMR techniques[75]. The main conclusion of the French worker's study was that the Al_{13} pillaring agent is made from 12Al octahedra surrounding 1Al tetrahedron.

When pillared smectites with tetrahedral substitution are calcined, there was no evidence of a reaction between pillars and the smectite surface. On the contrary, in pillared beidellite a deep structural transformation was found to occur which was interpreted as the growth of a three dimensional network

grafted on the two dimensional network of the clay. The resulting high surface area solid was considered as a two dimensional zeolite, whose acidic properties were found to be comparable with those of Y-type zeolites.

The study of pillared clays is still in its infancy. Future developments undoubtedly will lead to new pillared systems and new catalytic applications.

1.7 SOME ASPECTS OF THE CHEMISTRY OF ALUMINOSILICATE GLAZES

1.1.1 Structure of Ceramic Glazes

During the last fifty years, a number of theories of glass formation and structure have been postulated, the most relevant to the study of ceramic glazes being the crystallite theory and the random network theory. The crystallite theory suggests that when glass fusions are cooling, crystalline or small crystals are formed which then make up the main body of the glass. These crystals need only be very small in size and they only need to merge slowly into the amorphous surroundings so that only a limited short range order exists.

The random network theory of Zachariasen and Warren[164] has been the subject of much criticism but it does provide practical ceramics with a good working model. The theory is based on the fact that the main building block in silicates is the silicon-oxygen tetrahedron, many of which can be arranged in a three-dimensional repeating pattern forming a network by sharing of the corner atoms.

Glazes and glasses also contain either metallic cations which according to this theory take up various positions in ther interstices of the silicate network. The silicon-oxygen tetrahedron is known as a network former while the species from which the cations are derived are known as network modifiers. Zachariason set out a number of conditions which must be fulfilled for any oxide to exist in the vitreous or 'glassy' state.

(i) The free energy of the vitreous oxide should not be much higher than that of the crystalline oxide.

(ii) The oxygen atoms in the network cannot be shared by more than two atoms of silicon or metal.

(iii) The coordination number of the cations should be low.

(iv) The polyhedra may have common angles but not common faces or edges.

The following oxides all exist independently in the vitreous state as well as in mixtures with other oxides.

B_2O_3	P_2O_3	M_2O_3	Sb_2O_3
SiO_2	GeO_2	P_2O_5	Al_2O_3
	Sb_2O_5		

The random network theory outlined provides a good working model for glaze technologists but the most recent ideas indicate that this approach has to be modified for results indicate that glass cannot be assumed to be a simple supercooled liquid since external conditions, when altered during firing process, have been found to induce changes in structure.

Steinberg,[165] whilst concentrating most of her work on strontium challenges the basic concept that bivalent cations are modifiers but suggests that they are in fact the chief building unit as previously suggested by Belov,[5(G)] working with x-ray diffraction. The strontium silicate structure is considered to adapt itself to the cation size rather than the cation merely filling suitable sites in a rigid lattice. The small cations though are still considered to be modifiers, as in the Zacharissen model, although Steinberg has shown that when a mixture of large and small cations are involved, the small cations can significantly alter the physical properties of the glaze, an effect which is more noticeable at certain cation radius ratios. She suggested that perhaps the structure is affected not so much by the ratio of the cationic radii as by the ratios of their bondstrengths

with oxygen. Although Steinberg's work involved the use of strontium primarily for aesthetic reasons after movement away from lead containing glazes, she claims to have proved the theory of Belov that divalent cations have a major effect on the structure of silicate glasses.

1.7.2 The Role of Raw Materials Aluminosilicate Ceramic Glazes[2,38,39]

Many raw materials are used in the preparation of ceramic glazes by there is no universal method for classifying glaze formulae; the particular method used depends on the point of view of the worker, whether he is a glass technologist, craft potter and chemist.

One customary method is to classify glaze materials into acidic, basic and amphoteric oxides, the molar sum of each group being expressed as an integer, as follows for potash feldspar.

K_2O	Al_2O_3	$6SiO_2$
basic	amphoteric	acidic

The acidic oxides such as silica are described as glaze network formers whilst, the basic oxides such as calcium oxide, magnesium oxide etc are described as network modifiers, so that by and large the system falls into line with the random network theory.

The method of introduction of various species affects the properties of the glaze quite profoundly. It is possible for two glazes to have the same molecular formula but different physical properties, purely because the constituent elements are introduced through the addition of different chemical species.

The most common method of introduction of a large number of elements into glazes is by using abundant silicate materials such as various feldspars, kaolinite, montmorillonite etc. Other components are added as required to give the glaze its desired properties. The silica content can be increased by addition

of either quartz or flint, while aluminium content can be increased by addition of alumina (Al_2O_3). Group I and Group II oxides are used to act as network modifiers to produce low temperature fusing mixtures by combination with various silica and alumina based formers. The modifiers are not necessarily added as oxides, but often in the carbonate of nitrate form. Thermal decomposition of the anion occurs to yield an oxygen anion liberating gaseous products.

1.7.3 Thermal Reactions of Clay Minerals and Other Ceramic Materials

Clay minerals are hydrous phyllosilicates principally of Al, Mg, Fe(II)and Fe(III)and less frequently other ions such as Li and Ni. Larger cations such as K, Na, and Ca are also involved in certain mineral groups. The main anions involved are O^{2-} and $(OH)^-$ but F^- ions are important in some cases. Almost by definition, clay minerals have particle sizes less than one micron and these small sizes are very important in relation to their thermal reactions. Frequently it is convenient to treat the chemical behavior of clay minerals in terms of their idealized formulae such as $Mg_3Si_4O_5(OH)_4$ for talc and $(Mg\ Li\ Al)_3\ Si_4\ O_{10}\ (OH)_2$ for hectorite. The principal thermal reactions and the appropriate temperature ranges in which they occur are considered in the following categories as summarised in tables 1.7.1 and 1.7.2

1.8 SOLID STATE NMR SPECTROSCOPY OF ALUMINOSILICATES INCLUDING CLAY MINERALS

1.8.1 Introdution

Although Nuclear Magnetic Resonance spectroscopy NMR has been a useful tool for examining the structure of molecules in solution since the early 1950s, it has only been since 1980 that developments in high field superconducting magnets and magic-angle spinning (MAS) have made NMR routinely useful for

Table 1.7.1 A Summary of Thermal Reactions for Dioctahedral Minerals

Kaolinite $Al_2Si_2O_5(OH)_4$ 1:1 type	Predehydroxylation State	—> 450 - 550°C	Metakaolin $Al_2Si_2O_7$	—> 900°C	Spinel type phase	—>1000-1100°C Mullite $Al_6Si_2O_{13}$
Pyrophyllite $Al_2Si_4O_{10}(OH)_2$ 2:1 type		—> 650°C dehydroxylate	Pyrophyllite	—> 950 - 1000°C		—> Mullite $Al_6Si_2O_{13}$
Montmorillonite	—> 150°C — 250°C	Montmorillonite anhydride	—>700°C Montmorillonite dehydroxylate	1000°C	—> Spinel type phase	1150°C Mullite
Muscovite 2:1 type		—> 750°C Muscovite dehydroxylate	—> 1050°C	—>Spinel type phase	—> 1250°C	Coriandum α–Al_2O_3 Mullite & other phase

Table 1.7.2 A Summary of Thermal Reactions for Trioctahedral Minerals

Serpentine $Mg_3Si_2O_5(OH)_4$ 1:1 Type	→ 550°C	Serpentine dehydroxylate	→ 600°C Forsterite (olivine) Mg_2SiO_4	→ 1100°C Forsterite + Enstatite $MgSiO_3$
Talc $Mg_3Si_2O_{10}(OH)_2$ 2:1 type	→ 900 - 1000°C Enstatite			
Saponite 2:1	→ 550°C	Saponite dehydroxylate	→ 750°C Enstatite	
Vermiculite 2:1	→ 500 - 800°C	Vermiculite dehydroxylate	→ 850°C Enstatite	
Chlorite $(MgAl)_6(SiAl)_4O_{10}(OH)_8$ 2:1 type	→ 450°C - 550°C	partial on complete dehydroxylation	→ 800°C Olivine	

examining the structure of solids.

NMR spectroscopy examines the local structural environment of atoms to at most the third and fourth nearest neighbours. For crystalline silicates, ^{29}Si and ^{27}Al MAS NMR has already proven useful in examining the validity of the aluminium avoidance principle, the extent of Al(4)/Si order and disorder, in determining the extent of polymerisation, determining the number of crystallographically distinct sites, estimating bond strength sums and Si-O-Si(Al) bond angles and detecting the presence of Al(4) and Al(6). As the NMR behavior of more nuclides (including ^{11}B, ^{15}N, ^{17}O, ^{19}F, ^{23}Na, ^{25}Mg, and ^{31}P) becomes better understood, it is clear that MAS NMR will become a powerful tool for examining the environment of a wide variety of species in a broad range of inorganic solids. The most significant applications are and will continue to be those problems that cannot be addressed using diffraction of TEM methods.

1.8.2 ^{29}Si NMR Studies of Aluminosilicate Minerals

To date, most studies of the solid-state NMR behavior of minerals have emphasised ^{29}Si. In addition to being a critical cation in silicate minerals, ^{29}Si can be observed at natural abundance (4.7%) and has spin I = 1/2, so that quadrupole effects do not occur.

For silicates with silicon as the only tetrahedral cation and for ordered Al/Si alumino silicates, the ^{29}Si peaks are typically quite narrow (1-4ppm full width at half-height [FWHH], with one peak for each crystallographically distinct site. Ordered low albite for examples produces three peaks corresponding to the three Si sites (Fig. 1.11).

Fig. 1.11 ^{29}Si Spectrum for Low Albite

Al (4) Si disordered phases while often containing only one tetrahedral site generally produce ^{29}Si spectra containing multiple peaks. These peaks arise from silicon with different numbers of Al(4) next nearest neighbours[45,46,50]. The peaks for these materials are usually broader than for ordered aluminosilicates probably because of greater than next nearest neighbour effects. In most naturally occurring silicates Si is tetrahedrally coordinated by oxygen. Such silicons have chemical shifts in the range of -60ppm to -120ppm relative to TMS. In a few high-pressure phases Si is known to be octahedrally coordinated by oxygen, eg stishovite which has a chemical shift of -191.1 ppm.

The nomenclature used to donate the polymerisation state of each silicate tetrahedral unit was originally proposed by Englehardt[93] as a result of his studies on ^{29}Si NMR of silicates in solution. In this system, isolated SiO_4 groups are denoted Qm units. Hence the extent of polymerisation of SiO_4 tetrahedra is described by the notation $Q^m(nAl)$, where m denotes the number of bridging oxygens to which Si is coordinated (0 - 4) and n is the number of Al(4) NNN atoms (0-4 for framework silicates, 0-3 for sheet silicates). Hence all silicate anions can be described by combinations of Q^m units where the superscript refers to the number of Si atoms linked via oxygen bridges to the central silicon. On this basis Q^o represents isolated SiO_4^{4-} groups, Q^1 disilicates and chain-end groups, Q^2 middle groups in chains, Q^3 chain branching sites and Q^4 fully cross-linked framework sites.

The first studies of the ^{29}Si MAS NMR behavior of silicates was by Lippmaa et al [45,46], who examined a variety of synthetic and natural materials. On the basis of their results they concluded that the ^{29}Si chemical shifts are determined primarily by the type of condensation of the SiO_4 tetrahedra. Increasing condensation from Q^o to Q^4 leads to increased diamagnetic shielding of the the ^{29}Si nucleus, and was found to approximately equal the effect observed for solutions. In other words, for ^{29}Si, chemical shifts were mainly affected by the electron density on the oxygen atoms of the SiO_4 tetrahedra and the nature of neighbouring atoms linked or coordinated to these O atoms influences the shift.

^{29}Si MAS NMR has been successfully used to probe the fine structure of aluminosilicate crystal structures. In these, the aluminium atoms can play two possible roles. Either they occupy octahedral sites and do not really form part of the aluminosilicate framework of linked tetrahedra, or more often, they occupy tetrahedral sites and do form part of the aluminosilicate framework. In the latter case, the chemical shift of a particular silicon atom depends on how many aluminium atoms are in its second coordination sphere. For instance, a Q^4 silicon atom in an aluminosilicate framework is surrounded by four other tetrahedral atoms and of these any number between zero and four may be aluminium atoms (ie AlO_4^{5-} tetrahedra). It is found that the chemical shift increases with decreasing number of aluminium neighbours, from -84ppm with four Al neighbours (as in nepheline $KNa_3(AlSiO_4)_4$) to about -108ppm with no aluminium neighbours as in quartz (SiO_4). The crystal structure of natrolite $Na_2(Al_2Si_3O_{10})2H_2O$ contains two types of Q^4 silicon atoms with three and two neighbouring aluminium atoms, respectively. This is reflected in the 29Si NMR spectrum which shows two peaks at - 87.7 and -95.4ppm. In some alumino silicates the Al/Si distributions are disordered over the tetrahedral sites which is indicated by a broadening of the NMR lines. An extreme example is sanidine $K(AlSi_3O_8)$ in which the Al/Si positions appear to be completely disordered. Its NMR signal gives a very broad linewidth which is about 20ppm at half-height.

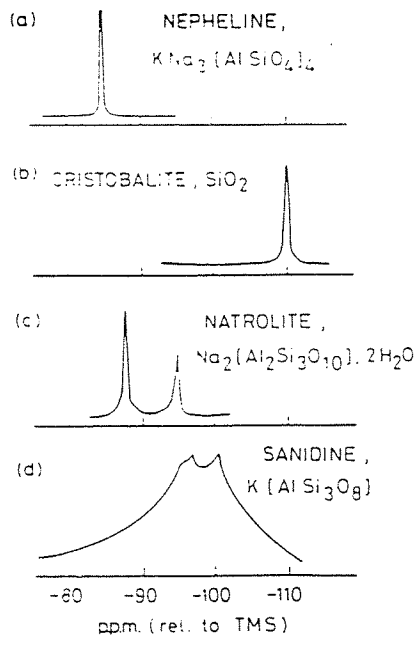

Fig. 1.15 Schematic ^{29}Si NMR Spectra of Silicates Containing Different Q4 Silicon Atoms (after Lippmaa et al)

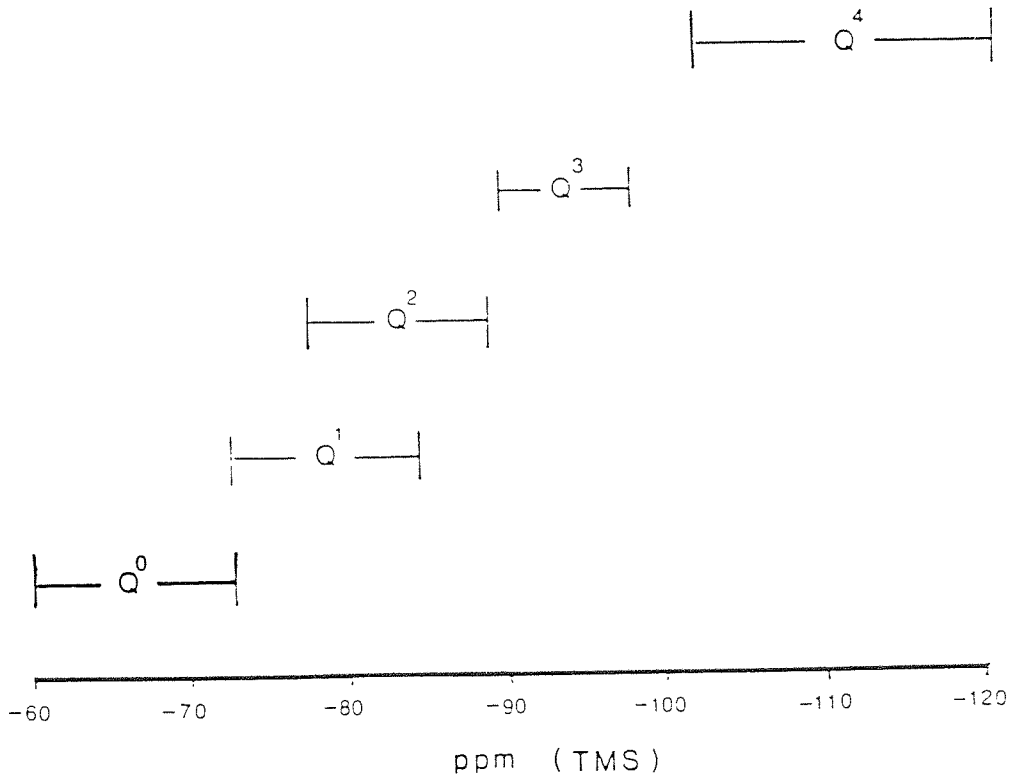

Fig. 1.12 ^{29}Si Shift Ranges for Silicates with No Al(4) or Al(6)

Fig. 1.13 ^{29}Si Shift Ranges for Framework and Sheet Silicates with Differing Numbers of Al(4) NNN

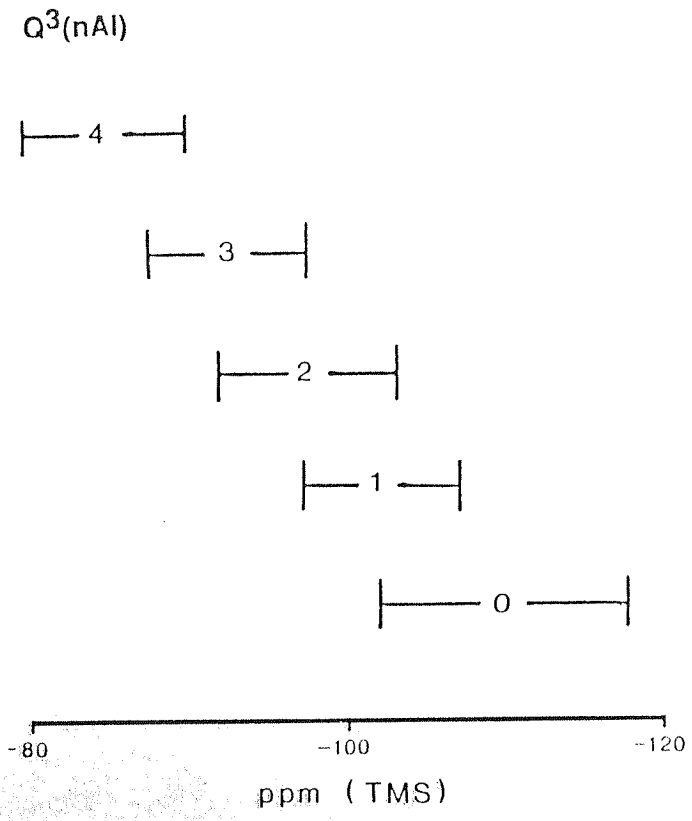

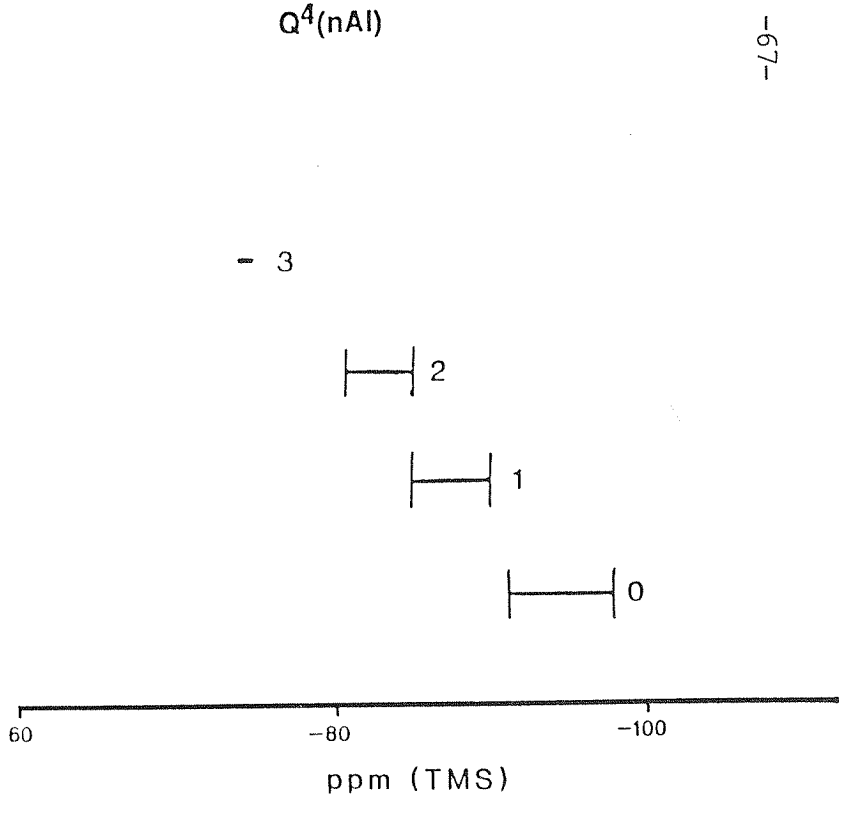

Fig. 1.13 ^{29}Si Shift Ranges for Framework and Sheet Silicates with Differing Numbers of Al(4) NNN

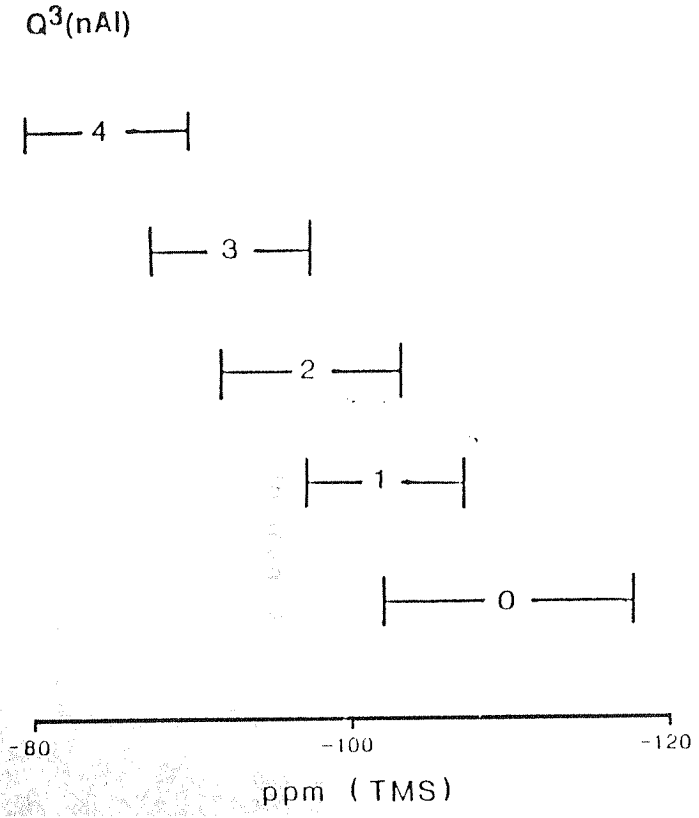

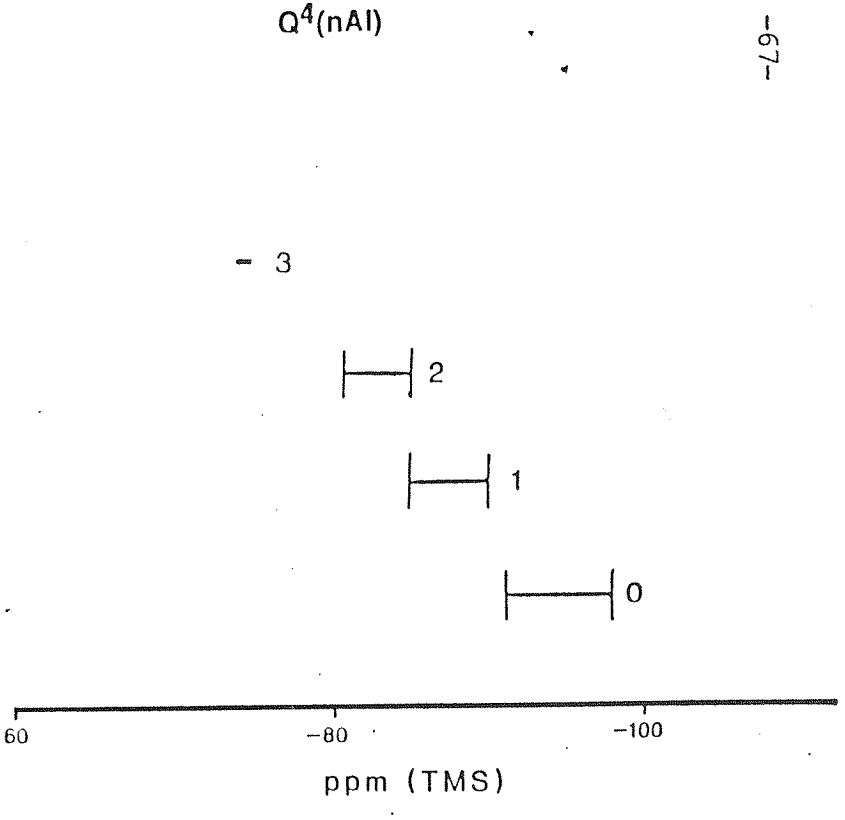

Lippmaa et al proposed that the chemical shifts for phases of each polymerisation state (Q^0 to Q^4) with no tetrahedral aluminium, should fall into discrete and analytically useful ranges depending on the number of Al NNN atoms, 0-4. Recent work [50] on a wider variety of silicates has shown that these correlations do not exist but that there is considerable overlap in these ranges. Fig. 1.2 shows the presently known ranges of silicon-29 chemical shifts for silicates with no tetrahedral aluminium. Much of the overlap of these ranges is due to the effects of octahedrally coordinated aluminium. Fig. 1.13 shows that, for silicates, silicon-29 MAS NMR can be used quite effectively to determine the extent of polymerisation of the SiO_4 tetrahedra.

The effect of tetrahedrally coordinated Al is to decrease the shielding at silicon ie to give less negative ^{29}Si chemical shifts. Fig.1.13 shows the presently known ranges of chemical shifts for Q^4(OAl) through Q4(4Al) materials.[76] This correlation has been extended to sheet silicates Q3 structures by Kinsey et al.[52] illustrated in Fig.D. Table shows the isotropic chemical shifts for some representative Q^0 to Q^4 silicates.

The ^{29}Si NMR spectrum of a calcium silicate, xonolite is shown in Fig. 1.14. The silicate anion of xonotlite is an infinite double chain or ladder with a cross link on rung at every third tetradedron in each chain as shown schematically below. Two types of silicon are present therefore -Q^2 and Q^3- and in the relative amounts of 2:1 respectively. The NMR peaks appear in the appropriate positions for Q^2 and Q^3 silicon atoms and their intensities are in the ratio 2:1 as expected.

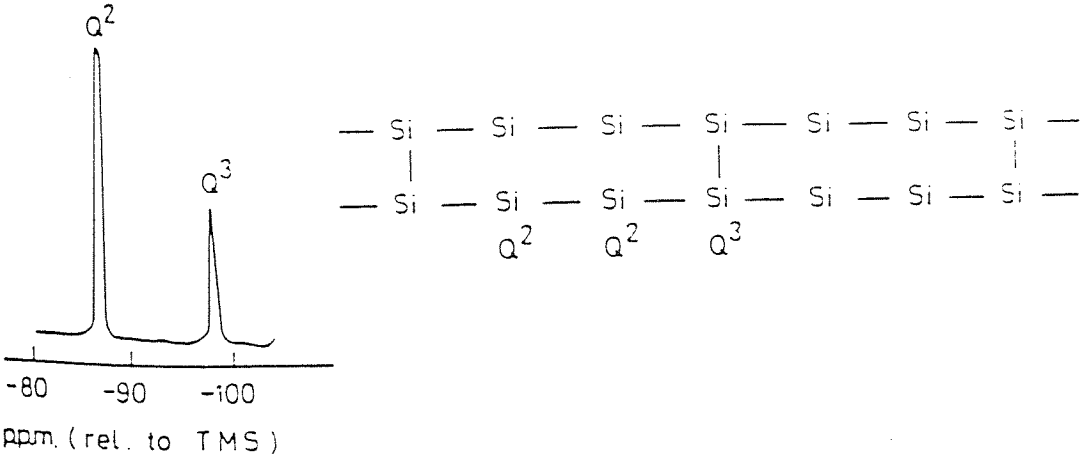

Fig. 1.14 The ^{29}Si NMR Spectrum of Xonotlite (after Lippmaa et al[45])

Perhaps one of the more important applications of ^{29}Si MAS NMR to date has been in the examination of the structrue of zeolite catalyst and sorbent materials[75]. One of the most important results of this work is that ^{29}Si MAS NMR can easily distinguish Si atoms with different numbers of next nearest neighbour (NNN) Al atoms in Al(4)/Si disordered aluminosilicates, and thus that the NMR data can be used to accurately determine the Si/Si + Al(4) ratios along with simulations assuming Gaussian peak shapes. All peaks in these spectra represent Q^4 sites, and the numbers next to the peaks in the (Si/Si + Al(4) = 0.83) spectrum give the number of NNN Al atoms associated with each peak. It is clear from these spectra that as many as five types of silicon sites [Q^4(OAL)-Q^4(4Al)] are present. It is clear that the average number of NNN Al atoms decreases as Si/Si + Al(4) increases and that it is possible to simulate the spectra very accurately. Similar spectra have been obtained by other workers for Al/Si disordered framework silicates. An early interpretation of spectra of this sort was that they indicate that the aluminium avoidance principle[36] is violated in these materials.[69] Recent work has shown that although the Al/Si distributions can be thought of as random they still obey aluminium avoidance.

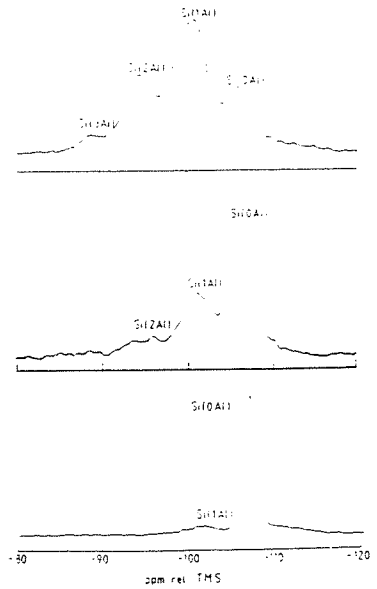

Fig. 1.16 ^{29}Si MAS NMR spectra of Faujasitic Zeolites with Differing Si/Si + Al(4) Ratios.

The study of MAS NMR has also been applied to the study of cements and concrete[37]. Despite their commercial importance, the chemistry of cements (mixed calcium silicates) is not well understood, mainly because the material is

amorphous and of variable composition. ^{29}Si MAS NMR has thrown much light on the reaction mechanisms of tricalcium silicate and dicalcium silicate, the main components of Portland cement, with water. While the anhydrous cement cannot is composed entirely of orthosilicate (Q^0) units, the hydrated material contains chain-end groups (Q^1) and, as hydration progresses, an increasing amount of middle units in polymer chains (Q^2). It is now clear that cement hydration relies on the formation of silicate polymers and that this reaction is responsible for the great mechanical strength of hydrated cements.

A very recent and useful addition to the literature on ^{29}Si in zeolite was the work by Fyfe et al on the Ultra-high Resolution ^{29}Si MAS NMR of sorbate and temperature induced changes in the lattice structure of ZSM-5. By preparing extremely high crystalline, highly siliceous samples and by careful optimization of all experimental parameters Fyfe et al obtained ^{29}Si spectra of ZSM-5 zeolite with linewidths of 0.06ppm (6Hz) at a proton frequency of 400MHz, yielding a spectrum for the unloaded zeolite in which 21 out of 24 resonances were observed. This represents a very considerable improvement over even the best resolved ^{29}Si spectra of zeolites and clearly makes possible the observation of changes induces in the lattice structure by both temperature and the presence of organic sorbates.

By comparison to the large amount of data available on zeolites and related aluminosilicates, relatively little has been reported in the literature on ^{29}Si NMR applied to clay minerals and layered silicates, until quite recently. Sanz and Serratosa[51] were among the first to carry out a detailed ^{29}Si and ^{27}Al MAS NMR study of 2:1 phyllosilicates. It was found that differences in ^{29}Si chemical shift values between these phyllosilicates were due to differences in the composition of the octahedral sheet. For example talc shows a single component at -97ppm and pyrophyllite one at -94ppm. Both talc and pyrophyllite have only one type of silicon (in the tetrahedral layer) and all silicons are in the same chemical environment. In the micas, phlogopite and muscovite, differences of environments for silicon were found to be a consequence of Al/Si distribution. Four possible discrete environments for silica were found within the tetrahedral sheet ie SiO_4 surrounded by three SiO_4, two SiO_4 and one AlO_4, one SiO_4 and two AlO_4, and three AlO_4. By analogy to the case for zeolites, they gave signals

with less negative values for the chemical shift as Al content decreased. Serratosa et al also considered the effect of second neighbour cations, including interlayer cations on the ^{29}Si signal position, and found that the line positions of tetrahedral silicon depends on the nature of the cations located as second neighbours of these nuclei in (i) the tetrahedral sheet (ii) the octahedral sheet (iii) the interlayer region. Kinsey et al[52] extended Serratosa's study to a wider range of layer silicates and clay minerals including the smectite clays montmorillonite and hectorite. These workers found that there was a systematic deshielding at silicon (less negative shift) with a decreasing Si /[Si + Al(4)] ratio and that there was a trend towards more positive chemical shifts for tetrahedrally coordinated Al with decreasing Si/Si + Al(4) ratio. No systematic relationship between the chemical shift of octahedrally coordinated Al and the Si/[Si + Al(4)] ration was found.

In a recent addition to the literature on ^{29}Si NMR of clays, Weis et al[90] published ^{29}SiNMR results on 2:1 layer silicates and reported correlations among chemical shift, structural distortions and chemical variations. The American workers found that with increasing substitution of Al(C.N. = 4) and increasing total layer charge, the ^{29}Si NMR chemical shifts for specific types of Q^3(nAl) sites in 2:1 layer silicates became progressively deshielded (less negative). This de-shielding was related to both structural distortions caused by a mismatch of the tetrahedral and octahedral sheets and by compositional variations in the octahedral sheets. One measure of structural distortion in 2:1 layer silicates, the amount of tetrahedral rotation within the crystallographic a-b plane, was linearly related with ^{29}Si chemical shift. In accordance with the findings of previous authors, ^{29}Si chemical shifts in tetrahedral phyllosilicates were systematically more negative (more shielded) that ^{29}Si chemical shifts in analogous dioctahedral structures. This difference is apparently related to a greater total electronegativity of the octahedral cations coordinated to the apical oxygen in trioctahedral phases (three Mg^{2+} cations) as compared to dioctahedral phases (two Al^{3+} cations). One for one substitution of Mg for Al in dioctahedral phases and Li for Mg in trioctahedral phases (both of which increase the negative 2:1 layer charge) seemed to cause deshielding at silicon, apparently due to a lower average electronegativity of the cations coordinated

to the apical oxygen. Different interlayer cations only caused small changes in the ^{29}Si chemical shift which was in agreement with the findings of Sanz and Serratosa.[51]

Layer charge in smectites (and also vermiculites) is closely related to properties such as swelling, cation-exchange-capacity and catlysis. Analysis by NMR is obviously an important new method of determination of layer charge in these minerals. In addition, NMR analysis of layer charge has important applications to petrologic studies of clay minerals such as mixed layer illite/smectite. Development of high layer charge in the smectite component of illite/smectite has been suggested to occur in K-deficient environments. Using ^{29}Si NMR data, the layer charge of the illite and smectite components of illite/smectite can be estimated independently.

Since the pioneering papers by Lippmaa and Engelhardt [45,46,47] a considerable amount of attention has focused on correlating ^{29}Si chemical shifts with crystal structural parameters. These parameters include the mean Si-O bond lengths, the secant of the mean Si-O-T bond angle[69] (or the mean secant), the sum of the Brown and Shannon bond strengths to the four oxygens coordinated to the silicons of interest,[50] and quite recently the prediction of group electronegativity sums from ^{29}Si chemical shifts.[44] Lippmaa et al [47] found that one structural factor which strongly affects the ^{29}Si shifts is the change in the Si-O-Si bond angle between interconnected SiO_4 tetrahedra. This is best illustrated by disilicates and cyclosilicates. Generally the high Si-O-Si bond angles give a high field shift due to increased diamagnetic shielding of the silicon nucleus, eg

		$\delta^{29}Si$/ppm
$Sc_2Si_2O_4$	SiOSi = 180°	-87.7
ß-$Y_2Si_2O_7$	SiOSi = 180°	-92.9

		$\delta^{29}Si$/ppm
$In_2Si_2O_7$	SiOSi = 180°	-95.3
$Ca_3Si_2O_7$	Si-O-Si = 133°>x>150°	-74.5
$Zn_4[Si_2O_7]$		-77.9

^{29}Si chemical shifts were also found to be affected by distortions of the SiO_4 tetrahedra. According to g eneral shielding theory, any distortion of t he symmetrical electron density distribution around the nucleus should cause paramagnetic (low-field shifts). This is best illustrated by different polymorphs of Ca_2SiO_4 and Al_2SiO_5.

	$\delta^{29}Si$		$\delta^{29}Si$
$\propto - Ca_2SiO_4$	-70.3	Al_2SiO_5 (Andallisite)	-79.8
β - Ca_2SiO_4	-71.4	Al_2SiO_5 (Kyanite)	-82.9
γ - Ca_2SiO_4	-73.5	Al_2SiO_5 (Sillimanite)	-87.1

In the above polymorphs the cation coordination changes regularly. Calcium coordination changes from $\propto$ = 6, β = 8, to ... = 10. Aluminium coordination changes from 5/6, 6, to 4/6. It was found that ^{29}Si shifts paralleled a decrease in coordination number. Lippmaa et al related the increased shielding (more negative) with coordination increase to the Pauling bond strengths. A decrease in cation coordination corresponds to a higher Pauling electrostatic bond strength S where S is given by

$$S = \frac{\text{Cation charge}}{\text{Coordination number}}$$

A decrease in coordination number therefore means more covalent bond character between the cation and oxygen. Using the same arguments cations with higher charge/radius rations (and higher electronegativities) such as Be^{2+}, Zr^{4+} and Al^{3+} shift the ^{29}Si chemical shift to the high field end, while Mg^{2+}, Na^{+}, Li^{+} and Ca^{2+} display low field shifts.

The anisotropy of the ^{29}Si shielding tensor has also received some attention and may become a useful tool for examining the symmetry of silicon sites. Grimmer et al[54] have shown that for silicon sites with axial symmetry (ie three Si-O bonds of almost equal length and one either longer or shorter) the shielding at silicon is less in the long Si-O bond direction and greater in the short Si-O bond direction. Smith et al[50] have determined the full shielding tensors for a variety of natural and synthetic silicates. Their results showed that the shielding anisotropy $\Delta\sigma\ [=\sigma_{33} - 1/2\ (\sigma_{11} + \sigma_{22})]$ and the asymmetry parameter

$\eta\ [=(\sigma_{22} - \sigma_{11})/(\sigma_{33} - \sigma_i)]$ are generally largest for soro - and chain silicates and smallest for framework silicates, although there are exceptions. In these expressions σ_{11}, σ_{22} and σ_{33} are the greatest, intermediate and smallest elements of the shielding tensor respectively; the isotropic chemical shift σ_i is one-third the trace (Tr) of the shieding tensor

$$\text{ie}\quad \sigma_i = 1/3\quad \text{Tr}\ (\sigma_{11} + \sigma_{22} + \sigma_{33})$$

1.8.3 ^{29}Si MAS NMR Studies of Ceramics and Glasses

The new possibilities of the ^{29}Si NMR method in the study of the structure and devitrification of silicate and aluminosilicate glasses have been investigated by a number of workers. The structure of glasses and ceramic materials has for a long time remained a somewhat elusive subject because the powerful x-ray diffraction methods are of limited value, particularly in addressing questions relating to short-range order in such disordered solids. Although x-ray absorption studies can provide information on short-range order, NMR technique have, in this respect, proved to be definitely superior.

One of the fundamental problems in the chemistry of non-crystalline solids is the distribution of the structure and the geometry of the main structural units present in glasses. It is well known that silica glasses contain SiO_4 tetrahedra interconnected by bridging oxygens. Increasing incorporation of alkali oxides into binary alkali-silicate glasses leads to a transformation of the bridging oxygens into non-bridging oxygens. More and more SiO_4 tetrahedra of the Q^n

type with three and less bridging oxygens are formed at the expense of SiO_4 tetrahedra with four bridging oxygens.

Among the first successful ^{29}Si NMR studies of glasses was carried out by Lippmaa et al[166] who carried out a ^{29}Si MAS NMR study of the structure of lead silicate glasses. Glasses of various composition $PbO{\cdot}SiO_2$, $(PbO)_2{\cdot}SiO_2$ and $(PbO)_4{\cdot}SiO_2$ were studied and the influence of thermal treatment was followed by ^{29}Si MAS NMR crystallisation of $PbO{\cdot}SiO_2$ glasses was found to be a complex process leading to a structure identical with that of the mineral alamosite.

Similar studies on soda-silica glasses by Duppree et al[62] showed that introduction of Na_2O into the SiO_2 network caused the progressive replacement of SiO_4 tetrahedra containing three bridging, and one non-bridging oxygen. When the addition of Na_2O reached 33mol%, all the SiO_4 tetrahedra were found to be replaced by the non-bridging type. On further increase of Na_2O there was progressive replacement by SiO_4 tetrahdedra with two non-bridging oxygens until complete replacement was achieved at 50mol% Na_2O. In binary alkali silicate and soda-line glasses a binary rather than a random distribution of Q type silicons was observed. Substitution of other modifier oxides for Na_2O changed the local environment of ^{29}Si and ^{23}Na in such glasses. This effect was found to be determined not only by the amount of modifier added, by by the nature of the cation.

Other independent studies have concluded that the ^{29}Si chemical shifts of alkali silicate glasses, are little different from those of crystalline compounds of the same composition[60,61]. However, linewidths behave quite differently. ^{29}Si linewidths for glasses are larger than those of the corrsponding crystalline materials by an order of magnitude. This reflects directly the structural differences the glassy and crystalline state. The long range order of the lattice is one of the basic properties of the crystalline state and in the simplest alkali silicates only a single type of SiO_4 unit is present. Due to this uniformity the linewidth is very small, typically of the order of 1ppm. In contrast to this, in

type with three and less bridging oxygens are formed at the expense of SiO_4 tetrahedra with four bridging oxygens.

Among the first successful ^{29}Si NMR studies of glasses was carried out by Lippmaa et al[166] who carried out a ^{29}Si MAS NMR study of the structure of lead silicate glasses. Glasses of various composition $PbO{\cdot}SiO_2$, $(PbO)_2{\cdot}SiO_2$ and $(PbO)_4{\cdot}SiO_2$ were studied and the influence of thermal treatment was followed by ^{29}Si MAS NMR crystallisation of $PbO{\cdot}SiO_2$ glasses was found to be a complex process leading to a structure identical with that of the mineral alamosite.

Similar studies on soda-silica glasses by Duppree et al[62] showed that introduction of Na_2O into the SiO_2 network caused the progressive replacement of SiO_4 tetrahedra containing three bridging, and one non-bridging oxygen. When the addition of Na_2O reached 33mol%, all the SiO_4 tetrahedra were found to be replaced by the non-bridging type. On further increase of Na_2O there was progressive replacement by SiO_4 tetrahdedra with two non-bridging oxygens until complete replacement was achieved at 50mol% Na_2O. In binary alkali silicate and soda-line glasses a binary rather than a random distribution of Q type silicons was observed. Substitution of other modifier oxides for Na_2O changed the local environment of ^{29}Si and ^{23}Na in such glasses. This effect was found to be determined not only by the amount of modifier added, by by the nature of the cation.

Other independent studies have concluded that the ^{29}Si chemical shifts of alkali silicate glasses, are little different from those of crystalline compounds of the same composition[60,61]. However, linewidths behave quite differently. ^{29}Si linewidths for glasses are larger than those of the corrsponding crystalline materials by an order of magnitude. This reflects directly the structural differences the glassy and crystalline state. The long range order of the lattice is one of the basic properties of the crystalline state and in the simplest alkali silicates only a single type of SiO_4 unit is present. Due to this uniformity the linewidth is very small, typically of the order of 1ppm. In contrast to this, in

glasses where there is no long range order, the geometry of the individual SiO_4 tetrahedron varies around the mean geometry. Each individual SiO_4 unit corresponds to a definite ^{29}Si chemical shift and the observed broadening of the signals relative to the signals of the crystalline compounds in an indicator of the distribution of the geometry of the SiO_4 units.

Murdoch et al[56] used ^{29}Si NMR to study the effect of network modifying cations on silicate and alumino silicate glasses. It was found that the NMR linewidth increased (reflecting a broader range of environments) as the polarising power of the cation was increased. Smaller, more highly charged cations created a greater variety in the distribution of silicate and aluminate tetrahedra. The validity of Lowenstein's rule[36] was also tested for glasses and it was concluded that due to the dependence of the NMR linewidth on Si/Al ratio, an aluminium avoidance effect was indeed present, and Lowenstein's rule was not disobeyed, even in highly disordered multi-component systems.

1.8.4 Aluminium - 27 MAS NMR Studies

^{27}Al is a very favourable nucleus for NMR investigations it has 100% natural abundance, with $I = 5/2$ and a chemical shift range of about 450ppm. The ^{27}Al linewidth is a sensitive function of the symmetry of the nuclear environment. As with other quadrupolar nuclei of non-integer spin the central ($1/2 \leftrightarrow 1/2$) transition is normally the only one observed and is independent of the quadrupolar interaction to first order, but is affected by second order quadrupole effects which are inversely proportional to the magnetic field.

Muller et al[83] were the first to carry out a systematic investigation of ^{27}Al MAS NMR spectra of polycrystalline aluminates (at 70.4MHz). They found that the isotropic ^{27}Al chemical shifts depend primarily on the coordination of aluminium with respect to oxygen. For tetrahedral coordination, chemical shifts of 55 to 80 ppm from $Al(H_2O)_6^{3+}$ are observed, while octahedral Al resonates at 0-22ppm. These results fully agree with the studies of Akitt et al[167] in

aqueous solutions of different aluminium species. As the structure of a number of aluminates has not been fully established by XRD due to the difficulty of obtaining single crystals, these results are of considerable value for structural elucidation in silicates, aluminosilicates and other non-crystalline solids. The presence of a range of ^{27}Al chemical shifts both for four and six-coordinated aluminium indicates that the shift is influenced not only by the coordination number but by other effects such as the composition of the second coordination sphere and the nature of the cation.

There have been several attempts to examine the variation in the chemical shift of tetrahedral aluminium with structure and composition, especially the Si/Si + Al(4). [49] Fyfe at al examined the ^{27}Al MAS NMR behaviour of zeolites

[85]. Their results showed that while there is a tendency for the chemical shift to become less shielded (more positive) with decreasing Si/Si + Al(4), there is also considerable scatter in the data. Fyfe et al attributed the scatter to the presence of aluminium rich domains with essentially constant Si/Si + Al(4) that become less abundant as the bulk Si/Si + Al(4) increases . Because the four tetrahedral NNNs to Al are all silicons (for zeolites with Si/Si + Al(4)> 1) the variation in the ^{27}Al chemical shift was therefore attributed to greater than - NNN effects, to differences in the non-framework cations and to structural variations (ie bond distances and bond angles).

Kinsey et al[52] found that for sheet silicates there was better correlation of tetrahedral ^{27}Al chemical shift with Si/Si + Al(4). These workers found a trend of increasingly positive chemical shift with decreasing Si/Si + Al (4) for the dioctahedral sheet silicates. the trioctahedral sheet silicates appeared to be displaced about 3ppm to less positive values. Correlations of octahedral ^{27}Al chemical shift with structure or composition are less well known, although the shielding at octahedral aluminium increases with increasing polymerisation.

CHAPTER 2

CHARGE TRANSFER INTERACTIONS IN CLAY MINERALS

2.1 INTRODUCTION

2.1.1 Electrically Conducting Organic Solids

Although the majority of inorganic and organic compounds exhibit low electrical conductivity in the solid state, certain classes of organic compounds do exhibit semi conductivity; the most prominent among these being polyacetelenes, polypyrolles and charge-transfer complexes. A great deal of research has been carried out during the last few years on such materials, but because of problems of atmospheric instability, degradation and brittleness, none have been commercially exploited.[3] Some of the better known organic conductors are described below.

Polyacetelenes consist basically of conjugated systems, Fig. 3.1a containing a skeleton of alternate double and single carbon to carbon bonds as in graphite. Polyacetelene itself has only modest electrical conductivity in the range 10^{-9} ohm^{-1} cm^{-1} to 10^{-5} ohm^{-1} cm^{-1}, comparable to semiconductors such as silicon since the π electron system is not completely delocalised. However, on doping polyacetylene with suitable inorganic comounds such as Br_2, SbF_5 and the alkali metals, conductivities as high as 10^3 ohm^{-1} cm^{-1} have been obtained[3].

Other conducting organic materials include polyparaphenylene (Fig 3.1b) (consisting of long chains of benzene rings) doped with $FeCl_3$, and polypyrolle (Fig. 3.1c) which is a heterocyclic molecule with a a five-membered C_4H_5N ring polymerised to give a long chain structure which effectively has alternating double and single bonds giving a delocalized π electron system.

In recent years there has been much effort directed to the study of two-component organic systems, in which one component is a π electron donor and the other is an electron acceptor. Some of these charge-transfer complexes behave as highly conducting synthetic metals, and a few are superconducting at low temperatures. Charge-transfer complexes are formed by the partial or total transfer of an electron from a donor to an acceptor molecule. By far the

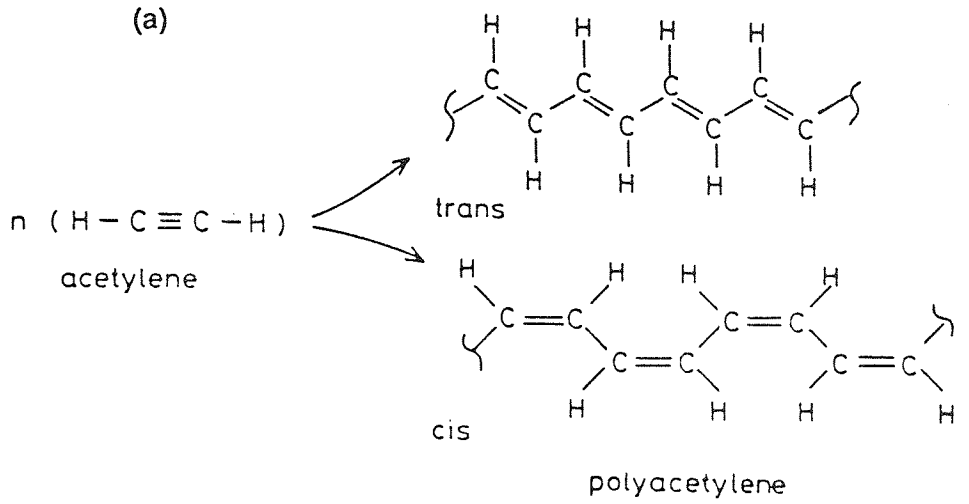

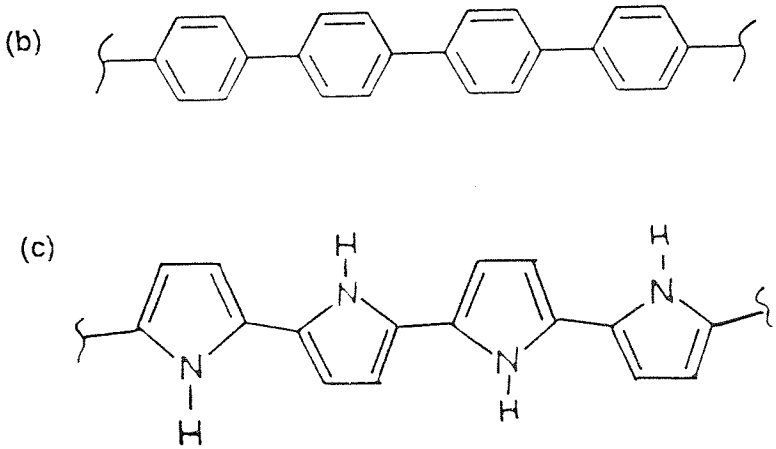

Fig. 2.1 (a) Polyactyclene (b) Poly paraphenylene (c) Poly pyrrolle

(b) (a)

Fig. 2.2 (a) TTF (b) TCNQ

most widely investigated conducting charge-transfer complex is the TTF -TCNQ system where TTF (tetrathiafulvalene) is a moderately strong electron donor and TCNQ (tetracyano-p-quinodimethane) is a powerful electron acceptor.

TTF itself is a planar, symmetrical molecule, easily oxidised to the radical cation and dication:

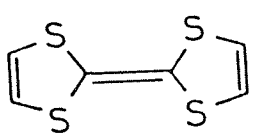

TTF

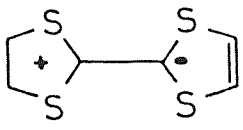

TTF^+

cation

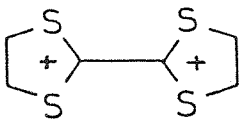

TTF^{2+}

dication

In the single crystal form TTF molecules are found to have their central double bonds aligned along one of the crystal axes. If the crystals are placed in an electrical field, conduction is possible by the transfer of an electron from a surface molecule to the anode and it can be replaced by another electron from a neighbouring molecule along the axis. Figure 3.3 is a stereoscopic projection showing TTF molecules stacked along the c-direction.

The structure of the TTF-TCNQ complex (Fig 2.4) takes the form of segregated donor/acceptor stacks.[31] Face-to-face molecules are interlocked and laterally displaced so that an exocyclic C=C lies over a ring of the molecule directly below.

The phenomenon of electrical conductivity results from the extensive π orbital overlap due in turn to the face-to-face stacking mentioned above. The extensive π overlap results in a delocalisation of electrons along one-dimensional stacks, enabling charge-density wavefunctions to form,[10] giving relatively free electron motion throughout the molecular network.

Apart from TTF-TCNQ many other charge-transfer complexes have been made where TTF is the donor molecule ef the metallotetrathiafulvalene system[9] such as $TTF_3(CuCl_2)_5$ where the acceptor is the chloride salt of a transition metal.

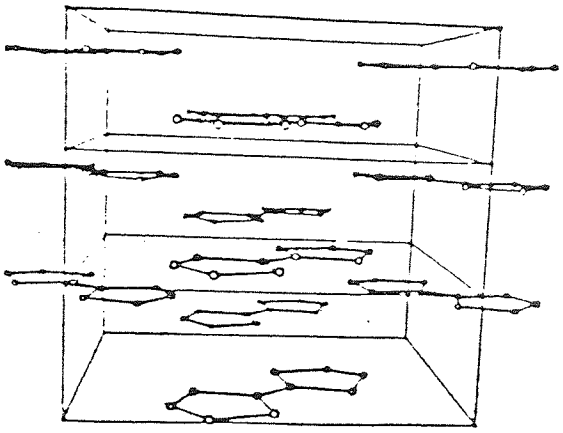

Unit Cell View of TTF

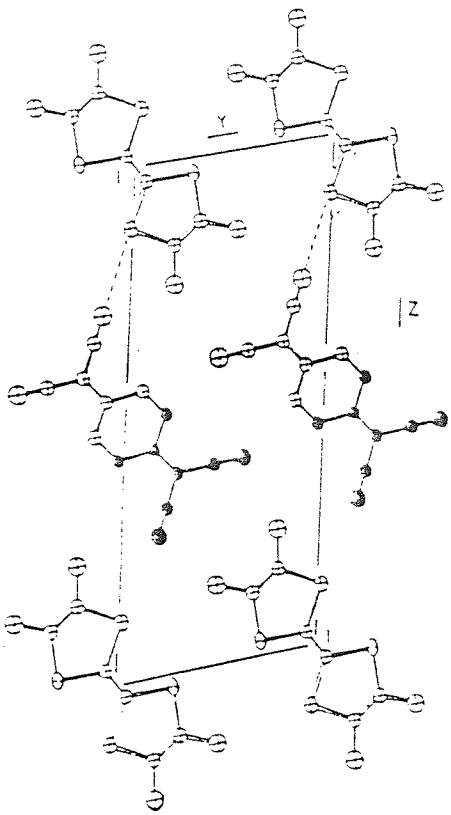

Fig **2.4** Crystal Structure of TTF - TCNQ

The unifying features of these materials are:

(i) The crystal lattices of conducting CT complexes consist of segregated stacks of planar donor and acceptor ions.

(ii) The stacks are partially charged eg $TTF^{0.59+}TCNQ^{0.59-}$.

(iii) The crystals are one-dimensional conductors, with the direction of highest conductivity being along the stack axis.

2.1.2 Charge Transfer Interactions in Smectite Clays

Although the technological potential of CT complexes is considerable, they have found little extensive application due to the brittle nature of their crystals. The problem is therefore of finding some form in which they can be used and applied easily, and at the same time retain their conducting properties. One way would be to incorporate the donor/acceptor system into a polymer matrix, but this would result in a loss of their one-dimensional nature. However, if the system could be intercalated within a lamellar or layered structure it might be possible to retain the stacking in two dimensions as in the single crystal form. Such a layered structure is found in the smectite minerals montmorillonite and hectorite.

2.1.3 The Present Work

Intercalation of organic species via a charge-transfer mechanism is not a new concept [5,21]. One of the best known cases of charge transfer intercalation is that of benzidine, which upon adsorption is converted to its coloured radical cations.[5]

Thomas and co workers studied the intercalation of benzidine with montmorillonite (which proceeds by electron transfer and intercalation of benzidine) and showed by means of an elegant ^{57}Fe Mossbauer study[21] that structural iron III accepted an electron to become reduced to iron II. Recent work by Macbride[13] and Schoonheydt[17] on TMB and proflavine adsorption by clays has led to a better understanding of charge-transfer mechanisms.

A strong interest in organotellurium charge-transfer compounds within our laboratory[27] led to the idea that other electron donors might enter into charge-transfer reactions with smectite clays; initial experiments concentrated on a study of TTF interactions with montmorillonite[30]. However, during the course of this work a paper was published by Van Damme et al[24], which described results on the intercalation of TTF with smectite clays. The major techniques used were XRD, IR and UV spectroscopy. Van Damme concluded that TTF could easily be intercalated in smectite clays and that the intercalated species were TTF^+ cations, implying that charge transfer within the clay lattice had taken place. Their evidence pointed to intercalated molecules having orientations perpendicular to the clay sheets and a lack of formation of molecular aggregates with metal-like properties.

Our work began by optimising conditions for adsorption of TTF by various montmorillonites, hectorite and laponite (a synthetic hectorite with no detectable paramagnetics), and was extended to a study of TTF interactions with interlamellar transition metal ions. Subsequently, ion exchange reactions of similar clays with $TTF_3(BF_4)_2$ were carried out. In contrast to the French workers, ESR and ^{57}Fe Mossbauer were the main techniques used in our work, while XRD, IR and UV-diffuse reflectance provided only complimentary evidence.

2.2 CHEMICALS

The clays used were montmorillonite, hectorite and laponite RD. The montmorillonite was obtained from Berk Ltd.

Composition: SiO_2, 52.2; Al_2O_3, 12.8; Fe_2O_3, 10.2;
TiO_2, 0.6; MgO, 0.5; CaO, 2.2;
K_2O, 0.4; Na_2O, 0.1;
H_2O (<105°C), 12.3; H_2O (>105°C), 6.6%.

Cation exchange capacity: 80 meq $100g^{-1}$.

The montmorillonite was converted to the sodium form prior to use by treatment with a solution of sodium chloride (5M).

Laponite RD (manufactured by Laportes Ltd) was virtually free of paramagnetics. It was used in the sodium form (cation exchange capacity: 70 meq $100g^{-1}$).

For some experiments laponite was exchanged with Cu^{2+} (via $CuCl_2$ H_2O in aqueous solution) and with VO^{2+} (via $VOSO_4$ in aqueous solution). Tetrathiafulvalene (TTF) was obtained from Aldrich Chemical Co. $[TTF]_3$ $(BF_4)_2$ was prepared following the literature. Acetonitrile (GPR) was used as a solvent for contacting clays with TTF and was obtained from Aldrich Chemical Co.

2.3 PHYSICAL TECHNIQUES

2.3.1 Conductivity Measurements

Precise electrical conductivities were measured by compacting small samples of the doped clays into thin discs using a standard IOT hydraulic press. The dimensions of the discs were recorded using a micrometer, accuracy (0.001mm). The faces of the discs were sputter-coated with 99.9% Aluminium, and having checked that no edge coating had occurred, gold contact wires were attached using a silver suspension paste. Three to five current readings were taken for each sample in the potential range 4.00v to 20.00v.

2.3.2 X-ray Powder Diffraction

Initial X-ray measurements were carried out using a Phillips PW1710 Automatic Diffractometer. Measurements were made on powdered samples (1.5 mm thick) in aluminium holders, using filtered Cu $K\alpha$ radiation. All data was processed by micro-computer and results were given in tables of angle (2θ), relative peak intensity, and d_{001} spacing (in angstroms).

Later X-ray work was carried out on a Phillips Diffractometer using Co Kα radiation (wavelength 1.791 Å). Each sample was prepared by evaporating from a solution of n-pentane, onto a glass slide. This was done to orient the clay particles in a certain direction to the x-ray beam.

2.3.3 Electron Spin Resonance

Electron spin resonance spectra were carried out on a JEOL PE-1x spectrometer operating in the x-band microwave region. All spectra were recorded at a modulation frequency of 100 KHz for normal high sensitivity measurements. Spectra were calibrated with a standard manganese (Mn^{2+}) samples incorporated into a magnesium oxide host lattice. The field sweep ranges used were 3500 $\pm$ 500 G and 2500 $\pm$ 2500 G.

2.3.4 Infra-Red Spectroscopy

Initially, IR spectra were recorded on a Parkin-Elmer 599B IR spectrometer, equipped with a D99 data station. Samples were prepared as kBr discs and run between 4000cm^{-1} and 250cm^{-1}. Selected samples were repeated later on, on a Perkin-Elmer Fourier Transform IR spectrometer. Between 10 and 20 scans were recorded for each sample. No further enhancement of the spectra was observed after 20 scans.

2.3.5 Diffuse - Reflectance Spectroscopy

Diffuse - Reflectance spectra were recorded using a Pye Unicorn SP800 instrument with a Diffuse-Reflectance attachment. Magnesium Oxide was used as a standard and samples were run between 800 and 200 cm^{-1}.

2.3.6 UV-Visible Spectroscopy

Ultra-violet/Visible spectra were run between 800 and 200cm-1 on a Pye-Unicam SP1800 UV spectrophotometer. Acetonitrile was used as a solvent blank.

2.3.7 ^{57} Fe Mossbauer Spectroscopy

^{57}Fe Mossbauer spectra were measured with a constant acceleration spectrometer of standard design. Isomer shifts are relative to iron metal.

2.4 EXPERIMENTAL

2.4 Part 1 : Clay - TTF Reactions

A series of reactions were carried out in which accurately weighed quantities of TTF dissolved in acetonitrile were added to sodium montmorillonite. The concentration of TTF was varied from 10 millimoles to 300 millimoles of TTF per 100g of dry clay. In a further set of reactions the contact time between clay and TTF was varied.

2.4.1 Procedure 1

(a) Sodium montmorillonite (1g) was stirred in acetonitrile (15ml) in a two-neck 50ml round-bottom flask. A known quantity of TTF dissolved in the minimum of acetonitrile was then added to the clay. The mixture was gently refluxed with stirring for two hours. After two hours, the product was filtered under vacuum and washed with two 25ml portions of acetonitrile. The filter cake was air-dried in a desiccator for one week before grinding in an agate pestle and mortar. A set of ten such reactions was carried out, with the TTF concentration stepped up gradually from 10 millimoles to 300 millimoles.

(b) In a separate set of experiments a known quantity of TTF (50 millimoles) was added to sodium montmorillonite (1g). The mixture was refluxed as before but for different contact times, progressing from 1 hour to 6 hours. For subsequent preparations it was decided to use a reaction time of 4 hours as the clay showed no further colour change upon washing after this time.

(c) Reactions based on procedure 1 were carried out in which smectite clays exchanged with different interlayer cations such as Cu^{2+} and VO^{2+}. The preparations are summarised in table 2.1 below:

Table 2.1

Clay Used	Interlayer Cation	Concentration of TTF millimoles/100g clay
* montmorillonite	Na^{+}	50, 100, 150
* montmorillonite	Cu^{2+}	50, 100, 150
* hectorite	Na^{+}	50, 100, 150
laponite	Na^{+}	50, 100
laponite	Cu^{2+}	50,75, 100
laponite	VO^{2+}	50

2.4.2 Procedure II

Clays were contacted with TTF using a slightly different prodecure from I, to eliminate the effect of UV light and refluxing temperatures (40 - 45°C) which could cause decomposition of TTF molecules.

A weighed quantity of clay (1g) was stirred in acetonitrile (10ml) for 15 minutes. TTF (150 mmoles) was dissolved in the minimum amount of acetonitrile and added to the clay slurry, in conditions of darkness. The reaction vessel was covered with aluminium foil to eliminate light. The mixture was stirred for 48 hours at ambient temperature (20°C). After 48 hours the product was removed by centrifugation, washed with acetonitrile (2 x 25 ml) and air-dried for a week.

2.4.3 Part II : Ion Exchange Reactions with $[TTF]_3(BF_4)_2$

In the previous experiments, uptake of neutral TTF molecules had relied mainly upon an adsorption mechanism, a different approach was adopted using ion-exchange[21] as the main "driving force" for incorporation of the organic cations into the clay. The fluoroborate salt of the TTF monocation was ion-exchanged quantitatively with sodium laponite, and the release of Na^+ ions was monitored by a flame emission method. The uptake of TTF^+ cation was monitored by UV-visible spectroscopy.

2.4.4 Preparation of $TTF_3\ (BF_4)_2$ [20]

$$3\ TTF + 2HBF_4 + H_2O \xrightarrow{CH_3CN} \underset{(I)}{TTF_3\ (BF_4)_2} + 2\ H_2O$$

Preparation of the fluoroborate salt was based on the above stoichiometric equation, where (I) is a purple-black crystalline solid, soluble in hot acetonitrile, but sparingly soluble in cold acetonitrile.

TTF crystals (1.75g) were dissolved in hot acetonitrile (60ml). Hydrogen peroxide (30%, 0.324 g) was added to the solution of ice-cold fluoroboric acid (48%, 1.084g). This mixture was added dropwise with stirring to the TTF/CH_3CN solution. The product was then refrigerated for one hour.

Approximately 1.15g of black shiny crystals were formed. The product was suction filtered and washed with cold acetonitrile to remove impurities. A second crop of crystals (300mg) was obtained by evaporation of the solvent to 30ml.

2.4.5 Addition of $[TTF]_3$ $(BF_4)_2$ to Clay

As shown in table 3.2, five standard solutions of $[TTF]_3$ $(BF_4)_2$ in hot acetonitrile were prepared by dissolving accurately weighed quantities of the salt and making up to 25ml in graduated volumetric flasks.

Concentration of $[TTF]_3(BF_4)_2$ (meq per 100g clay)	Mass of $[TTF]_3(BF_4)_2$ mg^{-1}	Volume of CH_3CN ml^{-1}	Mass of Clay g^{-1}
40 meq	31.4	25	0.1
50 meq	39.3	25	0.1
60 meq	47.2	25	0.1
70 meq	55.0	25	0.1
80 meq	62.9	25	0.1

Each of the standard solutions of $[TTF]_3(BF_4)_2$ was added to Na^+ laponite (0.1g) in a round bottom flask. The mixtures were gently refluxed for 48 hours with stirring at ambient temperature. After 48 hours the supernatent was removed by centrifuging the contents of the flask. The clay was separated, washed with acetonitrile (2 x 10ml) and air-dried for one week.

RESULTS AND DISCUSSION

2.5.1 Appearance of Products (Procedure 1)

Table 2.3 Clays Contacted with TTF (>50mmoles)

	Colour Before Contact with TTF	Colour After Contact with TTF
Na^+ Montmorillonite	Yellow	Dark Brown
Cu^{2+} Montmorillonite	Yellow/Green	Dark Brown
VO^{2+} Laponite	Green/Blue	Light Brown
Cu^{2+} Laponite	Blue	Dark Brown
Na^+ Laponite	White	White
Natural Hectorite	White	Light Brown

Table 2.4 Clay Contacted with $[TTF]_3(BF_4)_2$

	Colour Before Contact with $[TTF]_3(BF_4)_2$	Colour After Contact with $[TTF]_3(BF_4)_2$
Na^+ Laponite		
40meq		purple/brown
50meq		purple/brown
60meq	white	purple/brown
70meq		purple/brown
80meq		purple/brown
Cu^{2+} Laponite	Blue	Brown
Na^+ Montmorillonite	Yellow	Brown
Cu^{2+} Montmorillonite	Yellow/Green	Brown

2.5.2 Electron and Resonance Results

Table 2.5 ESR Results for Clays Before Contacting with TTF

	g - value (± 0.002)	Appearance of Signal
Na^+ Montmorillonite	-	Extremely Broad
Cu^{2+} Montmorillonite	g = 2.102	
Na^+ Laponite	-	No Signal
Cu^{2+} Laponite	g_{11} = 2.264 $g_{\perp}$ = 2.015	Anisotropic Four Line Spectrum
Vo^{2+} Laponite	g_{11} = 1.944 $g_{\perp}$ = 1.948	Anisotropic Eight Line Spectrum
TTF (crystals)	-	No Signal
TTF/CN	-	No Signal

ESR Results

Table 2.6 Clays Contacted with TTF by Procedure 1

	Concentration of TTF/mmoles	g - value (±) 0.002	Appearance of Signal
Na^+ Montmorillonite + TTF	<50	-	No Signal
	50	-	No Signal
	150	g = 2.005	Weak, broad signal
Cu^{2+} Montmorillonite + TTF	50	g = 2.002	Signals broadened by interference from paramagnetic framework centres
	100	-	
	150	g = 2.0075	

ESR Results

Table 2.7 Clays Contacted with TTF Using Procedure I

	Concentration of TTF_3 mmoles^{-1}	g - value (± 0.002)	Appearance of Signal
Cu^{2+} Laponite + TTF	50	g = 1.999	Strong, sharp single line resonances with complete loss of the anisotropic Cu^{2+} signal
	75	g = 2.007 (3)	
	100	g = 2.004 (7)	
VO^{2+} Laponite + TTF	50	g_{11} = 1.939	Anisotropic signal retained, but with reduction in intensity
		g_1 = 1.948	Slight change in g_{11}
Na^{+} Laponite + TTF	50	-	No signal detected
	150	-	

ESR Results

Table 2.8 Clays Contacted with TTF Using Procedure II

	TTF added mmoles^{-1}	g - values ± 0.002	g - values repeated after 3 months
Na^+ Montmorillonite +TTF	150	g = 2.025	g = 2.0067
Na^+ Laponite	150	g = 2.027	No Signal
Cu^{2+} Laponite	150	g = 2.027	g = 2.005

Table 2.9 Na^+ Laponite Ion-Exchanged with $[TTF]_3(BF_4)_2$

Concentration of $[TTF]_3(BF_4)_2$ /meq per 100g clay	g - value (± 0.003)
20	2.0066
50	-
60	2.0045
70	2.0045
80	2.0045
$[TTF]_3(BF_4)_2$ (crystalline)	2.0066

2.5.3 UV-Visible Spectroscopy Results

Table 2.10

	Wavelength nm^{-1}	Energy cm^{-1}
TTF in CH_3CN	434	23,000
	581	17,200
$CuCl_2$ in CH_3CN	432	23,000
(TTF + $CuCl_2 2H_2O$) in CH_3CN	573	17,452
	523 sh	19,120
	434	23,000
	396 sh	25,252
	335	29,850
	300 sh	33,333
	259	38,610
	239	41,841
TTF_2 $CuCl_4$ in CH_3CN	880	11,363
	500	20,000
	380	26,315
$TTF_3[Cu(NO_3)_2]$ in CH_3CN	680	14,705
	530	18,868
	365	27,397
	260	38,461

ESR Results

Table 2.8 Clays Contacted with TTF Using Procedure II

	TTF added mmoles^{-1}	g - values ± 0.002	g - values repeated after 3 months
Na^+ Montmorillonite +TTF	150	g = 2.025	g = 2.0067
Na^+ Laponite	150	g = 2.027	No Signal
Cu^{2+} Laponite	150	g = 2.027	g = 2.005

Table 2.9 Na^+ Laponite Ion-Exchanged with $[TTF]_3(BF_4)_2$

Concentration of $[TTF]_3(BF_4)_2$ /meq per 100g clay	g - value (± 0.003)
20	2.0066
50	-
60	2.0045
70	2.0045
80	2.0045
$[TTF]_3(BF_4)_2$ (crystalline)	2.0066

2.5.3 UV-Visible Spectroscopy Results

Table 2.10

	Wavelength nm^{-1}	Energy cm^{-1}
TTF in CH_3CN	434	23,000
	581	17,200
$CuCl_2$ in CH_3CN	432	23,000
(TTF + $CuCl_2 2H_2O$) in CH_3CN	573	17,452
	523 sh	19,120
	434	23,000
	396 sh	25,252
	335	29,850
	300 sh	33,333
	259	38,610
	239	41,841
TTF_2 $CuCl_4$ in CH_3CN	880	11,363
	500	20,000
	380	26,315
$TTF_3[Cu(NO_3)_2]$ in CH_3CN	680	14,705
	530	18,868
	365	27,397
	260	38,461

2.5.4 Diffuse-Reflectance Results

Clays Contacted with TTF

Table 2.11

	Wavelength nm^{-1}	Energy cm^{-1}
Cu^{2+} Montmorillonite + TTF	510	19,607
	430	23,256
	335	29,850
$CuCl_2$/Laponite +TTF	500	20,000
	385	25,974
$Cu(NO_3)_2$/Laponite +TTF	520	19,230
	430	23,255
	390	25,641
	262	38,168
Na^+ Montmorillonite +TTF	670	14,925
	495	20,202
	262	38,168
Na^+ Laponite	-	-

Table 2.12 UV- Visible Spectroscopy Results

Clays Ion-Exchanged with $[TTF]_3(BF_4)_2$

	Wavelength nm^{-1}	Energy cm^{-1}
$[TTF]_3(BF_4)_2$ in CH_3CN	573	17452
	515 sh	19417
	432	23148
	397 sh	25188
	375 sh	26666
	335 sh	29850

Table 2.13 Supernatent Solutions Collected on Completion of Ion-Exchanged Experiments

	Wavelength nm^{-1}	Energy cm^{-1}
40 meq	450 sh	22,222
	355	28169
70 meq	570	17438
	490 sh	20408
	425	23529
	355	28169
80 meq	625	16000
	467	21413
	417	23980
	355	28169
80 meq SUPERNATENT $+NA^{+}$	617	16181
	457	21881
	412 SH	24271
	347	28818

Table 2.14 Diffuse-Reflectance Results

Na-Laponite Contacted with $[TTF]_3(BF_4)_2$

	Wavelength nm^{-1}	Energy cm^{-1}
40 meq	480	20833
	260	38461
60 meq	660	15151
	480	20833
	260	38461
70 meq	652	15337
	475	21520
	260	38461
110 meq	473	21141
	258	38759

2.5.5 Flame Emission Spectroscopy Results

Table 2.15 Standard Solutions of Nalin CH_3CN

Concentration ppm^{-1}	Transmittance %
90	100
80	85
70	80
60	70
50	62
40	56
30	51

Transmittance	Concentration ppm^{-1}
63	53
58	47
55	44
49	38
48	37

2.5.6 Conductivity Results

Table 2.16

	Potential V	Current μA	Conductivity Ω^{-1} cm^{-1}
Na^+ Montmorillonite	5.00	0.37	6.85×10^{-9}
	10.01	0.85	7.87×10^{-9}
	15.00	87.00	5.32×10^{-9}
	20.00	330.00	1.53×10^{-9}
Na^+ Montmorillonite +TTF (150 mmoles)	2.00	0.10	2.86×10^{-8}
	10.00	0.25	3.58×10^{-8}
	14.00	0.45	5.32×10^{-8}
	16.00	0.60	5.30×10^{-8}
Cu^{2+} Montmorillonite +TTF (150 mmoles)	2.00	0.015	3.60×10^{-9}
	10.00	0.025	2.99×10^{-9}
	14.00	**0.070**	**2.99×10^{-9}**
	16.00	0.080	2.82×10^{-9}
Laponite +TTF (150 mmoles)	2.00	1.20	4.60×10^{-8}
	10.00	4.70	5.34×10^{-8}
	14.00	9.10	5.55×10^{-8}
	16.00	11.70	5.33×10^{-8}

Conductivity Results

Table 2.17

	Potential V	Current μA	Conductivity Ω^{-1} cm^{-1}
Laponite	2.00	0.15	5.41×10^{-9}
	10.00	0.85	7.53×10^{-9}
	14.00	1.36	9.31×10^{-9}
	16.00	1.40	11.40×10^{-9}
Laponite + $[TTF]_3(BF_4)_2$ (70 meq)	2.00	0.034	2.80×10^{-9}
	10.00	0.061	3.42×10^{-9}
	14.00	0.082	3.96×10^{-9}
	16.00	0.085	4.01×10^{-9}
Laponite + $[TTF]_3(BF_4)_2$ (80 meq)	2.00	0.055	6.31×10^{-9}
	10.00	0.061	8.75×10^{-9}
	14.00	0.069	9.31×10^{-9}
	16.00	0.093	13.40×10^{-9}

2.5.7 X-Ray Diffraction Results

Table 2.18 For Clays Contacted with TTF

	d_{001}/Å	Δ/Å
Na^+ montmorillonite	15.3	5.7
Cu^{2+} montmorillonite	13.3	3.7
Na^+ montmorillonite +TTF (150 mmoles)	15.0	5.4
Cu^{2+} montmorillonite +TTF (50mmoles)	14.3	4.7
Cu^{2+} montmorillonite +TTF (150mmoles)	16.1	6.5
Na^+ laponite	12.5	3.9
Na^+ laponite +TTF (150mmoles)	12.4	3.8
Cu^{2+} laponite	12.8	3.4
Cu^{2+} laponite +TTF (50mmoles)	14.5	4.9
Cu^{2+} laponite +TTF (150mmoles)	17.8	8.2

2.5.8 ^{57}Fe Mossbauer Results

Table 2.19 ^{57} Fe Mossbauer Parameters for Montmorillonite Before and After Treatment with TTF

Clay	^{57}Fe Mossbauer Parameters		Origin
	δ^a (mm s^{-1})	Δ^b (mm s^{-1})	
Na^+ Montmorillonite	0.36	0.45	iron III
	0.38	1.06	iron III
Na^+ Montmorillonite +TTF (exp A)	0.36	0.48	iron III
Na^+ Montmorillonite +TTF (exp B)	0.36	0.44	iron III
Na^+ Fuller's Earth	1.13	2.52	iron II
	0.43	0.86	iron III
	0.27	0.42	iron III
Na^+ Fuller's Earth +TTF	0.36	0.54	iron III

2.4.7 Measurement of the Extent of Ion-Exchange

(i) Sodium Release Monitored by Flame-Emission Spectroscopy

The supernatents collected in the previous experiment were tested for the amount of sodium ion released by the clay. Firstly, a calibration curve was prepared by running a set of standard solutions containing from 30ppm to 90ppm of Na^+ (present as NaI) in acetonitrile. The supernatents were then aspirated into the flame photometer. Transmittance values are obtained directly and converted to concentration of Na^+ released by reading off the calibration curve. A sodium release curve was then plotted, to give an idea of the rate of ion-exchange occurring as the concentration of TTF^+ in increased.

(ii) TTF^+ Uptake Monitored by UV-Visible Spectroscopy

Since the TTF^+ radical absorbs strongly in the UV-Vis region any one strong absorption can be used to follow the loss of TTF^+ from the external solution by observing changes in the absorbance values of that peak.

Fresh solutions of $[TTF]_3 (BF_4)_2$ in acetonitrile were prepared which had exactly the same concentration as those used in contacting the clay. UV spectra were recorded, between 800nm and 200nm, for each of these solutions, and a plot of absorbance values versus concentration of TTF^+ was made. Similar spectra were recorded for the supernatent solutions. The concentration of TTF was obtained from the calibration curve.

2.6 DISCUSSION

(A) EXPERIMENTS WITH TTF

2.6.1 Appearance of Products

The most striking feature concerning the physical appearance of the clays treated with solutions of TTF in acetonitrile, was the intense brown colour

developed by all of the clays, with one notable exception. The brown colour became evident immediately on contacting the clay with TTF, and not after minutes. The effect of prolonged reaction time (two to four hours) enabled the doped clay to retain the brown colour when washed with acetonitrile, compared with those treated for, say, less than an hour. Based on their appearance after contact with TTF, the clays could be divided into two groups:

(a) Clays containing transition metal cations either in the octahedral layer or as exchangeable cations.

(b) Laponite (in the sodium-exchanged form), a synthetic hectorite in which transition metal cations such as Fe^{3+} have been replaced by Mg^{2+} and Li^{+}. On contact with TTF solutions laponite does not undergo any detectable colour changes from the original white colour.

However, laponite which has previously been ion-exchanged with Cu^{2+} and VC^{2+} did give an intense brown colouration. These facts alone would appear to suggest that the brown colour is a function of the interaction between TTF and charge deficient metal ions present either in the clay lattice as with sodium montmorillonite, or in the interlayer region alone.

2.6.2 ESR Data

ESR results for the doped clays show significant changes from those obtained for the starting materials. The signal from sodium montmorillonite was too broad for measurement, but on addition of TTF (150mmoles) a weak, broad signal was observed centred at g=2.005 (Fig. 3.7). Copper II exchanged montmorillonite gave an isotropic signal centred at g=2.012. Addition of a small amount of TTF (50mmoles) resulted in a signal centred at g=2.0075. The broad isotropic signal due to Cu^{2+} montmorillonite has disappeared on addition of TTF, being replaced by a single line resonance. Although this original was stronger than that obtained for Na^{+} montmorillonite +TTF, it was nevertheless broadened due to interference from paramagnetic framework centres present in the montmorillonite lattice.

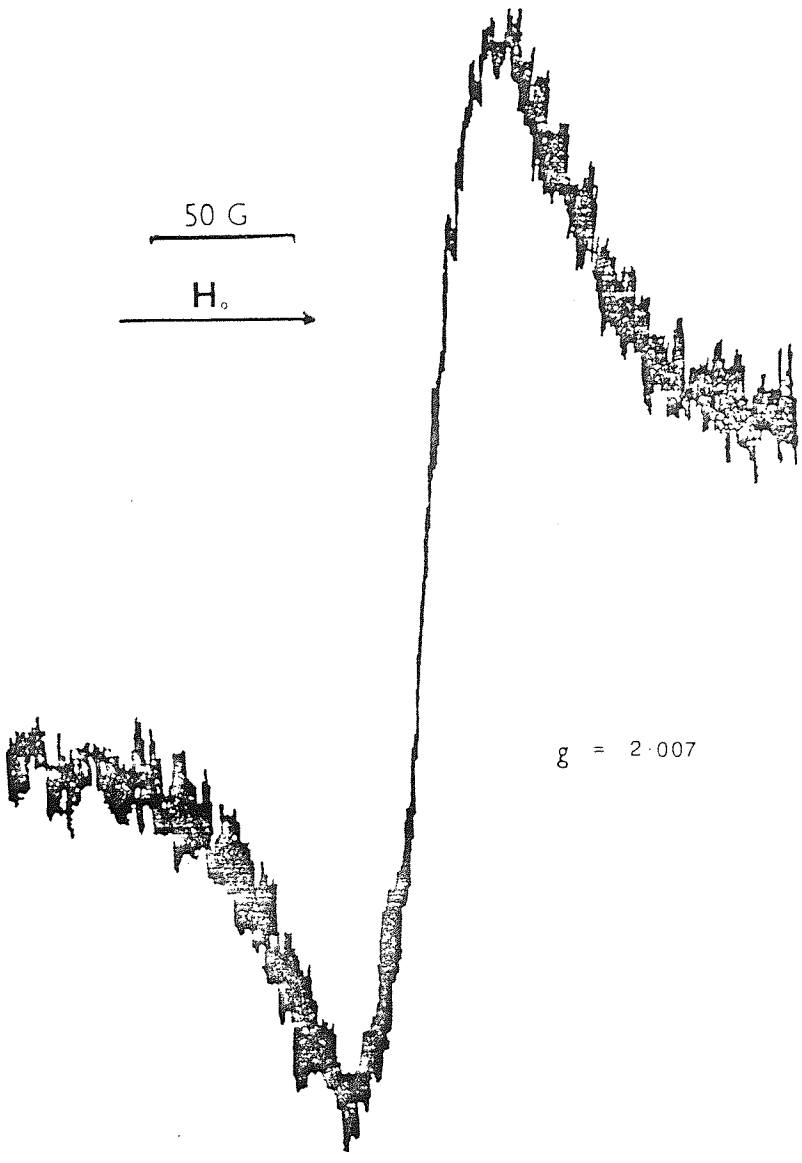

Fig. 2.6 Na^+ Mont + TTF (150 mmoles)

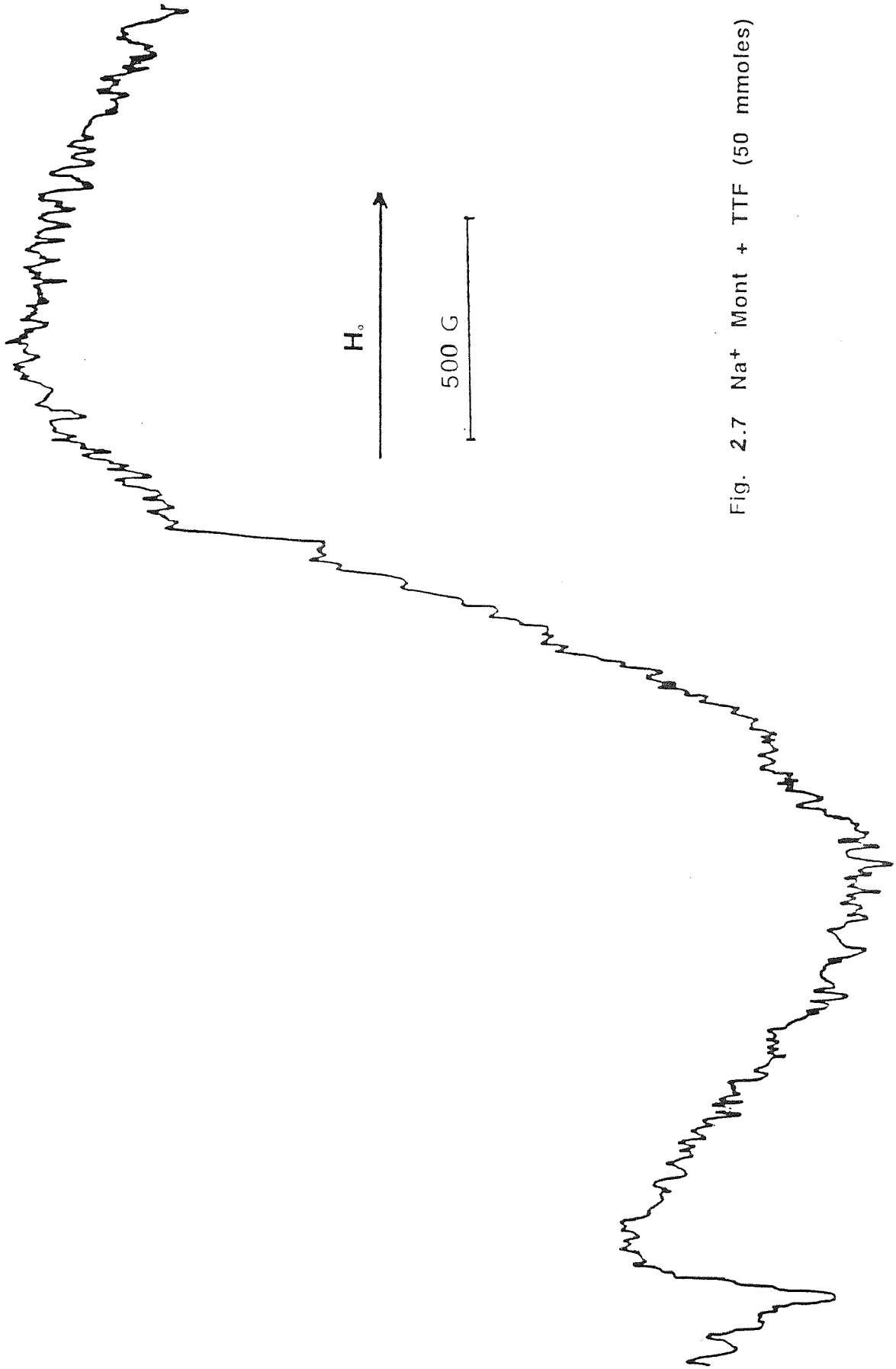

Fig. 2.7 Na^+ Mont + TTF (50 mmoles)

Fig. 2.8 Cu^{2+} Mont + TTF (150 mmoles) (ESR)

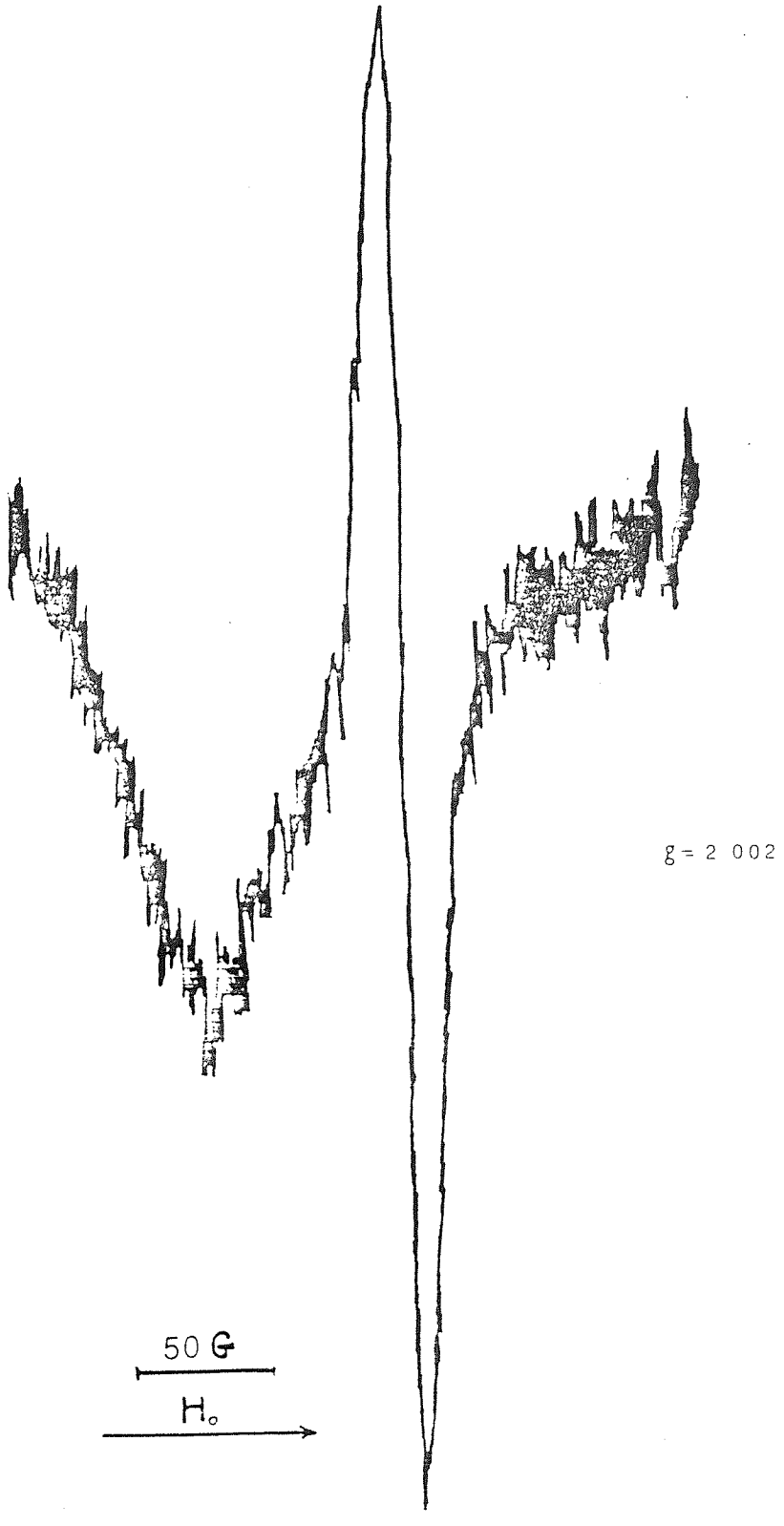

The ESR results for laponite were rather more interesting. Laponite itself and laponite contacted with TTF gave no detectable ESR signal. The Cu^{2+} and VO^{2+} exchanged forms of laponite gave well resolved, axial and anisotropic spectra with the following g values:

Cu^{2+} laponite $g_{11} = 2.264$ $g_{\perp} = 2.015$

Vo^{2+} laponite $g_{11} = 1.944$ $g_{\perp} = 1.948$

As shown in figure 3.5 both spectra are indicative of Cu^{2+} and VO^{2+} ions present in an environment with restricted rotation between the silicate layers[32,33].

For Cu^{2+} laponite the addition of TTF even at moderately low concentration (50mmoles) results in the complete disappearance of the anisotropic spectrum, being replaced by a sharp single-line resonance centred at g = 1.999 (Fig.3.5.6). At higher TTF levels the signals were sharper still with g = 2.0073 and g = 2.0047 at 75 and 100mmoles TTF loading respectively.

The single-line resonances obtained with g-values close the the free elctron value (g-2.0023) suggest that there is a free radical species present, and most likely to be the TTF monocation TTF^{+}. This is probably formed by electron donation from TTF to interlayer Cu^{2+} ions resulting in the formation of a Cu-TTF charge transfer complex.

In sodium montmorillonite there are no transition metal ions in the interlayer region. Even so, on addition of TTF a brown coloured product results in the ESR spectrum (a single line resonance at g-2.0005) provides evidence for the formation of the TTF^{+} monocation radical. The most likely explanation for this is electron transfer from TTF to framework Fe^{3+} cations. The ESR spectrum of the vanadyl laponite plus TTF shows the anisotropic components of the VO^{2+} laponite spectrum but there is a marked reduction in the intensity of the anisotropic components. This does not rule out the possibility of an interaction between VO^{2+} and TTF, but as the VO^{2+} species is less easily reduced than Cu^{2+} and Fe^{3+} it would require a greater concentration of TTF than was actually

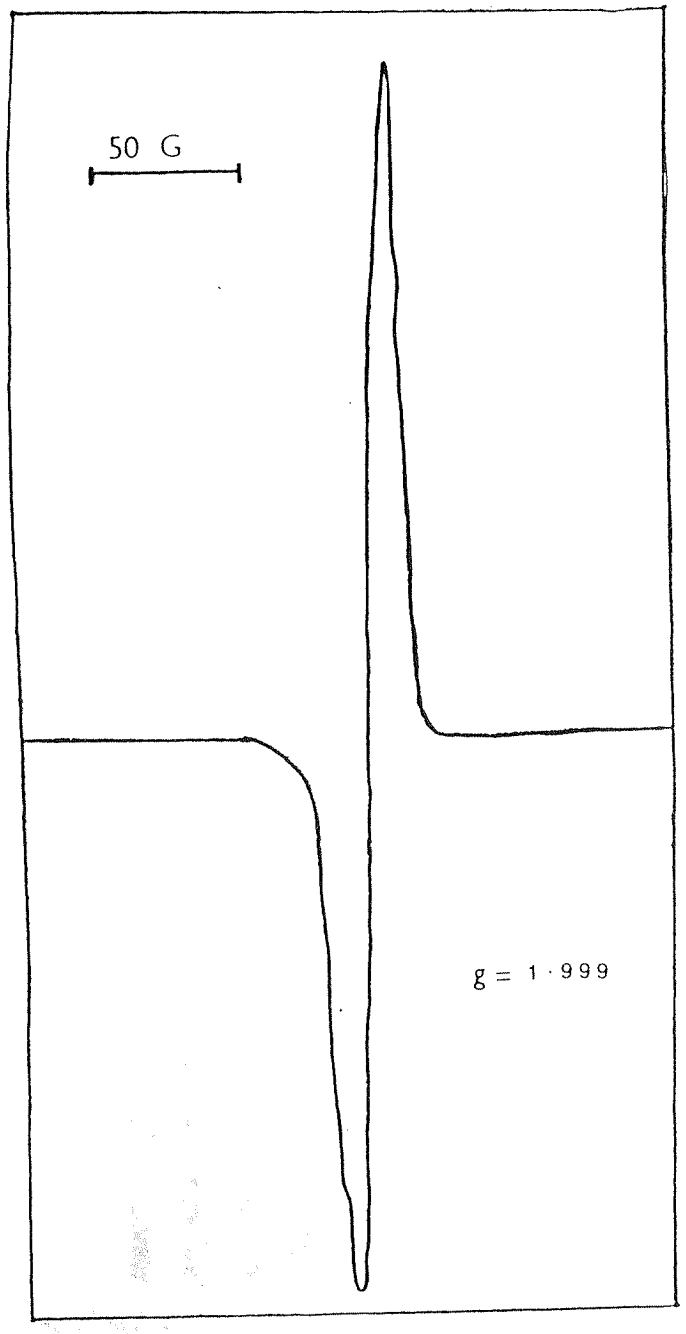

Fig. 2.5(B) ESR Spectrum for Cu^{2+} - Laponite + TTF

+ TTF

50 meq

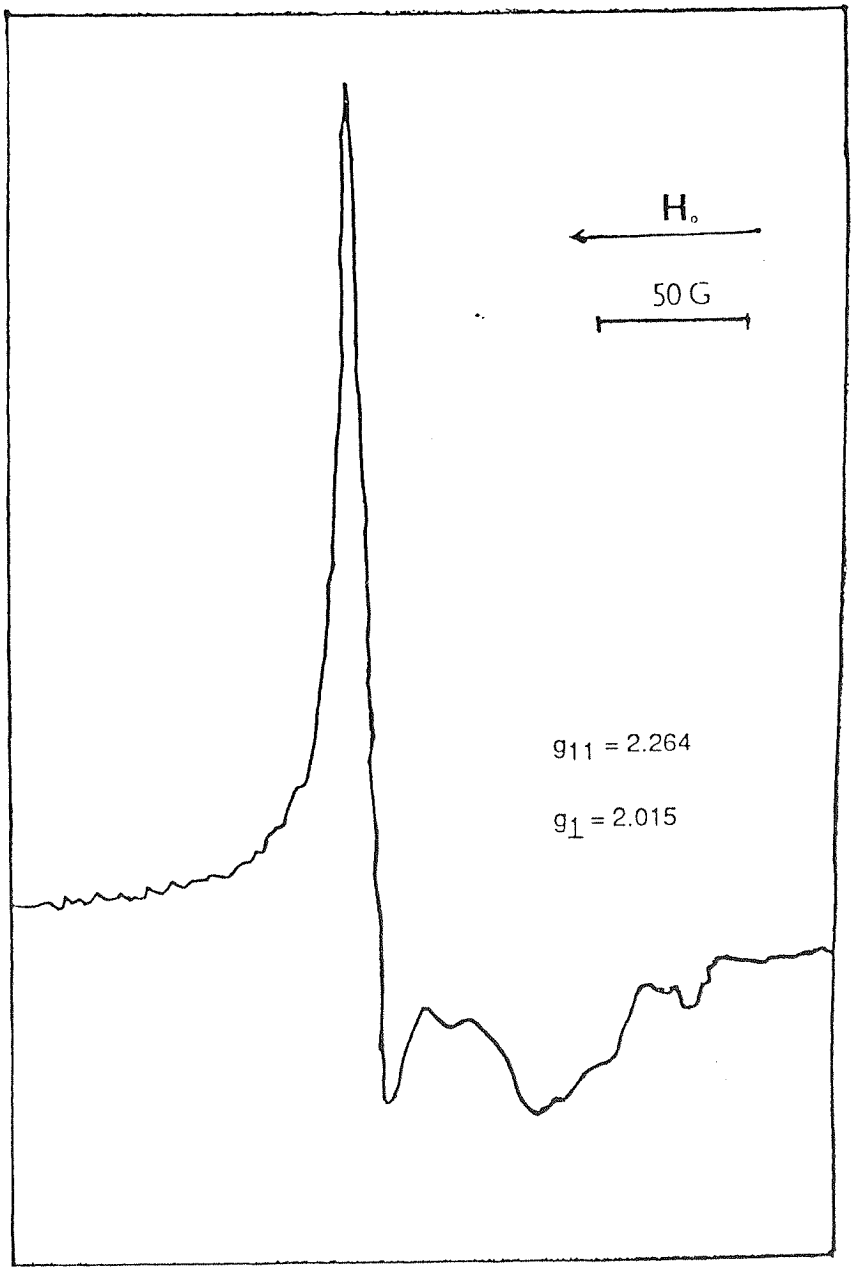

Fig. 2.5(A) ESR Spectrum for Cu2+ - Laponite

applied. The brown colour of the Cu^{2+} laponite and TTF points to a similar sort of interaction as that between Cu^{2+} and Fe^{3+} and TTF.

A likely explanation based on the evidence from the ESR results particularly for Cu^{2+} laponite and TTF is a redox reaction between TTF and the elctron deficient interlayer cation: Cu^{2+} has a d^9 configuration and Fe^{3+} a d^5 configuaration. both therefore are electron acceptors due to partially vacant d-orbitals. the following type of reaction can therefore be envisaged:

$$Cu^{2+} + TTF \text{ ------> } Cu^{+} + TTF^{+}$$

$$Fe^{3+} + TTF \text{ ------> } Fe^{2+} + TTF^{+}$$

Cu^{+} is d^{10} and non-paramagnetic and hence not detectable by ESR. This explains the disappearance of the anisotropic Cu^{2+} signal. Fe^{2+} is d^6 (low spin) and also unobservable by ESR. An important question which now arises is that of the possibility of association between the reduced metal ions and the TTF^{+} radical. The ESR spectra show strong sharp resonances particularly for Cu^{2+} laponite and TTF. they do not appear to be broadened by interactions with other species such as Cu I. If there was any possibility of even a loose association between Cu I and the TTF^{+} radical, in the form of a charge transfer complex - this means that the radical electron would spend some of its time on the Cu I ion as well, which would cause considerable broadening of the ESR signal. No significant broadening is observed which points to a lack of coordination between Cu (I) and TTF^{+}. The g-values of the TTF doped clays agree well with those obtained by Wudl et al [12] for TTF^{+} species in acetonitrile. the slight variations may be due to the different (more restricted) intracrystalline environment of the silicate lattice.

Clays which were contacted with TTF by procedure II (ambient temperature, longer reaction time and exclusion of light) gave similar ESR results to thos obtained by procedure I. No ESR signal was detected for TTF crystals and TTF dissolved in acetonitrile. The ESR data show that organic radicals may be generated either by reaction with interlayer transition metal ions (Cu^{2+} laponite and Cu^{2+} montmorillonite) or with structural iron (montmorillonite).

2.6.3 Diffuse Reflectance Data

Diffuse reflectance spectra for clays not treated with TTF showed very little change from the MgO standard. This lack of excitiation bands in the starting-clays implied a lack of any significant chromophores. However, clays doped with TTF showed a number of weak, broad absorption bands most prominent in the visible region of the electromagnetic spectrum. The ε max and absorption energies of these peaks were compared with those obtained for solution spectra of TTF in CH_3CN and TTF + $CuCl_2.2H_2O$ in acetonitrile.

For TTF in acetonitrile, there are two intense peaks centred at 434nm and 581nm, corresponding to absorption energies of 23,000 and 17,200cm^{-1} respectively. By reference to the literature[11] these peaks can be ascribed to the monomeric form of the TTF^+ cation.[9]

The reflectance spectrum of Cu^{2+} montmorillonite + TTF (fig.3.9) shows weak bands at 430 nm (23256cm^{-1}) and 510nm (19607cm^{-1}). Both of these bands can be attributed to the two principal absorption maxima of the TTF^+ dimer $(TTF^+)_2$.[10] Cu^{2+} laponite + TTF showed peaks at 430 nm (23526 cm^{-1}) and 520nm (19230 cm^{-1}), again indicating the existence of TTF^{+2} dimeric units. On the other hand sodium laponite + TTF showed no sign of any absorption peaks. This observation also correlates well with the ESR data where no radical species was detected for Na^+ laponite + TTF. The reflectance spectrum of Na^+ montmorillonite + TTF showed one relatively weak band at 495nm, compared to Na^+ montmorillonite alone.

On the whole reflectance spectra are very broad and weak. This may in part be due to the amorphous nature of the clay mineral as a result of which absorption bands tend to overlap and become obscured. The solution UV-VIS spectrum of TTF + $CuCl_2.2H_2O$ in acetonitrile showed a number of absorption bands and shoulder between 573nm and 239 nm (table 3.10). The reflectance spectrum of laponite exchanged with $CuCl_2.2H_2O$ and subsequently contacted with TTF, showed a marked difference in ε max values from the solution spectrum. It is interesting

Fig. 2.9 UV-Visible, Diffuse Reflectance Spectra

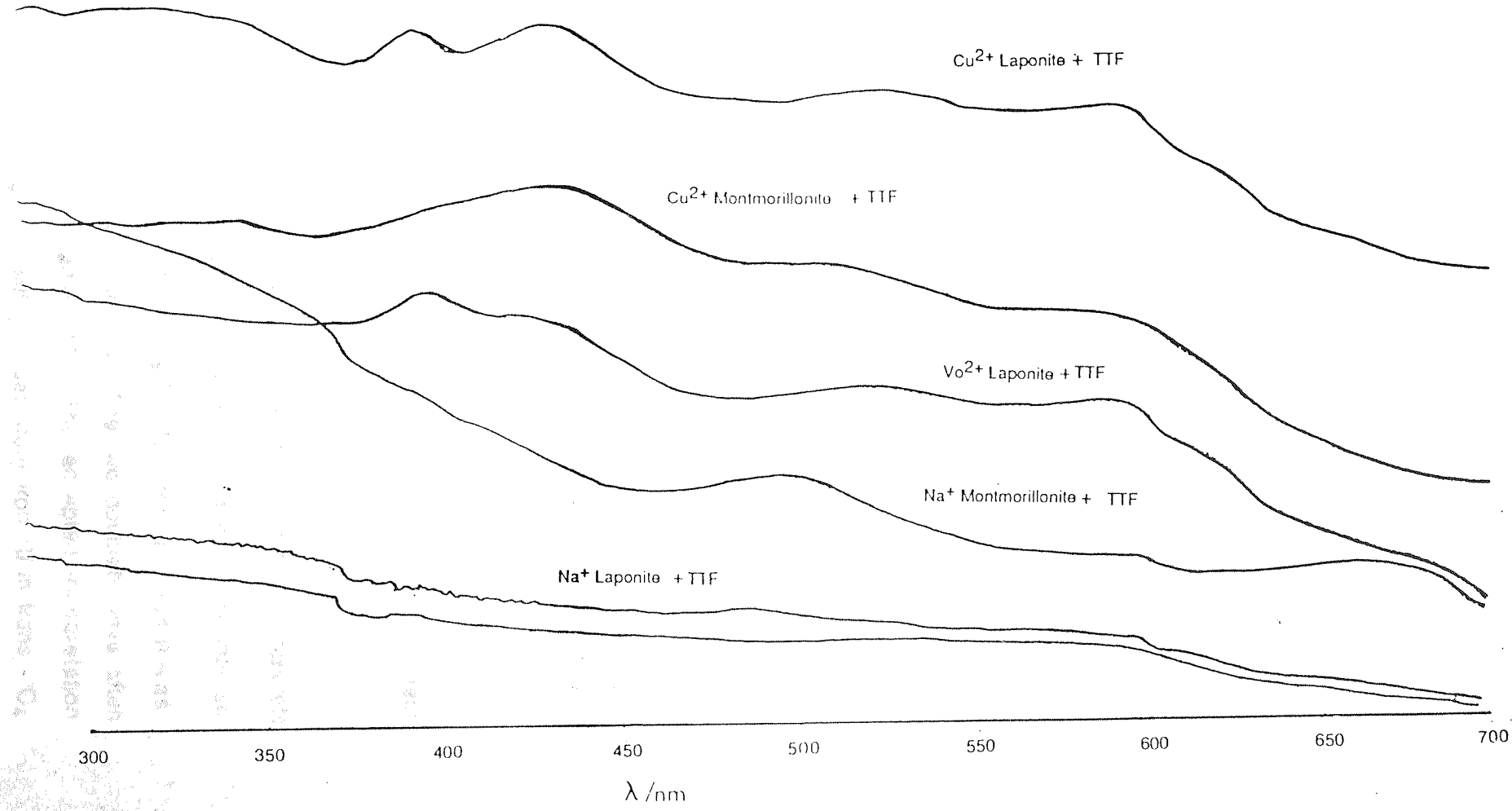

to note that on comparing spectra for Cu^{2+} montmorillonite + TTF against Na^{+} montmorillonite + TTF, there is only one band in the Na^{+}mont. + TTF (at 495 nm), while there are three bands in the Cu^{2+} mont. + TTF. One of these three bands corresponds approximately to the single band in Na^{+} mont. + TTF. The other two bands however, are also common to Cu^{2+} laponite + TTF. This supports evidence in favour of two distinct charge-transfer interactions, one from TTF to the framework iron III cations, and the other from TTF to the interlayer Cu^{2+} cations. The intensity of the former band would be less than that of the latter because there is a relatively small amount of substitution of Fe^{3+} for Al^{3+}. This is actually observed in practice (Fig.3.9).

Thus the evidence from reflectance spectra alone suggests that there is some sort of charge transfer occurring which is due to the TTF. It is speculated that a different TTF moiety exists in the intracrystalline clay environment than in solution.

2.6.4 ^{57}Fe Mossbauer Data

In their study of the interaction of benzidine with montmorillonite, Thomas et al used a clay which contained both structural iron III and iron II.[21] On treatment with benzidine the iron II doublet (δ = 1.36, Δ = 2.77 mm s^{-1}) increased in intensity at the expense of the iron III doublet (δ = 0.59, Δ = 0.65 mm s-1). These observations illustrated the value of Mossbauer spectroscopy to detect charge transfer to structured iron III.

We were able to fit our Na^{+} montmorillonite Mossbauer spectrum to two doublets (table 3.19) the inner doublet (δ = 0.36, Δ = 0.45 mm s^{-1}) being more intense than the outer doublet (δ = 0.38, Δ = 1.06 mm s^{-1}). No structural iron II was detected for this sample of Na^{+} montmorillonite. The two doublets have often been observed for monmorillonite samples[28]. The accepted interpretation suggests that the larger quadrupole splitting arises from iron III in trans - $O_4(OH)_2$ sites (M) and the larger from iron II in cis - $O_4(OH_2)$ sites (M2), and is

consistent with a point charge model.[25] However a recent electron diffraction study of a Wyoming montmorillonite showed that 75 - 100% of the M1 sites were occupied by iron III[34]. Thus the assignment of the most intense doublet to M2 sites is unlikely to be correct. Cardile and Johnston[26] have reassessed their Mossbauer data for montmorillonite and have shown that the fit obtained is to some extent a function of the constraints within the fitting program. Since the iron content of montmorillonite is low, the Mossbauer parameters will be sensitive to variations in the geometrical arrangement of neighbouring cations and even to the more distant interlayer ions.

On contact with TTF, results of variable consistency were obtained. In some experiments, definite evidence for the generation of iron II was obtained (δ = 1.13, Δ = 2.52 mm-1 s^{-1}). More normally, however, only a modified ironIII spectrum was obtained. This is in agreement with cardile and Johnston's view that the spectrum will be influenced by near and more distant ions. The data are consistent with the view that there is indeed a small degree of charge transfer from TTF to structural iron III although this is not always enough to produce iron III to be detectable by Mossbauer spectroscopy.

2.6.5 X-Ray Diffraction Data

Copper II montmorillonite gave a d_{001} value of 13.3A° which is consistent with interlayer Cu^{2+} ions coordinated to two monolayers of water; hence the increase in basal spacing (Δ) of 3.7A° when the thickness of an elementary clay sheet (9.6A°) is subtracted from the observed d_{001} value. On treatment with TTF at low loadings a d_{001} value of 14.3A° is obtained, corresponding to a basal spacing increase (Δ) of 4.7A°. When treated with TTF at high loading (150 mmoles), a basal spacing increase of 6.5A° (d_{001} = 16.1A°) is observed. Na^{+} montmorillonite on treatment with 150 mmoles TTF gave rise to a d_{001} value of 15.0A°, corresponding to a basal spacing increase of 5.4A°. For the montmorillonite clays such increases in the basal spacing values are consistent

with the basal spacing achieved when planar molecules are introduced between the silicate layers. The most likely orientation of the TTF molecule is one with its molecular plane parallel to the silicate layers (Fig. 3.10c).

Copper II laponite treated with TTF at low loadings shows a d_{001} value of 14.5A°, which implies a basal spacing increase of 4.9A° when TTF is introduced. At high TTF loadings (150 mmoles) a d_{001} value of 17.8A°, corresponding to a basal spacing increase of 8.2A°. A d value of 8.2A° is in agreement with unpublished results by Monsef-Mirzai,[29] and also closely agrees with figures obtained by Van Damme et al. On the basis of such high basal spacing values, the French workers proposed two possible orientation for intercalated TTF molecules.[24] However, in view of our diffuse reflectance results for Cu^{2+} laponite + TTF we believe that a basal spacing value of 8.2A° is consistent with $(TTF)_2^+$ dimers present between the silicate layers (Fig. 3.10). The dimeric $(TTF)_2^+$ units may be present as aggregates parallel, and perpendicular to the clay sheets. Both orientations are easily accommodated with the basal spacing value of 8.2A°, (Fig. 3.10a, 3.10b).

2.6.6 Conductivity Data

In contrast to Van Damme et al, we observed an order of magnitude increase in conductivity of some of the clays treated with TTF. The mechanism for conduction is almost certainly an ionic one. It is speculated that the mobility of the interlayer ions may be increased by the increase in basal spacing. The increase in conduction cannot be attributed to the charge transfer process since Na^+ laponite + TTF shows a similar enhancement of conductivity as other clays.

(B) EXPERIMENTS WITH $[TTF]_3$ $(BF_4)_2$

2.6.7 Na+ Release and XRD Data

We had hoped to observe enhanced conductivities for TTF treated clays and felt that ion-exchange of $[TTF]_3^{2+}$ might enhance the TTF loading of the clay. A flame emission method was used to monitor the concentration of Na^+ released by the clay as different amounts of $[TTF]_3^{2+}$ salt were added. From the results, a Na^+ release curve was plotted (Fig. 2..14) of Na+ released (meq/100g of clay) versus concentration of $[TTF]_3(BF_4)_2$ added.

As expected, the graph showed that there is an increase in the amount of sodiun ion released as the concentration $[TTF]_3$ $(BF_4)_2$ added is increased. Between 40 and 50 meq of $[TTF]_3^{2+}$ added, there is relatively little ion exchange occurring as indicated by the low amount of Na^+ released. After addition of 60 to 75 meg of the salt (when the cation-exchange capacity of the clay is exceeded) there is a sharp rise in the amount of Na^+ released. Ion exchange prodeeds to approximately 75% completion on treating laponite with 80 meq of $[TTF]_3(BF_4)_2$. The ion exchange process was also followed by monitoring the intensity of the UV-vis spectra of $[TTF]_3(BF_4)_2$ in the supernatent with similar conclusions.

After carefully air-drying the clays ion-exchanged with $[TTF]_3(BF_4)_2$, the samples were analysed by XRD in order to observe any changes in the basal spacing measurement of the clay. This was done by following the intensity changes in low angle reflections (<10°). At 40 and 50 meq of $[TTF]_3^{2+}$ loading, no low angle reflections were observed, implying lack of intercalation of the $[TTF]_3^{2+}$ species. At 60 meq a slight bump at around 2θ values of 7° began to emerge but was considered too broad for accurate measurement. However at 70 meq, a reasonably sharp peak appeared at 2θ values of 5.9° corresponding to a d_{001} value of 17.5A°, and a basal spacing increase of 7.9A°

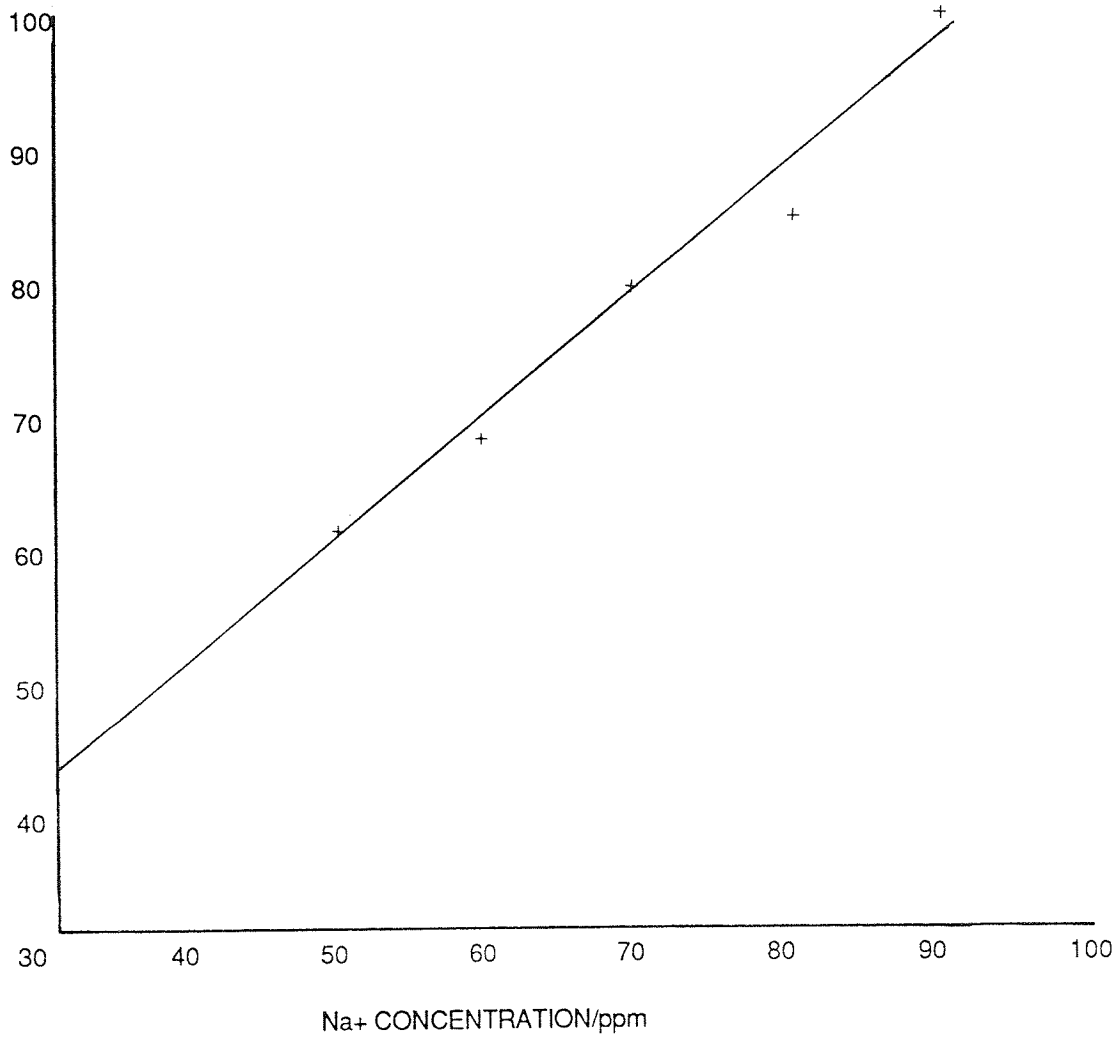

Calibration Curve Conc. Na+/ppm VS Transmittance Using Flame Emission

SODIUM RELEASE CURVE

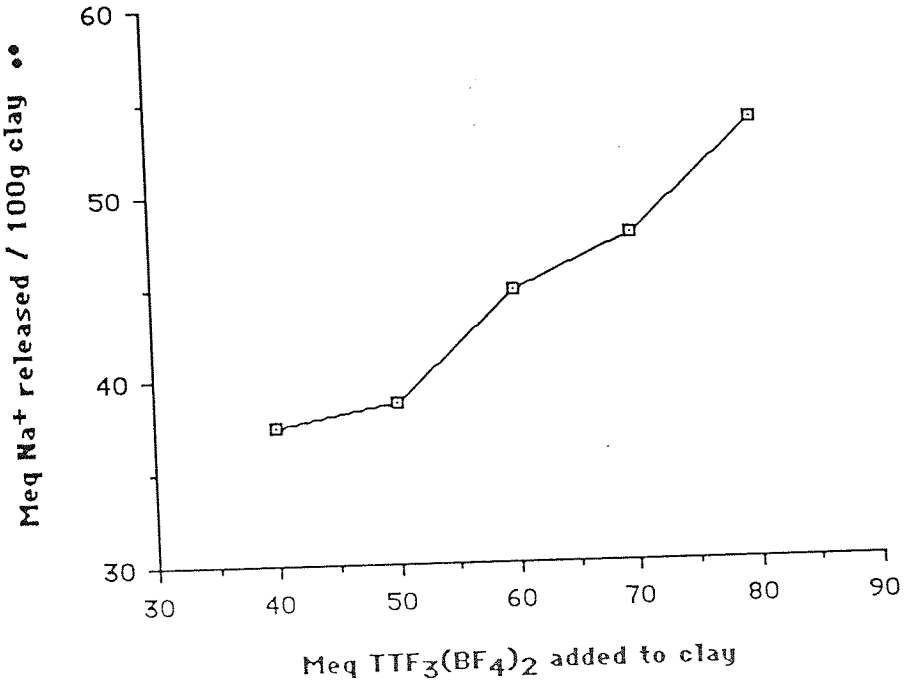

Fig. 2.12 ESR Spectra for Laponite Ion-Exchanged with $TTF_3(BF_4)_2$

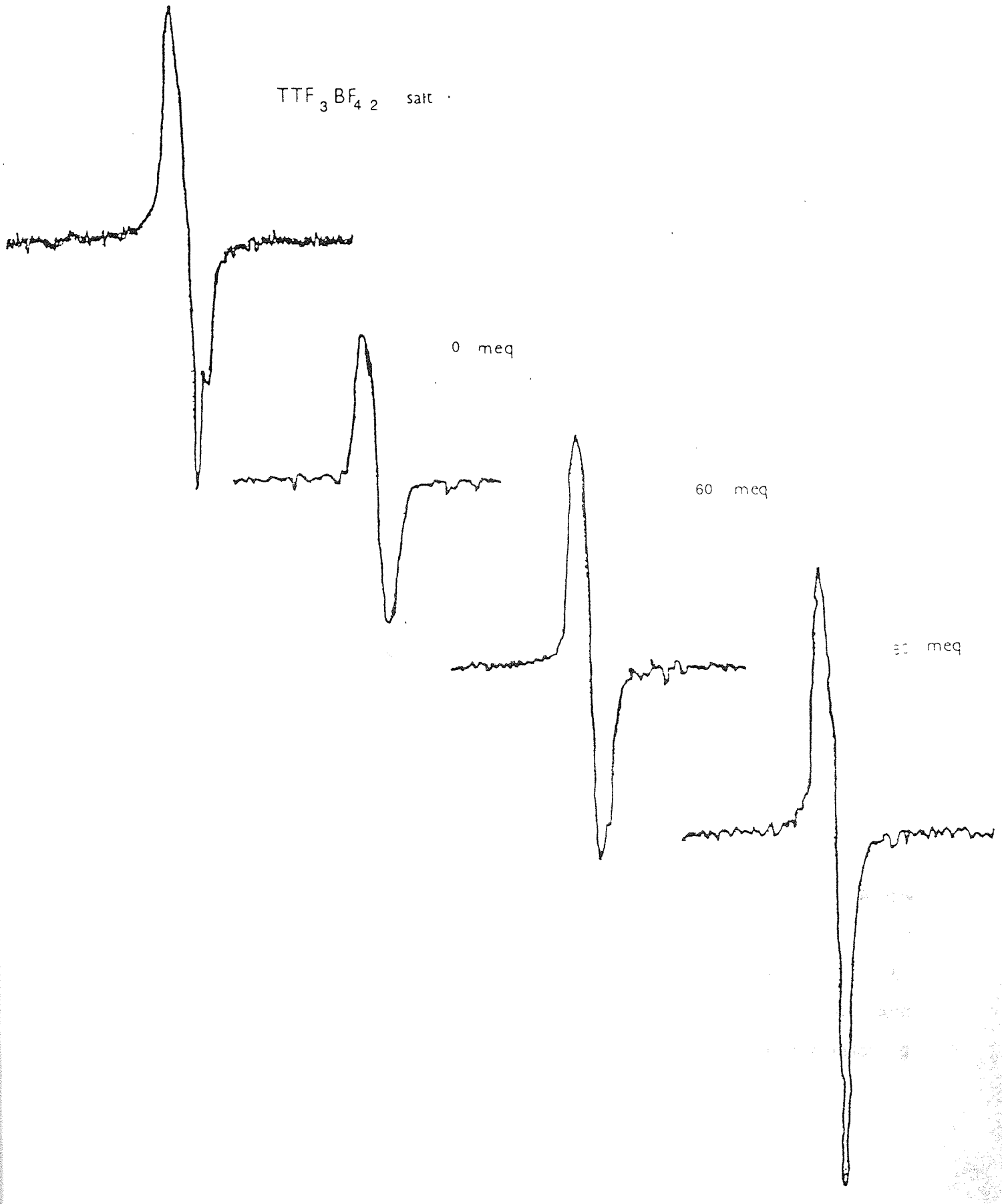

2.6.10 UV - Vis and Diffuse Reflectance Data

The UV-Vis spectrum of $[TTF]_3(BF_4)_2$ in acetonitrile shows a strong band at 316nm (19,800 cm^{-1}) with a series of shoulders at 250,290, 305, 335, 375 and 397 nm. The diffuse reflectance spectra for Na^+ laponite treated with $[TTF]_3(BF_4)_2$ (Fig 3.19) are dominated by a broad but strong band between 445nm and 500nm and with a λmax of 475 -480nm. The intensity of this band increases significantly with increasing concentration of $[TTF]_3(BF_4)_2$ added to the clay. This band is attributable to one of the local excitiation bands for the $[TTF]_2^+$ dimer.[10] The increase in intensity can be correlated with an increase in the concentration of the chromophore. The other noticeable band is a weak broad, band at 660nm (15,151cm^{-1}). The significant thing to note from the UV data is that the main band in solution at 432nm is shifted to higher wavelength (lower energy) of 475nm. The absorbing moiety in the clay is therefore different from that in solution. It is known that the TTF moieties in $[TTF]_3(BF_4)_2$ exist as trimeric units where the cofacial molecular planes are located parallel to the c-axis, separated by the same distance, with lateral overlap of the TTF moieties of about 0.79A°. However in view of the X-ray and ESR data we speculate upon the existence of a mixture of $[TTF]_2^+$ dimeric and TTF^+ monomeric units.

2.6.11 Infra-Red Data

IR spectra were run for the whole series of ion-exchanged Na^+ laponites. At low $[TTF]_3(BF_4)_2$ loading, the spectra were mostly obscured by the dominant vibrations due to the silicate lattice. At 70 meq however a good deal of useful evidence was obtained. IR spectra were also recorded for Na^+ laponite and $[TTF]_3(BF_4)_2$ separately. From the IR spectrum of $[TTF]_3(BF_4)_2$ the following assignments were made:

Fig. 2.13 UV-Visible Diffuse Reflectance Spectra for Lapo
Exchanged with $TTF_3(BF_4)_2$ (meq)

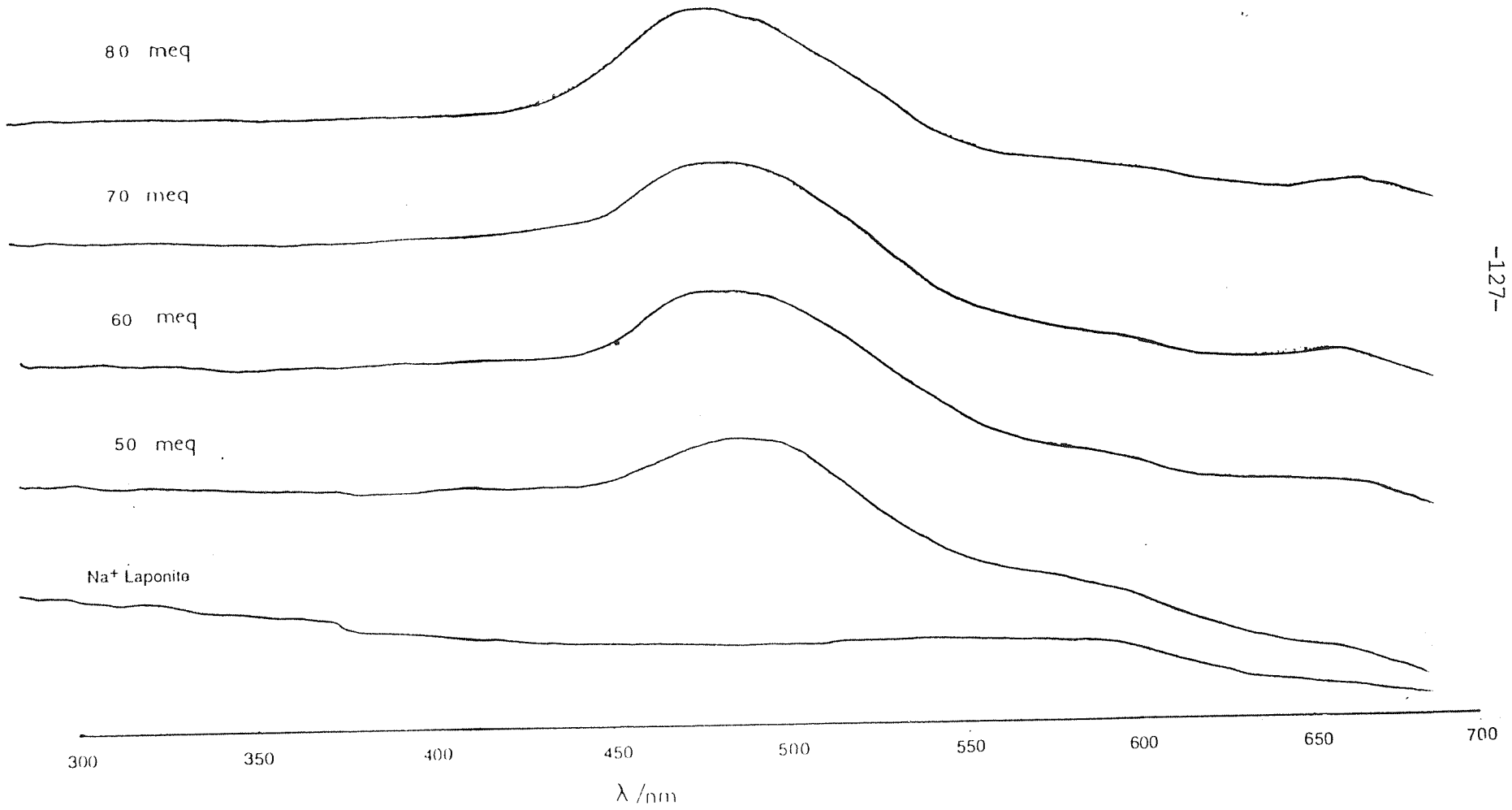

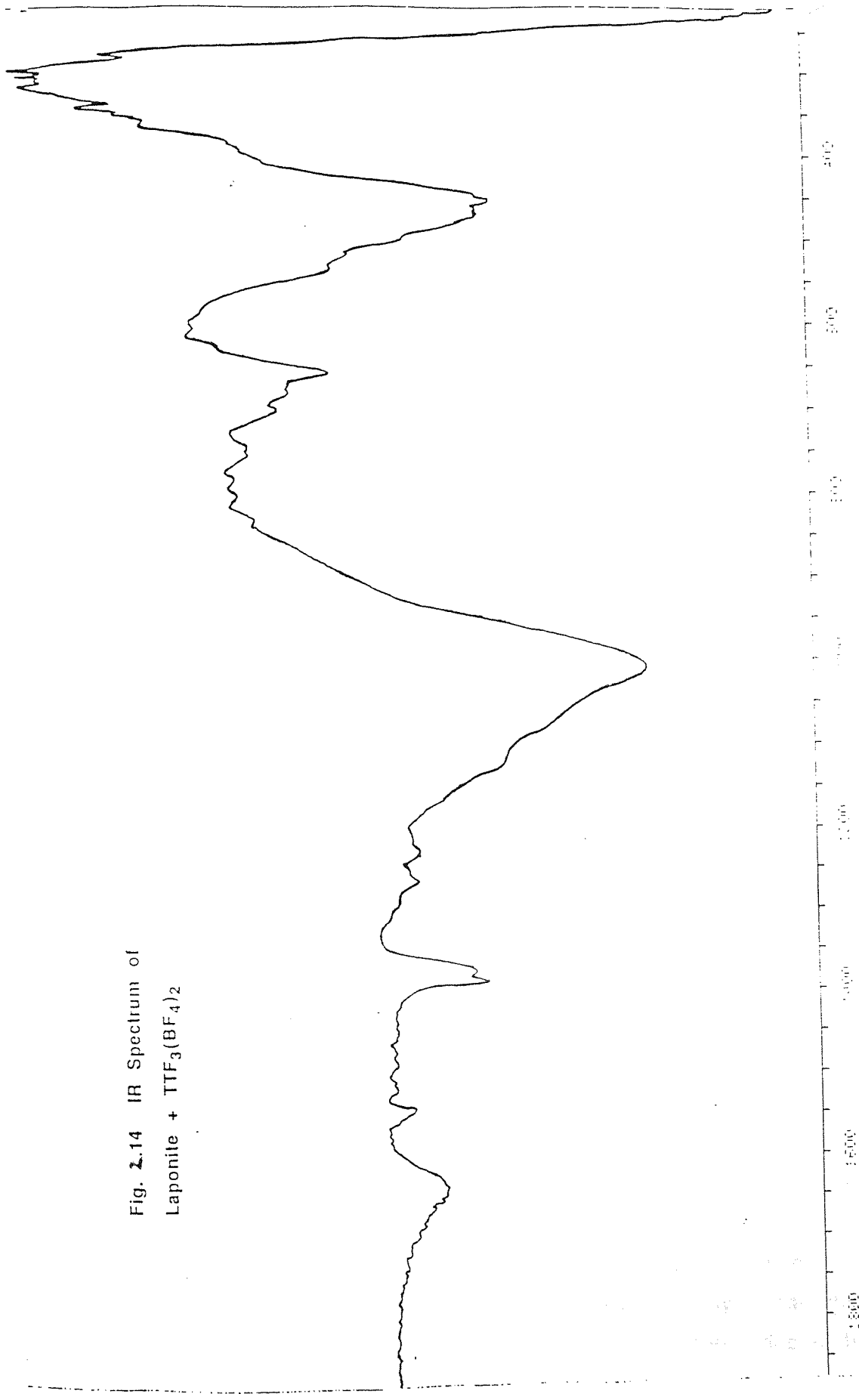

Fig. 2.14 IR Spectrum of Laponite + $TTF_3(BF_4)_2$

The medium intensity peak at 730 — 736 cm^{-1} is attributable to the skeletal C-S vibrations of the TTF ring. The peak at 823 - 829 cm^{-1} is attributable to the C-H out-of-plane bending vibrations. The strong band at 1341cm^{-1} can be assigned to the C=C vibrations in the fivemembered ring. Strong bands at 1040cm^{-1} are due to the BF_4^- function.

The IR spectrum of Na^+ laponite + $[TTF]_3(BF_4)_2$ at 70 meq loading (Fig. 3.14) clearly shows a number of bands which are due to the TTF function. It is noteworthy that the position of most of the bands had shifted quite significantly. This implied that the vibrations were modified by spatial constraints imposed by the silicate lattice.

The band appearing at 1341 cm^{-1} in the salt appeared as a very strong intense split doublet at 1373 and 1384cm^{-1}. As this was attributed to C=C vibrations in the five membered ring the very significant shift of about 40cm^{-1} to higher wavelength means that less energy is needed for this bond to vibrate in the silicate lattice than in the crystalline $[TTF]_3(BF_4)_2$ itself. This shift is consistent with the $[TTF]_3^{2+}$ trimer or $[TTF]_2^+$ dimer units held on the silicate surfaces or in between the clay layers. The splitting of the band into a doublet can be explained by the fact that in the salt itself there is more than one source of C=C vibration (in the five-membered ring) since there are three TTF units in a $[TTF]_3(BF_4)_2$ moiety. Upon intercalation between silicate layers, one of the TTF units may be closer to the silicate surface than the other, and this could cause a slight modification of the C=C vibrational frequency.

The band at 823 - 829cm^{-1} which is ascribed to the C-H out-of-plane bending, appears at 826cm^{-1} with medium intensity. This means that there is little or no perturbation of the normal vibrational frequency of this bond (by interaction with silicate layers) and hence it experiences a similar environment to that in the salt itself. The medium intensity peak at 743cm^{-1} due to C-S skeletal vibrations in the ring, occurs at 742cm^{-1} in the doped clay. Again there is little or no freqency shift which implies that the five-membered ring units are not perturbed by the silicate lattices.

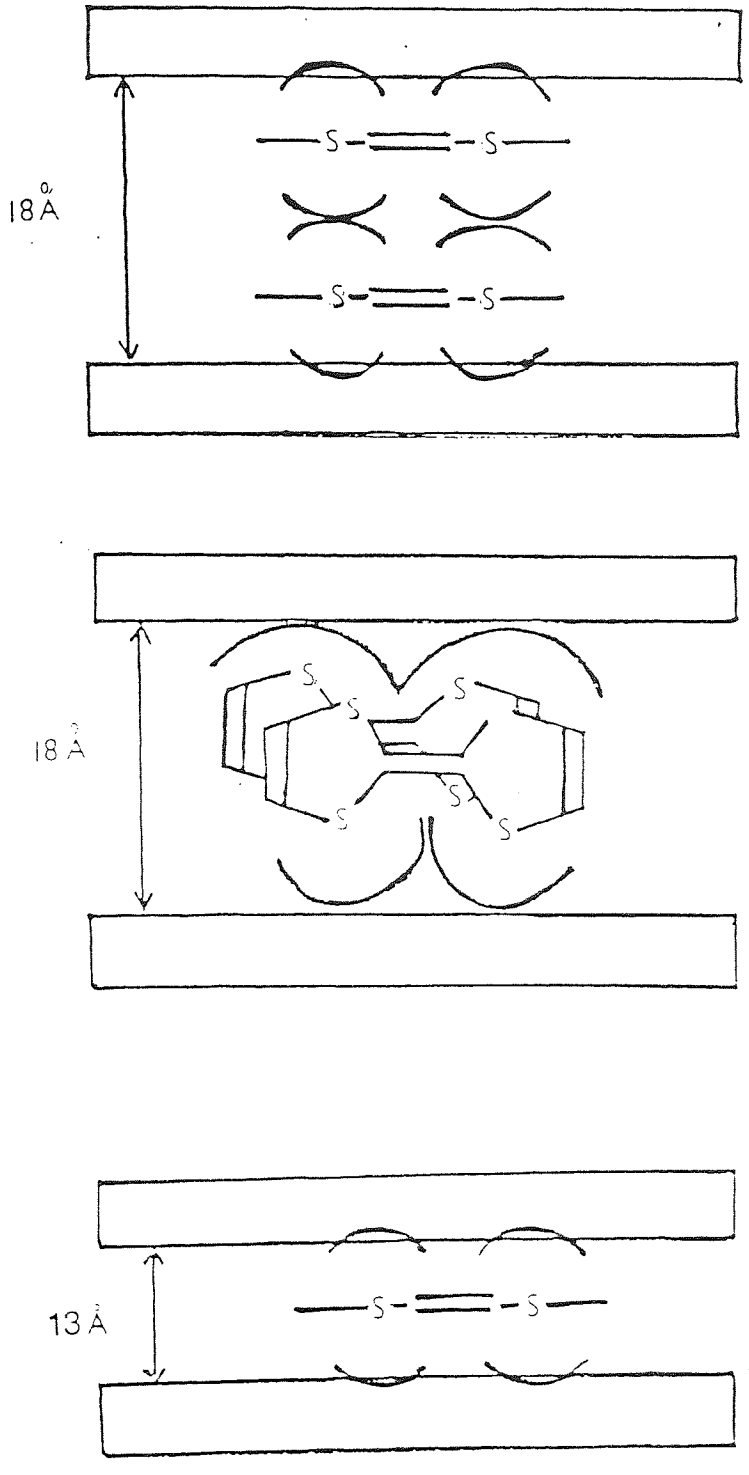

Fig. 2.10 Some Probable Orientations of TTF Intercalated in Laponite

A weak intensity band at 2553 cm^{-1} is tentatively assigned to the S-H stretching mode because no other groupings absorb near this frequency. We believe that a sulphur hydrogen interaction could be possible if one of the sulphurs in the TTF ring was in the proximity of an Si-O group protruding from the silicate planes. A S-H interaction would also modulate the vibrational frequency of the O-H bond by causing it to be stretched and weakened. The O-H stretch would be shifted to a higher frequency. Our evidence backs up this argument as a new O-H stretching band appears in the clay doped with $[TTF]_3(BF_4)_2$, which was not present either in the clay itself or in the $[TTF]_3(BF_4)_2$ salt.

The infra-red evidence points to the probability that the TTF moieties are in a similar environment to that experienced in the fluoroborate salt. They are most likely present as dimeric units (x-ray evidence) and are immobilised in between the silicate layers. Since the C-H bonds experience similar vibrations to those in the trimer units in the salt, we speculate that the dimer units are orientated with their molecular planes parallel to the silicate layers (Fig. 3.15).

2.6.12 Conductivity Data

By contrast to the clays doped with TTF, the $[TTF]_3$ $(BF_4)_2$ exchanged laponite shows no increase in conductivity.

2.7 CONCLUSIONS

It has been shown that TTF can be intercalated in clays of the smectite group. Contrary to the French workers, however, our evidence pointed to the existence of both intercalated dimeric $[TTF]_2^+$ and monomeric TTF^+ units. Charge transfer interactions to interlayer transition metal ions and to structural ion in the clay lattice were shown to occur. The intercalated species was an organic radical and there was no association with interlayer cations. Interlayer Cu^{2+} was reduced to Cu^{1+} in a redox reaction. The orientation of the intercalated species

was found to be dependant on the concentration of the TTF. At low TTF concentration the intercalated species was thought to be monomeric TTF^+ with it molecular plane perpendicular to the silicate sheets. At high TTF concentrations the intercalated species were dimeric $[TTF]^+_2$ aggregates , orientated either parallel or perpendicular to the clay sheets.

The ion-exchange reaction between Na^+ laponite and $[TTF]_3(BF_4)_2$, which was monitored quantitatively, was found to proceed slowly at low concentrations of $[TTF]_3(BF_4)_2$, but proceeded rapidly when the C.E.C of the clay was exceeded, and was accompanied by intercalation. The intercalated species were believed to be dimers oriented with their cofacial molecular planes parallel to the silicate sheets.

CHAPTER 3

A STUDY OF REDOX CATALYSTS IMMOBILISED ON CLAY MODIFIED ELECTRODES

3.1 INTRODUCTION

The catalytic properties of clays have been known for a long time[5] and there is renewed interest in the pillaring of clays, a procedure which can hold the interlayer spacing of smectite clays at some predetermined value thereby enabling the clays to show a similar size selectivity to that of zeolites. The immobilisation of complex catalysts in clay structures is an area of growing interest since apart from the obvious advantages of heterogeneous catalysis, clay colloids have been known to influence the specificity of incorporated catalysts as well. Recently clay modified electrodes were developed in which a smectite clay ion-exchanged with a redox active species was deposited as a thin film on the electrode surface.[112] The modification of electrode surfaces for example by covalent attachment or with polymer films is currently an active area of research.[112]

Ghosh and Bard[112] were the first to describe the electrochemical behavior of clay-modified electrodes. These workers studied the voltammetric responses of the $[Ru(bpy)_3]^{3+/2+}$ and the $[Fe(bpy)_3]^{3+/2+}$ couples immobilised at clay coated electrodes. Their clay films were cast on glassy/carbon and platinum electrodes, and results showed that the voltammetric behaviour at all these electrodes is comparable. Ghosh and Bard used finely divided platinum and polyvinyl alcohol (PVA) in order to make the films and found that platinum was necessary to make the films more sturdy. In a follow-up study the same authors reported that the $[Ru(bpy)_2\ bpy(COO)_2]$ complex showed catalytic activity in clay/RuO_2/PVA films[114].

Anson and Liu[115] described the electrochemical behaviour of cationic complexes of the type $[Os(bpy)_3]^{3+/2+}$ and $[Co\ (tpy)_2]^{2+}$ incorporated at clay-coated graphite electrodes. These authors also compared the differences in formal redox potentials of redox couples in solution and when incorporated in montmorillonite coatings, and in coatings of Nafion (sulphonate fixed charge-sites). They concluded that the factors responsible for the binding of cations in the two coatings were clearly different. In particular clay coatings were found to stabilize the lower oxidation state of each redox couple, whereas

in Nafion the more highly charged complex was more tightly bound. This meant that factors in addition to simple electrostatic interactions between the incorporated cations and the fixed anionic groups contributed to the thermodynamics governing the incorporation equilibria in montmorillonite coatings.

Uchida, Chang and Itaya[116] recently reported the incorporation of negatively charged species at electrodes coated with a hydrotalcite (HT) like clay. Because of its positively charged brucite-like layers and negatively charged interlayers it is known that anions such as Cl-, NO_3^- and SO_4^{2-} located in the interlayers of HT could be substituted for other anions via anion-exchange reactions. The Japanese workers ion exchanged $[Mo(CN)_8]^{4-}$ and $[Fe(CN)_6]^{n-}$ type anions and reported a voltammetric behaviour comparable to that seen in other clays.

Davison and McWhinnie[117] showed that for a platinum electrode coated with a thin film of $[Co\ (bpy)_3]^{3+}$ exchanged hectorite the $[Co\ (bpy)_3]^{3+}$ was reduced to $[Co(bpy)_3]^{1+}$ by passage of a current. The Co(I) oxidation state was identified by uv-visible diffuse reflectance spectroscopy. These workers also managed to show that the cobalt complex acted as a redox catalyst for the conversion of nitrobenzene to aniline. The clay film prepared by Davison was not robust. In the present work our aims were to develop a more robust clay film, to incorporate other metal complexes such as $[Cr(bpy)_3]^{3+}$ and to study the voltammetric behaviour of platinum electrodes coated with clays doped with $[Co(bpy)_3]^{3+}$ and $[Cr(bpy)_3]^{3+}$ complexes. As the hectorite - $[Co(bpy)_3]^{3+}$ using UV-vis and IR spectroscoy by Davison[118], we therefore attempted to probe the nature of $[Cr(bpy)_3]^{3+}$ adsorbed on laponite.

3.2 CHEMICALS

The ligand 2,2' - bipyridyl was obtained from Aldrich Chemical Co Ltd. Chromium trichloride hexadydrate (analar) and sodium perchlorate were obtained from BDH. Distilled methanol and distilled water were used in the preparations.

3.3.1 Synthesis of Tris-bipyridyl Chromium III Perchlorate (Following Gillard and Mitchel)

After a few modifications to the basic method used by Gillard and Mitchel to prepare $[Cr(en)_3]^{3+}$ complexes the following prodedure was adopted.

Chromium III chloride hexahydrate (0.3g) was dissolved in dry, distilled methanol ($20cm^3$) and transferred to a $100cm^3$ round-bottomed flask. A few zinc granules, previously washed with dilute HCl, were added to the solution which was then refluxed gently for thirty minutes.

The ligand 2,2' - bipyridine (3.5g) was dissolved in the minimum quantity of methanol and added slowly to the refluxing solution down the sides of the condenser. Refluxing was continued for two hours. Excess sodium perchlorate dissolved in a minimum of distilled water was added to the mixture. After stirring for about fifteen minutes the mixture was filtered over a fluted paper and transferred to a 100ml beaker. Excess solvent was slowly boiled off before allowing the yellow solution to cool slowly. Yellow microcrystals which crystallised out of the solution were filtered under vacuum and recrystallised from water.

3.3.2 Preparation of Tris-bipyridyl Chromium III - Chloride by Using a Jones Reduction Method

The Jones Reductor was prepared by following the literature[23]. A long glass column fitted with a stop cock at one end, was packed with amalgamated zinc (prepared by stirring granulated zinc (300g) in a mercuric chloride solution (2%) in a beaker for 10 minutes, then decanting the $HgCl_2$ and washing with water). Glass wool was placed in position above the stop-cock and the end of the column was fitted into a $250cm^3$ three-neck flask with an argon inlet.

Perchloric acid was passed slowly through the column to activate the zinc. The column was then connected via an air-tight seal to the three neck-flask

containing a suspension of 2,2-bipyridyl ligand (3.5g) in distilled water (90ml). The flask and its contents were deoxygenated using argon.

Sufficient $CrCl_3.6H_2O$ was dissolved in $HClO_4$(0.1M) to make up a 0.2M solution of Cr^{3+}(aq). This solution was then poured slowly down the column and allowed to stand until the green coloured solution turned to a sky-blue indicating reduction of Cr^{3+}(aq) to Cr^{2+}(aq).

The stop-cock was opened and Cr^{2+}(aq) solution ($10cm^3$) was added slowly with stirring to the deoxygenated suspension of the ligand. After complete addition of the Cr^{2+}(aq) solution a purple-black solution was obtained. As this stage the argon inlet was replaced by oxygen which was bubbled through the solution for about one hour. The yellow microcrystals of $[Cr(bpy)_3](ClO_4)_3.3H_2O$ which appeared on the sides of the flask were suction filtered, washed with ethanol and recrystallised from water.

3.3.3 Preparation of Trisbipyridyl Chromium III Perchlorate Using a Modified Mehta/Baker Method.[119]

$HClO_4$ (0.1M) was prepated by dissolving 60% $HClO_4$ (7.03g) in distilled water and diluting to $500cm^3$. A 0.2M $Cr(aq)^{2+}$ solution was made by adding a known weight of $Cr(OAc)_2.2H_2O$ to previously deoxygenated $HClO_4$(0.1M). This procedure was carried out in a nitrogen filled glove-box. The dark blue suspension obtained was further deoxygentated to remove all traces of oxygen.

2,2'-bipyridine ligand (2g) was dissolved in methanol ($10cm^3$) and added to a three-neck flask containing deoxygenated water (90ml) adjusted to pH2 by addition of perchloric acid. Addition of the bipyridyl ligand raised the pH to about 7 which required further addition of perchloric acid.

The $Cr(aq)^{2+}$ solution (10ml) was then quickly added to the bipyridyl suspension whilst a flow of nitrogen was maintained through the flask. A black/purple colouration was obtained corresponding to the presence of $[Cr(bpy)_3](ClO_4)_2$. The nitrogen intlet was replaced by oxygen which was bubbled through the black solution for an hour. Yellow microcrystals of the perchlorate salt $[Cr(bpy)_3](ClO_4)_3.3H_2O$ were formed on the sides of the flask. The crystals

were removed by vacuum filtration (on a sintered funnel), washed with ethanol and recrystallised from water.

3.3.4 Preparation of Tris-bipyridylcobalt III Perchlorate

Cobalt II chloride hexahydrate (2.4g) ($CoCl_2.6H_2O$) was dissolved in distilled water ($50cm^3$) and refluxed gently in a $250cm^3$ round-bottom flask. 2,2'-bipydrine (4.7g) was dissolved in ethanol ($10cm^3$) and added dropwise via a dropping funnel the $CoCl_2$ solution. After complete addition a yellow/brown solution was obtained which was refluxed for a further thirty minutes.

After thirty minutes hydrogen peroxide (H_2O_2) (30% ω/v,$10cm^3$) and hydrochloric acid (1.18sp.g, $10cm^3$) were added separately to the $CoCl_2$ solution. The mixture was refluxed for a further thirty minutes before being transfered to a $250cm^3$ conical flask and evaporated slowly until a syrup consistency was obtained. Water ($50cm^3$) and perchloric acid $HClO_4$ (60%, $10cm^3$) were then added to the mixture. On warming a brown residue was depositied and the hot solution was filtered over a fluted filter paper to remove the brown inorganic compound. The yellow filtrate was slowly evaporated and yellow crystals which formed on cooling, were filtered under vacuum and recrystallised from warm water.

3.4 EXPERIMENTS TO STUDY THE NATURE OF THE ADSORBED $[Cr(bpy)_3]^{3+}$ SPECIES ON CLAYS

3.4.1 Preparation of Clay Doped with $[Cr(bpy)_3](ClO_4)_{3\cdot 1/2}\ H_2O$

70 meq of $[Cr(bpy)_3]\ ClO_4\cdot_{1/2}\ H_2O$ (≈ 0.5g) was weighed into a $100cm^3$ conical flask and dissolved in deionised water ($50cm^3$). Laponite (Na+ form, 1g) was added to the solution, the flask was stoppered and shaken for 48 hours. The clay was then removed from solution by centrifugation and washed several times

Table 3.4.4 Elemental Analysis Data

1) $Cr(bpy)_3(ClO_4)_3.1/2H_2O$ **(Gillard/Mitchel Method)**

Required	C = 46.6			
	H = 3.1			
	N = 10.1			
Found				
	C	49.4	51.4	53.2
	H	3.2	3.5	3.6
	N	12.4	12.7	13.8

2) $Cr(bpy)_3(ClO_4)_3.1/2H_2O$ **(Jones-Reduction Method)**

Required	C = 46.6			
	H = 3.1			
	N = 10.1			
Found				
	C	46.7	46.5	46.9
	H	3.1	3.0	3.5
	N	10.3	10.1	10.6

Table 3.4.5 Elemental Analysis Data

3) $Cr(bpy)_3(ClO_4)_3.1/2H_2O$ (Modified Mehta/Baker Method)

Required C = 46.6

N = 10.1

H = 3.1

Found

C	46.2	46.0	46.2
H	3.2	3.2	3.0
N	10.0	10.2	10.5

4) $Co(bpy)_3(ClO_4)_3.3H_2O$

Required C = 40.1

H = 2.9

N = 9.1

Found

C	40.1	40.5
H	2.7	2.5
N	9.0	8.6

Table 3.4.4 Elemental Analysis Data

1) $Cr(bpy)_3(ClO_4)_3.1/2H_2O$ (Gillard/Mitchel Method)

Required	C = 46.6			
	H = 3.1			
	N = 10.1			
Found				
	C	49.4	51.4	53.2
	H	3.2	3.5	3.6
	N	12.4	12.7	13.8

2) $Cr(bpy)_3(ClO_4)_3.1/2H_2O$ (Jones-Reduction Method)

Required	C = 46.6			
	H = 3.1			
	N = 10.1			
Found				
	C	46.7	46.5	46.9
	H	3.1	3.0	3.5
	N	10.3	10.1	10.6

Table 3.4.5 Elemental Analysis Data

3) $Cr(bpy)_3(ClO_4)_3.1/2H_2O$ (Modified Mehta/Baker Method)

Required C = 46.6

N = 10.1

H = 3.1

Found

C	46.2	46.0	46.2
H	3.2	3.2	3.0
N	10.0	10.2	10.5

4) $Co(bpy)_3(ClO_4)_3.3H_2O$

Required C = 40.1

H = 2.9

N = 9.1

Found

C	40.1	40.5
H	2.7	2.5
N	9.0	8.6

with deionised water to remove any extraneous or physically adsorbed ions. The colloid like clay was reslurried in a minimum amount of deionised water, transferred to a petri-dish and allowed to air dry for a week.

3.4.2 Preparation of $[Co(bpy)_3](ClO_4)_3 : Cr^{3+}$ (5%)

For ESR studies it was desirable to prepare the $[Cr(bpy)_3]^{3+}$ complex in a dilute form. In the hope that the $[Co(bpy)_3](ClO_4)_3.nH_2O$ lattice is isostructural with that of the chromium salt, attempts were made to grow dilute crystals of the Cr in the Co complex. Five per cent weight of the chromium complex ie 0.5g of Co complex and 0.025g of the Cr complex were separately dissolved in $100cm^3$ of deionised water. The two solutions were then mixed intensively and evaporated on a hotplate to yield crystals of $[Co(bpy)_3](ClO_4)_3: Cr^{3+}$.

3.5 CHEMICAL REDUCTION OF $Cr(bpy)_3^{3+}$ LAPONITE AND $[Co(bpy)_3]^{3+}$ - LAPONITE

(i) $Cr(bpy)_3^{3+}$ - Laponite (1g) was placed in a three neck $50cm^3$ round bottom flask, covered with deionised water ($10cm^3$) and deoxygenated for about thirty minutes. $NaBH_4$ (0.037g, 1.0mmol) was added and stirring was commenced. After stirring for 5 minutes the yellow colour of the clay turned to a pink/red colour, which eventually faded and returned to yellow on prolonged stirring. Addition of excess $NaBH_4$ resulted in the clay taking on a dark blue colour. The dark blue colour could be maintained as long as a flow of nitrogen was maintained in the flask. Attempts to obtain diffuse reflectance spectra were unsuccessful due to the highly air-sensitive nature of the reduced laponite - $Cr(bpy)_3^{+}$ product.

(ii) $[Co(bpy)_3]^{3+}$ - laponite (1g) was stirred for one hour with $NaBH_4$ (0.037g, 1.0mmol) in deionised water ($10cm^3$); a flow of nitrogen was

maintained throughout the experiment. In accordance with the results obtained by Davison[117] the yellow coloured clay turned dark blue after a few minutes stirring in the presence of $NaBH_4$.

3.5.2 Electrochemical Reductions[118]

$[Cr(bpy)_3]^{3+}$ Laponite was ground into a fine powder and allowed to flocculate from acetonitrile suspension onto the surface of a bright platinum electrode (approx 2.0cm^2). The electrode was positioned horizontally in a conical flask together with a piece of platinum foil. A previously deoxygenated acetonitrile solution (1.0M) in tetrabutyl ammonium hexafluorophosphate, was used as supporting electrolyte. Currents in range 2 - 10 mA were applied to the electrode but no colour change to the clay was observed.

The above procedure was repeated for $[Co(bpy)_3]^{3+}$ laponite, and as reported by Davison[118], passage of a small current (2 - 10 mA) resulted in the appearance of the deep blue $[Co(bpy)_3]^{1+}$ on the cathode.

3.6 PREPARATION OF A MECHANICALLY ROBUST CLAY-MODIFIED ELECTRODE

Two procedures were developed, both of which produced robust and electroactive clay-films.

(i) Polyvinyl alcohol (PVA) (0.2g) was dissolved in a 40:60 mixture of ethanol and water (100cm^3). The solution was cooled to room temperature. Laponite (0.5g) was suspended in the solution and dispersed using a mechanical paddle stirrer for about one hour. A small amount of the slurry was carefully deposited on a bright platinum electrode surface so as to cover virtually all of the electrode. The slurry was left to air-dry overnight. The other side of the platinum electrode was treated similarly. After air-drying a thin clay film was formed on both sides of the electrode.

(ii) Platinum II chloride (0.05g) and PVA (0.66g) were added to a 40:60 ethanol-water mixture which was then refluxed for three hours in order to obtain an homogenous suspension.

Laponite (10g) was dispersed in distilled water (100cm^3) using ultrasound for a duration of 30 minutes in order to generate extremely small clay particles. The slurry was then centrifuged for one hour at 5000 rpm. The supernatent liquid was decanted off and 5g of the Pt-PVA suspension. The mixture was refluxed for a further one hour to obtain a colloidal clay suspension. The clay film was cast by depositing a drop of the Pt/PVA/clay suspension onto both sides of the platinum electrode and allowing to air-dry.

(iii) After complete drying the clay-modified electrodes were dipped in a 0.1M solution of either $[Cr(bpy)_3]$ $(ClO_4)_{3\cdot 1/2}$ H_2O or $[Co(bpy)_3]$ $(ClO_4)_3$ $.3H_2O$ for one hour. The clay films were then washed in a stream of deionised water to remove physically adsorbed species and again allowed to air-dry before use.

3.7 THE ELECTROCHEMICAL CELL

The apparatus used for the cyclic voltammetry experiments is shown in Fig. 3.2. An existing electrochemical cell was modified to allow nitrogen to be bubbled through the supporting electrolyte.

A 0.1M solution of Bu_4NPF_6 in acetonitrile was used as the supporting electrolyte. The complete electrochemical cell consisted of

(i) A working electrode ie a bright platinum foil (1cm^2) modified by a clay film on both surfaces.

(ii) A reference electrode which consisted in our case of a second identical platinum foil.

Fig. 3.2. THE ELECTROCHEMICAL CELL

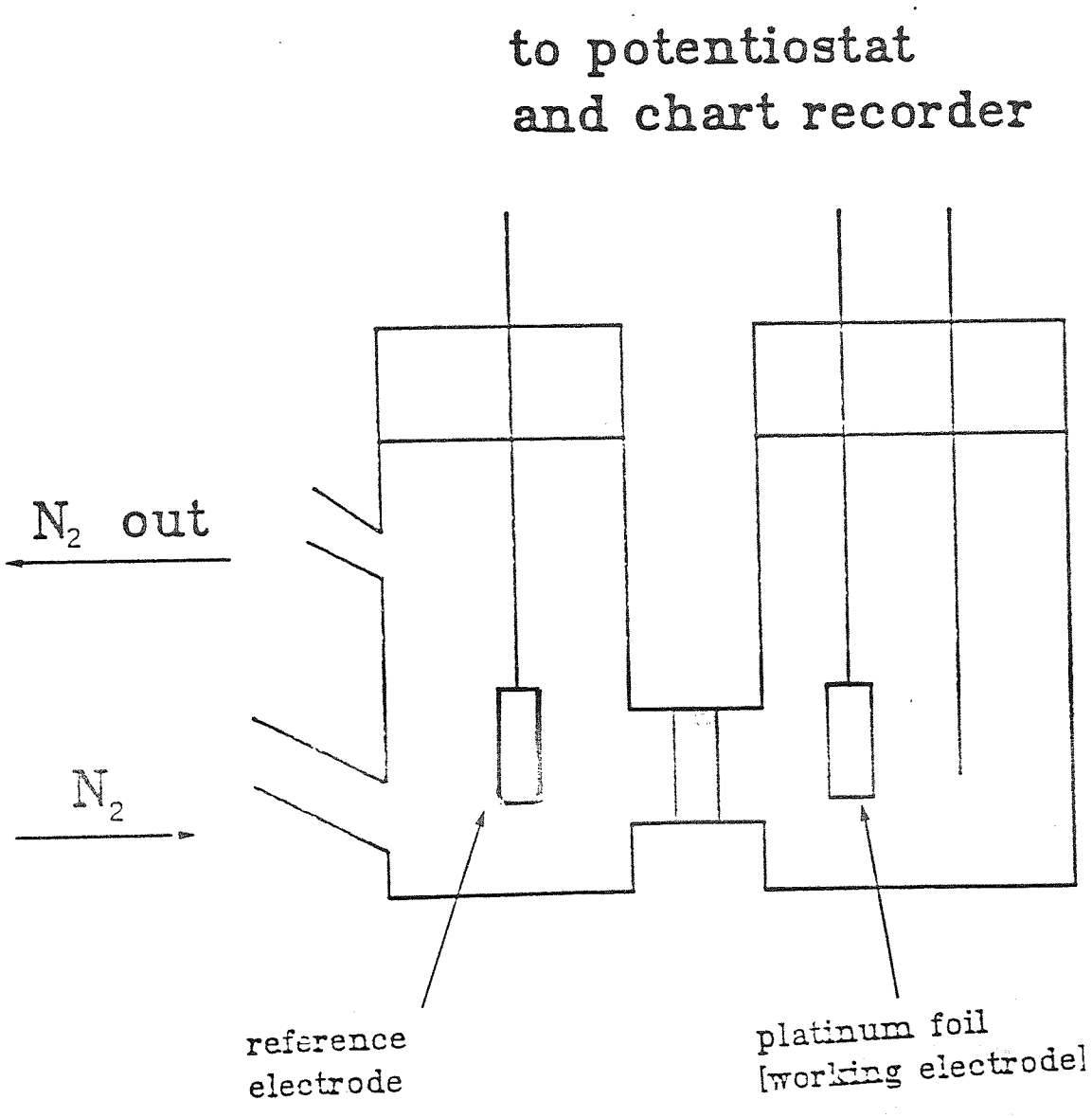

(iii) A counter/auxiliary electrode which was simply a sheathed platinum wire.

The geometry of the electrochemical cell was found to be a crucial factor in the experimental work. The best arrangement of electrodes was to separate the reference electrode from the working and auxilliary electrodes which were housed in the same compartment. A porous membrane separated the two main compartments of the cell. The supporting electrolyte was deoxygenated by bubbling nitrogen through the cell for about 10 minutes. Cyclic voltammograms obtained are discussed at a later stage.

3.8 A SPECTROSCOPIC EXAMINATION OF THE NATURE OF ADSORBED $[Cr(bpy)_3]^{3+}$

3.8.1 UV-Visible Diffuse Reflectance Data

$[Cr(bpy)_3]^{3+}$ in aqueous solution has a well characterised electronic absorption spectrum. As recorded earlier in the results section, the most important bands are a strong UV-band near 308-312nm which is assigned to the π->π^* transitions of the ligands and a complex band near 346nm which is due mainly to d->d character. The diffuse reflectance spectrum for laponite + $[Cr(bpy)_3]^{3+}$ consists of two new reflectance bands at 480 - 485nm, at 532nm and two relatively weak bands at 480-485nm, at 532nm and two relatively weak bands at 552nm and 610nm. In a study of the photoreactivity of adsorbed $[Cr(bpy)_3]^{3+}$ and $[Ru(bpy)_3]^{2+}$ complexes, Abdo et al observed the evolution of UV bands at 530nm and 470-80nm which were obtained after irradiating $[Cr(bpy)_3]^{3+}$ -hectorite films[122]. These bands were attributed to the photoaquation of the chromium (III) complex in the clay interlayer regions. Specifically, the French workers attributed the 470-80nm bands to $[Cr(bpy)_2(H_2O)_2]^{3+}$ and the band at 530nm due to the $[Cr(bpy)_2(OH)_2]^{+}$ species which suggested that photoinduced decomposition of $[Cr(bpy)_3]^{3+}$ on clay leads to the simultaneous formation of the diaquo - and dihydroxo- species. Our

Table 3.4.6 UV - Visible Spectroscopy Results

Complex	Wavelength nm^{-1}		
$Cr(bpy)_3 (ClO_4)_3.1/2H_2O$ GILLARD/MITCHEL METHOD			
A	286	295	308
B	285	295	308
C	286	295	308
$Cr(bpy)_3 (ClO_4)_3.1/2H_2O$ JONES REDUCTION METHOD			
A	287	293	307 sh
B	287	296	307 sh
C	286	294	307
$Cr(bpy)_3 (ClO_4)_3.1/2H_2O$ MEHTA/BAKER METHOD			
A	280	295	308
B	280	295	308
$Co(bpy)_3 (ClO_4)_3.3H_2O$			
A	317		451
B	315		451

3.4.7 FT Infra-Red Results for $Cr(bpy)_3^{3+}$/Laponite (70 meq loading)

	Laponite	Laponite/ $Cr(bpy)_3^{3+}$ (1)	Laponite/ $Cr(bpy)_3^{3+}$ (2)
Wavelength cm^{-1}	3642	3713	3713
	1642	3690	3690
	1011	3436	3441
	654	1636	1635
	448	1608	1606 (db)
		1566	1599
		1534	1586
		1490	1563
		1476	1494
		1461	1476
		1442	1460
		1423	1444
		1325	**1423**
		1011	1384
		761	1317
		741	1007
		690 (sh)	762
		675 (sh)	739
		654	652
		530	466
		466	448
		448	

(1) = $Cr(bpy)_3^{3+}$ prepared by Mehta/Baker Method

(2) = $Cr(bpy)_3^{3+}$ prepared by Jones-Reductor Method

Table 3.4.8 UV-Visible Diffuse Reflectance Results for Laponite/$Cr(bpy)_3^{3+}$

	Wavelength (nm^{-1})			
Laponite/ $Cr(bpy)_3^{3+}$ (1)	480	532		
Laponite/ $Cr(bpy)_3^{3+}$ (2)	485	532	552	610
Laponite/ $Cr(bpy)_3^{3+}$ (3)	485	532	552	610

(1) Gillard/Mitchel Method

(2) Jones-Reduction Method

(3) Mehta/Baker Method

results lead us to speculate that the diffuse reflectance bands also have the same origin. It was previously discovered that the lights within our laboratory do indeed cause some UV-irradiation[33] (the laboratory is not fitted with windows). The clay interlayer region contains plenty of labile water molecules in the vicinity of the $[Cr(bpy)_3](ClO_4)_3$. It is therefore not implausible for a small degree of photoaquation to occur. This is borne out by the weakness of the diffuse reflectance bands which would be expected to be considerably stronger in the presence of larger amounts of UV light eg sunlight.

3.8.2 Infra-red Data

Infra-red spectra of $[Cr(bpy)_3]^{3+}$ exchanged laponite and $[Cr(bpy)_3](ClO_4)_3 \cdot 1/2H_2O$ are shown in Fig. 3.5.2. Since the IR spectra of $[Cr(bpy)_3]^{3+}$ system have been studied in detail it will not be discussed further. No new bands appear on the clay + complex spectrum other than those which are present on the spectrum of the complex itself. The very slight modifications of the IR bands (if any) favour a structure of the adsorbed complex where the fundamental nature of the ligand is left unchanged and that the overall symmetry of the complex is unaltered.

3.8.3 Electron Spin Resonance (ESR) Data

ESR spectra were recorded at 9.55GHz for powdered samples of $[Cr(bpy)_3](ClO_4)_3.1/2H_2O$ crystals, $[Cr(bpy)_3]^{3+}$ doped into $Co(bpy)_3(ClO_4)_3 3H_2O$ and for laponite exchanged with $[Cr(bpy)_3]^{3+}$. Figure A shows the powder ESR spectrum for $[Cr(bpy)_3](ClO_4)_3.1/2H_2O$ at 9.55GHz scanned over a magnetic field range between O and 5000G; Fig. B shows the 9.55GHz spectrum of laponite- $[Cr(bpy)_3]^{3+}$ at the same range. Fig. A clearly shows a highly anisotropic spectrum. From the very large spread of the observed lines along with the high intensity of the "forbidden" lines at low magnetic field strength, it is clear that zero-field splitting, due to higher order spin-orbit coupling and a low symmetry

ligand field, is large; so large in fact that some of the high-field transitions are well outside the range of our magnet (max 10KG). This, together with the large linewidths of the lines limits the accuracy of the g-values. From the powder spectrum of $[Cr(bpy)_3]^{3+}$ the transition corresponding to $m=^1/_2 <--> -^1/_2$ is clearly observed and a g-value is calculated at g=1.995. A sharp free-radical like resonance at g=2.007 is also observed. The linewidth covered by the $m=^1/_2 <--> -^1/_2$ transition is about 200G. Two hyperfine lines (for ^{53}Cr) of the $^1/_2 <--> -^1/_2$ transition are also observed at 3200G and 3550G. The $m= +^1/_2 <--> m= +^3/_2$ transition is also observed as an anisotropic multicomponent resonance at g = 4.670 and g = 3.370. The approximate spread of the transition is about 1000G.

Fig. 3.5 is a powder ESR spectrum of a magnetically dilute sample of $[Cr(bpy)_3]^{3+}$ ie 5% $[Cr(bpy)_3]^{3+}$ in an isostructural, diamagnetic $[Co(bpy)_3]^{3+}$ lattice denoted as $[Co(bpy)_3]^{3+} : Cr^{3+}$. A sharp $m=^1/_2 <--> -^1/_2$ resonance is observed at g = 1.995, but a much broader $m= ^1/_2 <--> ^3/_2$ resonance with a linewidth of about 1500G. It appears therefore that our attempts to grow a magnetically dilute $[Cr(bpy)_3]^{3+}$ crystal were not successful. One reason may be that the two complex lattices $[Cr(bpy)_3](ClO_4)_3 \cdot ^1/_2 H_2O$ and $[Co(bpy)_3](ClO_4)_3 \cdot 3H_2O$, are not completely isostructural as was first thought. It may be that the different number of associated watermolecules may be the cause of a disrupted $[Co(bpy)_3]^{3+} : Cr^{3+}$ crystal.

In a recent study of the electronic and molecular structure of $[Cr(bpy)_3]^{3+}$ using ESR and optical spectroscopy Hauser et al recorded single crystal and powdered ESR spectra for $[Cr(bpy)_3]^{3+}$ doped into an isomorphous Rh(III) lattice use a Q-band spectrometer operating at a frequency of 35GHz, and covering a magnetic field range of up to 17KG. Even under such conditions the high-field transitions were still out of the range of their magnets. However they recorded g-values for powdered samples of $Rh(bpy)_3(PF_6)_3 : Cr^{3+}$ of $g_{11} = 1.984$ and $g_{\perp} = 1.976$.

We can account for our very broad spectra by considering the case for d^3 octahedral complexes. The combined action of any field of lower symmetry and spin-orbit coupling produces the zero magnetic field splittings D and E, which separate the $m = \pm 3/2$ states. The application of a magnetic field then removes the remaining degeneracy of the Kramers doublets. The allowed transitions are those where $\Delta m = 1$.

Fig. 3.5.1 Energy Levels for a d^3 (Chromium) Complex

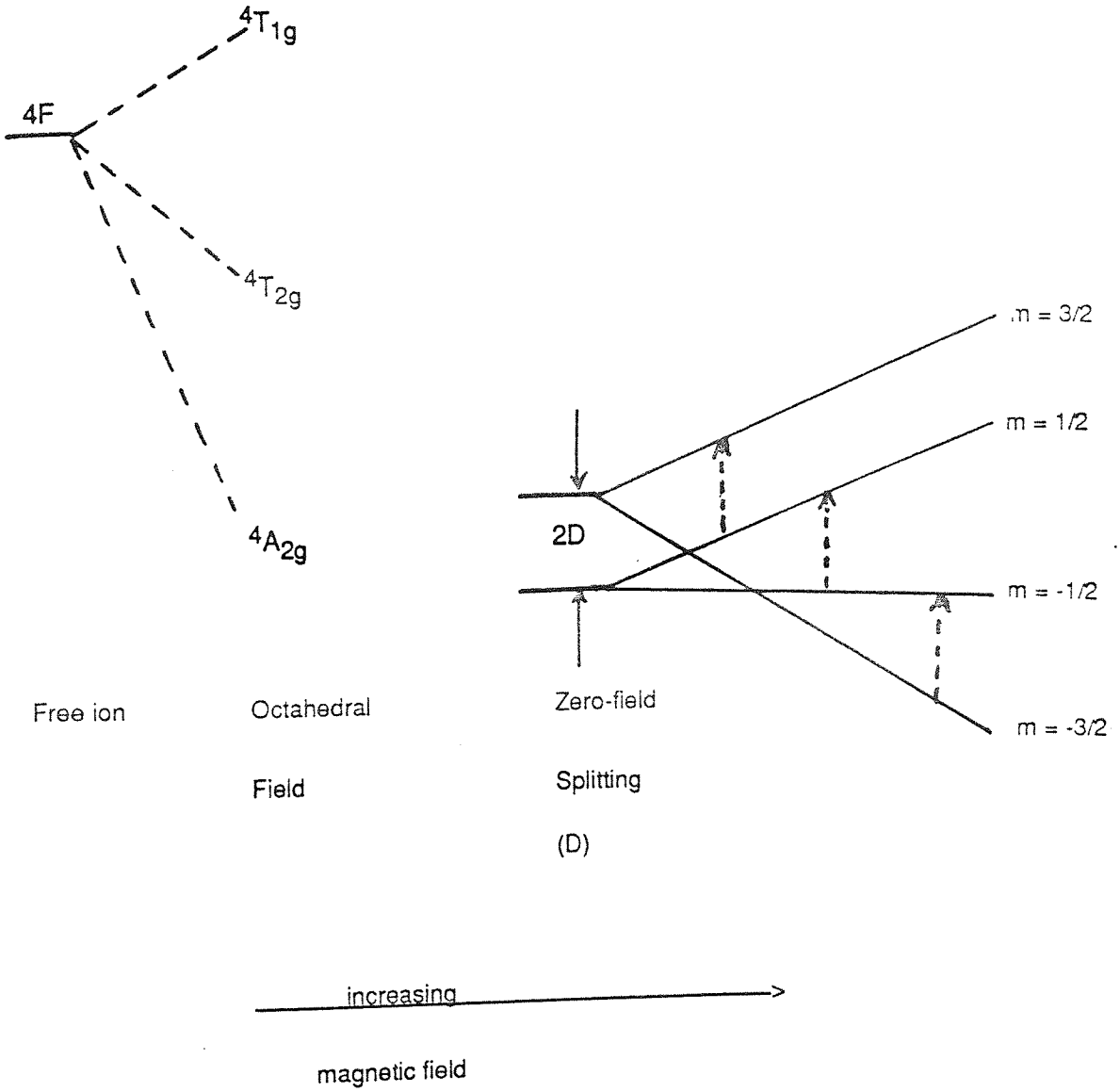

We can account for our very broad spectra by considering the case for d^3 octahedral complexes. The combined action of any field of lower symmetry and spin-orbit coupling produces the zero magnetic field splittings D and E, which separate the $m = \pm 3/2$ states. The application of a magnetic field then removes the remaining degeneracy of the Kramers doublets. The allowed transitions are those where $\Delta m = 1$.

Fig. 3.5.1 Energy Levels for a d^3 (Chromium) Complex

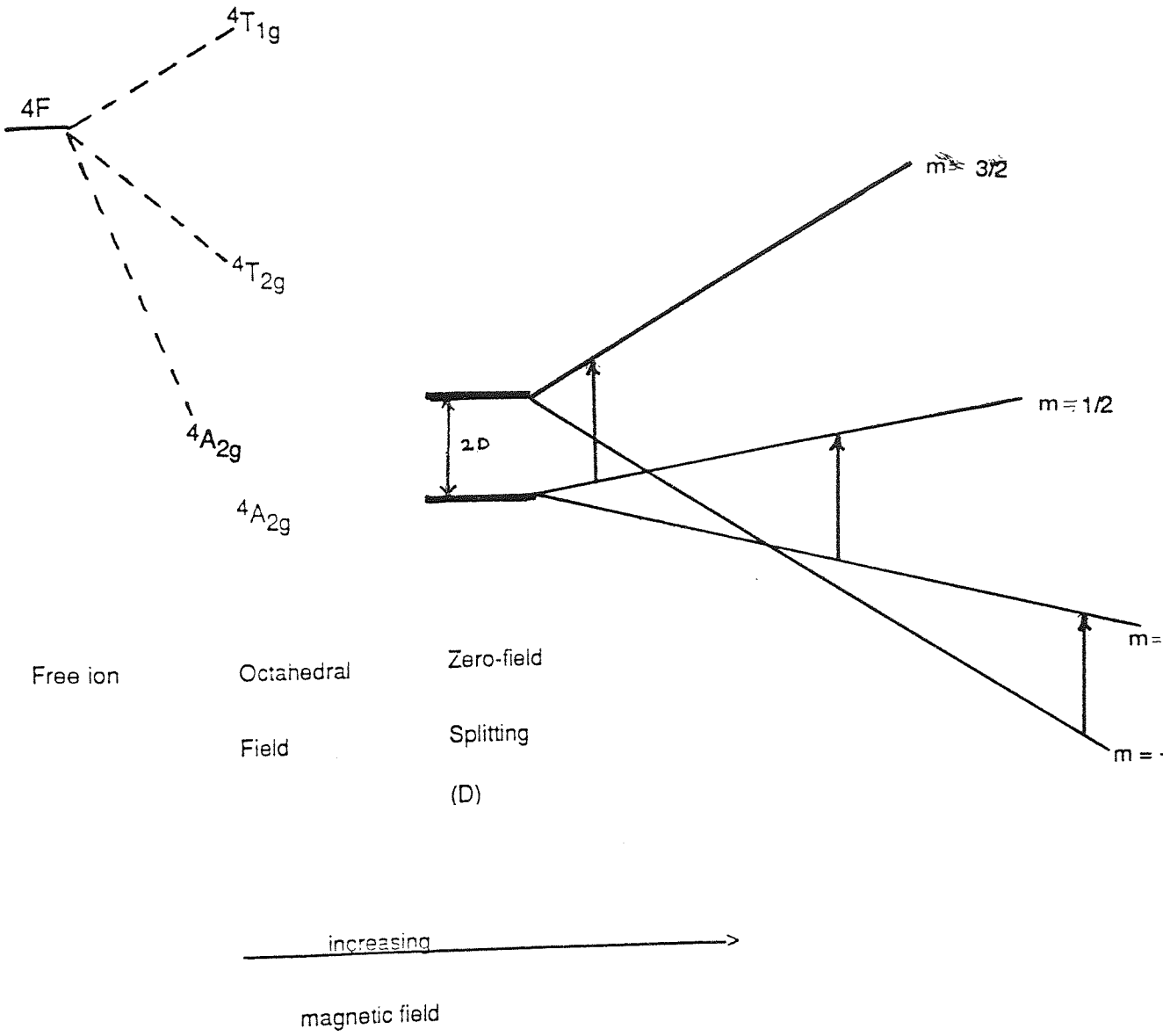

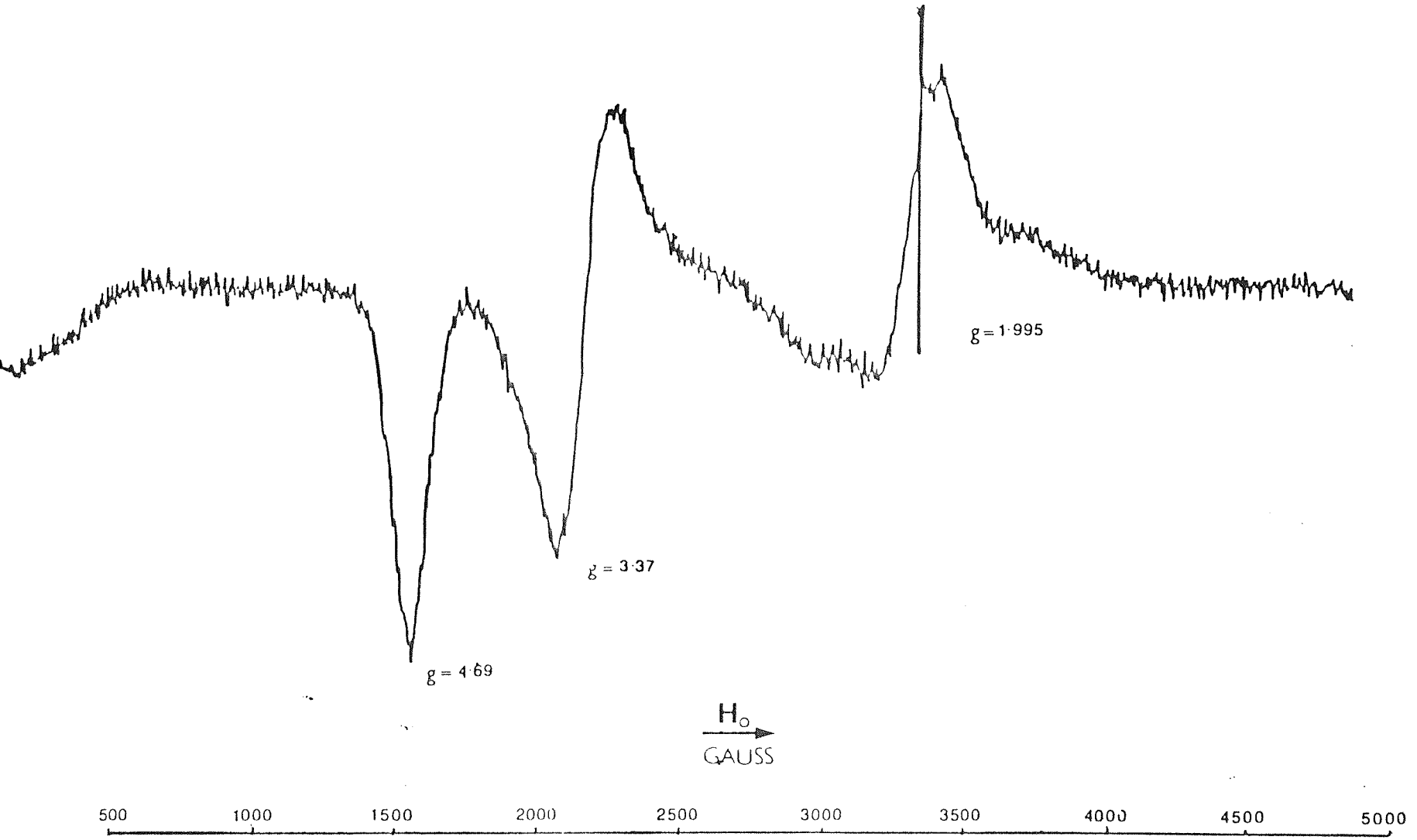

Fig. 3.3 ESR Spectrum of $[Cr(bpy)_3](ClO_4)_3.1/2H_2O$ (micro crystalline powder)

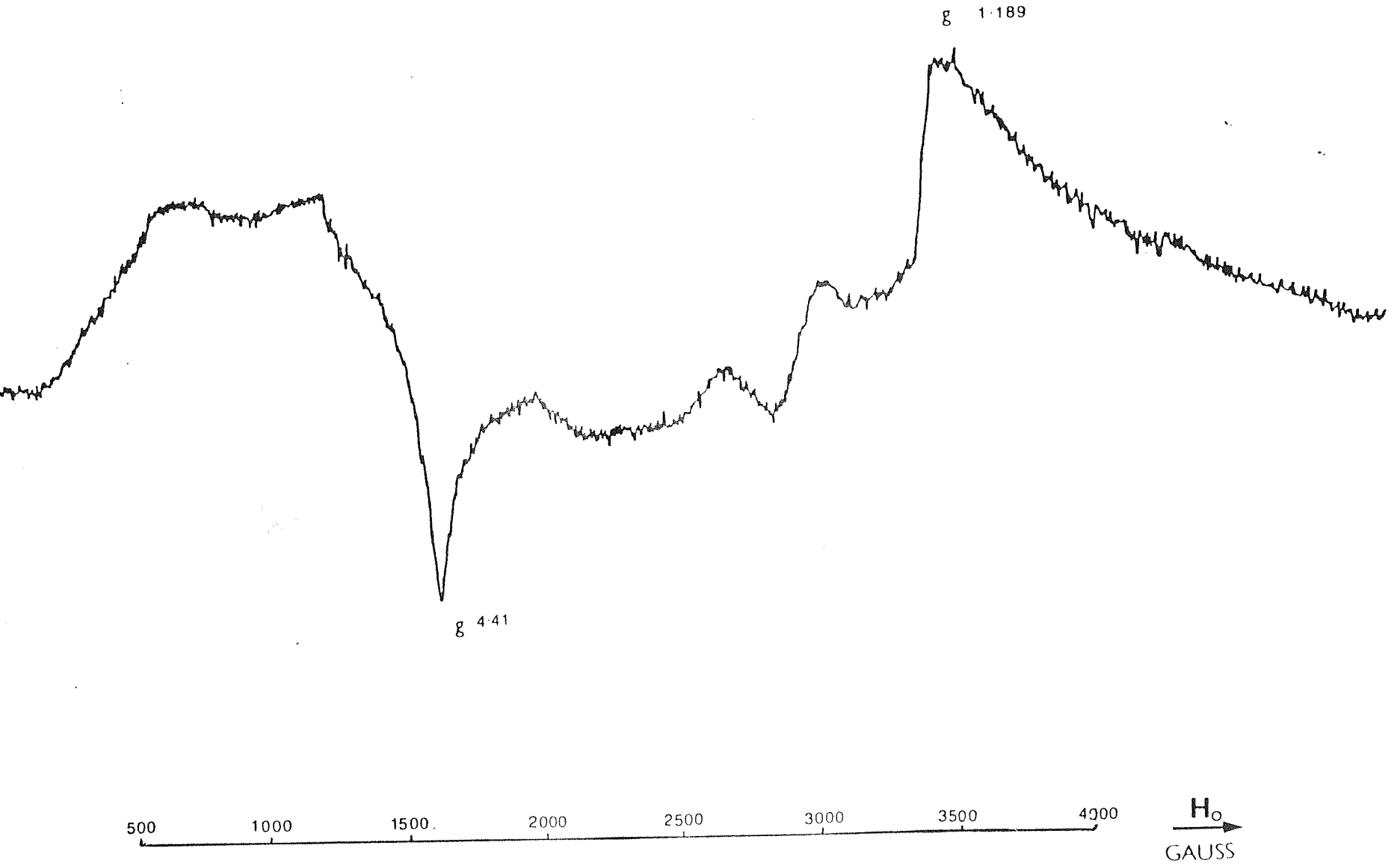

Fig. 3.4 ESR Spectrum of Laponite Exchanged with $[Cr(bpy)_3](ClO_4)_3.1/2H_2O$

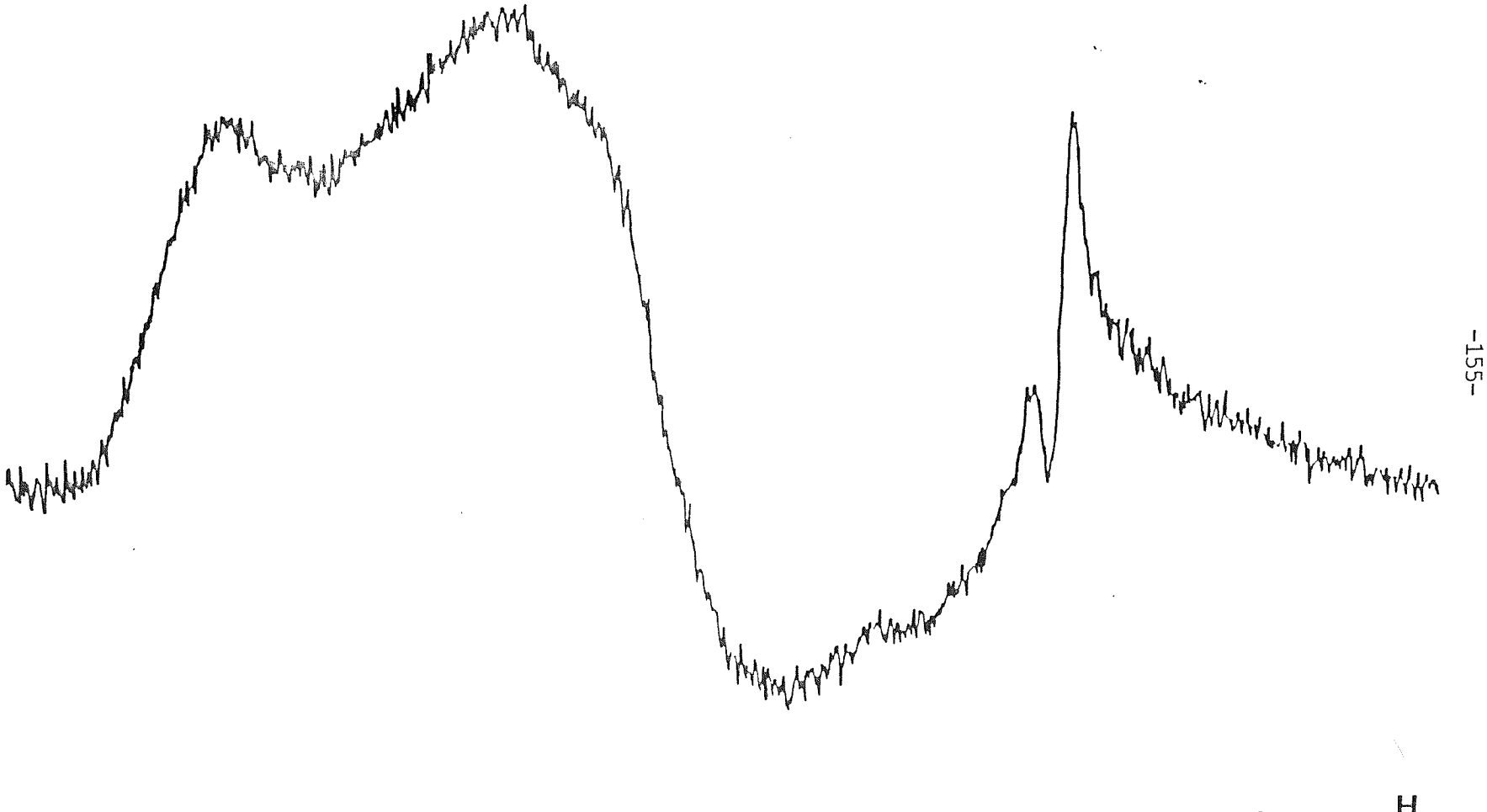

Fig. 3.5 ESR Spectrum of $[Co(bpy)_3]:Cr^{3+}$ (5% Cr^{3+})

(A)

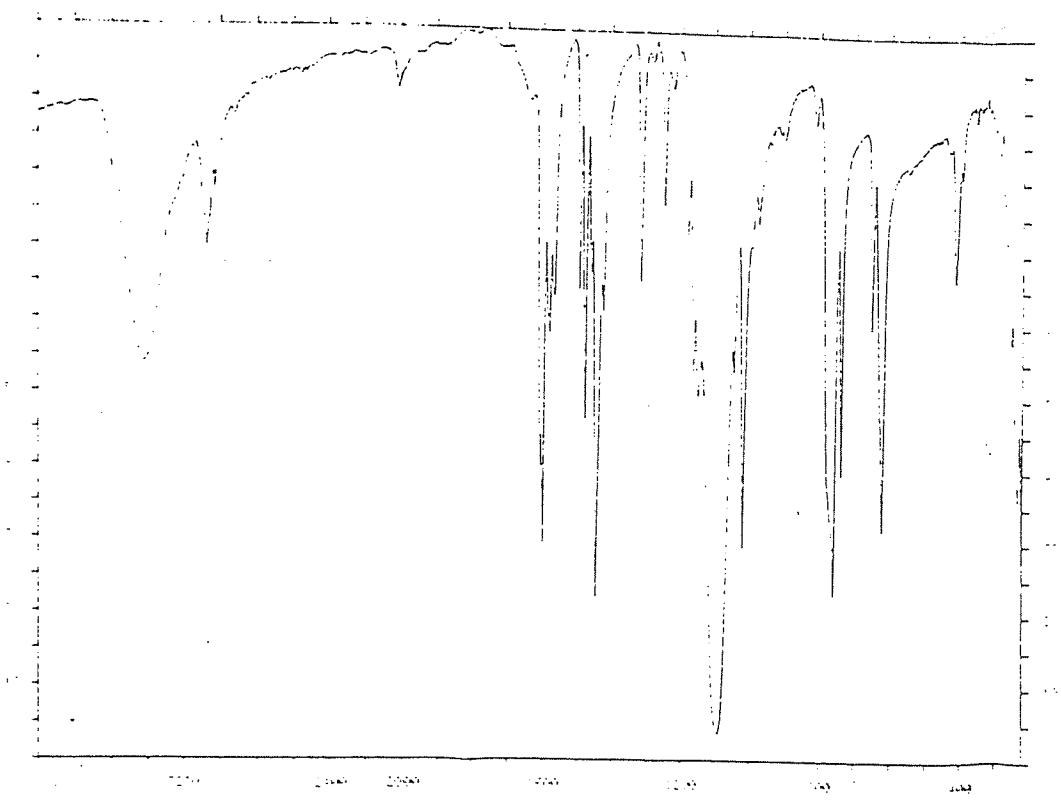

(B)

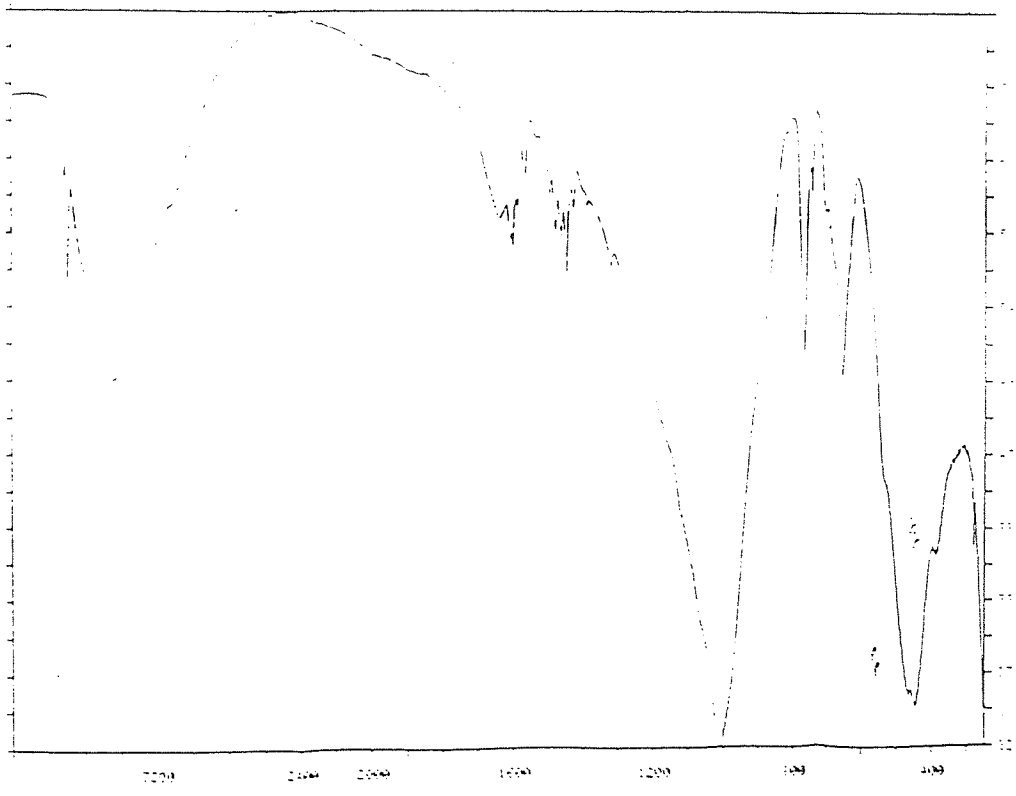

Fig. 3.5.2 IR Spectra of

(A) $Cr(bpy)_3(ClO_4)_3.1/2H_2O$

(B) Laponite Exchanged with $Cr(bpy)_3^{3+}$

The allowed transitions are m = 1/2 to -1/2, m = -1/2 to +3/2. The first two occur at relatively low magnetic field strengths and hence can be observed in our case. The m = - 3/2 to -1/2 transition is not observed however, since it occurs at much higher field strength.

The ESR spectrum for laponite exchanged with $[Cr(bpy)_3]^{3+}$ (ie Laponite - $Cr(bpy)_3^{3+}$) is shown in Fig.3.4 There is clearly a significant difference in the lineshapes. Firstly, the g-values are slightly changed. The m = -1/2 $<\!\!\rightarrow$ 1/2 transition is much broader (300G) and has a g-value of g = 1.989. The m=1/2 $<\!\!\rightarrow$ 3/2 transition is again clearly observed and has an anisotropic powder lineshape, but the g-value of the low-field anisotropic component is now changed to g= 4.410 (previously g = 4.670 in the $Cr(bpy)_3^{3+}$ crystals) whereas the other higher-field component is missing altogether. Nevertheless the anisotropy of the $[Cr(bpy)_3]^{3+}$ system is still retained. Normally for hydrated complexes in the interlayer region of a clay mineral, a solution-like environment is expected[32] as interlayer water molecules are known to be present in the second and third coordination spheres of the complex. In solution we should expect an isotropic resonance corresponding to the m=-1/2 to +1/2 transition at around g = 2.0, but since the anisotropic components are clearly retained for the laponite - $Cr(bpy)_3^{3+}$ spectrum, this means that the overall symmetry of $[Cr(bpy)_3]^{3+}$ (in crystalline form) is also retained in the interlayer region of the clay. The most likely explanation for differences in spectral lineshapes and altered g-values may be due to several reasons. Firstly, as suggested by McGarvey, the spin of the Cr^{3+} ion may be sensitive to nearby dipoles caused by water molecules which are in abundance in the interlayer region of the clay. Also there may be constraints imposed on the octahedral symmetry of the complex by the silicate layers. It is possible that the C_3 axis of the hromium complex is perpendicular to the plane of the silicate layers. This has been shown to be the case for CuII complexes adsorbed onto clay minerals[32,33]. Non-isostructural lattices may be another reason for the broadness of the spectral components.

However, in view of the UV-visible diffuse reflectance results where evidence was produced for photo induced decomposition of the $[Cr(bpy)_3](ClO_4)_{3\cdot 1/2}H_2O$ to the diaquo- and dihydroxo species, it is probable that the presence of these two new species may affect the spin of the ESR-active Cr^{3+} complex. Indeed for $[Cr(bpy)_3]^{3+}$ in the interlayer region of the clay significant changes may be effected by the presence of the dihydroxo and diaquo species on the resultant ESR spectra.

3.8.4 Conclusion

Evidence from ESR, IR and UV-Visible spectroscopy strongly suggests the presence of $[Cr(bpy)_3]^{3+}$ adsorbed onto laponite. There is little evidence from any of these sources for any major structrual changes to the chromium III complex itself; its structure appears to be similar to that in the solid-state perchlorate salt. However, UV-visible diffuse reflectance data points to the presence of photodecomposition products namely the diaquo and dihydroxy chromium III complexes. X-ray diffraction data complement the above spectroscopic date in that the $[Cr(bpy)_3]^{3+}$ laponite shows d-spacings of 17.8 and 18.2Å, representing an increase of more than 8Å over the basal spacings for laponite. The increased basal spacing values are typical of those observed for clays pillared by metal complexes.

3.9 DISCUSSION

3.9.1 The Clay Films

The necessity for us to develop a mechanically robust clay film to modify a platinum electrode arose because of the fragility of the electrode system used by Davison[118]. On repeating Davison's experiments it was clear that even slight movement of the supporting electrolyte led to displacement of the clay particles from the electrode surface, thereby limiting the usefulness of the electrode.

However there appeared to be some disagreement in the literature reports about the strength and electrochemical characteristics of differently prepared clay films. For instance, Ghosh and Bard in their preliminary paper found that in the absence of platinum or PVA their clay films, which initially consisted of colloidal montmorillonite dispersions, developed cracks upon drying and were electroinactive whereas similar films containing platinum and PVA were electroactive. On the other hand, other workers such as Anson[115] and Yamagishi[123] found that it was not necessary to include polyvinyl alcohol or finely divided platinum in the clay coatings to observe electroactivity of incorporated redox reagents.

In our initial experiments we prepared films from colloidal dispersions of both montmorillonite and laponite in an ethanol/water mixture with and without PVA. It was found that films without PVA were prone to cracking and peeling, lacked uniformity in their surface coverage and did not adhere properly to the electrode surface. Films containing a small amount of PVA however were considerably stronger and surface coverage was more uniform. Cyclic voltammograms for both types of film incorporating $[Co(bpy)_3]^{3+}$ are shown in Fig. 3.6. Both voltammograms were recorded under identical scanning conditions on a Princeton Applied Research (PAR) Model 173 potentiostat/glavanostat with a model 175 programmer linked to an Apple II microcomputer with appropriate software. Clearly both films show electroactivity although the film with PVA shows a considerably higher peak potential (Ep) and peak current (ip). It is probably due to the poor binding and non-uniformity of the non-PVA clay coating. The only problem encountered with the clay coating with PVA arose when after a week, the film began to peel off as one layer. In subsequent procedures a film preparation method similar to that of Ghosh and Bard was used. The film quality was considerably improved compared to previous films. In this procedure, finely divided platinum and PVA were added to a colloidal clay dispersion prepared by ultrasonication. The film quality was considerably improved over the first two methods. After incorporation of $[Co(bpy)_3]^{3+}$ and $[Cr(bpy)_3]^{3+}$ the initially white clay coating took on a deep yellow colouration of uniform intensity suggesting that the underlying film coating is also reasonably uniform in thickness and density. The mechanical

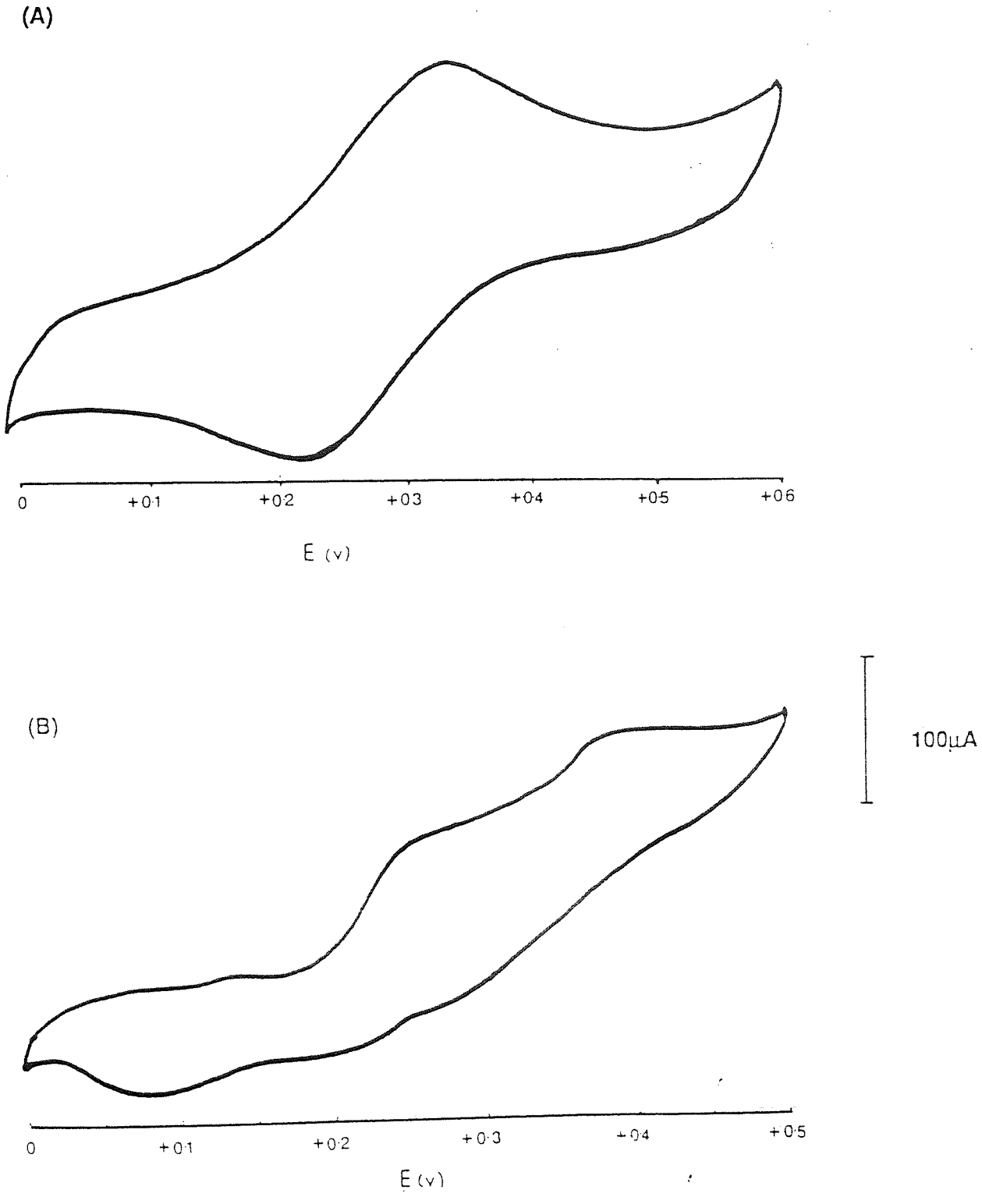

Fig. 3.6 Cyclic Voltammograms of $[Co(bpy)_3]^{3+}$ Immobilised on a Laponite-coated Platinum Electrode

(A) With Finely Divided Platinum

(B) Without Finely Divided Platinum

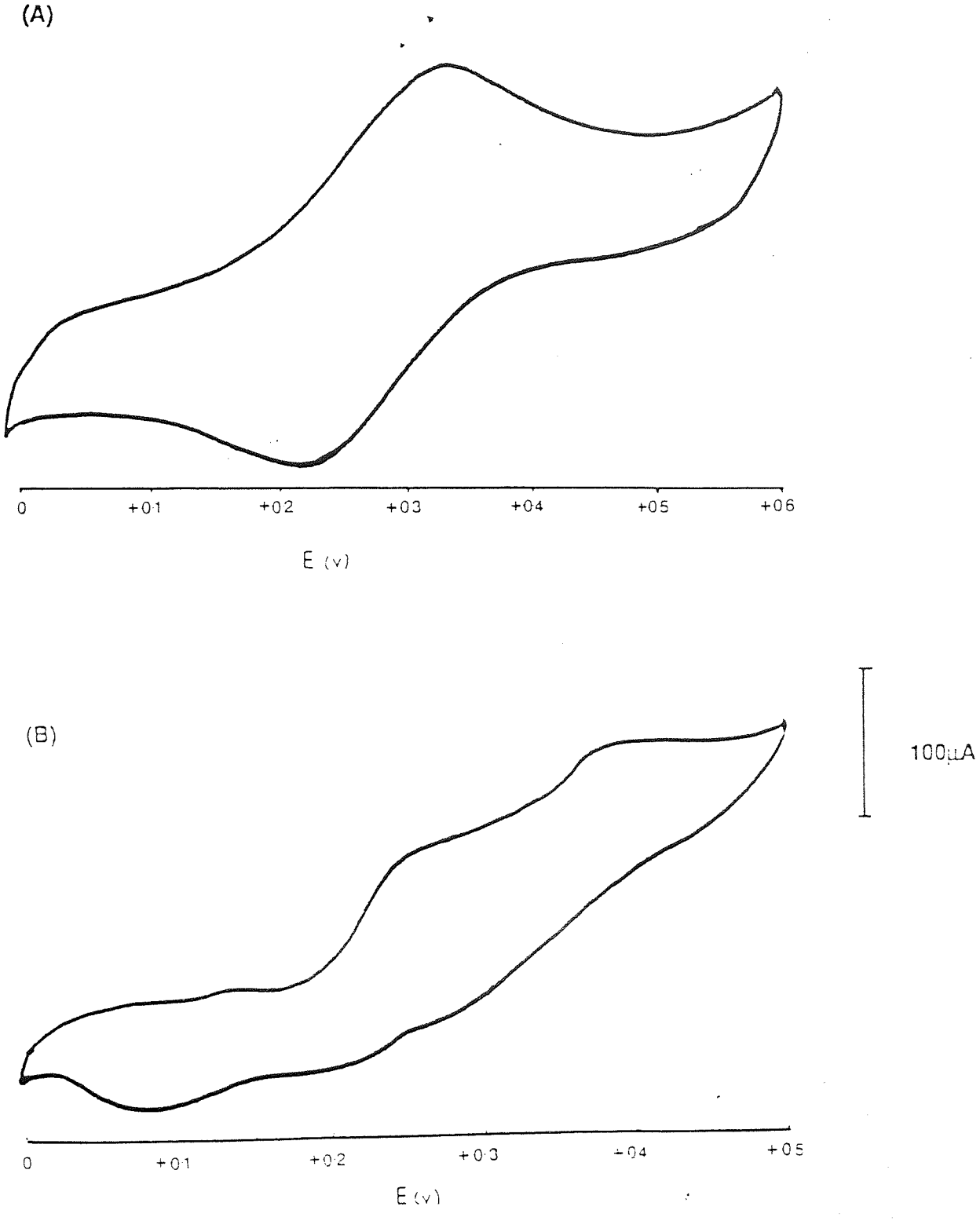

Fig. 3.6 Cyclic Voltammograms of $[Co(bpy)_3]^{3+}$ Immobilised on a Laponite-coated Platinum Electrode

(A) With Finely Divided Platinum

(B) Without Finely Divided Platinum

strength of the film and its adhering properties were significantly improved as the film could not be removed by washing in hot water but only by using hot acids. The film lasted without cracking or peeling for longer than seven months. This preparation was therefore used throughout this work.

Ghosh and Bard have speculated that the role of platinum in the films is not so much to generate electroactivity as to make the films more sturdy, although reasons as to why are still unclear. Also they suggested that the role of PVA is to enhance the gellation properties of the clay by creating a greater communication between clay particles through layer edge-to-edge interactions[4], thereby giving the film better binding qualities and a stronger voltammetric response. However, although this assumption may not be incorrect, we believe that the role of ultrasound as a means of dispersal, and the resultant size of the clay particles, has been somewhat neglected. In a separate study we have shown that in accordance with the results of Suslick and Green[124], ultrasonication considerably enhances the intercalation and adsorption of large molecular moieties; this effect is believed to be due to the generation of very small clay particles rather than ion-exchange. In the same way it is likely that it is the very small particle size of the clay which is responsible for increased uptake of $[Co(bpy)_3]^{3+}$ and $[Cr(bpy)_3]^{3+}$ resulting in a stronger voltammetric response.

3.9.2 Electrochemistry of $Co(bpy)_3^{3+}$ Immobilised at a Clay Modified Platinum Electrode

Cyclic voltammograms for the clay modified platinum electrodes with incorporated $[Co(bpy)_3]^{3+}$ using two different potentiostats. Fig. 3.6 and 3.7 shows the different responses of the two istruments. Fig.3.6 was obtained from a Princeton Applied Research Model 173 potentiostate, the response being monitored and displayed on a computer screen, whereas Fig. 3.7 was obtained under the same conditions using a Hi-Tek Waveform Generator and a Hi-Tek Potentiostat (type DT 2101) linked to a conventional x-y chart recorder. The Princeton instrument did not have the necessary software to enable continuous

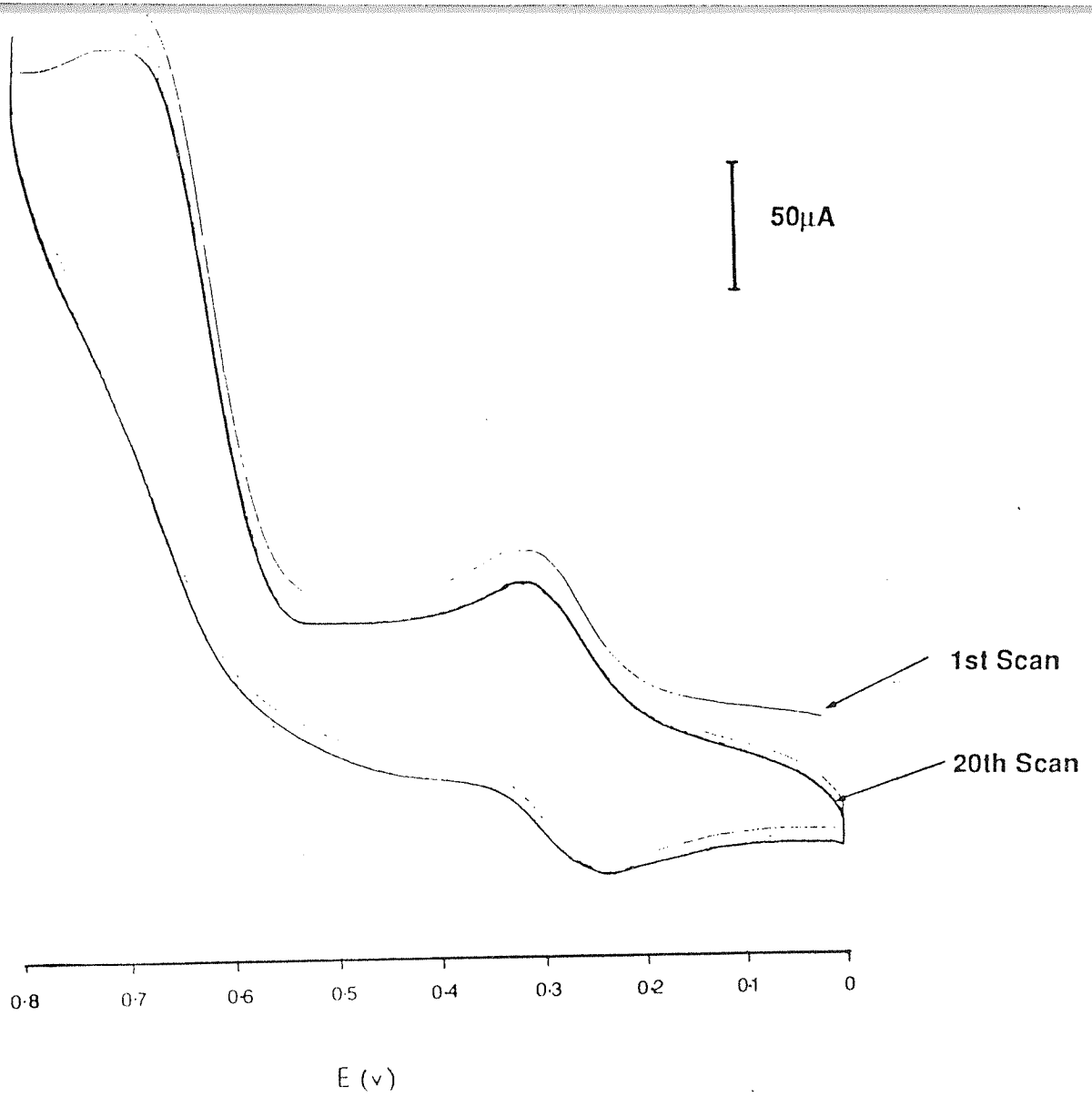

Fig. 3.7 Cyclic Voltammogram Showing the $[Co(bpy)_3]^{3+/2+}$ Couple Immobilised at a Laponite-Coated Platinum Electrode

cycling of the voltammogram and the signal response is not as well defined. Both wave forms were generated by scanning between 100mv and 800mv. There is a clear difference between the instrument responses. Voltammogram A shows a fully reversible waveform. The anodic (oxidation) of 450mv with respect to a saturated calomel electrode (SCE) and the cathodic (reduction) wave occurs at a peak potential (Epa) of 350mv. For the Hi-Tek potentiostat, the anodic wave occurs at 250mv and the cathode ware occurs at 350mv. Another significant difference is that the Hi-Tek instrument recorded an irreversible wave (in addition to the first one) between 500mv and 800mv. In contrast the PAR instrument showed nothing even up to 1000mv. The Hi-Tek instrument therefore appeared to be more sensitive and subsequent experiments were carried out using this.

The cyclic voltammograms for $[Co(bpy)_3]^{3+}$ are now considered in more detail. Fig. 3.12 shows the voltammogram for the $[Co(bpy)_3]^{3+/2+}$ couple in acetonitrile (0.1M solution) at an uncoated platinum electrode. The response is almost identical in shape and peak potential to that of $[Co(bpy)_3]^{3+}$ immobilised on a clay coated platinum electrode. This shows that the electrochemical identity of the $[Co(bpy)_3]^{3+}$ moiety is retained in the clay film and that it freely diffuses through the clay film. The voltammetric response is seen to decay with successive cycling ie the peak currents decrease during initial potential scans, but after about 10 to 20 repeated cycles. The steady voltammogram does not show a further decrease after 30 min, cycling indicating that the $[Co(bpy)_3]^{n}$ $[Co(bpy)_3]^{n-1}$ couple is fairly strongly incorporated in the clay interlayer region. The initial decrease in peak current might be due to the attainment of an exchange equilibrium between $[Co(bpy)_3]^{3+}$ and the cations in the supporting electrolyte, or to a loss of poorly adhered clay film layer during the potential scan.

On scanning between potentials of -0.1v and +0.8v at a scan rate of 50mv/sec, the response obtained is displayed in Fig. 3.7. Between -0.1v and +0.5v the response appears to be that of a fully reversible wave; between potentials of +0.5v and +0.8v an irreversible wave is generated. There appear to be two distinctly separate reactions occuring at two different potentials. Each

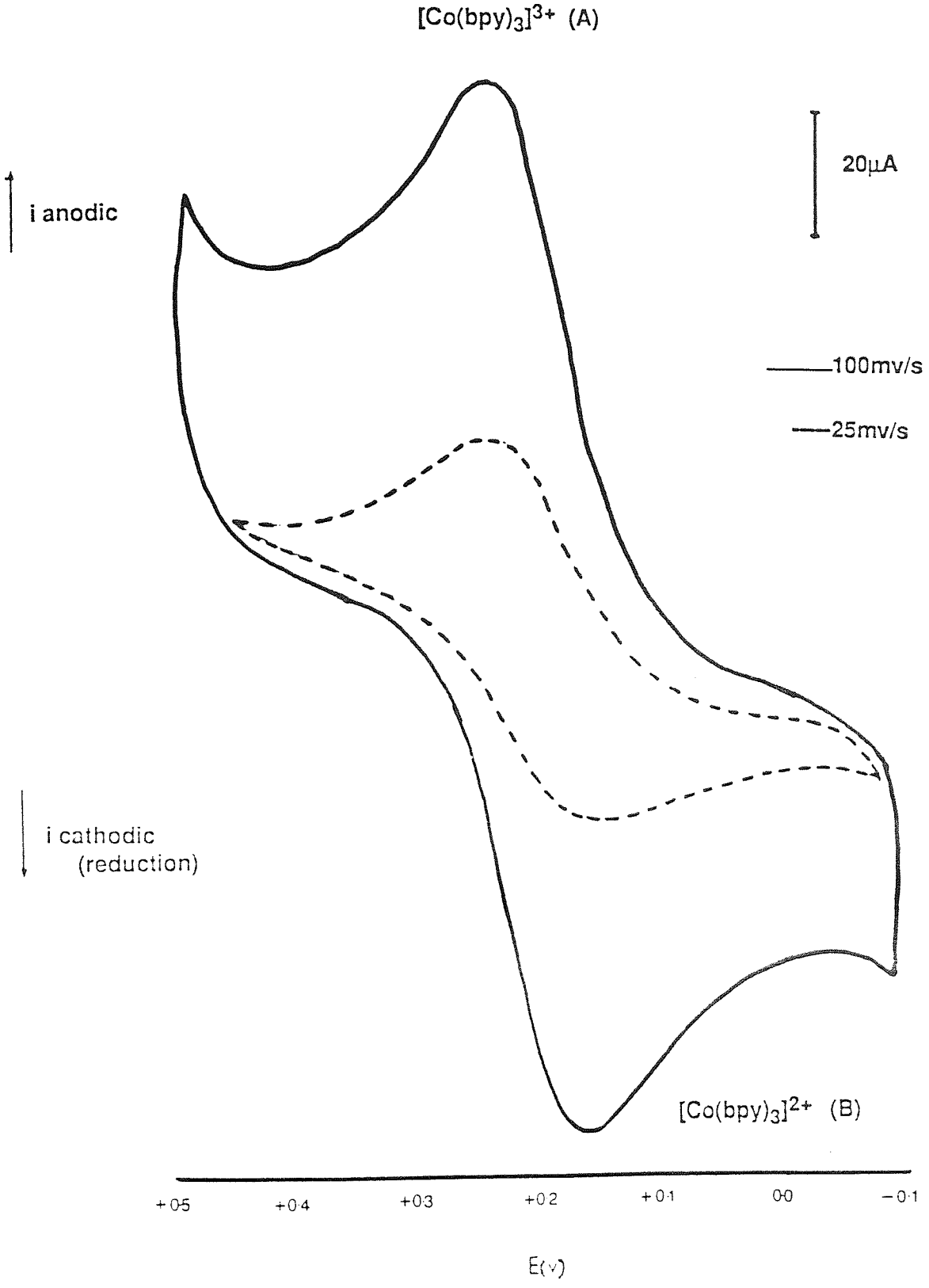

Fig. 3.8 Cyclic Voltammogram for $[Co(bpy)_3]^{3+/2+}$ Immobilised at a Laponite Coated Platinum Electrode

wavefrom was then considered separately by obtaining separate voltammograms in the two potentail ranges.

Fig. 3.9 shows the voltammetric responses for the $[Co(bpy)_3]^{3+}$ system scanned between potentials -0.1v and +0.5v, over a range of scan rates varying between 25mv/sec to 200mv/s. As the scan rate is increased the peak currents for anodic and for the cathodic responses also increase. It can be seen from table 3.1 that for each different scan rate the ratio of the cathodic to anodic current is not 1, and that the anodic current is actually greater than the cathodic current for each scan rate. This confirms the initical indications that the charge transfer reactions manifested by the waveform are quasi-reversible and non-Nernstian. The peak potentials however are consistent and do not change with increasing scan rate. The anodic peak potential occurs at 250mv and the cathodic peak potential at 170mv (wrt SCE).

Table 3.1 Anodic Peak Current Versus (Scan rate)$^{1/2}$

ipa (μA)	Scan rate ($\sqrt{}$) (mv/sec)	$\sqrt{}^{1/2}$
270	**10**	**3.16**
330	25	5
470	50	707
575	100	10
695	150	12.25
813	200	14.14

Table 3.1 Anodic Peak Current Versus (scan rate)$^{1/2}$

A plot of anodic peak current (ip) versus the square root of the scan rate ($\sqrt{}^{1/2}$) is shown in Fig. 3.10, and it can be seen that there is a linear relationship between ip and $\sqrt{}^{1/2}$. This shows that the waveform is of the diffusion controlled type [125]. Normally one would expect a surface wave for

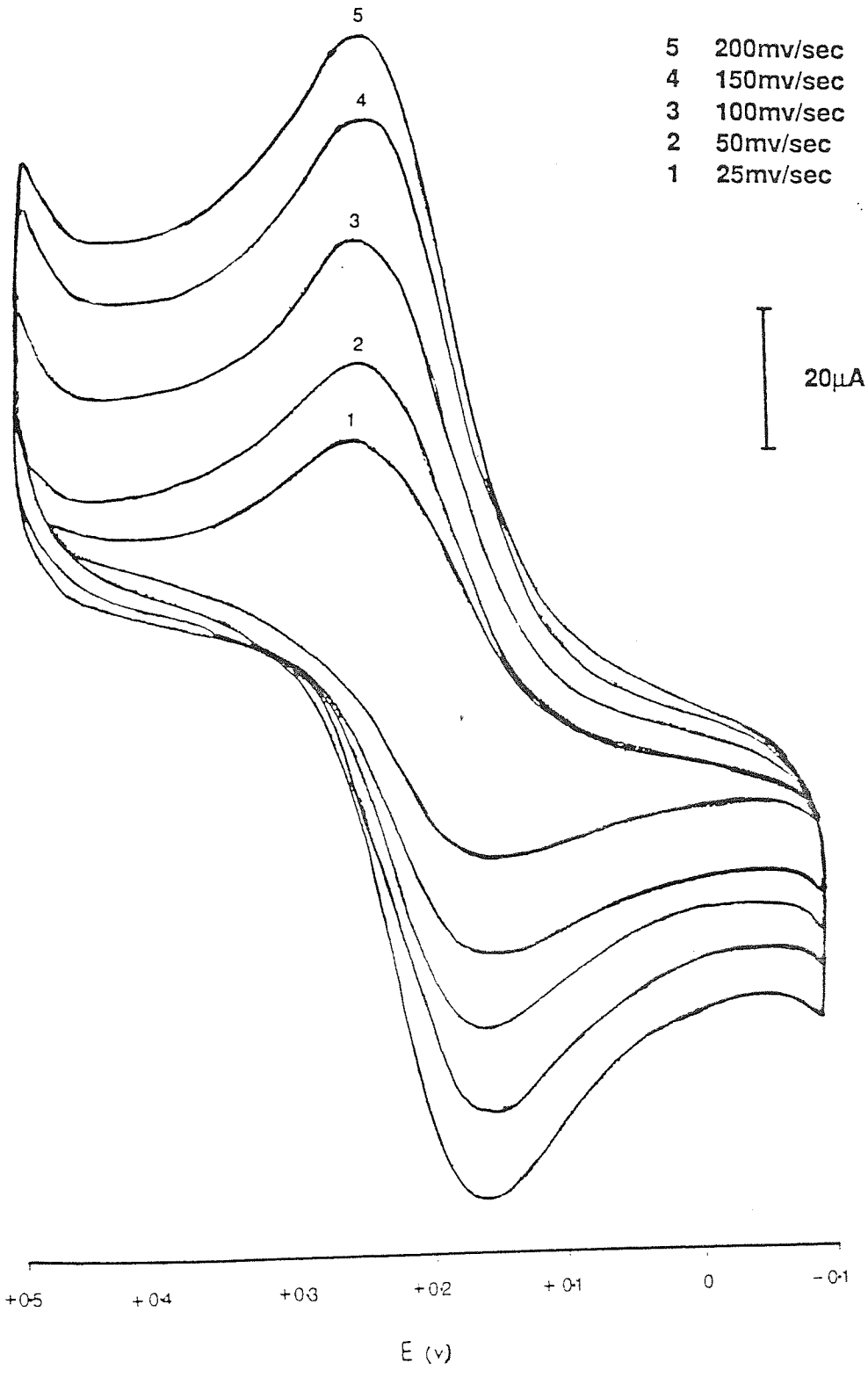

Fig. 3.9 Cyclic Voltammograms Showing Effect of Increasing Scan Rate (mv/s) for $[Co(bpy)_3]^{3+/2+}$ Immobilised at a Laponite-Coated Platinum Electrode

Fig. 3.10 Shain-Nicolson Plot ipa (μA) Versus (Scan rate)$^{1/2}$

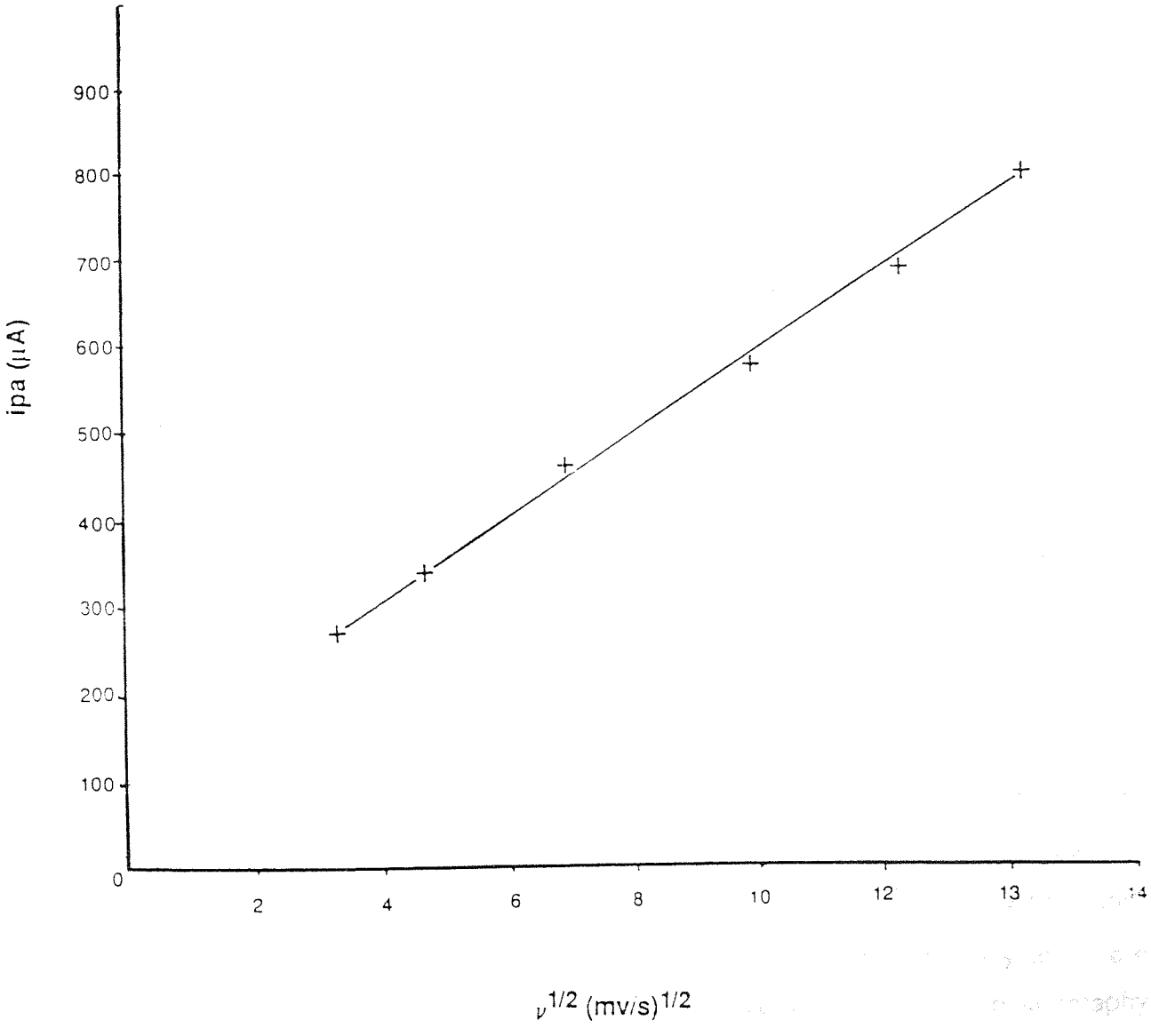

such modified electrodes. The diffusion type voltammetric behaviour observed in the present case shows that the charge transport within the film itself it limited by diffusion of the $Co(bpy)_3]^{3+}$ to the electrode surface. Alternatively charge transport within the film may be limited by an electron hopping mechanism within the individual clay film layers, as there are many of these layers present making up the clay film[112]. The cyclic voltammogram for $[Co(bpy)_3]^{3+}$ in the potential range +0.5 to +0.8v is shown in the Fig. 3.7 (scan rate 50mv/sec). Again continuous cycling reduces the peak current, the reasons for this being as discussed above. In this case the peak current is about 240μA.

In a different experiment we carried out a potential scan at more negative potentials using the Hi-tek potentiostat. Previous scans using the PAR potentiostat did not show any of reduction or oxidation waves at potentials between 0.0v and -2.0v. However, as shown in Fig.3.11 the Hi-tek instrument clearly shows the presence of three further distinct reduction waves occurring at peak potentials of -0.35v(A), -1.03v(B) and -1.52 volts (C). For the reduction waves at 1.03v and -1.51v the peak cathodic currents are approximately 190μA and 55μA respectively indicating substantial limiting peak current flow for the reduction processes. The corresponding anodic wave is not as well defined. However, there is some evidence that there are corresponding components to the reduction waves B and C although they are poorly defined in comparison. We speculate that components B and C may be reversible. In contrast, component A does not show any anodic component and is irreversible.

To our present knowledge $[Co(bpy)_3]^{3+}$ has not been studied as an immobilised species on clay, although electrochemical (particularly polarography) studies of $[Co(bpy)_3]^{3+}$ in solution are well documented. Vicek[126] and Martin and Waind[127] were the first to find the cobalt I state polarographically and were successful in preparing the corresponding perchlorate salt. Using polarography Martin and Waind were able to define the electrochemical reduction of $[Co(bpy)_3](ClO_4)_3$ in aqueous solution. Tanak and Sato[128] studied the AC polarographic behavior of $[Co(bpy)_3]^{2+}$ and $[Co(bpy)_3]^{3+}$ in acetonitrile. The

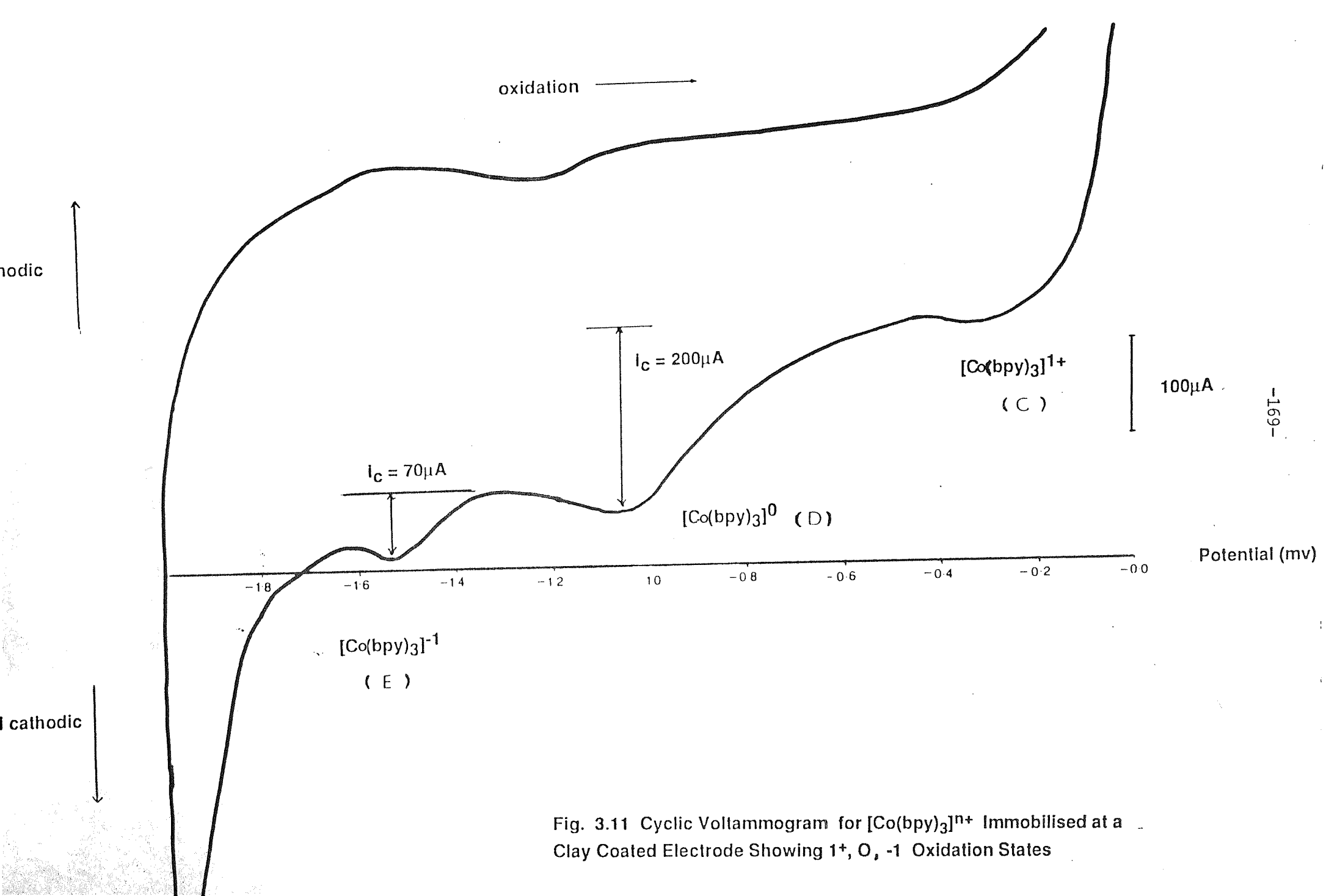

Fig. 3.11 Cyclic Voltammogram for $[Co(bpy)_3]^{n+}$ Immobilised at a Clay Coated Electrode Showing 1^+, O, -1 Oxidation States

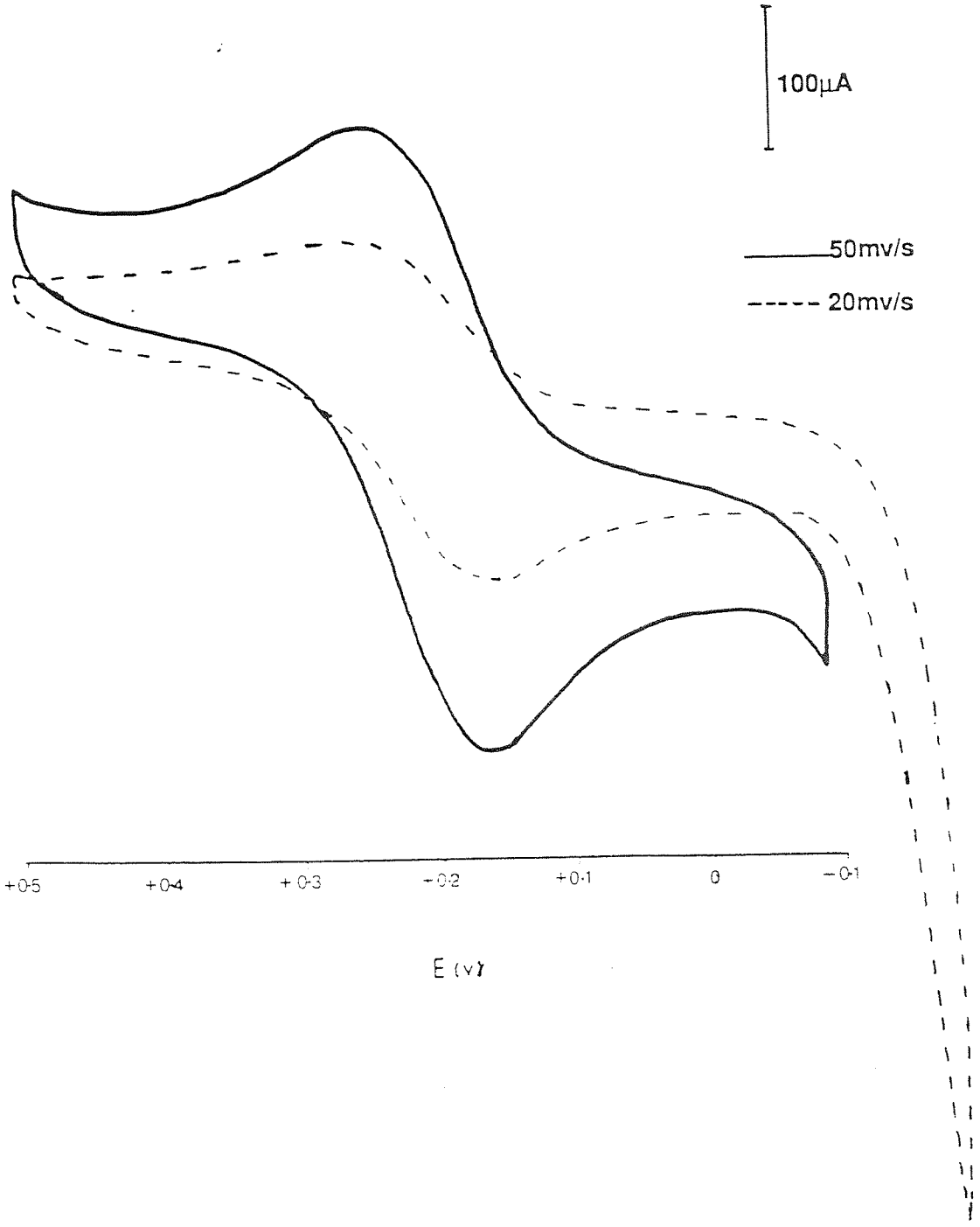

Fig. 3.12 Cyclic Voltammogram for $[Co(bpy)_3]^{3+/2+}$ in MeCN at a Platinum Electrode Relative to ScE

These authors proposed the following reaction scheme for the electrochemical reduction of $[Co(bpy)_3]^{3+}$:

$$[Co(bpy)_3]^{3+}$$

$$+ e$$

$$\|$$

$$[Co(bpy)_3]^{2+}$$

$$+ e$$

$$\|$$

$$[Co(bpy)_3]^{1+}$$

$$+ 2e$$

$$\|$$

$$[Co(bpy)_3]^{-1}$$

and suggested that the reason why the reduction process to the cobalt (O) complex was not observed was probably because the cobalt (O) bipyridine complex is not sufficiently stable in acetonitrile, and therefore the cobalt I complex is reduced directly to the cobalt (-I) state. Our cyclic voltammogram for $[Co(bpy)_3]^{3+}$ at the bare Pt electrode is in agreement with the above reaction scheme.

In order to calculate the number of electrons transferred between each reduction step we used the following general relationship [130] which applied at standard temperature and pressure;

$$\Delta E_{pk} = \pm \frac{59.2}{n} \text{ mv} \qquad \text{or} \qquad n = \frac{59.2}{\Delta E_{pk}}$$

where ΔEpk is the difference between the two peak potentials under consideration and n is the number of electrons transferred. The reduction waves are labelled A to E starting with the most positive peak. The difference between the peak potentials and the number of electrons transferred is tabulated below:

Electron Transfer Step	ΔEpk (mv)	n
A to B	60	1
B to C	50.6	1
C to D	68	1
D to E	50	1

The reversible composite wave is attributed to the well-documented $Co(bpy)_3^{3+}$/ $Co(bpy)_3^{2+}$ couple. As can be seen from the above table this is a one-electron fully reversible redox reaction and occurs between peak potentials of +0.25 and +0.156 V, which compares favourably with finding of Tanaka and Sato who observed the same reaction at around +0.2mv. Having established that the identity of the cathodic wave at +0.156V is due to $[Co(bpy)_3]^{2+}$ (ie wave B) subsequent reduction waves C through D to E, are one electron-transfer steps are due to the $[Co(bpy)_3]^{1+}$ (wave C), $[Co(bpy)_3]^{o}$ (wave D) and $[Co(bpy)_3]^{-1}$ (wave E) complexes. However, for waves C to E we could not establish their reversibility as the anodic response was poorly defined.

The surprising result is the apparent detection of the $[Co(bpy)_3]^{o}$ complex which is believed to be unstable in acetonitrile. We speculate that the immobilised $[Co(bpy)_3]^{o}$ complex, when incorporated in the clay interlayer region, is more stable than in solution, hence its observation. The clay must therefore have a stabilizing influence on the (O) state complex.

Oxidation State of Complex	E peak (mv) vs SCE
$[Co(bpy)_3]^{3+}$	+ 0.25
+	
e	
‖	
$[Co(bpy)_3]^{2+}$	+0.156
+	
e	
‖	
$[Co(bpy)_3]^{1+}$	-0.35
+	
e	
‖	
$[Co(bpy)_3]^{o}$	-1.03
+	
e	
‖	
$[Co(bpy)_3]^{-1}$	-1.52

Table 3.2 A Reduction Scheme for Electrochemical Reduction of $[Co(bpy)_3]^{3+}$ immobilised at a Clay-Coated Electrode.

The apparent irreversible oxidation wave at +0.675 V is not considered to be due to the $[Co(bpy)_3]^{4+}$ complex as we first thought. This is known to be a highly unstable state and has not been detected previously. On the contrary, taking into account the relatively positive potentials applied, the wave is most probably due to the evolution and subsequent adsorption of oxygen at the platinum electrode. This may result from decomposition of small amounts of water which are present in the clay interlayer region and which can therefore affect the electrochemical processes.

On the basis of our results we propose the following reaction scheme for the electrochemical reduction of $[Co(bpy)_3]^{3+}$ immobilised in a clay matrix as shown in Table 3.2.

montmorillonite) shows one strong irreversible anodic wave at +0.3V and a weaker cathodic wave at -0.51V. The anodic wave at +0.3V probably corresponds to the same one at +0.89V on laponite, although the difference in potential is difficult to explain.

Fig.3.16 shows the effect of continuous cycling on the anodic wave scanned in the potential range OV to +1.0V (50mv/sec) in order to determine whether the system is diffusion controlled. It can be seen that between *0.5 V and +1.0V the wave is irreversible and that the anodic peak current is ca100μA. There is no returning cathodic wave suggesting that the elctron transfer step ($R - e^-$ ——>O) is rate limiting for this particular reaction. A steady rate voltammogram is reached after about 1- 20 scans and there is loss of the peak limiting diffusion current indicating that (a) the reaction is limited by diffusion of electroactive Cr^{n+} species to the electrode surface (b) weakly adhered layers of film are lost during initial scans.

Further evidence for a diffusion controlled system is provided by the fact that as the scan rate (√) is increased , the peak current increases with $\sqrt{1/2}$ although not in a linear fashion.

Fig. 3.17 shows the voltammogram for $[Cr(bpy)_3]^{3+}$ on laponite scanned between +2.0V and -2.0V. It is evident that at potentials less than zero (in the range) to -1.9V) a multistep series of reactions is occurring as shown by the several cathodic waves, Anods waves are also present but are less well defined. Broad cathodic waves are detected at peak potentials -0.2 to -0.3V, -0.5, -0.7V, -0.95v and -1.4V.

Fig. 3.18 shows the cyclic voltammogram for the same system above but scanned in a narrower potential range -0.5V t0 -1.9V and in a higher current range in order to reveal more detail. As before the anodic response is poorly defined but the presence of several inflexions suggests that some anodic current is present, and that these inflexions probably form the reversible components of the cathodic waves.. The cathodic response is more clearly defined that in Fig. 3.17 and it is possible to pick out the same peaks at -0.7V, -0.95 and-1.4V. Surprisingly the two waves at -0.95 and-1.4V appear to be split into doublet

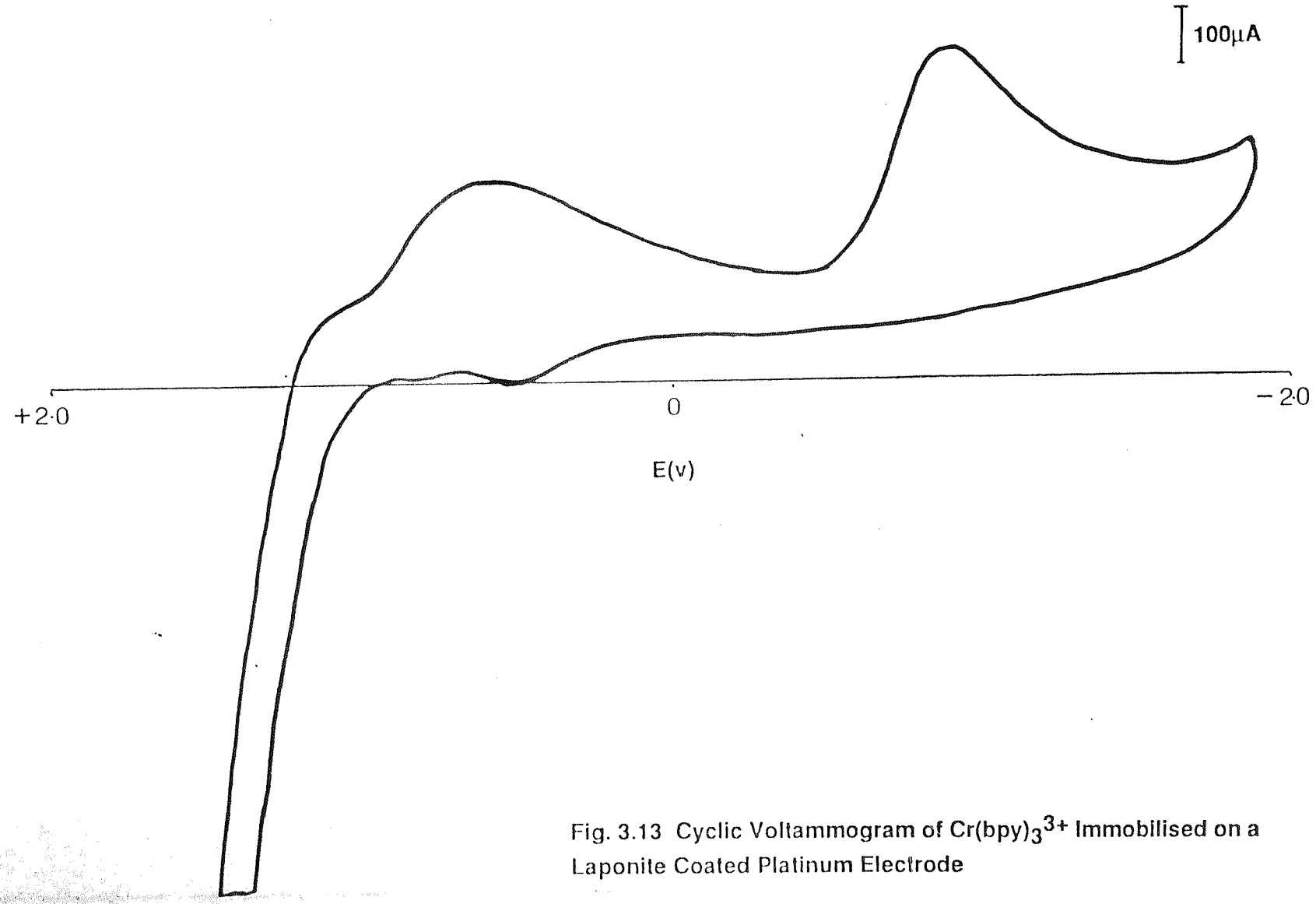

Fig. 3.13 Cyclic Voltammogram of $Cr(bpy)_3^{3+}$ Immobilised on a Laponite Coated Platinum Electrode

Fig. 3.17 Cyclic Voltammogram of $Cr(bpy)_3^{3+}$ Immobilised on a Laponite-coated Electrode

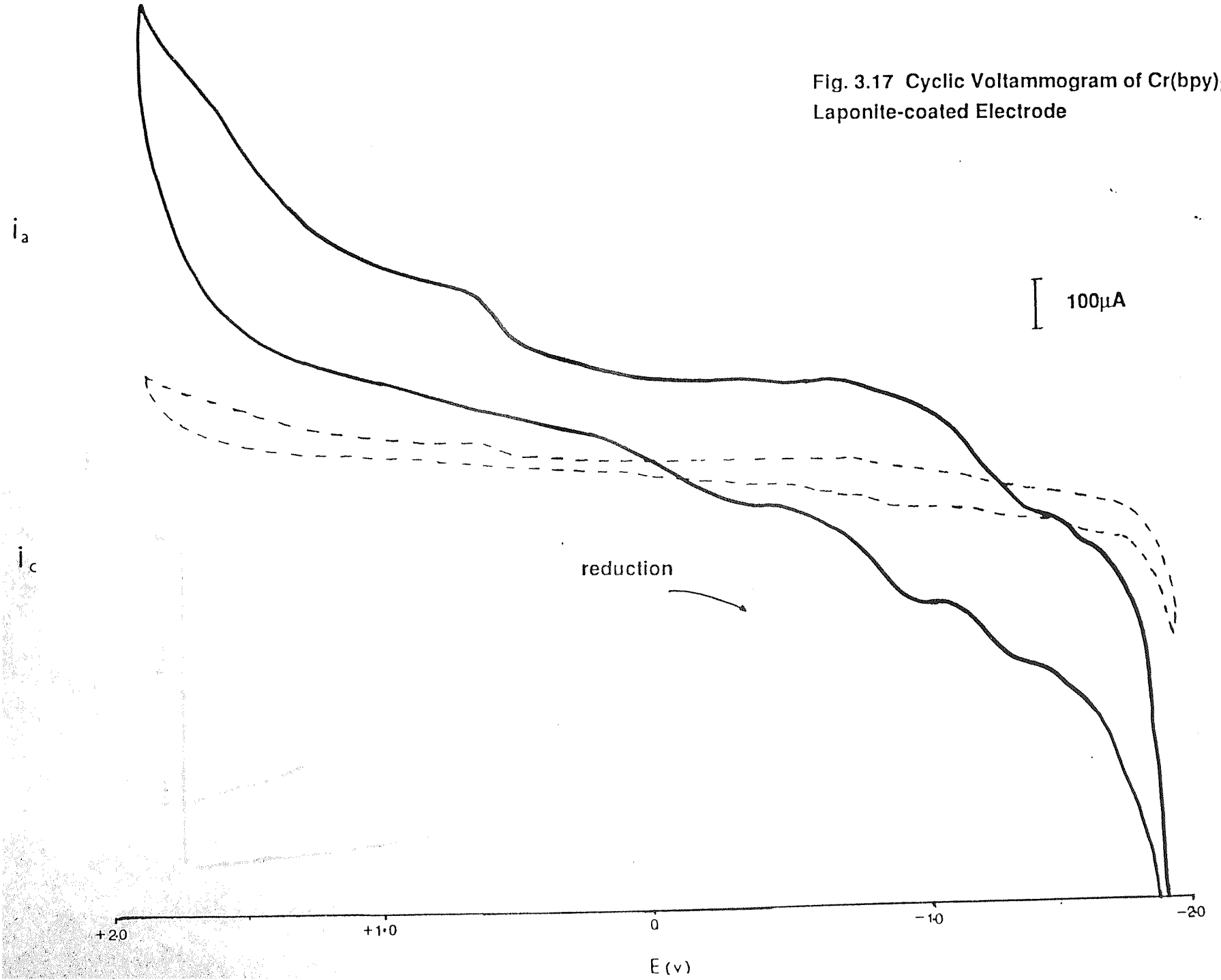

Fig. 3.18 C.V. for $Cr(bpy)_3^{3+}$ Immobilised at a Laponite-coated Pt. Electrode

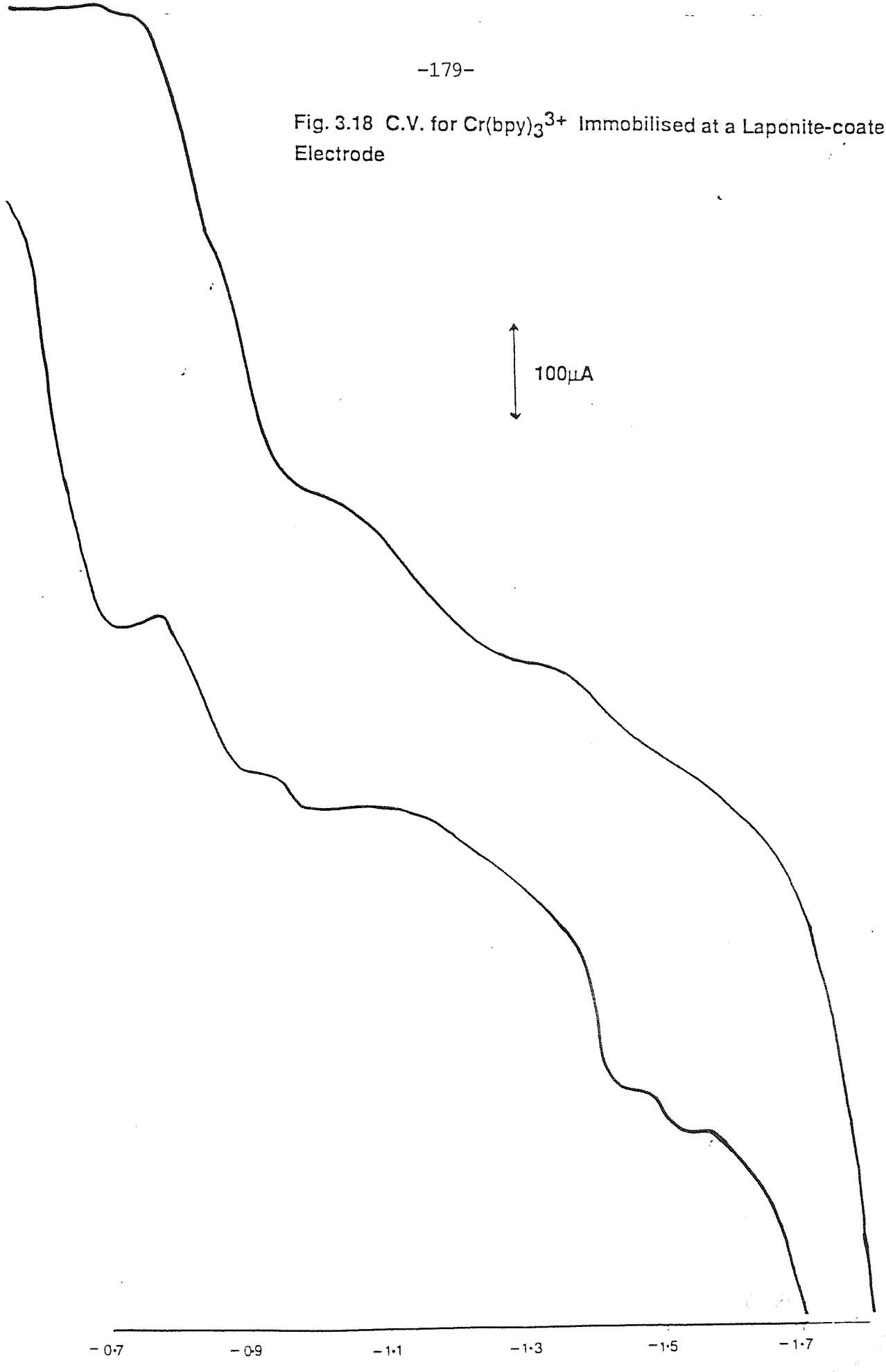

suggesting that at certain potentials there is more than one reaction occurring and that the reactions may not be simple one electron transfers but may involve species other than the $[Cr(bpy)_3]^{3+}$ complex.

The peak potentials of the cathodic wave although they are rather weak correspond very well with those observed by previous workers. For example the wave at ca-0.2v corresponds to the observed by Hughes andMacero at -0.210V. Similarly the peak at -0.72V is assigned to the reduction of the Cr(II) to the Cr(I) complex, and the wave at -1.4V is assigned to the Cr(I) to Cr(O) reduction. This then leaves the waves at -0.95V and -0.51V. Hughes and Macero did not observe either of these two waves for the reduction of $[Cr(bpy)_3]^{3+}$ in acetonitrile. However, both Mehta and Baker and Vlcek who studied the same reduction in aqueous solution detected either one or both of these waves. It is possible that the presenc of interlayer water may be interfering in the electrochemical process and that we are observing $[Cr(bpy)_3]^{3+}$ in two environments, one in acetonitrile and the other in water. If this is true, then the peak we have detected at -0.7V cannot be assigned simple to the Cr(III)——>Cr(II) one electron transfer. Instead if water happens to play a role in the reaction scheme, the -0.7V peak may correspond to the anomalous cathodic wave observed by Mehta and Baker at -0.72V. These workers recognised that the -0.72V wave was the result of the dissociation of the $[Cr(bpy)_3]^{3+}$ complex at the elctrode surface by the following mechanism:[119]

$$Cr\ (bpy)_3^{3+} + e^- \rightleftharpoons Cr(bpy)_3^{2+} \qquad E_{1/2} = -0.52v$$

$$Cr\ (bpy)_3^{2+} + 2H_2O \rightleftharpoons Cr(bpy)_2(H_2O)_2^{2+} + bpy$$

$$Cr(bpy)_2(H_2O)_2^{2+} + Cr(bpy)_3^{3+} \rightleftharpoons Cr(bpy)_2(H_2O)_2^{3+} + Cr\ (bpy)_3^{2+}$$

$$Cr(bpy)_2(H_2O)_2^{3+} + e^- \rightleftharpoons Cr(bpy)_2(H_2O)_2^{2+} \qquad E_{1/2} = -0.72v$$

Vlcek	Mehta/ Baker	Marcero/ Hughes	Present Work (Immobilised on Clay)	Assignments
-0.36		-0.210	≈ -0.20 v	CrIII——>CrII
	-0.51		-0.51	
-0.73	-0.72*	-0.715	-0.70	CrII ——>CrI
	-0.90*		-0.95*	
1.38	-1.30	-1.280	-1.40	CrI ——>CrO

* Assigned to side reactions due to presence of water

Table 3.2.1 Observed Electrode Potentials (V) for the Electrochemical Reduction of $[Cr(bpy)_3]^{3+}$

The reaction sequence involves the diffusion of $Cr(bpy)_3^{3+}$ to the electrode surface. Part of this complex is reduced at -0.51v (present data) but the remainder is catalytically dissociated at a potential of -0.7v (present data). The Ept values for the present work and for the work of the above-mentioned authors are tabulated in table 3.2.1

Application of the above reaction scheme does therefore seem plausible. We have already established that the reactions are diffusion controlled and that the electroactive material readily diffuses to the electrode surface. Secondly if we envisage the clay coating to be composed of many layers, there is a likelihood that only the outer layers are amenable to acetonitrile whilst the innermost layers may not be easily penetrated. This would provide the explanation for the existences of two environments (MeCN and H_2O) for the $[Cr(bpy)_3]^{3+}$. Thirdly, it has been shown by Abdo et al [122] that the diaquo and dihydroxy complexes are easily generated by exposure of hectorite- $[Cr(bpy)_3]^{3+}$ to UV light; the chromium complexes in coordination no II were generated this way. Our results also suggest that because of the doubly split cathodic waves at -0.95v + -1.4v certain side reactions may also be occurring.

3.9.4 Cycling Diagnostics for $Cr(bpy)_3^{3+}$ Immobilised on Montmorillonite

Fig. 3.15 shows the effect of increasing scan rate on the voltammetric response for $[Cr(bpy)_3]^{3+}$ on montmorillonite at a platinum electrode. Several important observations can be made. The anodic peak potential (Epa) shifts to more positive potentials while the cathodic peak potential (Epc) shifts to more negative potentials as the scan rate is increased. Both the anodic and cathodic peak currents increase with scan rate as shown in table 3.3.

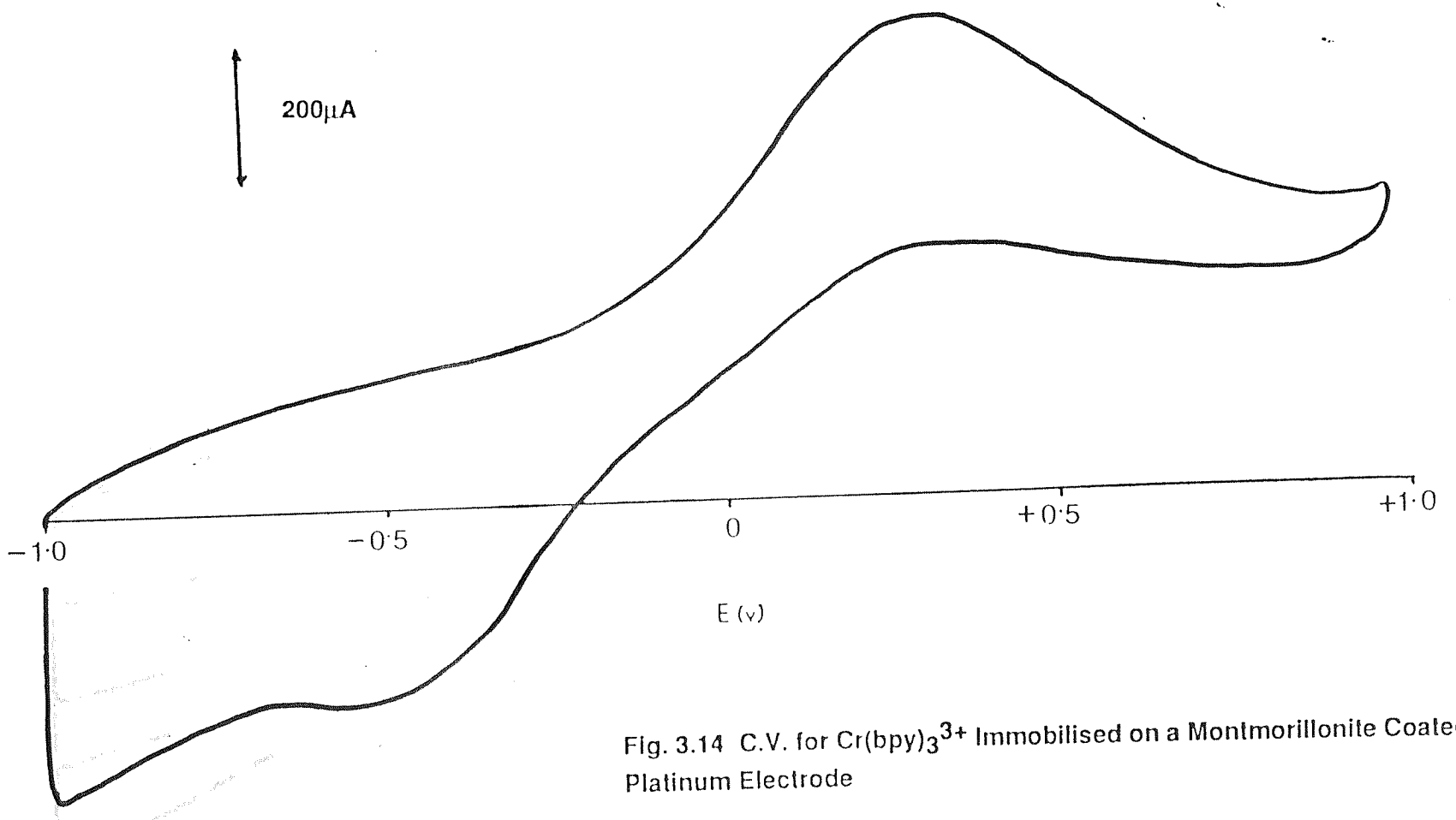

Fig. 3.14 C.V. for $Cr(bpy)_3^{3+}$ Immobilised on a Montmorillonite Coated Platinum Electrode

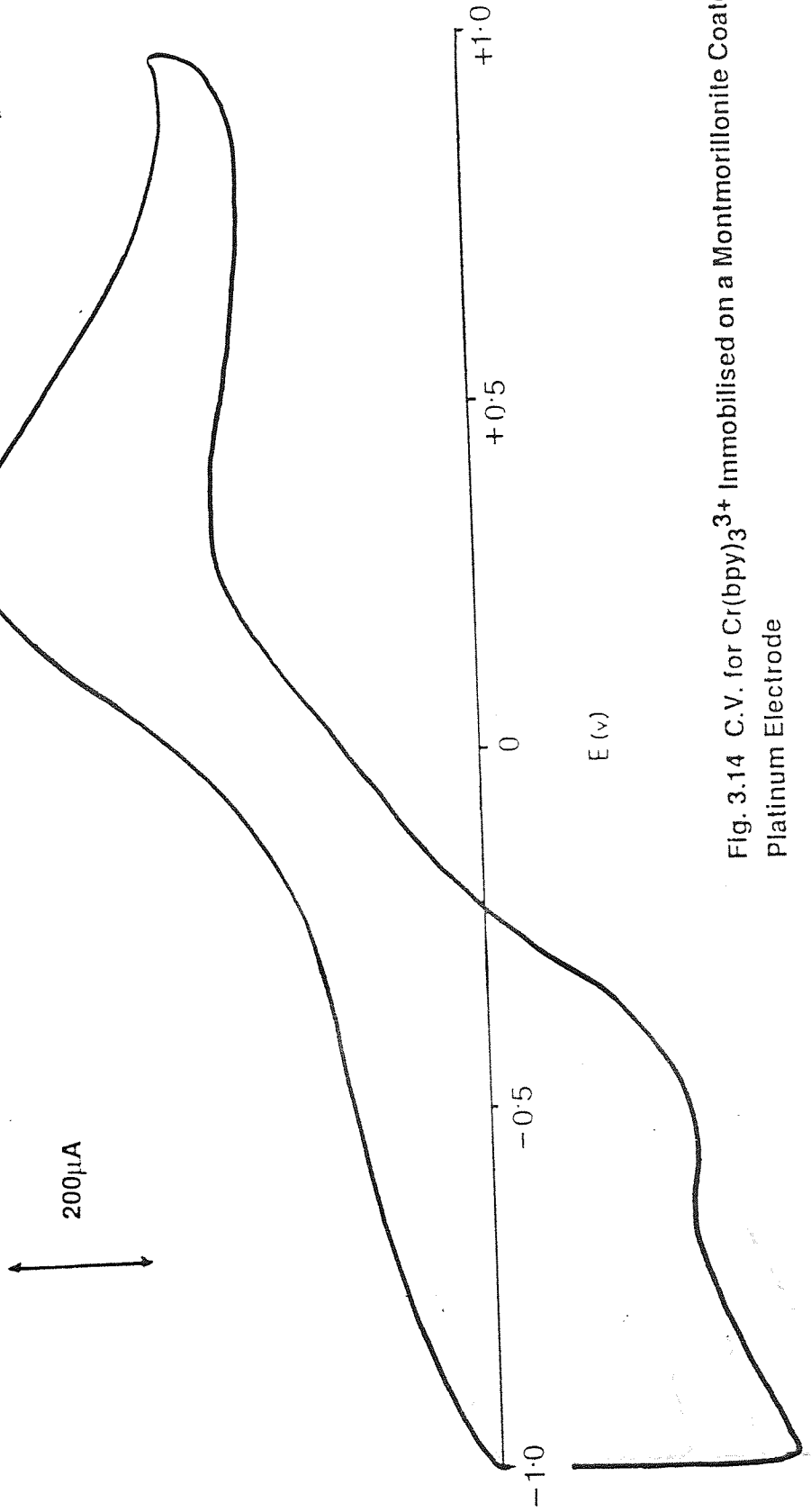

Fig. 3.14 C.V. for $Cr(bpy)_3^{3+}$ Immobilised on a Montmorillonite Coated Platinum Electrode

Fig. 3.15 C.V. for $Cr(bpy)_3^{3+}$ Immobilised on a Laponite-coated Pt. Electrode (Effect of Increasing Scan Rate)

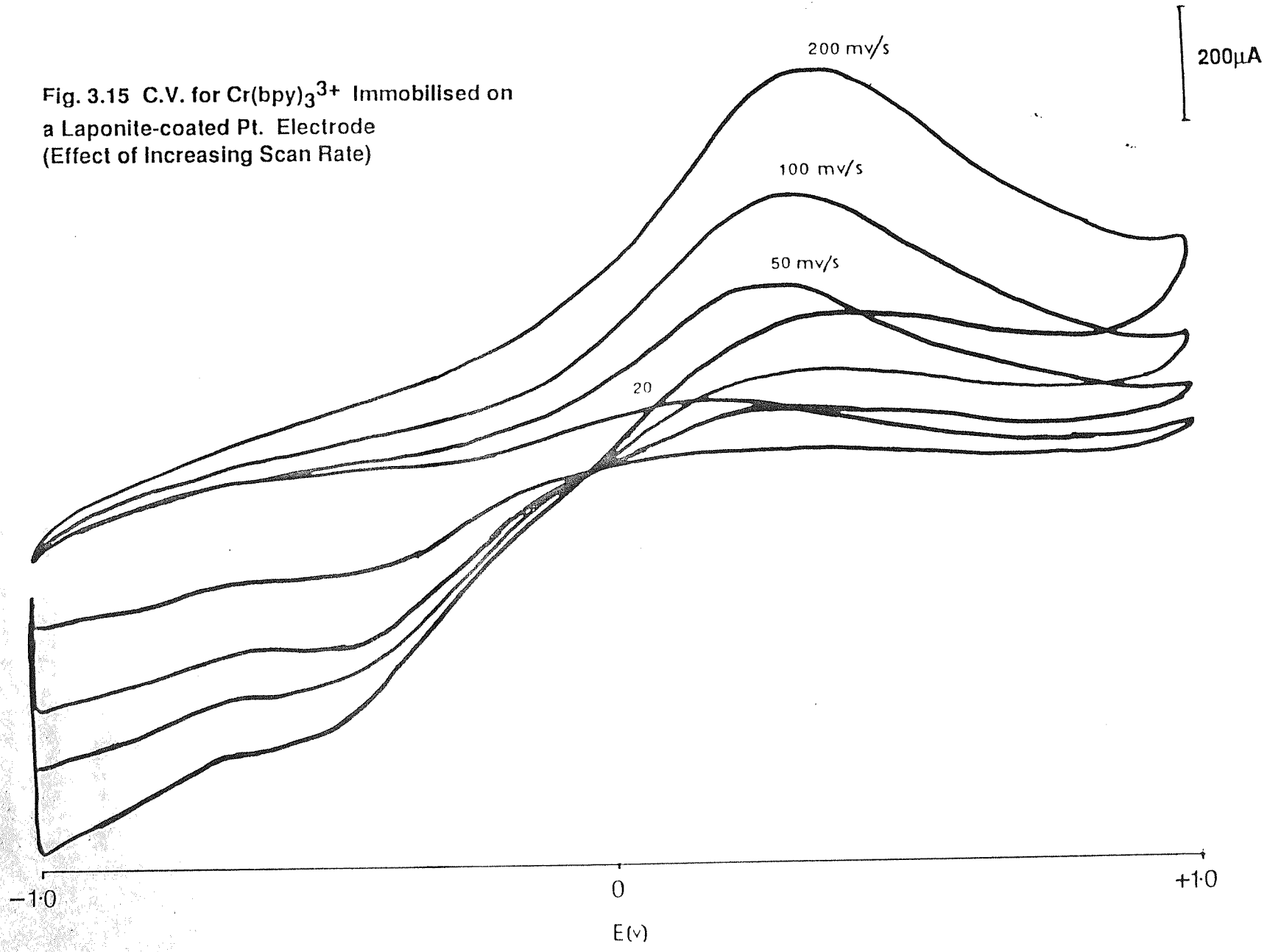

Scan rate (mv/s)	I_a (μA)	I_c (μA)	E_{pa} (V)	E_{pc} (V)
20	90	90	+0.1	-0.40
50	200	120	+0.25	-0.44
100	290	140	+0.31	-0.47
200	300	155	+0.34	-0.50

Table 3.3 Voltammetric Parameters for Cr $(bpy)_3^{3+}$ Immobilised at a Montmorillonite Coated Platinum Electrode.

The cycling diagnostics tabulated above parallel those for a slow change-transfer step between the potentials scanned. It is well known that for a slow charge-transfer step Epa and Epc (ie the peak potentials) no longer depend on the scan rate (dE/dt). Instead Epc shifts towards negative and Epa shifts towards positive potentials as dE/dt increases. As the charge transfer step moves through quasi-reversible to totally irreversible, the magnitude of this shift increases. The peak currents i_a and i_c remain almost proportional to the square root of the scan rate although the processes becomes less reversible as the values of $i_a + i_c$ decrease. Fig. 3.15 therefore indicates slow charge-transfer kinetics between +0.1v and -0.1v for $[Cr(bpy)_3^{3+}]$ on montmorillonite, although at present we are unable to comment on the oxidation states involved.

3.9.5 Conclusions

It has been shown that $[Co(bpy)_3]^{3+}$ and $[Cr(bpy)_3]^{3+}$ are reduced to the $[Cr(bpy)_3]^{1+}$ complexes, both chemially using $NaBH_4$ and electrochemically[117]. In the present work we were successful in preparing a clay film, with or without finely divided platinum, which adhered well to the electrode surface and was

mechanically robust. Above all the clay films when dipped into solutions of the $[Co(bpy)_3]^{3+}$ and $[Cr(bpy)_3]^{3+}$ complexes became electroactive when a potential was applied to the clay coated electrode; also the redox active complexes could be regenerated catalytically making the clay-coated electrodes reusable.

The cyclic voltammograms obtained for $[Co(bpy)_3]^{3+}$ and $[Cr(bpy)_3]^{3+}$ (using TBAP/CH_3CN as supporting electrolyte) give considerable information about the redox processes occurring within the clay film at different potentials. By selecting certain potential windows it was possible to identify specific redox reactions occurring in that potential range only. The voltammograms were found to be of the diffusion controlled type, ie the limiting peak current was controlled by the diffusion of electroactive material to the electrode from the clay film.

For $[Co(bpy)_3]^{3+}$ immobilised at a clay coated electrode, a one-step oxidation and four-step reduction wave was observed. The $Co(bpy)_3^{3+}$/ $Co(bpy)_3]^{2+}$ couple was identified as a composite reversible wave. The observed cathodic waves corresponded to one-electron step wise reduction of Co (III) and Co(I) to Co(-I).

The electrochemistry of immobilised $[Cr(bpy)_3]^{3+}$ was found to be more complicated than the simple one-electron stepwise reduction of Cr(III) through Cr(II) to Cr(I). In the present work, from the Epk values of the cathodic reduction waves it was concluded that as well as the simple Cr(III) -> Cr(II)-> Cr (I) reduction there were additional waves corresponding to the dissociation of $[Cr(bpy)_3]^{3+}$ into the diaquo context. The presence of interlayer water is thought to influence the dissociation and provide a more complicated pathway to reduction of the chromium III complex.

Incidentally, the UV-visible results also strongly suggest that $[Cr(bpy)_3](ClO_4)_3 \cdot 1/2H_2O$ undergoes photo-induced decomposition to the diaquo and dihydroxy complexes. The common factor between clay-modified

electrochemical reduction and decomposition of $[Cr(bpy)_3]^{3+}$ and photo-induced decomposition is obviously the presence and high concentration of labile interlayer water molecules which are easily exchanged for biyridyl ligands, thereby creating new catalytic pathways. Obviously it would appear that electrochemical reduction is a more controllable process, since comparatively little is know about the quantum yields of light induced reactions for adsorbed or intercalated photoreactive moieties.

Another point of interest which arises is whether they have any useful meaning below oxidation state II, ie do the electrons go into the metal ie do the electrons go into the metal eg orbitals or the ligand π^* orbitals. It is known that complexes of $bipy^{(-)}$ can exist if electrons go into the ligand π^* orbitals. In fact Nakamoto's [107] i.r. study of $[Cr(bpy)_3]^{n+}$ showed that the Cr-N stretching frequency ($\sqrt{}$ CrN) was found to be independent of the oxidation state n. Certain workers [128] have carried out electrochemical reductions of $[Cr(bpy)_3]^{3+}$ and $[Co(bpy)_3]^{3+}$ and by the addition of controlled amounts of the biyridyl ligand and the corresponding electrode potential changes have managed to comment on the most likely occupancy of the electrons to either π^* (ligand) or e_g (metal) orbitals.

The fact that the clay modified electrons could be used at least several times giving reproducible results indicates the possible value of these systems as redox catalysts. By improvement and optimisation of the existing set-up, it is envisaged that by carefully controlling the potential window applied at the clay-coated electrode, certain desired catalytic reactions can be carried out. It could therefore be possible to control the catalysis of certain reactions more easily than by using conventional means. The type of system described in this work adds a new dimension to pillared clays by facilitating the ingress of molecules and providing a controllable redox-catalysis mechanism.

reason for using acetonitrile rather than aqueous solutions was to avoid reduction of water and therefore evolution of hydrogen which is known to occur for aqueous solutions at sufficiently negative potentials. The Japanese workers found that the cobalt II complex gave a one-step oxidation and four step reduction wave and the cobalt III complex, a five-step reduction wave when tetraethyl ammonium perchlorate was used as a supporting electrolyte. The $[Co(bpy)_3]^{2+}$ complex gave a one-step oxidation wave from cobalt II to cobalt III at around +0.2v (vs SCE while $[Co(bpy)_3]^{3+}$ gave a reduction wave from cobalt III to cobalt II at almost the same potential. Morinaga [129] carried out a voltammetric study of the reduction of $[Co(bpy)_3]^{3+}$ to $[Co(bpy)_3]^{2+}$, and found that the redox potential (ie measured difference between the Ep values) for the $[Co(bpy)_3]^{3+}$/ $[Co(bpy)_3]^{2+}$ couple was approximately 0.05v in acetonitrile. The more positive peak corresponded to the one-electron exchange reaction of the CoIII/CoII couple.

Fig. 3.7 and 3.11 show the two voltammograms which together represent the total voltammetric response for $[Co(bpy)_3]^{3+}$ immobilised on a clay matrix, using a solution of acetonitrile with tetrabutylammoniumperchlorate as the supporting electrolyte. The total response consists of a one-step oxidation wave and a four-step reduction wave as opposed to the 5 step reduction observed for $[Co(bpy)_3]^{3+}$ in acetonitrile solution at a bare paltinum electrode, as was also observed by Tanaka and Sato[128].

CHAPTER 4

A BRIEF INTRODUCTION TO HIGH-RESOLUTION SOLID-STATE NMR (WITH REFERENCE TO THE BRUKER AC300 SPECTROMETER)

4.1 Introduction

The introduction of pulse fourier transform methods undoubtedly started a new era of NMR spectroscopy that resulted in an unpredicted and intensive development of new experimental techniques. At the beginning enhancement of sensitivity was the most important aspect and attention focused quite naturally on ^{13}C-NMR spectroscopy, but we are now seeing progress in the NMR spectroscopy of less abundant nuclei and in solid-state spectra that nobody would have dreamed of even a few years ago. This expansion towards new applications is matched by an equally impressive growth of new experimental techniques which have virtually eliminated many of the older c.w. (continuous wave) techniques. Above all, the more extensive integration of computers into the NMR experiment provided the basis for a large number of investigations that are computer controlled.

4.2 Magnetic Interactions In The Solid State[85,45]

From an experimental viewpoint the main difference between the NMR spectroscopy of solids and isotropic liquids or solutions is that the spectra of solids are generally rather broad and featureless. For example the ^{1}H NMR spectrum of a typical organic solid can be a single line with a half-width of $10^{4}Hz$ or more. This contrasts with the solution-state spectrum of the same material, which may cover $10^{3}Hz$ or less and comprise many lines with half-widths less than $1Hz$.

From a theoretical point of view the main difference between solutions and solids, is that in the latter the nuclei experience one or more orientation dependent or anisotropic interations which lead to large splittings or broadening of the spectra. These interactions themselves contain much useful information.

The main interactions involving a nucleus with a magnetic moment which can occur in the solid state are:

1. The Zeeman interaction with the magnetic field.

2. Dipole-Dipole interactions with other nuclei.
3. Magnetic shielding by the surrounding electrons giving chemical shifts.
4. Spin-spin couplings to other nuclei.
5. Quadrupolar interactions which will be present for nuclei with spin > 1/2 only.

A general Hamiltonian for the interactions experienced by a nucleus of spin I in the solid state may thus be written as in equation (4.1).

$$H = H_Z + H_D + H_{CS} + H_{SC} + H_Q \qquad (4.1)$$

In a particular solid-state system, one or two of the terms will usually dominate the Hamiltonian and hence determine the spectral characteristics. In dilute spin -1/2 nuclei such as ^{29}Si and ^{13}C the main interactions which give rise to spectral broadening are the dipolar coupling and chemical shift interactions. Furthermore both of these interactions are anisotropic i.e. orientation dependent with respect to the external magnetic field, and are considered in greater detail.

4.2.1. The Dipolar Interaction (H_D)

This interaction arises from direct dipolar interactions between nuclei. For a solid containing a single type of spin I, with magnetogyric ratio γ_I, the interaction can be written as in eqn. (4.2) for two isolated spins

$$H_D = H_{II} = \frac{\gamma_I^2 \hbar^2}{r^3_{II}} \; I.\, D.\, I \qquad (4.2)$$

where r is the internuclear vector and D the dipolar coupling tensor.

The interaction between a pair of unlike spins I and S with magnetogyric ratios γ_I and γ_S is expressed in eqn. (4.3).

$$H_D = H_{IS} = \frac{\gamma_I \gamma_S \, h^2 \, I \cdot D \, S}{r^3} \quad (4.3)$$

Fig 4.1 illustrates the direct magnetic coupling between two magnetic moments in the presence of a large static magnetic field Bo. One nucleus produces a local magnetic field at the site of the other and vice versa. This local field can be thought of as having two components

(a) static, arising from the Z-projection of μ

(b) rotating, arising from the x/y component of μ as it precesses.

If we consider only the μ_{zj} term then the total field b_i will have a range of values depending on the statistics of whether the spins j are "up" or "down".

Apart from the small Boltzmann factor, up and down states are equally probable and thus the resonance absorption for spin I will occur at frequency.

$$Wi = (B_o + b_i)\,\gamma \qquad (4.5)$$

Since b_i has a range of values, so will Wi. As shown in fig. 4.2(b) the width of the resonance absorption reflects the root-mean-squared dipolar local field.

The role of the time-varying local fields is more subtle. If the nuclear spins involved have the same resonance frequency then the rotating local fields are resonant with the nuclear precession. This is what's needed to cause the spin to flip from "up" to "down" and vice-versa. They undergo mutually induced, energy conserving "flip-flop" transitions. In effect they irradiate each other with resonant radiation. These dynamic processes lead to the ability of strongly dipolar-coupled spin systems comprising like nuclei to disperse any local

differences in M_Z which may occur. This process is known as spin-diffusion. For unlike nuclei such as $^{13}C/^{1}H$ the rotating local fields are resonant and cannot bring about the energy-conserving flip-flop transitions. Hence the heteronuclear contribution to a dipolar dominated linewidth is less than that for a homonuclear case.

4.2.2. The Chemical Shift Interaction

This is due to the shielding effect on the nucleus of the fields produced by the surrounding electrons, and is expressed as:

$$H_{CS} = \gamma_i h I. \sigma.H \qquad (4.6)$$

The interaction is linear width the applied field and will be proportionately larger at higher magnetic field strengths. Since it involves the surrounding electrons, it is the most sensitive interaction to the geometry and identity of the other atoms surrounding a particular nucleus and will usually be the most 'chemically diagnostic' in NMR studies.

Since the electronic screening is a three-dimensional quantity, the chemical shift will be anisotropic i.e. orientation dependant. In solution state the average (isotropic) value is observed. In the solid state however, the chemical shift will be dependent on the orientation of the molecule in the magnetic field and the complete three dimensional nature of the nucleus may be determined. The three-dimensional nature of the shielding may be expressed as in eqn. (4.7).

$$H_S = g_N^2 \beta_N^2 I_i \sigma_i. H_o \qquad (4.8)$$

where, since I and H are both vector quantities σ must be a 3 x 3 matrix or second rank tensor. By a suitable choice of coordinate system σ_i may be converted to a diagonal form with three principal elements σ_{11} σ_{22} and σ_{33}. In the general case the observed shielding constant is denoted by σ_{av} and is a linear combination of the principal elements σ_{ii}.

$$\sigma_i = \sum_{j=1}^{3} \sigma_{jj} \cos^2\theta j \quad (4.9)$$

where the angles θ_j, are those between σ_{jj} and B_o. In solution, with molecules tumbling rapidly and isotropically averaging of σ occurs so that only one-third of the trace i.e. 1/3 $(\sigma_{ii} + \sigma_{22} + \sigma_{33})$ is observed. This can be rewritten as:

$$\sigma_i = Tr\,\sigma + 1/3 \sum_{j=1}^{3} (3 \cos^2\theta_j - 1)\,\sigma_{jj} \quad (4.10)$$

where Tr stands for trace. In the case of axial symmetry the corresponding equation is

$$\sigma_i = Tr\,\sigma + 1/3\,(3 \cos^2\theta_{11} - 1)\,(\sigma_{11} - \sigma_{\perp}) \quad (4.11)$$

$(\sigma_{11} - \sigma_{\perp})$ is commonly known as the value of the shielding anisotropy. The result of these facts is that for a single crystal containing nuclei which are all in translationally equivalent positions, the NMR spectrum consists of a single line whose frequency varies with the orientation of the crystal in Bo. For a microcrystalline powder sample, however, the distribution of nuclear orientations result in absorption over a range of frequencies giving a powder pattern. A schematic powder pattern for the case of axial symmetry is shown in fig. 4.3.

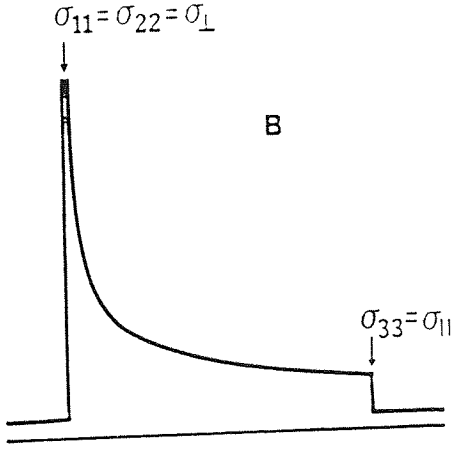

Fig. 4.3 Schematic Powder Pattern for the Case of Axial Symmetry

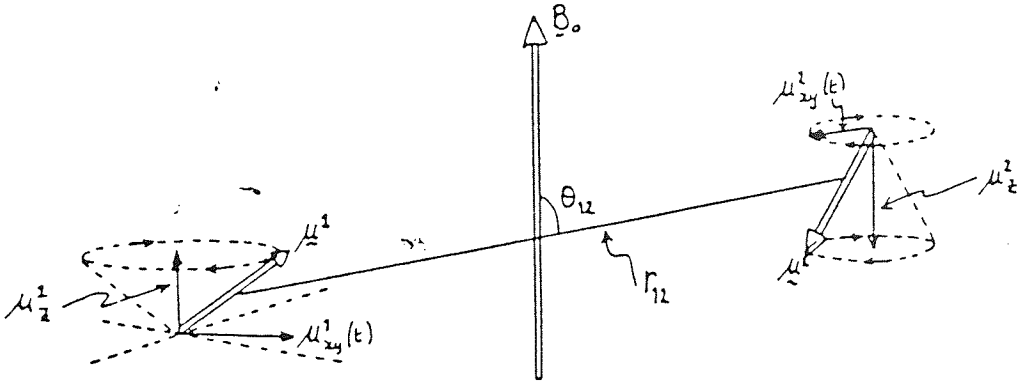

Fig. 4.1 The Dipole - Dipole Interactions Between Nuclear Magnetic Moments μ^1 and μ^2

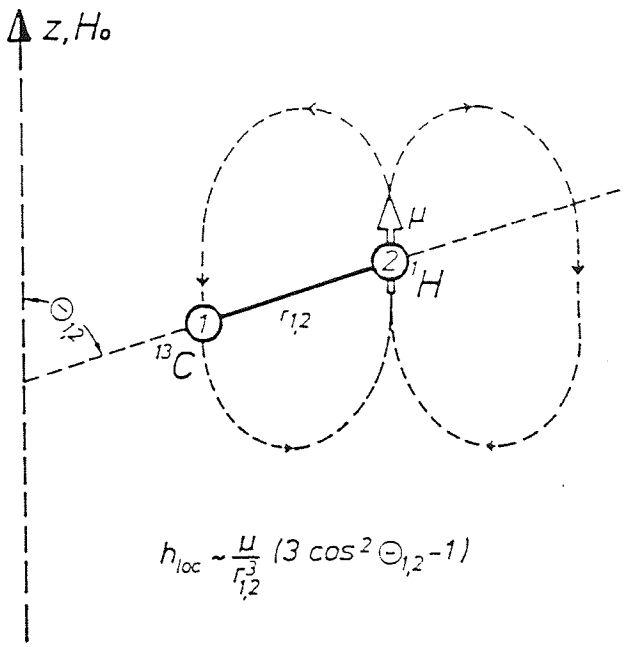

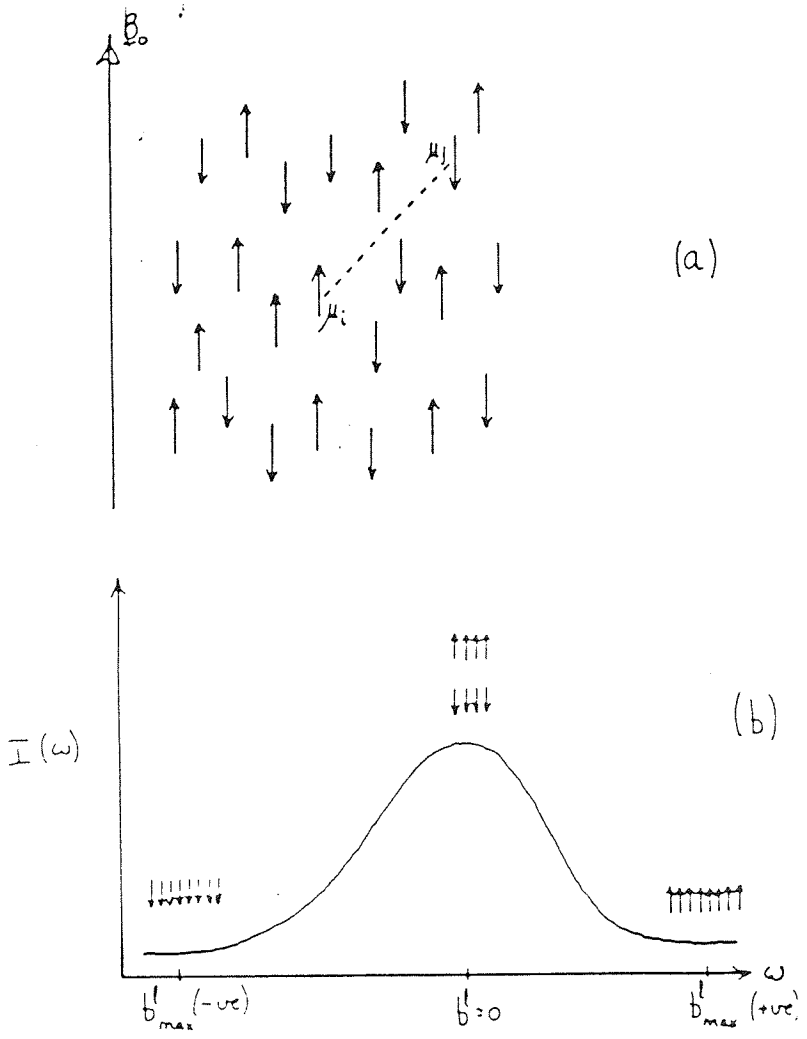

Fig. 4.2 A Qualitative Illustration of the Origin of Broad Lines in the NMR Spectra of Spin1/2 Nuclei in Solids

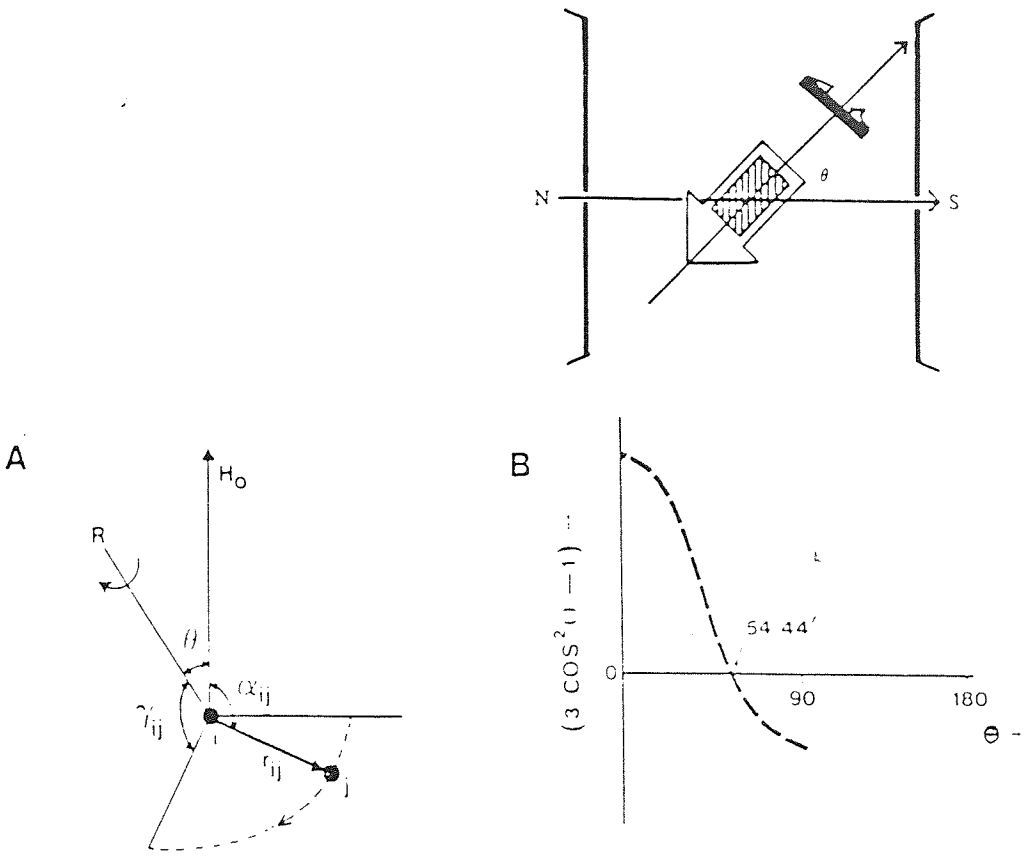

Fig. 4.4

(a) Definition of angles used in MAS

(b) Variation of the term $(3\cos^2\theta\text{-}1)$ as a function of θ

(c) Effect of magic angle spinning: by rotation about the magic angle, the time averaged value of all binding vectors becomes $54^o44'$

When $\theta = 54^{o}44'$, the prefactor to the first term becomes zero leaving only the second term, the value of which is now $\sigma_i I_z B_o$ which in turn yields the isotropic chemical shift σ_i.

4.4. QUADRUPOLAR NUCLEI WITH NON-INTEGRAL SPINS IN NON-CRYSTALLINE SOLIDS[85,42]

Generally in the case of nuclei with I > 1/2 the solid state NMR spectra are usually dominated by the nuclear quadrupole interaction. That is, the total Hamiltonian can be expressed as 4.14.

$$H = H_{ZEEMAN} + H_{QUADRUPOLAR} \quad (4.14)$$

and terms such as dipolar couplings, anisotropic chemical shifts and scalar spin-spin couplings may be neglected to a first approximation. The dipolar term will affect the spectrum as a line broadening. The quadrupolar term arises from the interaction of the nuclear charge with a non-spherically symmetric (Lower than tetrahedral symmetry) electric field gradient.

For a single spin I, the quadrupolar interaction may be represented as

$$H_{QUADRUPOLAR} = I \,.\, Q \,.\, I. \quad (4.15)$$

Since I is a vector quantity, Q is a second rank tensor which describes the three dimension at nature of the interaction. Q is defined as in (4.16) where e Q is the quadrupole moment and V is the electric field gradient tensor at the nuclear site.

$$Q = \frac{e\,Q}{2I(2I - 1)\,h} \,.\, V \quad (4.16)$$

As shown by eqn. (4.16) the interaction energy depends on

(i) quadrupolar moment Q

(ii) electric field gradient tensor ... E

(iii) Orientation of the field B_o with respect to the principal axis system of the electric field gradient tensor.

The components of ... E in its principal axis system (diagonalised form) are V_{11}, V_{22} and V_{33}, where

$$V_{33} >> V_{22} >> V_{11}$$

The efg arises from electrons ions or other charges in the material under study. Since all of these charges are outside the nucleus at which the components of ...E are evaluated in the interaction, Laplace's equation holds and $V_{11} + V_{22} + V_{33} = 0$. Hence the three components can be specified by two parameters (i) the field gradient q_{zz} and (ii) the asymmetry parameter η where

$$q_{zz} = V_{33}$$

and $$\eta = \frac{V_{22} - V_{11}}{V_{33}} \qquad (4.17)$$

When the efg exhibits rotational symmetry about the Z axis.

$$V_{11} = V_{22} \text{ and } \eta = 0$$

In this case the energy of the quadrupolar interaction depends only on Q, qzz and θ (the angle between Z-axis and B_o). The transition frequencies become shifted as shown in fig 4.5, and are given by eqn. 4.18. This effect is termed as first order quadrupole broadening giving a lineshape for I = 3/2 (e.g.^{23}Na) as in fig 4.6.

$$\nu_{m\text{->}\ m-1} = \nu_o + \frac{(2m-1)(3\cos^2\theta-1)\ 3eq_{22}Q}{8\ I\ (2I\ -1)h} \qquad (4.13)$$

where ν is a single nmr frequency in the absence of quadrupolar effects.

Several points of interest arise from equation 4.18.

(i) Due to the $(3\cos^2\theta - 1)$ dependence, dipolar and CSA interactions can be averaged to zero.

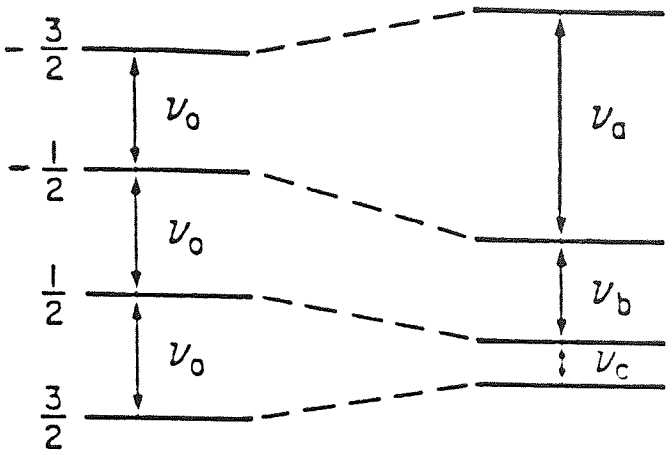

Fig. 4.5 Schematic Representation of the Energy Levels of a Spin I=3/2 Nucleus Resulting from the Zeeman Interaction with the Magnetic Field and the Quadrupole Moment of the Nucleus.

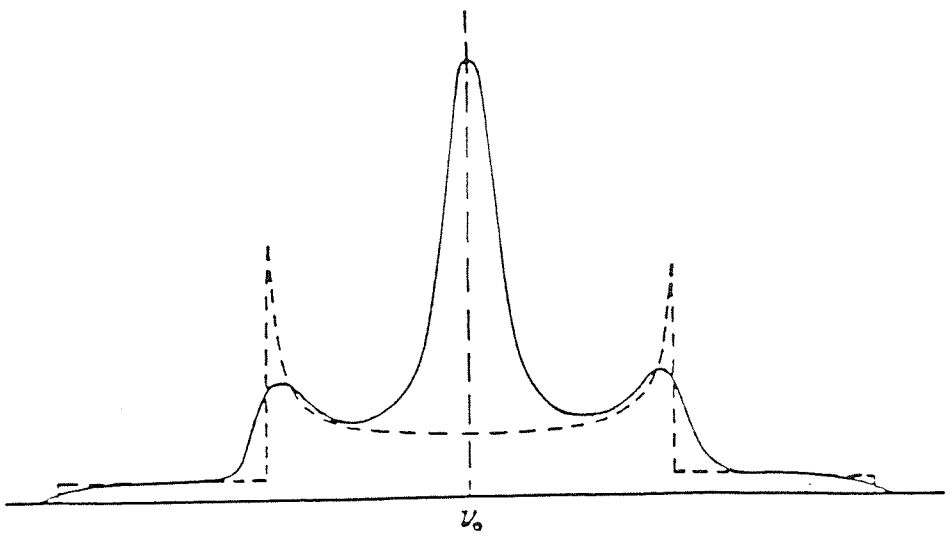

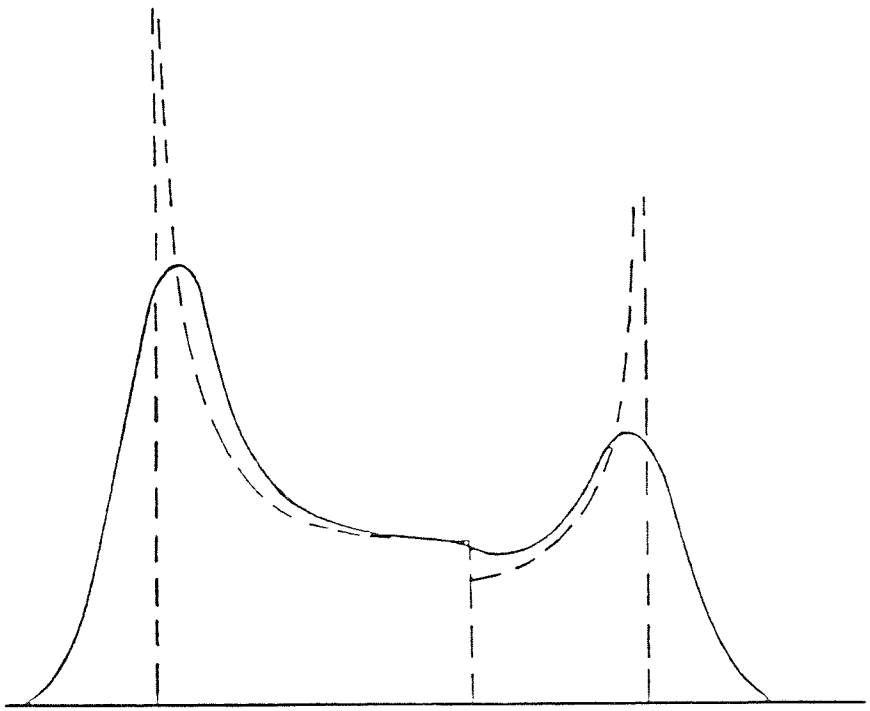

Fig. 4.7 Lineshape Observed for a Nucleus with Large Quadrupole Interaction

(ii) The transition frequency is not dependent on the magnetic field B_o.

(iii) For m = 1/2 the first oder frequency shift vanishes and central transition (m=1/2 - m = -1/2) for non-integer nuclei is not affected by first order quadrupole broadening.

Extension of the above analysis to second-order perturbation i.e. when larger crystal imperfections give rise to large efg's and a larger quadrupole interaction the transition frequency is given by equation (4.19).

$$\nu_{m\text{-}>\ m-1} = \nu_o + \frac{9}{64}\frac{2I+3}{4I^2(2I-1)}\left[\frac{eq_{22}Q}{h}\right]^2 \frac{1}{\nu_o}(1-9\cos^2\theta)\,(1-\cos^2\theta)$$

Equation 4.19 shows that when second order effects operate the transition frequency for non-integral nuclei no longer has a $(3\cos^2\theta-1)$ dependence and instead depends upon the $(1-9\cos^2\theta)(1-\cos^2\theta)$ term. The type of lineshape observed for a nucleus with large quadrupole interaction is shown by fig 4.7.

The effect of spinning on the solid state spectra of these nuclei has been treated theoretically by Maricq and Waugh[10] . The effects of second order quadrupole interaction are reduced but not completely removed by MAS. The pattern of the central line is narrowed and changed while its centre remains shifted. This residual structure will make the spectra of these nuclei less easy to interpret in cases where there are several peaks with small chemical shift differences between them than the spin 1/2 nuclei such as ^{29}Si.

An important recent contribution has been made in this area by Oldfield and co-workers who considered the effects of spinning at angles other than $54^o44'$ for the magnetic field. For a quadrupolar nucleus the spin will not be quantised about the Zeeman field direction and the "magic-angle" of $54^o44'$ will not be magic for this interaction which may dominate the spectrum. Thus as shown by equation 4.19, an angle other than the 'usual' magic angle may be magic for these

nuclei. In an important piece of work Meadows, Oldfield and coworkers[541] investigated the effect on the spectra of quadrupolar nuclei of spinning off of the "magic-angle". They observed that the best resolution was obtained at an angle other than $54^{o}44'$. In the case of ^{23}Na in Na_2MoO_4, the optimum line narrowing was obtained at $0=36^{o}$. From a theoretical analsis the optimum line narrowing depends on the assymmetry parameter. In all cases, although the major absorption is narrow, the lineshapes are very complex. Such experiments gave rise to the technique known as Variable-Angle-Spinning (VAS). The technique is likely to be of great use for studying quadrupolar nuclei in glasses and other non-crystalline solids, but at present its implementation is restricted by the relative high cost involved.

4.5. THE NMR SPECTROMETER: EXPERIMENTAL CONSIDERATIONS

The NMR spectrometer used to obtain all solid state spectra was a Bruker AC(E) 300MHz spectrometer which basically consist of

(i) the Console
(ii) the superconducting magnet
(iii) the solids accessory unit

4.5.1. The Solids Accessory Unit

The solids accessory for the AC spectrometer is a flexible and simple to use unit. This is reflected by the special rotor design for rotation at a well-defined constant angle. The rotors can be simply inserted and ejected on an air cushion and hence no electronic tuning or mechanical adjustments are necessary when changing samples. High power decoupling, cross-polarisation and high rotation speeds are combined with the possibility of multinuclear work. The basic unit consists of:

(a) Probehead: This is a multinuclear probehead, tuneable over one octave and designed only for high speed rotation under magic angle and high power decoupling.

(b) A Pneumatic Unit: This unit allows for simple sample changing and setting of rotation speed. A spinning rate meter is integrated.

(c) High Power Decoupling Unit: The selective proton decoupler is designed for 120W output power. There is also an extension for proton enhanced experiments using an additional rf - power amplifier for high power excitation of the X-nucleus.

For tuning the multinuclear probehead there is a special device mounted at the bottom of the probehead and allowing the operator to dial two given numbers corresponding to the correct resonance and matching condition of the nucleus to be investigated. Fine adjustment is achieved by changing the last digit of each number. Fig 4.8 illustrates the type of probehead used.

The sample diameter is 7 mm outer and 5 mm inner diameter, and the filling height is 9mm. The spinning speeds attained are normally greater than 5KHz.

4.5.2. Spinning Apparatus for the MAS Experiments

The spinning device used in the Bruker AC solids accessory unit derives from the designs of Andrew and Lowe shown schematically in fig 4.9.

Several factors are common to all MAS experiments. The materials used must be non-conducting in the coil volume, mechanically stable for machining purposes and for the large centripetal forces achieved, and if possible transparent in the experiment. Boron nitride, Kel-F are used ^{13}C studies but Delrin which is mechanically robust is used widely for other nuclei particularly ^{29}Si.

For any given sample the maximum spinning rate theoretically achievable is that where the peripheral velocity of the maximum diameter is equal to the speed of sound in the surrounding gas. In practice this is never realised; the approximate relationship of the spinning rate to sample diameter and spinning gas is that small samples in light gases spin fastest.

Aston University

Content has been removed for copyright reasons

4.5.3. The Andrew-Beams Spinner[85,174]

The spinner design used by Andrew was a modification of the gas turbine spinners described by Beams Hennirt and Garman . The drive for the system is produced by jets of high pressure gas through holes in a stator cone which impinge onto the conical bottom of the rotor containing the sample. As the sample rotates, a vacuum is created between the tip of the rotor cone and the apex of the stator. This in turn begins to create a gas bearing between the surfaces of the two cones, resulting in faster spinning until a limit is reached for a given gas pressure. The optimization of the spinner design has been well described and most literature data reported to date have been obtained using this tupe of apparatus. The Andrew-Beams spinner can be used with either electromagnets (M. A = 35°16' to the vertical) or superconducting magnets (M.A. = 54°44' to the vertical). The stators need not have flutes machined in them although it is usually easier to start them up if they do. In practice spinning rates in the range of 2.5 to 5.0 KHz or samples in containers of ca. 8 to 10mm outer diameter are obtained. This compromise gives acceptable spinning rates coupled with good sample volumes and with coil diameters which give RF pulses of sufficient power.

4.5.4. Setting of the 'Magic-Angle'

For maximum resolution the angle must be set as accurately as possible. A linebroadening of ca. 2.5% of the static linewidth is introduced for every degree that the spinning axis deviates from 54°44'. Most often this is done by setting the angle on an easily observable reference sample which has a resonance with a large shift anisotropy, and then changing to the sample of interest in a different spinner without changing the angle. However, the exact angle at which the sample spins is a function of gas pressure, spinner geometry and spinner packing.

Ernst and coworkers[105] have described a laser-based system in which the angle is measured by reflection of the light beam from the spinner surface. A much simpler technique of general applicability has been introduced by Frye and

Maciel who suggested adding a small amount of a quadrupolar nuclide directly into the sample. This is easily done by first spinning the sample and generating a small hole in the centre of the sample, or by adding a pressed disc of the material to the bottom of the container. K^+Br^- is normally used. Because the crystal symmetry is cubic a sharp absorption is observed for the central m = 1/2 to m = -1/2 transition but the other transitions m = 1/2 to m 3/2 and m = -1/2 to m = -3/2 also affect the spectrum. Sidebands separated by the spinning frequency are clearly observed in the spectrum and these are very sensitive to the exact angle of the spinning axis. The high sensitivity and short relaxation times makes the observation of ^{79}Br nucleus very simple. The spinning axis can be set to within 0.1^o of the magic angle.

4.5.5. Other Experimental Considerations[86,87]

All solid-state spectra in this work are obtained using pulse-FT techniques with the capability of increased sensitivity through efficient signal averaging[92]. The basic 90^o pulse is discussed briefly overleaf.

As shown in Fig 4. the M_z magnetisation is rotated by 90^o by a strong on resonance radio-frequency pulse applied along the x' direction in the 'rotating frame' (i.e. the whole sequence is considered to take place with respect to a coordinate system coincident along Z and rotating in the x',y' plane at the frequency of the applied radio frequency pulse which is equal to W_o for a pulse exactly on resonance). The magnetisation is now aligned along y' and its free induction decay may be detected and Fourier transformed to give the absorption spectrum. The above experiment, in terms of format and general principle involved is identical to the conventional pulse-FT experiment normally employed in high resolution NMR studies. In its application to solids, however, there are important differences:

(i) Because the solids absorptions are so broad, the decay will be very fast and an efficient receiver with a very short 'dead-time' must be used to acquire data as dose to

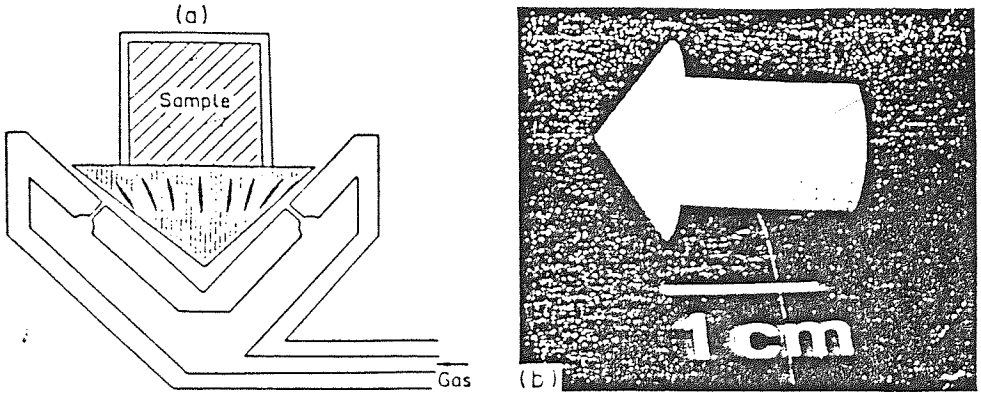

Fig. 4.10 The Andrew-Beams Turbine Spinner

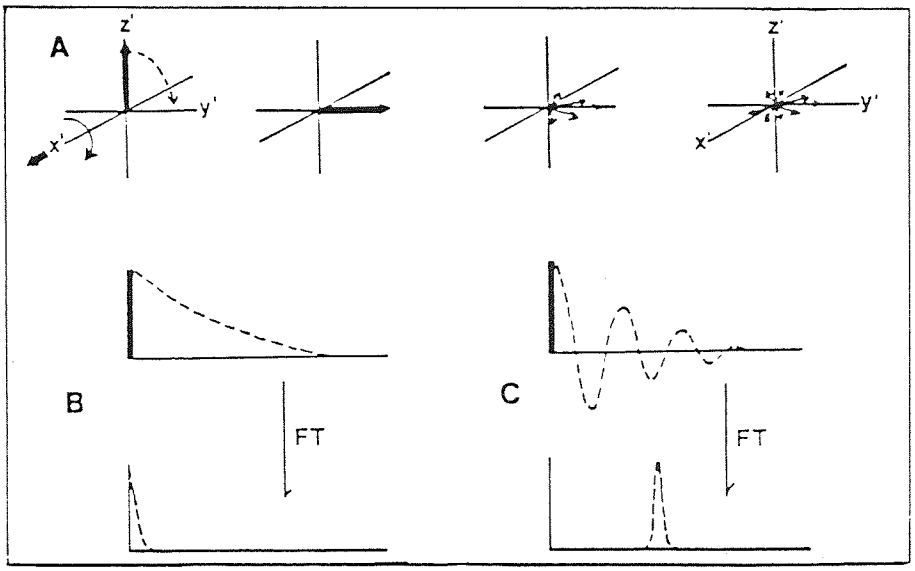

Fig. 4.11 Schematic representation of the pulse FT sequence in the rotating frame of reference showing (A) the behavior of the magnetisation as a function of time after being rotated 90° by an on resonance RF pulse applied along the x' axis and the subsequent dephasing of spins in x'y' plane. (B) + (C) magnetisation decay and its Fourier transform detection exactly on resonance and slightly off resonance respectively.

zero time as possible, as it is this data which defines the outermost parts of the spectrum.

(ii) Secondly, because the lines are so broad, very powerful pulses are needed to excite the whole frequency range of the spectrum.

(iii) The total frequency width that may be observed is a function of the digitizer.

These problems are easily overcome by using the commerical instruments available.

4.6. TYPICAL NMR PARAMETERS USED FOR OBSERVATION OF ^{29}Si, ^{23}Na AND ^{27}Al IN THE SOLID STATES. [95]

Tables 4 to 4. show representative NMR parameters for ^{29}Si, ^{23}Na and ^{27}Al nuclei for some typical caramic glazes samples. Generally because of the very low concentration of paramagnetic species the observation parameters did not vary greatly from sample to sample. Explanations of the NMR parameters are given in detail in the literature[92, 86, 87, 89].

Fig 4.12. and 4.13. show the differences in the ^{29}Si spectra of laponite obtained using two different spectrometers, the former spectrum being recorded on a Varian VH(300MH_z) NMR spectrometer while the latter was recorded on a Bruker AC300MH_z spectrometer. Fig 4.14. is the ^{29}Si NMR (MAS) spectrum for the model glaze Lap 1000 with decoupling. There is a significant difference between decoupling and non-decoupled spectra, the former showing more clarity and the presence of more signals as the lineshape is resolved. However, the decoupling technique was not used for other ceramic glaze preparations since no protons are likely to be present at firing temperatures above 1000^{o}C.

Table 4.7.1 ^{29}Si MAS NMR Parameters for Laponite Using Two Different Spectrometers

	Varian VH (300MHz)	Bruker AC (300MHz)
Frequency	59.584 MHz	59.580 MHz
Spectral Width	30,030 Hz	36,800 Hz
Acquisition Time	19.2 ms	139 ms
Relaxation Delay	15.0 sec	1.0 sec
Pulse Width	51^{o}	4.0^{o}
No. of Scans	550	8687
Decoupling	gated	-
Spinning Speed	4240 Hz	4749 Hz
FT Size	8K	8K

Table 4.7.2 ^{23}Na + ^{27}Al MAS NMR Parameters for a Model Feldspar Ceramic Glaze (SiO_2 + Na_2O + Al_2O_3 + CaO [F8]) Heated to $1300^{o}C$ Bruker AC 300 MHz

	^{23}Na	^{27}Al
Frequency	79.392 MHz	78.206 MHz
Spectral Width	16,129 Hz	31,250 Hz
Acquisition Time	254 ms	524 ms
Relaxation Delay	0.0 sec	1.0 sec
Pulse Width	10.0^{o}	15.0^{o}
No. of Scans	5,000	25,000
Spinning Speed	4600 hz	4630 Hz
FT Size	8K	8K

Fig 4.12.

^{29}Si MAS NMR Spectrum of Laponite

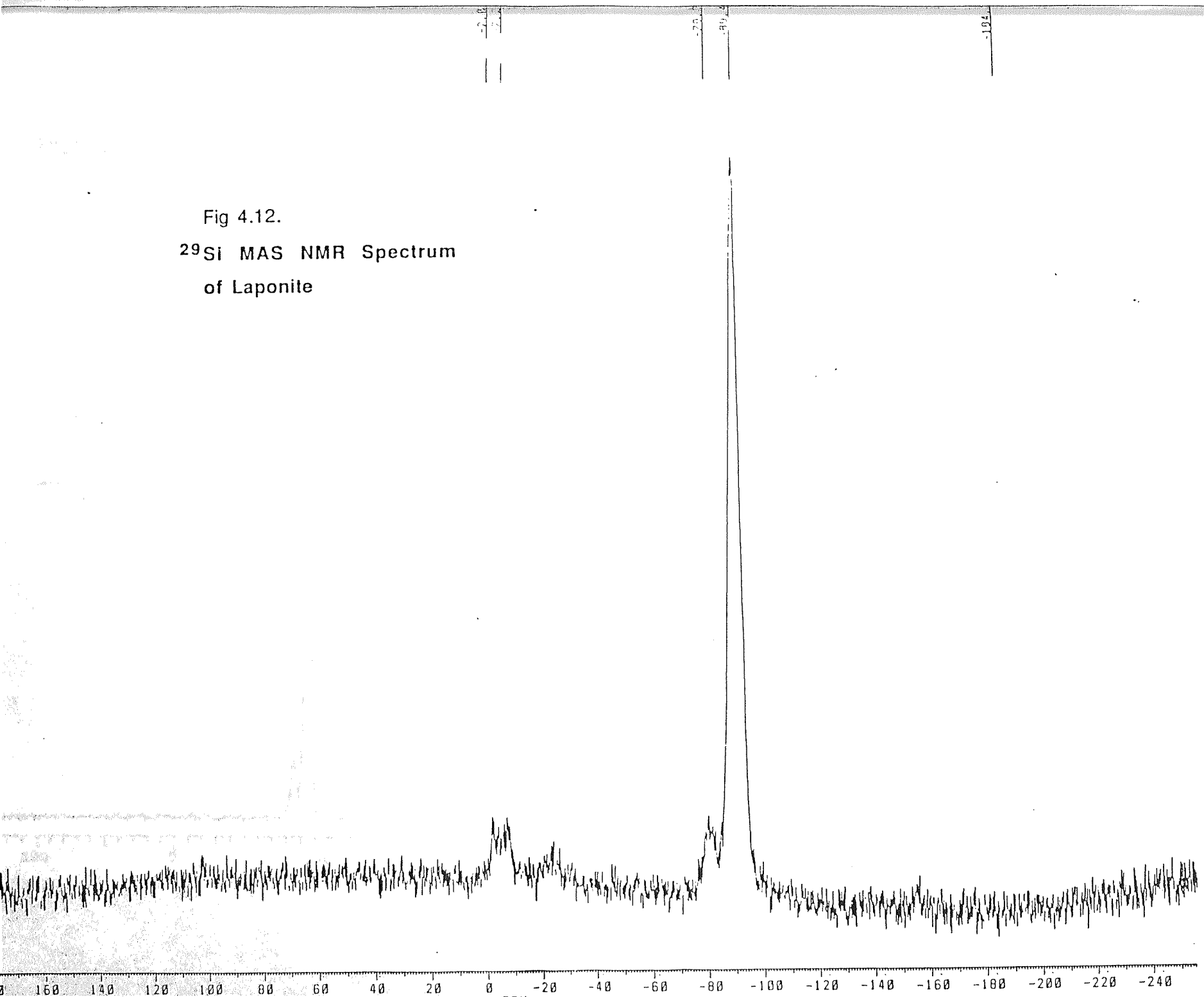

^{29}Si MAS NMR Spectrum

of Laponite

Varian VH(300MHz)

XFOLAR PULSE SEQUENCE
OBSERVE SILICON
FREQUENCY 59.584 MHZ
SPECTRAL WIDTH 30030 HZ
ACQ. TIME 19.2 MSEC
RELAXATION DELAY 15.0 SEC
PULSE WIDTH 51 DEGREES
AMBIENT TEMPERATURE
NO. REPETITIONS 550
GATED DECOUPLING
SPIN RATE 4240 HZ
DOUBLE PRECISION ACQUISITION
DATA PROCESSING
FT SIZE 8K

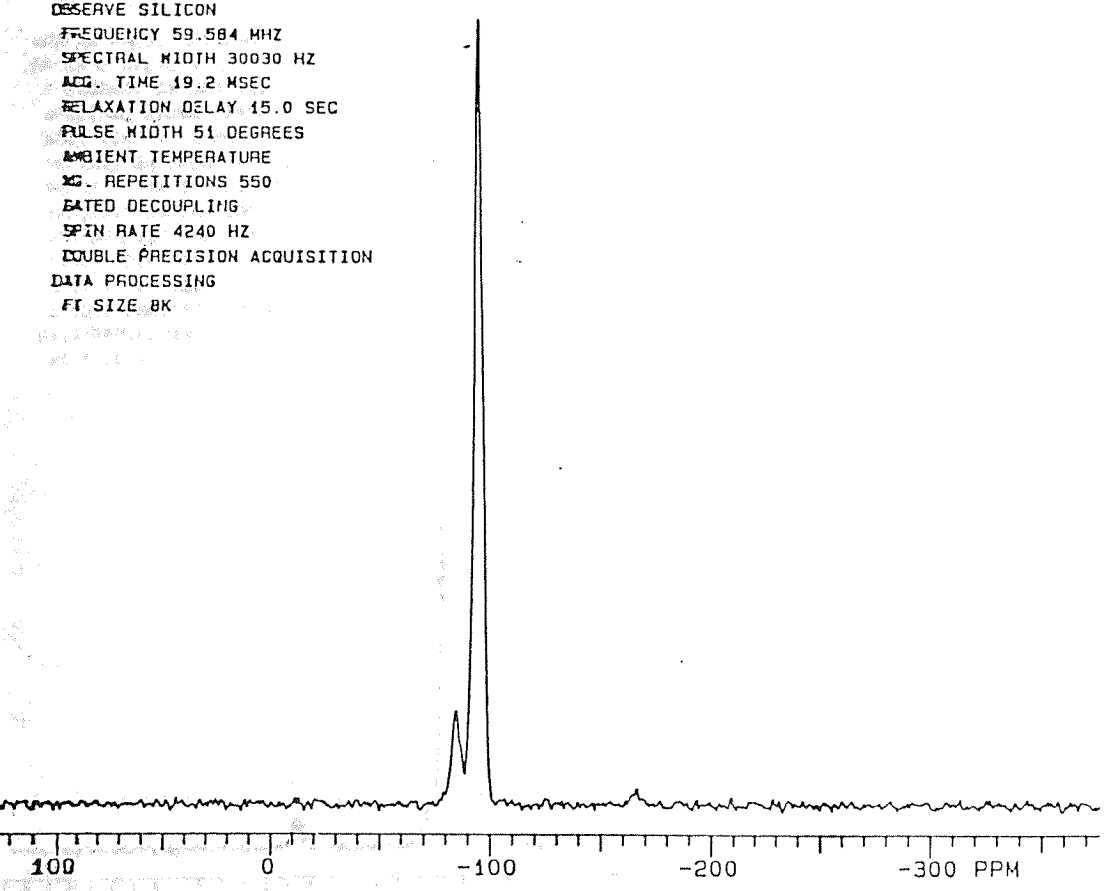

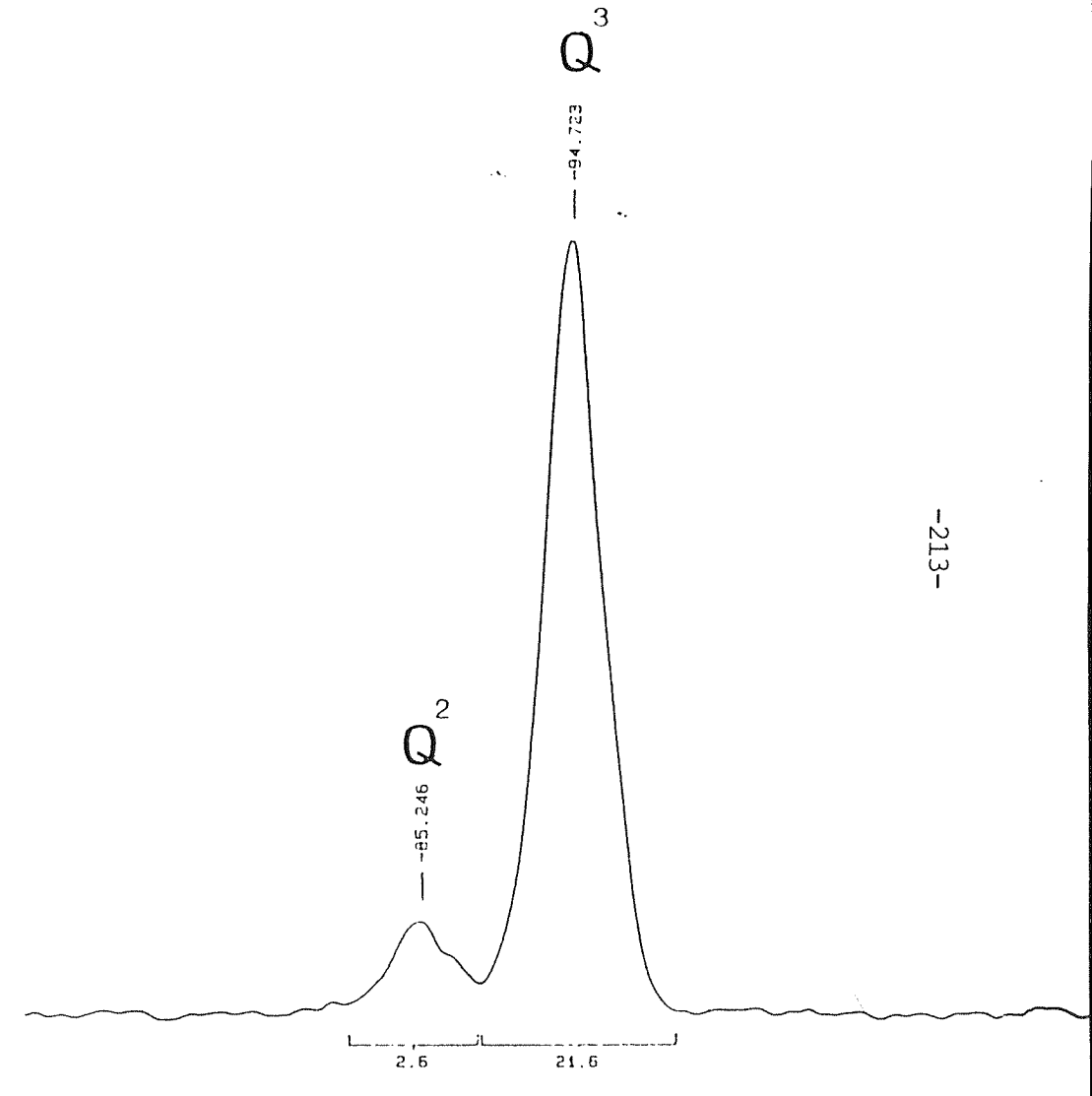

Varian VH(300MHz)

^{29}Si MAS NMR Spectra for the Model Glaze [Laponite + CaO] Fired at 1000

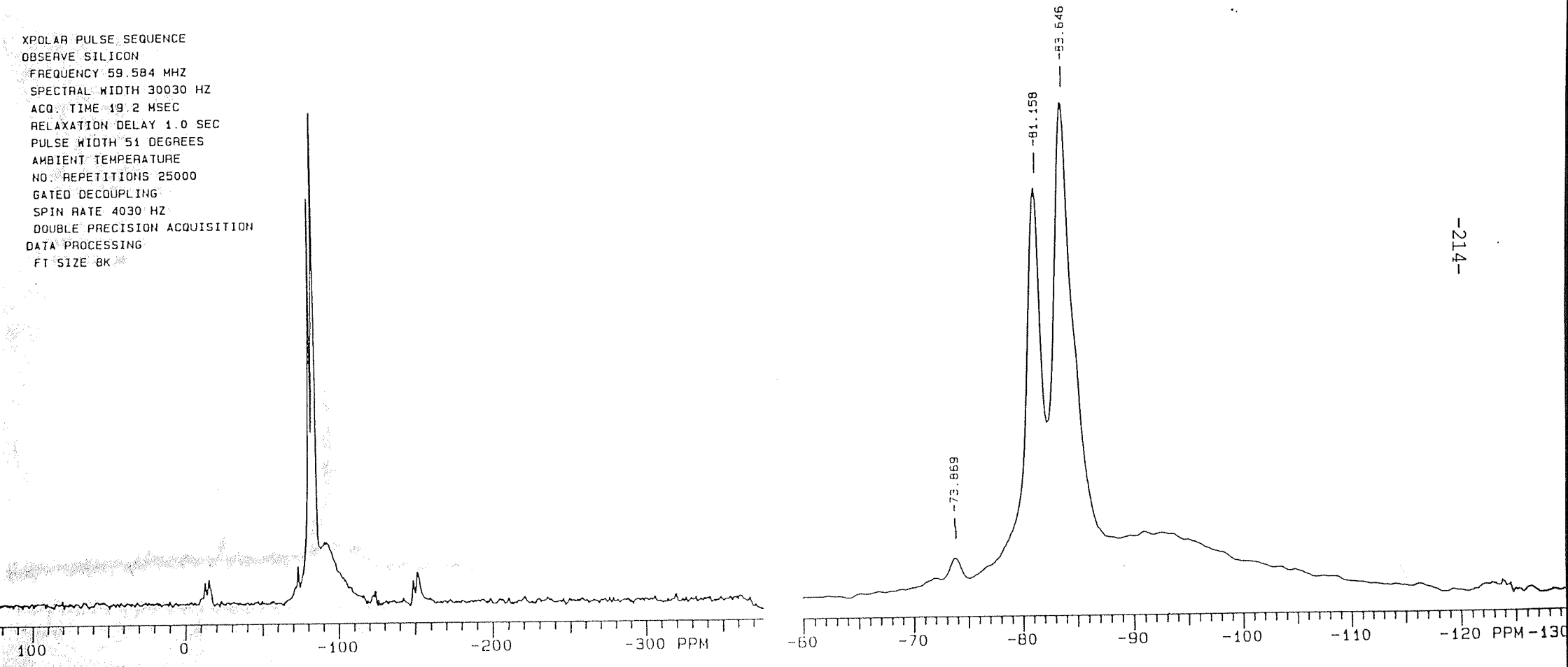

Fig 4.14.

Varian VH(300MHz)

LAPONITE + CALCIUM CARBONATE
HEATED TO 1000 C
SINGLE PULSE DECOUPLED
DSK
EXP1 PULSE SEQUENCE: XPOLAR
DATE 06-05-87
SOLVENT SOLID
FILE LAPONE

XPOLAR PULSE SEQUENCE
OBSERVE SILICON
FREQUENCY 59.584 MHZ
SPECTRAL WIDTH 30030 HZ
ACQ. TIME 49.0 MSEC
RELAXATION DELAY 15.0 SEC
PULSE WIDTH 51 DEGREES
AMBIENT TEMPERATURE
NO. REPETITIONS 310
GATED DECOUPLING
SPIN RATE 4030 HZ
DOUBLE PRECISION ACQUISITION
DATA PROCESSING
FT SIZE 8K

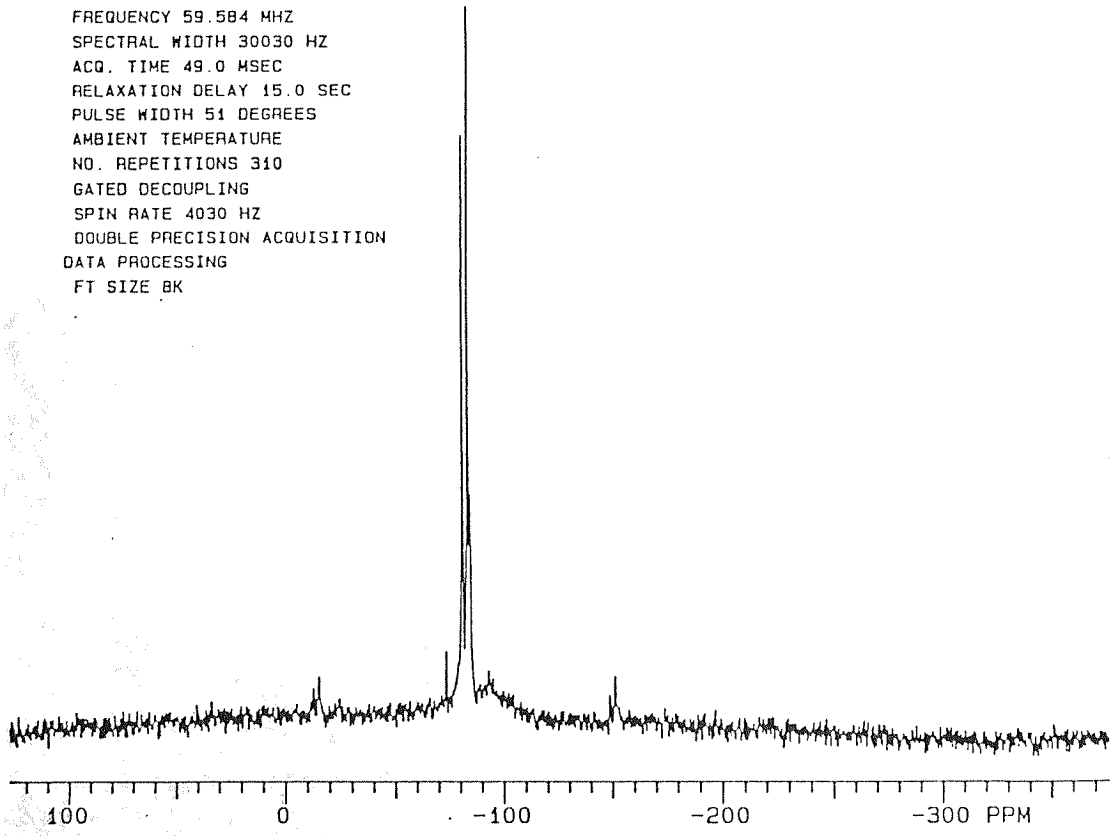

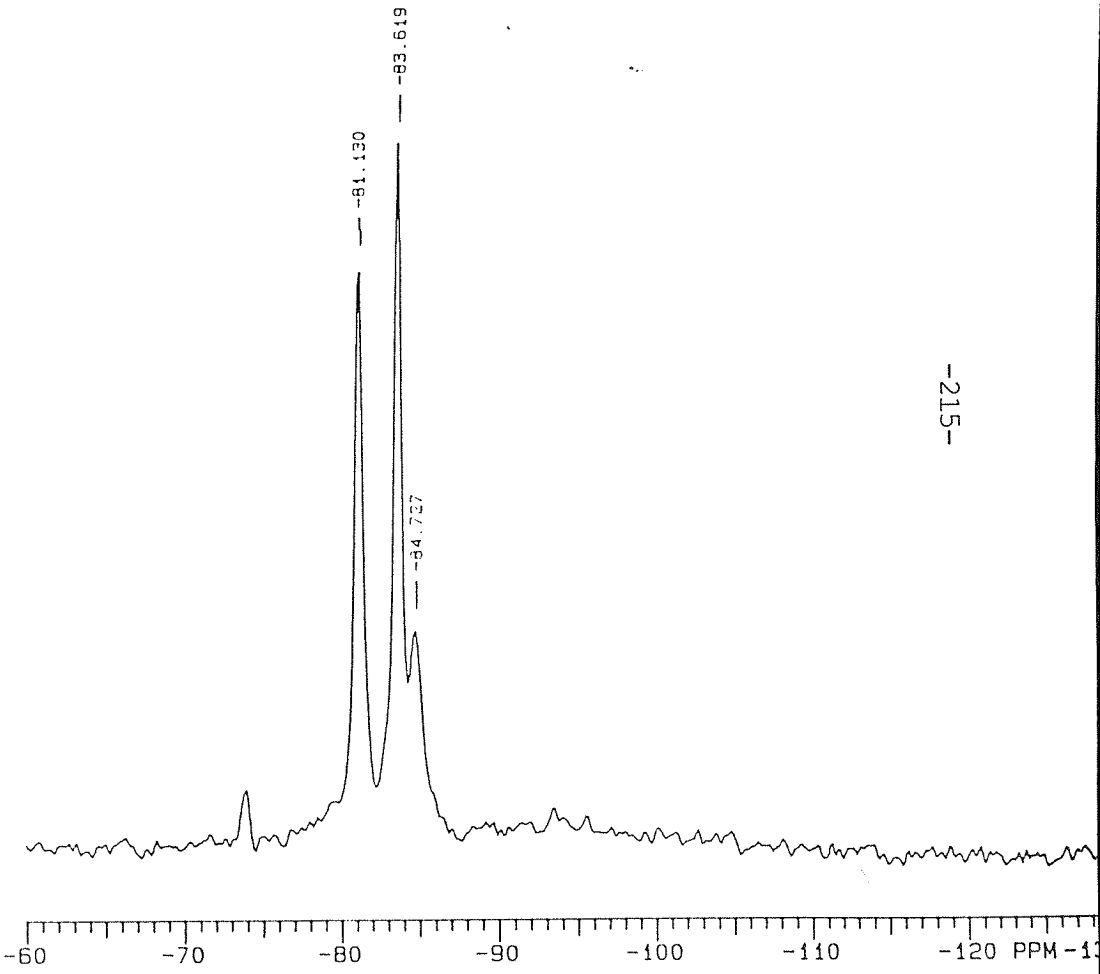

CHAPTER 5

A SOLID-STATE NMR INVESTIGATION OF SOME TOPOTACTIC REACTIONS OF LAPONITE AND ITS ROLE AS A CERAMIC GLAZE CONSTITUENT

5.1 INTRODUCTION

The scientific study of glass began at the beginning of the nineteenth century and today it is a rapidly developing subject, both in the development of new glassy materials with special properties and in the application of new scientific techniques to improve our understanding of the structure of glasses, glazes and related ceramic materials. In the context of this work ceramic glazes are defined as vitreous substances formed as a film of glass on a ceramic base by supercooling high viscosity mixtures of complex silicates.

A strong interest within our group in the chemistry of ceramic glazes, led previous workers to study the role of transition metal ions in colour forming reactions of ceramic glazes. Gillespie[28] used ^{57}Fe Mossbauer and magnetochemistry to evaluate the use of these techniques in the investigation of iron in weak ligand field environments similar to those encountered in a glaze environment. Electron spin resonance was used to study the structural environments of copper, iron and chromium ions in glazes. Ali's[29] work was concerned with the chemistry of the vanadyl IV complexes in glaze environments effect of different metal oxides on the coordination behaviour of Ni(II) in glaze environments. ESR, UV-Vis and Mossbauer spectroscopy were the major techniques used in probing the structure of these glazes.

Although such techniques proved to be fairly successful in elucidating the structural environments of the transition metal ion probes, it was only possible to speculate on the overall structure of the glaze. Very little light could be shed on the actual behaviour of the network or on the local environments of the main network forming silicate species. However, the advent of solid state MAS NMR promises to throw more light on the overall structure and bonding in glassy systems as some of the critical cations such as ^{29}Si, ^{27}Al, and ^{23}NA are NMR active. It has been shown that NMR spectra are excessively broadened by even low concentrations of transition metal ions. Thus the NMR method has one major limitation. On the other hand, the ESR technique is only sensitive to paramagnetic species. The present work is an attempt to evaluate the possibilities and limitations of MAS NMR in the study of complex ceramic glazes and related inorganic systems, and therefore to build

upon some of the results obtained by other physical techniques by previous workers.

In selecting a particular glaze system, the prinicpal prerequisite was to obtain glaze constituents which were free of paramagnetics. Bearing this in mind, the first system chosen for study is the synthetic 2:1 phyllosilicate clay mineral, laponite, which is free of structural iron and aluminium. Laponite also has the added attraction that it contains Li_2O, a potential glass forming oxide. The effect of firing temperature on and the addition of various modifier oxides to laponite are studied using ^{29}Si MAS NMR, XRD and I.R. spectroscopy.

A logical starting point in this work is to study the effect of different firing temperatures on the laponite clay mineral alone. This is because the laponite composition contains both glass and network forming oxides $[(Mg\ O)_4\ (Li_2O)_{0.2}(SiO_2)_7]$. As an interesting additional experiment we also consider the effect of firing temperature on the hydration state of the interlayer region of laponite, using ^{23}Na and ^{29}Si MAS NMR.

5.2 A COMBINED ^{29}Si MAS NMR/X-RAY DIFFRACTION STUDY OF THE THERMAL REACTIONS OF LAPONITE

5.2.1 Experimental

(a) Samples of laponite (5g) were placed in porcelain crucibles and fired in a carbolyte furnace at temperature of 200°C, 400°C, 600°C, 800°C and 1300°C for three hours at constant temperature. Fired samples were then covered with a lid and immediately placed in a vacuum desiccator to cool overnight.

(b) Samples fired between 200 and 800°C were divided into halves. After careful grinding in an agate mortar, one half was kept for analysis. The other half was rehydrated

by immersing in distilled water for one hour. Excess water, was then decanted off and the sample left to air-dry for about one week. The rehydrated sample was then carefully reground and analysed as before.

5.2.2 Results and Discussion

Table 5.1.1 ^{29}Si NMR Parameters for Laponite Field at Various Temperatures

	Q^0		Q1		Q2		Q3		Linewidth (FWHH)/Hz
	δ/ppm	I/I_1	δ/ppm	I/I_1	δ/ppm	I/I_1	δ/ppm	I/I_1	
Laponite					-84.1	(9)	-93.6	(91)	≈200Hz
DE 200					-85.9	(9)	-95.9	(91)	≈350Hz
DE 400			-81.8	(16)	-85.3	(33)	-90.8	(41)	>1000Hz
DE 600							-97.7		<50Hz
DE 800			-81.0	(41)	-83.5	(59)			<50Hz
DE 1300			-80.90	(20)	-83.5 -85.1	(30) (41)	 -96.1	 (9)	≈50Hz ≈1080Hz

Table 5.1.2 ^{29}Si NMR Parameters for Rehydrated Laponite Sample

	Q^0		Q1		Q2		Q3		Linewidth (FWHH)/Hz
	δ/ppm	I/I_1	δ/ppm	I/I_1	δ/ppm	I/I_1	δ/ppm	I/I_1	
RE 200	-	-	-	-	-85.3	(8)	-94.9	(92)	≈200Hz
RE 400	-	-	-	-	-85.3	(8)	0-94.9	(92)	≈300Hz
RE 600	-	-	-	-	-88.5 -85.6	}(10)	-98.0	(90)	≈310Hz
RE 800	-	-	-	-	-80.8	(40)	-83.3	(60)	45Hz,63Hz

Table 5.1.3 ^{23}Na NMR parameters for Various Hydration States of Laponite

	δ23Na/ppm (from NaBr)	$\Delta\sqrt{}$/Hz (FWHH)
Laponite	-15.3	1200
DE 200	-18.9	2100
DE 400	-18.9	2100
DE 600	-19.5	2300
DE 800	-17.5	2200
RE 200	-19.4	5800
RE 400	-8.8	1050
RE 600	-9.6	1050
RE 800	-13.7	1950

X-Ray Diffraction Results for Laponite Fired at 400°C, 800°C and 1300°C

	DE400	DE800	DE1300
d-spacing/Å	3.23	4.97	3.93
	2.50	3.32	3.88
	2.27	3.17	3.15
	2.09	3.12	3.16
	2.93	3.00	2.97
	1.91	2.95	2.87
	1.87	2.89	2.76
	1.60	2.63	2.53
		2.55	2.48
		2.50	2.46
		2.48	2.26
		2.11	2.04
		1.93	1.96
		1.80	**1.90**
		1.68	1.85
		1.48	1.77
			1.76
			1.50

Table 5.1.4 FTIR Spectroscopy Results for Laponite Dehydrated at Various Temperatures

	Firing Temperature of Laponite	
	DE 400	DE 800	DE 1300
IR Vibrational Frequencies/cm^{-1}		1130 sh	1160 sh
		1079 vb	1071 vb
		1012 m	1012
		975 sh	941
		932 sb	899
		893 m	855
		852 vs	
		795	760 -70 sh
		730	737]db
		725	724
		692 m	683
		680 sh	648
		650	580 sh
		580 sh	545
		549	512
		509	483
		481	460
		461	432
		430-405 sh	

5.2.3 ^{29}Si NMR Data

^{29}Si MAS NMR results are collected in table 5.1.1 for the series of dehydrated laponite samples (DE200 to DE1300), and the spectra are shown in figs. 5.1.1 and 5.1.2. Before discussing these results it will be instructive to begin by considering the spectrum of laponite at room temperature. The laponite spectrum (fig. 5.1.A) consists of two distinct peaks located at -84.1 ppm and -93.6 ppm relative to TMS. Using the Q^m notation proposed by Englehardt[93] these peaks are assigned to Q^2 and Q^3 type silicons respectively; where Q^2 means a silica tetrahedron connected to two other SiO_4 tetrahedra via bridging oxygens and two non-bridging oxygens. This assignment is valid because the laponite unit cell consists of silicons coordinated by four oxygen atoms and linked to three other silicons in two dimensions (hence the Q^3 assignment). The fourth and hence non-bridging oxygen is either linked covalently to the octahedral layer, or is a hydroxyl group. The Q^2 assignement is also valid because such units arise only at the broken edges of laponite unit cells. Hence silicons at exposed crystal edges are linked to two SiO_4 tetrahedra and have two non-bridging oxygens.

The relative intensities of the two silicon peaks also provide useful information in that the peak due to Q^3 silicon sites (-93.6 ppm) is ten times more intense than the Q^2 peak. Hence Q^3 sites in laponite are about ten time more numerous that Q^2 sites, a fact which can be ascertained from the unit cell structure of laponite which shows that Q^2 sites only occur at broken edges of unit cells. It occurred to us that the relative intensity of the Q^2/Q^3 sites could give an indication of the average size of clay particles in different layer silicates. For example in related clay minerals such as talc or montmorillonite, since the Si-O bond length and angles are not expected to vary, it is possible that the relative proportions of Q^2 and Q^3 sites can give at least a qualitative estimate of the size of unit cells. Both Q^3 and Q^2 sites however, are found to increase by about 2 ppm relative to that of room temperature laponite. The more shielded ^{29}Si resonance can be attributed partly to the Li^+ ions. At elevated temperatures the Li^+ cations become mobile and easily leave their octahedral sites and diffuse throughout the clay lattice. The linewidth of DE200 increases by about 150Hz compared to laponite.

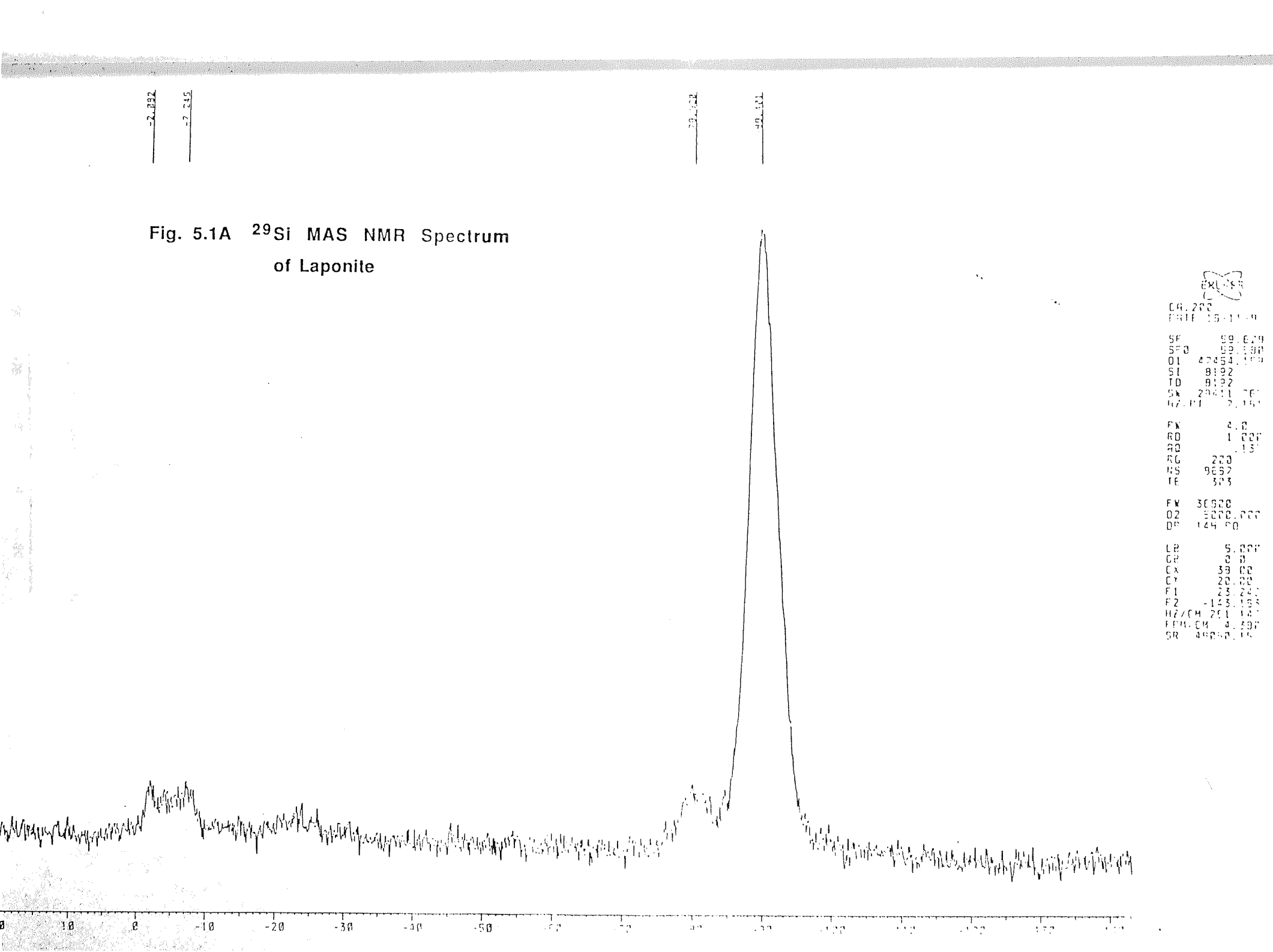

Fig. 5.1A ^{29}Si MAS NMR Spectrum of Laponite

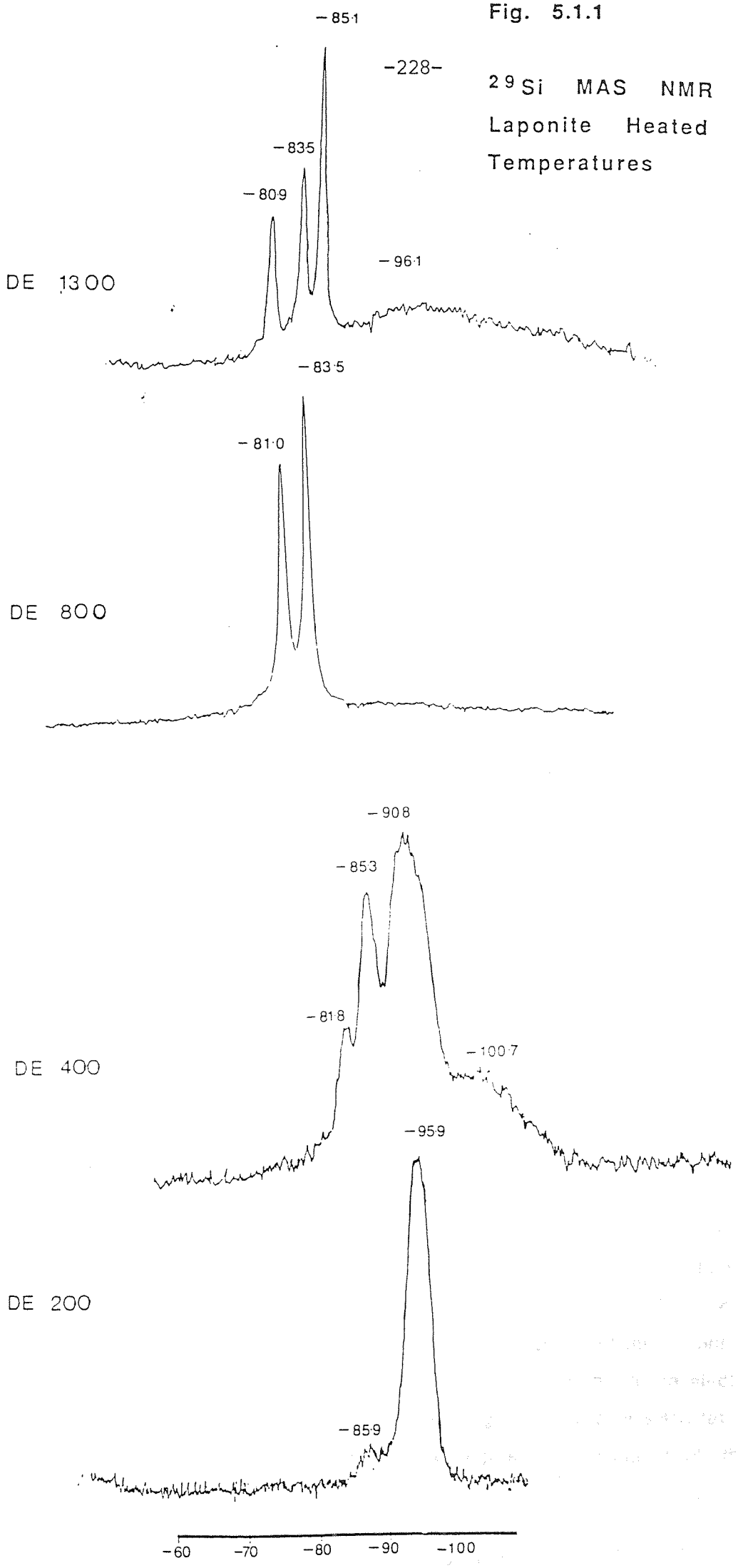

Fig. 5.1.1

^{29}Si MAS NMR Spectra of Laponite Heated at Various Temperatures

The ^{29}Si spectrum of laponite fired at 400°C (DE400) shows marked changes from the previous two samples. At least three broad overlapping peaks and a shoulder are observed. The linewidth increases almost five fold to about 1000Hz. The overlapping peaks and large linewidth indicate more disorder throughout the clay structure as well as a greater distortion of Si-O bond lengths and bond angles in the silicate network. The most intense peak at -90.8 ppm corresponds to the Q^3 sites of the silicate tetrahedral layers, but the shift value implies that the silicon atoms are more deshielded than normal trioctahedral tetrahedra.

Another point of interest which arises from the ^{29}Si NMR spectrum of laponite is the chemical shift value recorded for the Q^3 silicons (-93.6 ppm). Laponite has a structure similar to that of its 'parent' mineral talc, except that talc has neither aluminium nor lithium atoms in the octahedral layer. Instead talc contains only octahedrally coordinated magnesium and hence, since all the octahedral sites are occupied by Mg^{2+} cations there is no layer charge on the octahedral sheets. The ^{29}Si NMR spectrum of talc shows a Q^3 silicon resonance at -98 ppm relative to TMS[52]. The shift value for laponite is about 4.5 ppm deshielded with respect to talc. It should be remembered at this point that laponite has no detectable Fe^{2+} or Al^{3+} cations present. Nevertheless, Weiss et al[90] and Kinsey et al[50] have recorded different chemical shifts for slightly different forms of hectorite. Weiss and co-workers recorded a ^{29}Si shift of -94.2 ppm for hectorite which contained no Al(4) but had a small amount of Fe^{2+} substituted for Li/Mg in the octahedral layer. Kinsey et al recorded a ^{29}Si shift of -95.2 ppm for a hectorite sample containing Al (4) substituted for Si^{4+} in the tetrahedral layer, but which had no iron impurities in the octahedral layer.

For each of the above mentioned trioctahedral clays, the only differences are in the occupancy of the octahedral sheet by different cations, and these appear to have quite substantial effects on the ^{29}Si chemical shifts. The differences can be related to the different polarising power of the cations involved, or in more quantitative terms they can be related to the electronegativity values of the other cations to which the oxygen atoms of a silica tetrahedron are co-ordinated[90]. This in turn affects the degree of hybridisation of the oxygen

bonding orbitals[94]. Based on simple quantum mechanical calculations which take into account the paramagnetic contribution, the chemical shift becomes more shielded (more negative) as the cation electronegativity (EN) is increased.

This relationship has been expressed as[90]

$$\delta = - a\,EN + b$$

where δ = ^{29}Si chemical shift and a + b are empirical parameters.

For minerals which have a fixed octahedral occupancy such as the tricoctahedral minerals talc, laponite and hectorite (which have three), atom for atom substitution of an element with lower electronegativity should cause a corresponding deshielding at Si. Now because Mg^{2+} (EN = 1.2) is more electronegative than Li^{+} (EN = 1.0), one-for-one subsitution of lithium for magnesium in any octahedral mineral should cause a certain amount of deshielding at Si. Our results are highly consistent with this prediction since one-for-one substitution of Li for Mg ie talc versus laponite causes 4.5 ppm deshielding.

If we apply the same argument to the differences between synthetic (laponite) and natural hectorite, a similar conclusion can be reached. For example, consider the hectorite sample which has a small amount of Fe^{2+} in the octahedral layer. Fe(EN = 1.64) has a larger electronegativity than either Li or Mg and therefore causes more shielding at Si, and hence the more shielded value for this hectorite at -94.2 ppm.

The ^{29}Si spectrum of laponite fired at 200°C (DE200) shows that relatively little change occurs to the overall silicate network. Two distinct silicon peaks are present due to Q^2 and Q^3 sites as before, and their relative intensities are unchanged. The chemical shift of both Q^3 and Q^2 sites however is found to increase by about 2 ppm relative to that of room temperature laponite. The more shielded ^{29}Si resonance at -95.9ppm (an increase of -2.3 ppm) is attributed to the lithium cations. The linewidth increase by about 150Hz over the laponite spectrum. For laponite heated at 400°C (DE400) the ^{29}Si NMR spectrum shows marked changes from the previous two samples. At least three broad overlapping peaks and a shoulder are observed. The linewidth increases almost fivefold to about 1000Hz. The overlapping peaks and larger linewidth indicate greater disorder throughout the clay structure and as well as a greater distortion of Si-O bond lengths and bond angles in the in the silicate network. The most intense peak at -90.8 ppm corresponds to the Q^3 sites of the tetrahedral silica sheets, but the chemical shift value implies that the silicon atoms are more deshielded that those of the Q^3 silicons in untreated laponite. The Q^2 peak at -85.3 ppm is probably due to exposed crystal edges but the Q^3/Q^2 ratio is no longer 10:1 but 4:3. In other words the relative number of Q^3 sites is reduced. A rather simplistic explanation can be made in terms of the increased thermal vibrations at 400°C leading to the fracturing of the silicate sheets and to more disilicate or middle chain groups being exposed. Although not particularly compelling, in the absence of more assertive data, this remains in our view, a valid argument.

The ^{29}Si spectrum of laponite heated at 600°C consists of a single relativity broad and asymmetrical resonance with a peak maximum at -97.7 ppm. The asymmetry of the spectrum suggests that a lack of spectral resolution is preventing us from seeing any phases which may be present. The chemical shift at -97.7 ppm is assigned to Q^3 silica units but the silicon atoms are obviously much more shielded that in the previous samples. The chemical shift changes of the Q^3 resonance peak with increased temperature can be attributed to two possible sources. Firstly and probably more importantly to the diffusion of small cations[96] such as Li^+ and H^+ throughout the clay sheets and secondly to a certain amount of structural distortion of the crystallographic clay units.

Fig 5.1.2 ^{29}Si MAS NMR Spectra of Rehydrated Laponite Samples

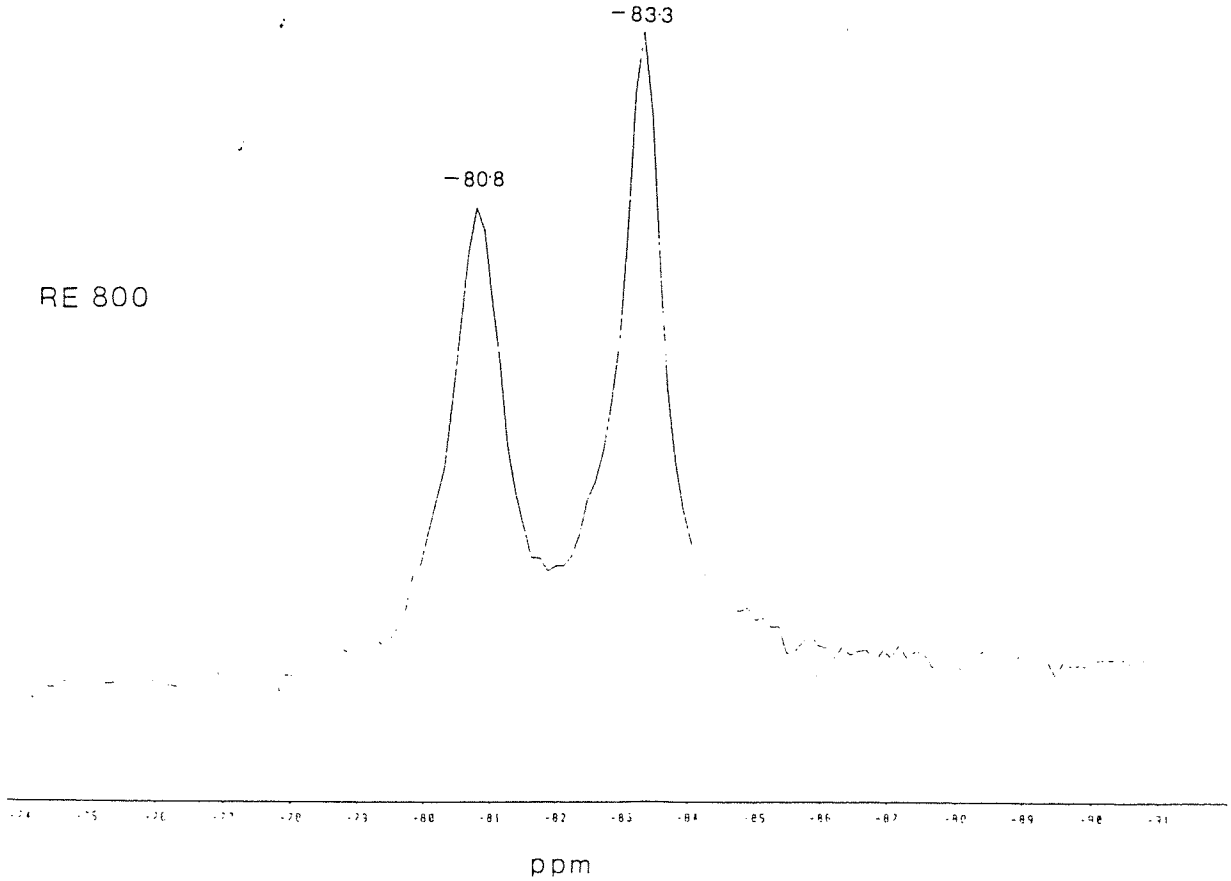

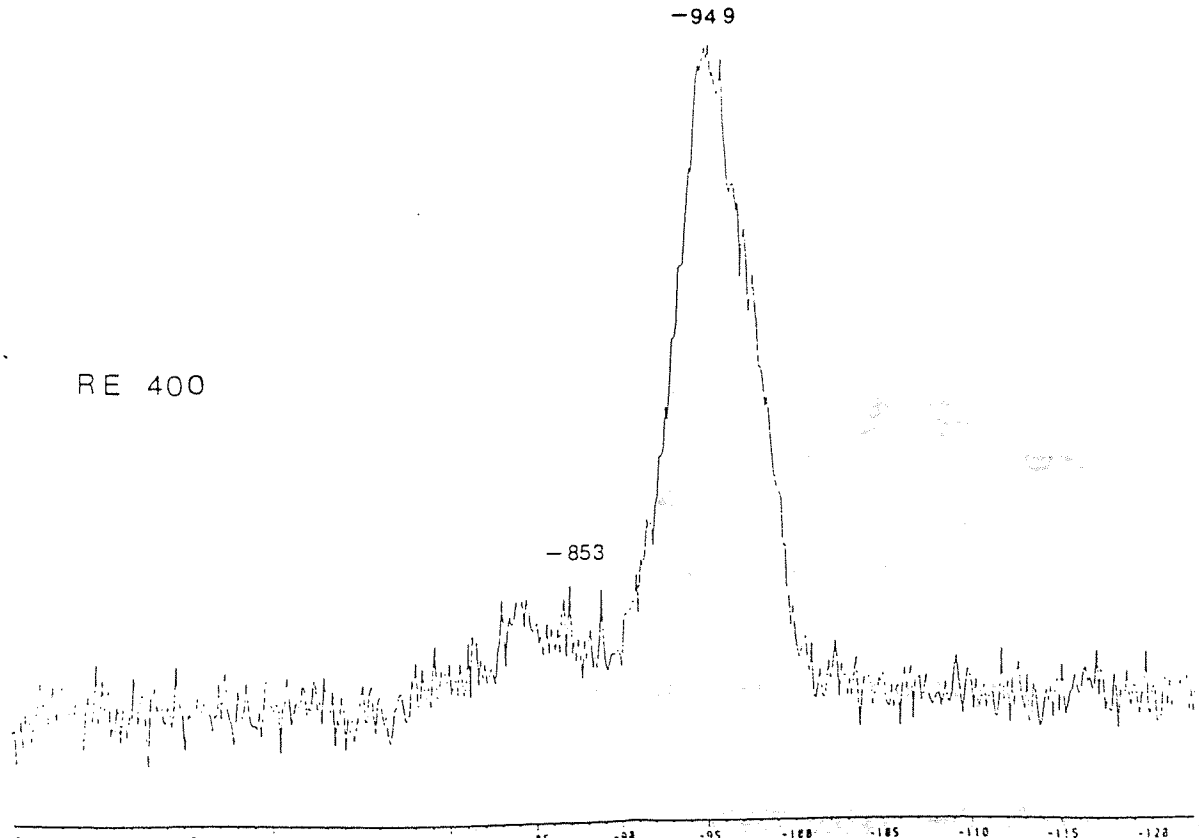

deshielded (ie less negative by -2.8 ppm with respect to room temperature laponite) at -90.8 ppm. It is our view that the chemical shift value, although it qualifies for a Q^3 silica resonance, cannot be justified in terms of the previous argument. However, it should be noted that the excessive linewidth of the spectrum (>1000Hz) reflects some of the changes occurring to the interlayer water and interlayer cation hydration spheres as a result of heating at 400°C. These in turn may affect the silicon resonance in tetrahedral sheets although the exact details are difficult to establish with the current data.

At 800°C (DE800) significant changes are seen to occur in the ^{29}Si NMR spectrum. Two sharp peaks at -81.0 ppm and -83.9 ppm are observed, arising from crystallographically distinct Q^2 silicon sites. Both peaks are assigned to middle chain groups, most probably to those of the pyroxene mineral enstatite which is known to be the main product in topotactic reactions (at 800°C) of trioctahedral minerals. The relative intensity of the peaks is in the ratio 2:3 respectively. The intensity values ^{+29}Si chemical shifts are in agreement with those obtained by Lippmaa et al[47] and Oldfield et al[44]. The assignment can be clarified by considering the structure of enstatite. The structure of orthorhombic enstatite is shown below, illustrating the three-dimensional nature of the crystal.

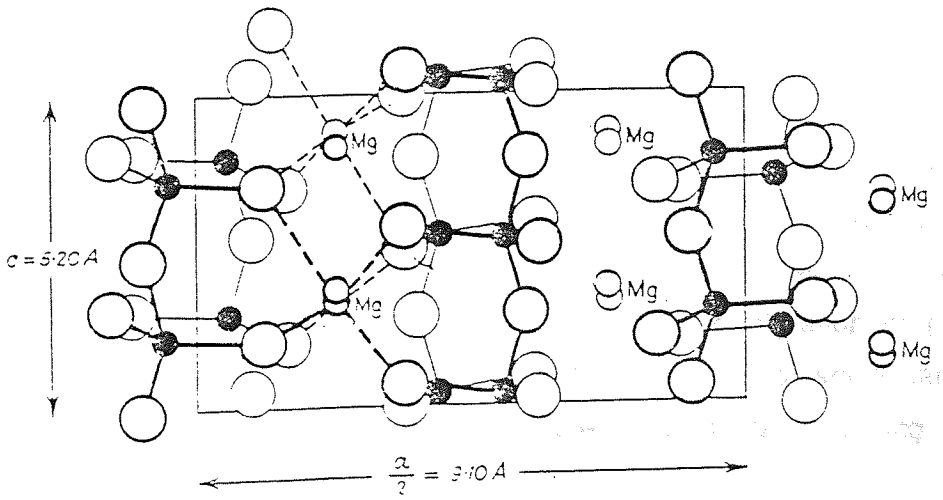

Fig 5.1.3 Diagramatic Sketch of Enstatite ($MgSiO_3$)

We shall consider first of all, the former of the two possible causes, namely that of cation diffusion[96]. Heating laponite to 200°C results in a diamagnetic shift of 2.3 ppm from -93.6 ppm to -95.9 ppm, indicating that the Q^3 silicons become more shielded. Some lithium ions present in the octahedral layer become mobile and due to their small radii, are able to diffuse through the octahedral and silica sheets into the interlayer regions of the clay. By diffusing out of their original sites a residual negative charge is left which is delocalised througout the octahedra sheet. Once in the interlayer region the lithium ions become associated with interlayer water molecules, and unlike sodium ions, are able to polarise the water molecules and split off protons. The protons may then diffuse back into the octahedral layer and thereby partly neutralise the negative charge. However, a certain amount of negative charge would still remain with the octahedral sheet : this would then lead to more electron density being associated with the Q^3 silicons bonded to the octahedral layer. The increase in electron density around a ^{29}Si nucleus is manifested as greater shielding and a diamagnetic shift of -2.3 ppm.

The stronger diamagnetic shift observed for laponite heated at 600°C is explained in similar terms. At 600°C most of the interlayer water would be expected to be lost, thereby eliminating a mechanism whereby protons could be formed. Nevertheless Li^+ ions are still expected to leave their octahedral sites and migrate towards the interlayer region leaving a negatively charged octahedral layer. No protons are present to neutralise this residual charge and therefore the ^{29}Si resonance is more strongly shielded due to the increase in electron density around the silicon nuclei. It should be remembered, however, that although Li^+ ions may diffuse into other regions of the clay, the overall charge on the clay particles remains the same. The absence of interlayer water at temperatures above 500°C has been confirmed by other workers using ^1H MASNMR[96]. If we follow the above argument then the observed linewidth increases up to 600°C may be correlated with the migration of protons and lithium ions throughout the clay lattice. The presence of small cations in the vicinity of the silicon nuclei would be manifested as a linebroadening.

The ^{29}Si chemical shift for laponite at 400°C however, appears to be anomalous if the above argument is accepted. This time the ^{29}Si chemical shift is

Magnesium ions are in six-fold co-ordination with oxygen and link together four chains. The top two chains have silicon atoms at positions 65 and 85 above a zero plane. The lower two have silicon atoms at positions 15 and 35. The uppermost chain has its vertices lying in an opposite direction to those in the lower chain. Hence there are two sets of equivalent silicons and therefore give rise to two distinct Q^2 silicon sites.

For laponite fired at 1300°C (DE 1300) the NMR spectrum consists of three sharp peaks each with a linewidth of less than 50Hz, and a broad silicate phase in the -92 to -96 ppm range. The two crystallographically distinct peaks at -80.9 ppm and -83.5 ppm with a ratio of 2:3, are assigned as before to enstatite. The sharp peak at -85.1 is assigned to the mineral orthoenstatite (or clinoenstatite) which is a high temperature form of enstatite[44]. This peak cannot be due to Q^2 silicons at exposed crystal edges because its linewidth is too sharp and it is the most intense peak. The very broad component at -92 to -96 ppm is probably due to residual silica. Its broadness suggests that it could be due to a glassy amorphous phase containing lithium ions, since lithium is the only glass forming element present in laponite.

^{29}Si NMR spectra for the rehydrated samples (RE200 to RE800) show only minor differences from those of the dehydrated samples. The spectra on the whole have broader linewidths by approximately 2 to 300 Hz. The chemical shift values are only slightly shifted by about 2 ppm in each case. No major changes in the lineshapes are observed except for RE400, where the previously distinct ^{29}Si peaks are lost and a spectrum similar to RE200 is observed.

5.2.4 ^{23}Na MASNMR Data

Fig. 5.1.3 shows the ^{23}Na MAS NMR spectra of the dehydrated and rehydrated laponite samples. Since ^{23}Na has a quadrupole moment the linewidth of the central line is broadened mainly by second order quadrupole interactions reflecting the co-ordination symmetry of the Na^+ ion [42]. The spectrum for room temperature laponite consists of a narrow central resonance line (with linewidth of 1200Hz and chemical shift of -15.3 ppm relative to NaBr) flanked

on one side by a broad shoulder. As laponite is successively dehydrated the ^{23}Na line position shifts to -19.5 ppm for DE200 and DE400, and -18.5 ppm for DE600. for DE800, however, there is a slight decrease in chemical shift to -17.5 ppm. The linewidth changes follow a similar trend. Room temperature laponite has a linewidth of 1.2KHz but for dehydrated samples the linewidth almost doubles to about 2.2KHz and remains constant until 800°C. Lineshapes for the dehydrated samples are also fairly similar - spinning sidebands are only observed for samples DE600 and DE800.

The sodium ions in room temperature laponite are surrounded by one monolayer of water molecules; the chemical shift value of -15.3 ppm is therefore indicative of this particular co-ordination state. Dehydrating the clay even at relatively low firing temperatures as 200°C for four hours means that the co-ordination state of the Na^+ ions is upset as the essentially dipolar association between Na^+ ions and water molecules is broken. At higher temperatures interlayer water is completely removed. The constancy of ^{23}Na lineshapes, linewidths and chemical shifts between DE200 and 600°C indicates that Na^+ ions occupy similar sites, probably close to the cavities in the silica sheets and that the co-ordination state is similar.

For the rehydrated clays, the ^{23}Na lineshape linewidth and chemical shift all show a markedly different trend. The linewidth for RE200 is very broad (=5.8KHz) and the ^{23}Na signal has a very assymetrical lineshape with spinning sidebands. Surprisingly, however, RE400 and RE600 have relatively sharp resonances with a much reduced linewidth (=1KHz) and no spinning sidebands. This lineshape is symmetrical. The spectrum of RE800 shows an asymmetrical lineshape with many sidebands and a linewidth of 2.95KHz. The chemical shift for RE200 is 19.4ppm which is very similar to that of the dehydrated clay DE200. For RE400 and RE600 the chemical shift is seen to fall dramatically to -8.8 to -9.6 ppm, but for RE800 it rises to -13.7ppm.

From these observations it appears that all three NMR parameters, linewidth, lineshape and chemical shift reflect the coordination symmetry of the Na^+ ions[53]. It is clear that the Na^+ ions occupy different sites and have different coordinations depending on thermal treatment and subsequent rehydration. For

Fig. 5.1.3 ^{23}Na MAS NMR Spectra of Dehydrated and Rehydrated Laponite Samples

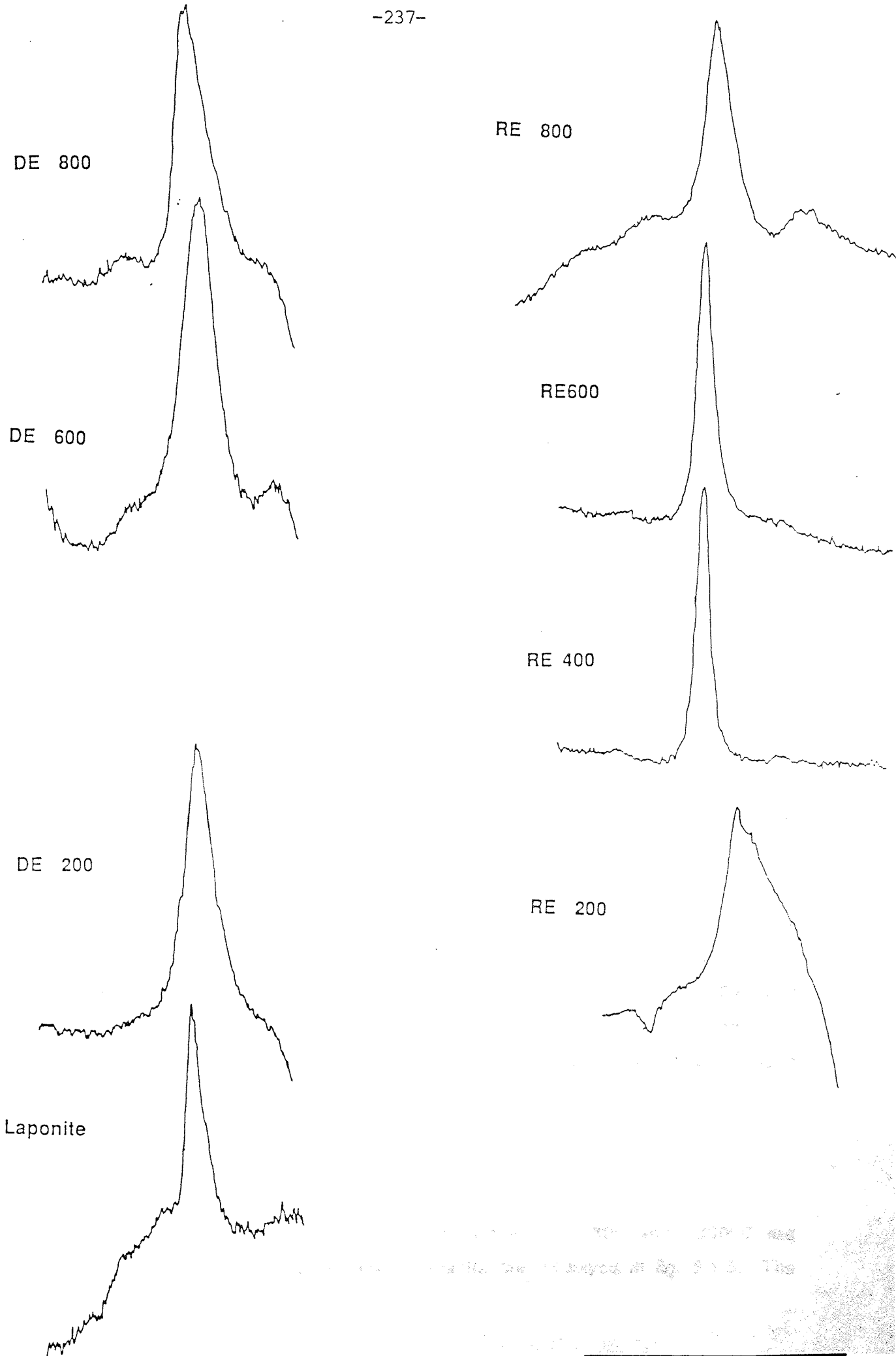

example RE200 gives a broad ^{23}Na NMR signal (5.8KHz) with a chemical shift similar to that of dehydrated clay DE200. Hence the symmetry of sodium ions near the cavities in the silica sheets is distorted by incoming water molecules. The clay interlayer region is forced apart by rehydration, but the Na^+ ions do not fully recover their previous coordination symmetry (as in room temperature laponite). Samples RE400 and RE600 though, appear to have recovered some sort of symmetry as indicated by relatively small linewidths and very symmetrical lineshapes. Here, it is likely that sodium ions are surrounded by more than one layer of water, making them very mobile. This explains the lack of distortion and broadening of the central resonance line and lack of spinning sidebands. the mobility of the Na^+ ions would reduce the quadrupolar interactions giving rise to such line broadening effects. For RE800 the Na^+ ions appear to have only partly recovered their symmetry. The lineshape and linewidth imply a similar coordination to Na^+ in room temperature laponite.

5.2.5 X-Ray Diffraction Data

X-Ray diffraction results, in the form of d-spacing values are summarised for the dehydrated laponite samples DE400, DE800 and DE1300. For sample DE400, the diffraction peaks could not be fitted to those of any mineral phase including Laponite itself. This confirms the findings from the ^{29}Si NMR results which indicate a highly disordered phase with no crystalline entity. In contrast, the clays fired at 800°C and 1300°C give d-values which correspond to the principal reflection peaks of enstatite. In addition DE1300 also shows evidence for the formation of clinoenstatite, which is also in broad agreement with the NMR results. Notably in DE800 there are peaks with d-values of 3.16, 2.86 and $1.40A^0$ corresponding accurately with the powder diffraction file data for enstatite, and in DE1300 d-values of 3.16, 2.87 and $1.50A^0$ which correspond to those of clinoenstatite.

5.2.6 Infra-Red Data

The infra-red results for laponite dehydrated at 400, 800 and 1300°C are summarised in table 5.1.4 and the i.r. spectra are displayed in fig. 5.1.5. The i.r.

spectra of laponite dehydrated at 800°C and 1300°C are different from those of DE400. The spectrum of DE400 showed the broad strong absorption band due to the silicate lattice vibrations normally observed for 2:1 layer silicates. In the layer silicates the SiO_4 tetrahedra are linked by sharing three of the four oxygens thereby forming sheets with a hexagonal network and a unit cell composition of $Si_2O_5^{2-}$. The spectrum of DE400 exhibits certain absorption bands which arise from a $Si_2O_5^{2-}$ lattice, for example, the very broad band centred at 1014cm^{-1} due to Si-O stretching mode, plus a strong band at 475cm^{-1} due to Si-O bending vibrations in the $Si_2O_5^{-}$ lattice. The presence of these bands alone indicates that there is no fundamental change in the clay lattice structure.

However, for laponite fired at higher temperatures, DE800 and DE1300, the i.r. spectra show no similarites with the DE400 spectrum. The high frequency range consists of a number of strong, sharp absorption bands. Particularly prominent is the appearance of sharp bands at 975, 932, 893 and 852cm^{-1} in DE800 and 941, 899, 855 in De1300. These are attributed to Si-O$^-$ or $^-$O-Si-O$^-$ stretching frequencies; in other words to the presence of non-bridging oxygens[104]. The ^{29}Si NMR results strongly suggest the formation of a Q^2 type chain silicate and of enstatite to be exact. The i.r. results are in agreement with the NMR results as a number of absorption bands can be assigned to those of enstatite in DE800. According to Gadsden[97] and Saksena[99], the i.r. spectrum for enstatite shows diagnostic bands at 1070-56cm^{-1} 1020 - 10cm^{-1} plus a sharp band at 942-28cm^{-1} which are assigned to the triply degenerate ω_3 frequency ie the motion of silicon against the oxygen atoms along the three axes of the pyroxene chain. Our own results agree well: we observe a shoulder at 1130cm^{-1}, a broad strong band at 1079cm^{-1}, 1012cm^{-1} and a sharp band at 932cm^{-1}. Other diagnostic bands are at 505 and 460cm^{-1}, attributed to Si-O$^-$ bending vibrations. We observe similar bands at 509cm^{-1} and 461cm^{-1}.

The i.r. spectrum of DE1300 shows evidence for the presence of a mixture of enstatite and clinostatite. Diagnostic bands for clinoenstatite are cited by Gadsden[97] at 1160(sh) 1012(s), 899(s) a doublet at 737cm^{-1} and 724cm^{-1}, and a weak band at 683cm^{-1}. In DE1300 bands of similar intensity are recorded at

Fig. 5.1.5
FTIR Spectra for Laponite
Fired at 400, 800 & 1300°C

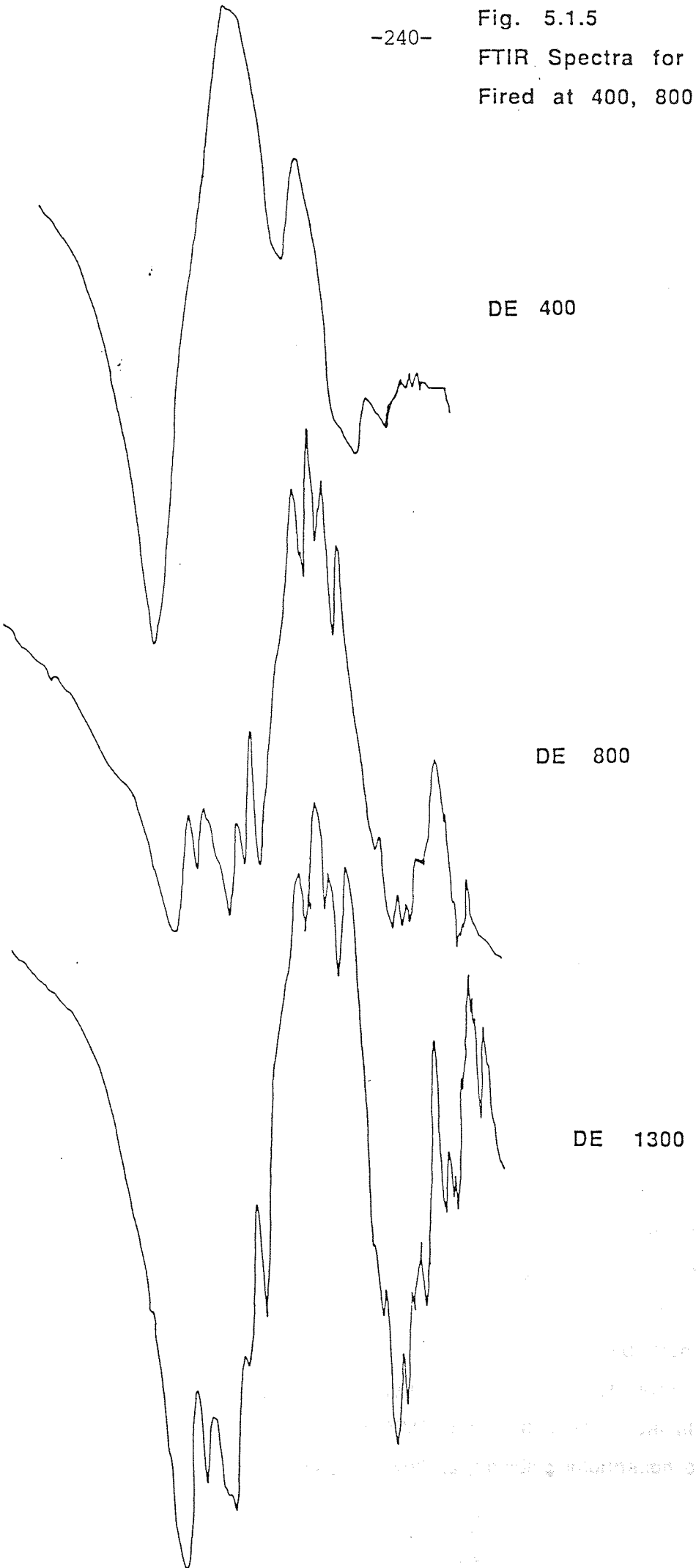

1152(sh), 1012(s), 900(s), a doublet at 737 and 725cm^{-1} plus a weak band at 684cm^{-1}.

5.2.7 Conclusions

^{29}Si MAS NMR proved to be a sensitive and versatile technique for studying the topotatic reactions of the synthetic smectite clay, laponite. The NMR results clearly show that at temperatures above 800°C the laponite structure breaks down and enstatite is formed. At 1300°C a certain amount of clinostatite is also formed in addition to enstatite. Thus the evidence leads us to speculate that at firing temperatures above 800°C there is a reorganisation of cations within the largely constant framework of oxygen anions, yielding maximum enstatite and a residual lithium silicate phase which is detected as a broad Q^3 phase by ^{29}Si NMR. If we assume that the ^{29}Si NMR method is able to detect all the ^{29}Si atoms, then by comparing the relative intensities of the ^{29}Si peaks we can postulate the following non-equilibrium reaction to occur:

$$\underset{\text{Laponite}}{(Mg\ Li)\ Si_4O_{10}(OH)_2} \xrightarrow{800^\circ C} \underset{\substack{\text{Enstatite}\\ 95\%}}{MgSiO_3} + \underset{\substack{\text{Lithium disilicate}\\ 5\%}}{Li_2Si_2O_5}$$

and:

$$(Mg\ Li)Si_4O_{10}(OH)_2 \xrightarrow{1300^\circ C} \underset{\substack{50\%\\ \text{Enstatite}}}{MgSiO_3} + \underset{\substack{40\%\\ \text{Clinoenstatite}}}{MgSiO_3} + \underset{10\%}{Li_2Si_2O_5}$$

The XRD and i.r. results broadly agree with the NMR results although the usefulness of these techniques is limited by the presence of slight impurities and the presence of other compounds. X-Ray reflection peaks and i.r. absorption bands often strongly overlap and have reduced or enhanced intensities. NMR on the other hand, is not greatly affected by the presence of more than one phase as it is a bulk technique. In fact, NMR allows at least a qualitative estimate of the amount of products formed, as well as providing information on the local

environments of silicate tetrahedra. ^{29}Si NMR was less was less effective in studying the rehydration of laponite. Chemical shifts were only slightly altered by the rehydration process. This was not surprising as no change in the silicate lattice had taken place. ^{23}Na MAS NMR however, proved to be a sensitive indicator for studying the coordination of Na^+ ions present in the interlayer region of laponite. Changes in the lineshape, linewidth and chemical shift were observed for each stage of dehydration and rehydration.

5.3 A ^{29}Si NMR STUDY ON THE EFFECT OF FIRING TEMPERATURE ON A CONSTANT COMPOSITION MODEL CERAMIC GLAZE

5.3.1 Experimental

Laponite (5g) was mixed with an equivalent (100%) molar ratio (based on SiO_2 content of the clay) of calcium carbonate until an homogenous powder was obtained. The powder was transferred to a porcelain crucible and fired in a carbolyte furnace at 400°C for three hours. After firing, the crucible was removed from the furnace, covered with a lid and placed in a vacuum desiccator overnight, before finally grinding to a fine powder. The procedure was repeated using indentical mixtures of laponite and calcium carbonate but at a range of different firing temperatures up to 1300°C.

5.3.2 Results and Discussion

Table 5.2.1 ^{29}Si NMR Results for the Model Glaze Laponite + CaO (100mol%) Fired at Various Temperatures

	Q_0		Q1		Q2		Q3		Linewidth
	δ	I	δ	I	δ	I	δ	I	Δν/Hz
Laponite	-	-	-	-	-84.1	(9%)	-93.6	(91%)	230Hz
Lap 400°C	-	-	-	-	-	-	-96.7	(100%)	195Hz
Lap 500°C	-	-	-	-	-	-	-95.8	(100%)	270Hz
Lap 600°C	-	-	-81.8 -79.6	(11%) (3%)	-89.2 -85.3	(20%) (28%)	-99.6 -93.8	(10%) (28%)	≈740Hz
Lap 700°C	-	-	-79.6	(25%)	-	-	-93.8	(75%)	100Hz,250Hz
Lap 800°C			-79.4	(55%)	-	-	-	-	50Hz,45Hz
Lap 900°C	-	-	-79.4	(55%)	-	-	-	-	50Hz,45Hz
Lap 1000°C	-	-	-81.1 -73.8	(31%) (8%)	-84.7 -83.5	(23%) (38%)	-	-	<50Hz
Lap 1300°C	-66.3 -62.2	(7%) (7%)	-72.3	(86%)	-	-	-	-	-50Hz

δ = Chemical Shift (ppm^{-1}) I = Relative Signal Intensities (% of sum of peak values)

Table 5.2.3 FT IR Results for the Modelled Ceramic Glaze Laponite + CaO (100mol%) Fired at Various Temperatures

IR Vibrational Frequencies cm^{-1}

Lap 400°	Lap 500°	Lap 600°	Lap 700°	Lap 800°	Lap 900°	Lap 1000°
3648	3677w	3679	3643vw	3642vs	3642vs	1637
3648	3417b	3469vb	3647b	3436	3441	1474
2982	2924w	2982	2924	2513	1636	1422
2887	2874m	2874	2874	1800	1477	1155
2660	2600sh	2600sh	2600sh	1590sh	1422	1121
2512	2513	2513	2513	1512sh	1077	1077
1800	1800	1800	1800	1418	1041	1011
1418	1422vb	1422vs	1422vs	1130	982	987
1014	1022	1027		1074	883	921
875	876	875	875	1008	724	900
				929	402	889
712	713	713	713	877		880sh
657	669	674	676sh	740sh		865sh
445	469	469sh	469	713		
				680-95		849
				646		724
				600-400		67

5.3.3 ^{29}Si MAS NMR Data

^{29}Si MAS NMR spectra for the ceramic glazes fired in the temperature range 400 to 1300°C are illustrated in fig. 5.2.1 and 5.2.2 and the ^{29}Si NMR parameters are recorded in table 5.2.1. ^{29}Si chemical shifts cover a range from -62ppm to -99.0 ppm. Distinctly different peaks are observed at each firing temperature implying that different phases may be formed depending on the firing temperature.

The ^{29}Si spectra for the model glazes fired at 400°C and 500°C (designated lap 400 and lap 500) both exhibit single peaks at -96.7ppm and -95.8ppm respectively. Both peaks are assigned to Q^3 type silicate tetrahedra. Whereas laponite alone (at room temperature) spectrum gave rise to a small proportion of Q^2 sites, these are not observed in the calcium- oxide containing glazes fired at 400°C and 500°C, a fact which may be due to the larger linewidths of the glaze spectra which tend to "absorb" the Q^2 peak. The chemical shift of lap400 is shifted by -3.3ppm upfield ie the Q^3 silicon sites are more shielded by about -3.3ppm relative to TMS. At 500°C, however, the chemical shift value drops back slightly to -95.8ppm. The diamagnetic shift of -3.3ppm can be envisaged in terms of the increased mobility of Li^+ (and possibly Mg^{2+}) ions which are able to diffuse throughout the lattice due to their small sizes. The slight variations in chemical shift are probably due to distortions of Si-O bonds which in turn affect the electron density on the oxygens of the silicate tetrahedral units. Nevertheless the results imply that no structural change involving Si-O bond breaking occurs to the Q^3 network at 400 and 500°C.

The NMR spectrum of the glaze fired at 600°C (lap 600) shows substantial changes from the previous spectra. Five distinct but overlapping peaks are observed ranging between -79 and -99.6ppm. As all the peaks are strongly overlapping it is difficult to measure the linewidth of individual peaks, so that the overall linewidth was at about 740 Hz (which is almost three times the linewidth of room temperature laponite). The two peaks at -79.6 and -81.8ppm with relative intensities of 3% and 11% are assigned to Q^1 type silicon sites. Peaks at -89.2ppm and -85.2ppm, with relative intensities of 20% and 28% are assigned to Q^2 units; the peak at -93.8ppm is assigned to Q^3 units and the rather

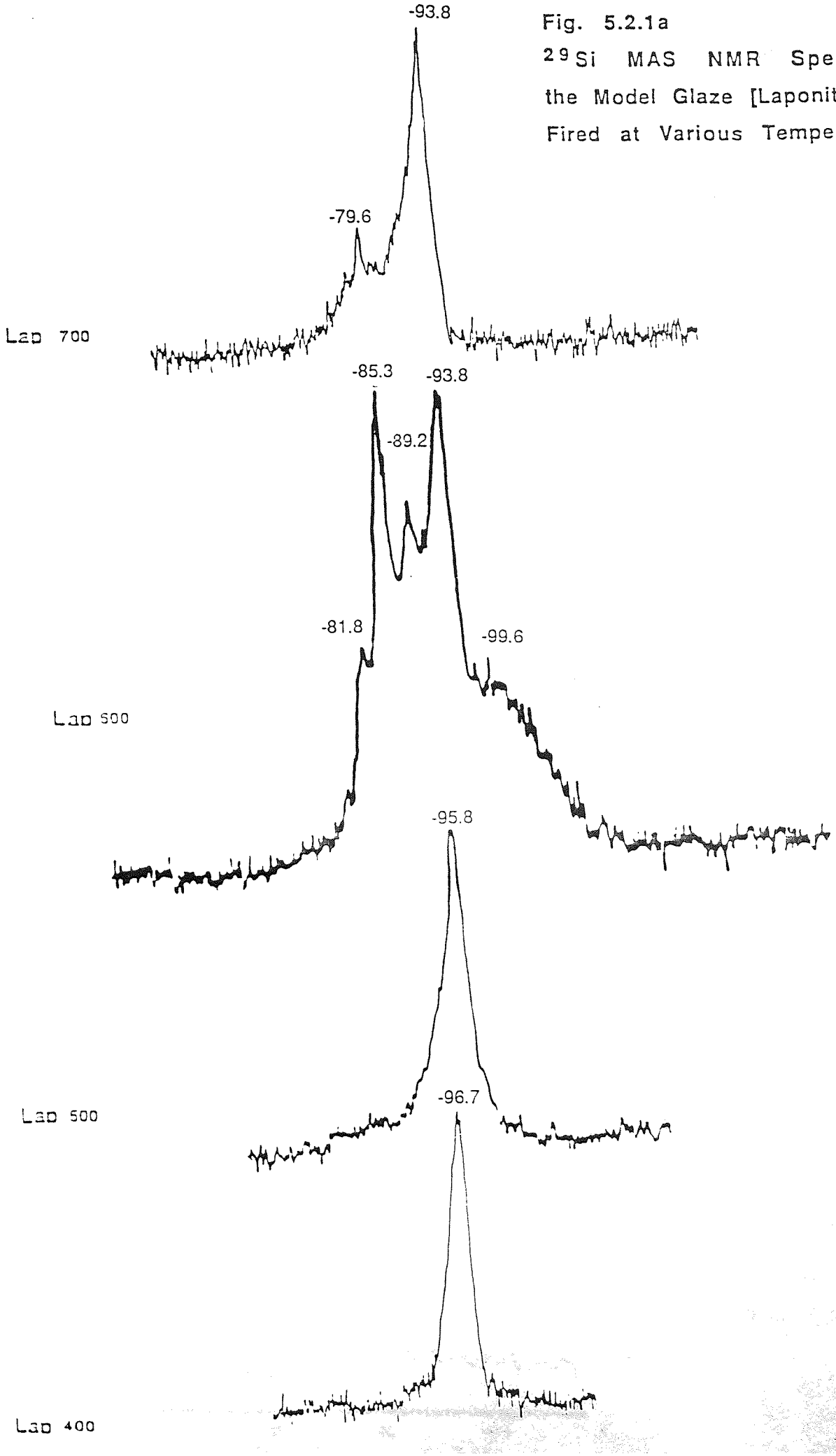

Fig. 5.2.1a
^{29}Si MAS NMR Spectra for the Model Glaze [Laponite + CaO] Fired at Various Temperatures

Fig. 5.2.1b
^{29}Si MAS NMR Spectra for the Model Glaze [Laponite + CaO] Fired at Various Temperatures

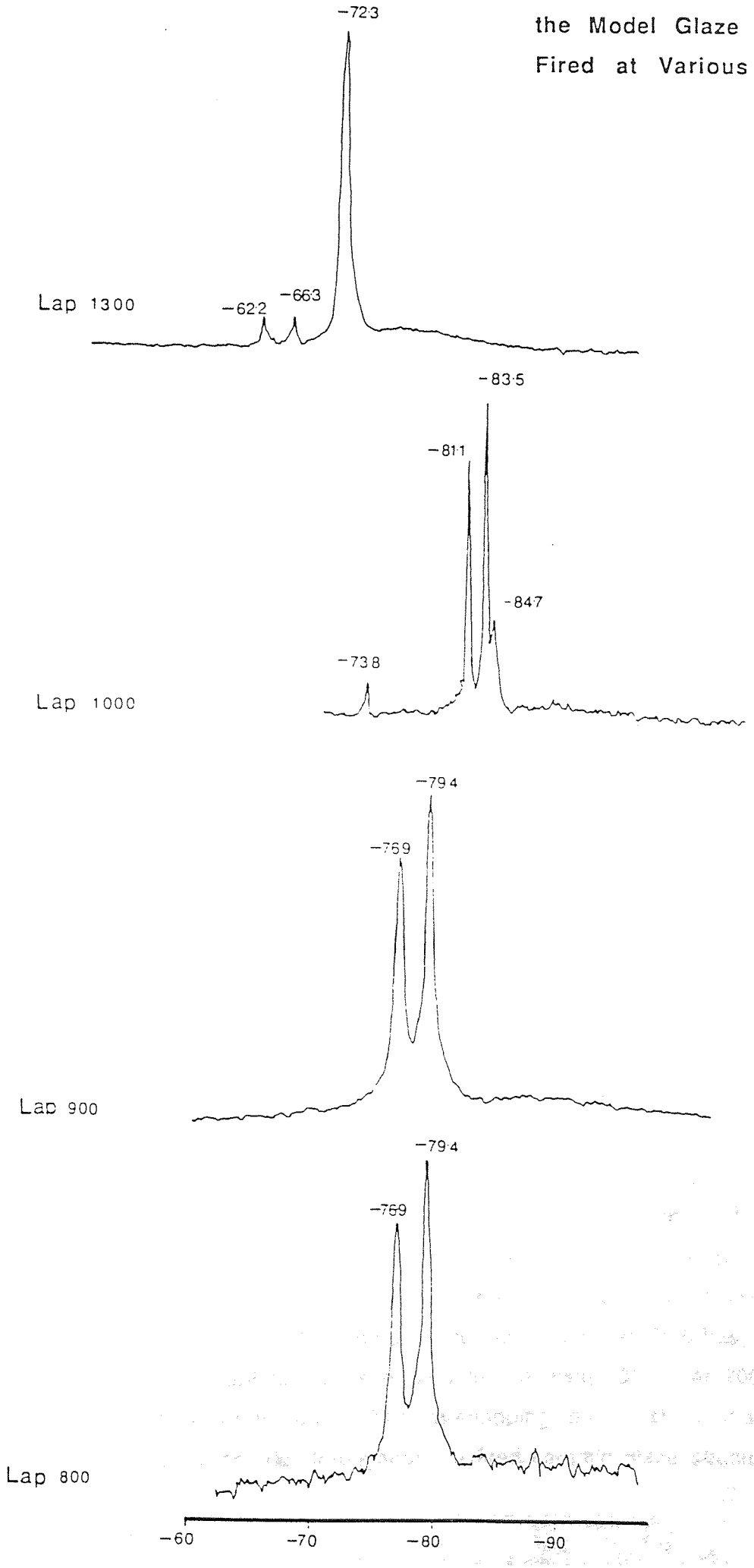

broad component centred at -99.6ppm is attributed to Q^3/Q^4 amorphous silica phase. Although the Q^3 units due to the tetrahedral silica sheets are still retained, their relative intensity is reduced as a variety of other silicon sites begin to appear. The relative proportion of Q^2 sites due to exposed crystal edges increases compared to the number of Q^3 sites, showing that at 600°C the clay lattice is considerably broken leading to the exposure of more crystal edges and hence a higher Q^2 signal intensity. Furthermore, the peak at -89.2ppm is tentatively assigned to Q^2 sites arising from silicate tetrahedra splintered from the crystal edges. The very broad component at -99.6ppm is most probably due to the formation of a glassy amorphous lithium silicate phase.

The large increase in the ^{29}Si linewidth for model glaze fired at 600°C indicates a substantial disordering of the silicate network. The stongly overlapping signals and the broadness of the resonance suggests that a lack of spectral resolution is preventing any further clarification of the spectrum. In a very recent study Fyfe and co-workers[91] were able to obtain unprecedented ultra high resolution ^{29}Si MAS NMR spectra of zeolite ZSM-5 in which twenty-one of the twenty-four possible resonances could be clearly resolved, with linewidths of the order of 5Hz giving an order of magnitude improvement in spectral resolution. This was done by preparing extremely pure and very crystalline samples of completely siliceous ZSM-5, and more importantly by carefully optimizing all of the NMR experimental variables. Similarly, it is conceived that if we were able to make necessary improvements to the NMR variables, at least the 'crystalline' portion of the spectrum obtained at 600°C would be resolved into a number of distinct peaks. The non-crystalline portion of the spectrum, exemplified by the broad component at approximately -103ppm (and assigned to an amorphous lithium disilicate phase) will not be affected by improvements in the resolution. At 700°C a simpler two line ^{29}Si spectrum is observed, but both components are fairly broad and overlap strongly. the dominant peak at-93.8ppm is again assigned to Q^3 units, while the smaller peak at -79.6ppm is assigned to Q^1 silicons. The approximate linewidths for the two peaks are 250 and 100Hz respectively. The peak due to Q^1 sites at -79.6 has its genesis in the spectrum for lap600, but is of very low intensity (3%). At 700°C it becomes much more prominent. The overlapping peaks show that there is still considerable disorder throughout the fired ceramic glaze structure.

The ^{29}Si spectra for samples fired at 800°C and 900°C show considerable departure from the preceeding spectra. At both temperatures, a two-line spectrum with sharp, distinct ^{29}Si peaks is observed. The lineposition, linewidth and relative intensity of the peaks is exactly the same in both glazes which implies that the same crystalline components may be present at both firing temperatures. The peaks have chemical shift values of -79.6 and -76.4ppm with relative intensities at 55% and 45% respectively. Both peaks are assigned to Q^1 silicon sites.

For the glaze fired at 1000°C, a different spectrum again is observed, with marked chemical shift changes. A four-line spectrum results, all the peaks have narrow linewidths (<50Hz) indicating the presence of four crystallographically distinct ^{29}Si sites. The smallest peak occurs at -73.8ppm is assigned to Q^1 silicon sites, as is the more intense peak at -81.1ppm. The two peaks at -83.5 and -84.7ppm are assigned to Q^2 silicon sites.

At 1300°C the ^{29}Si spectrum consists of three distinct silicon signals. The peak at -72.3ppm is assigned to Q^1 units (intensity 86%) amd the two smaller peaks at -66.3 and -62.2ppm assigned to Q^o units (intensity 7% each).

Table 5.2.2 is a qualitative representation of the distribtution of Q^n units at each firing temperature. Although they are not equilibria in the real sense they present a method of visualising the main changes in network structure or polymerisation state as factors such as temperature of the model glaze are altered. Each peak in the ^{29}Si spectrum is represented by one Q^n unit. Two or more peaks are simply given by $2Q^n$ or $3Q^n$ units as the case may be.

Thus it is clear that Q^3 or sheet structures, as present in the laponite, are the dominating silicate species up to 700°C although their relative proportions are decreased in relation to Q^2 silicate species as gradual breakdown of the network structure occurs. Above 700°C the Q^3 units are completely depolymerised by the effects of both temperature and modifying oxides. A variety of Q^1 species (mainly disilicates) dominate up to about 1000°C. At higher temperatures (1300°C) Q^o species (which represents isolated SiO_4 island structures) are formed.

5.3.5 Assignment of ^{29}Si Chemical Shift to Crystalline Phases

At glaze firing temperatures of 400°C and 500°C, the sheet silicate network of laponite remains intact as indicated by the dominance of the NMR signals due to Q^3 silicons. At 600°C and 700°C thermal vibrations become large enough to considerably disrupt the sheet structures which break down as a result. A variety of fractured or splintered silicate groups (broken off from the main unit cells of the clay lattice) are observed. The temperature range 600 - 700°C can therefore be envisaged as a transition temperature above which the existing network becomes destabilized. At and above 700°C the calcium carbonate decomposes to calcium oxide which then begins to exert its influence as a network modifier by breaking Si-O-Si linkages and creating $Si\text{-}O^-$ non-bridging oxygens, as shown by the large linewidths. The emergence of a peak at -79.6ppm is attributed to a crystalline calcium silicate phase. The two peaks present at 800 and 900°C at -79.6 and -76.6ppm are tentatively assigned to the crystalline calcium silicate rankinite. Our chemical shift values however are slighly different from those reported by Oldfield and Lippmaa. Oldfield et al[44] have calculated both the ^{29}Si chemical shifts for rankinite $Ca_3Si_2O_7$ at -79.4ppm, whereas Lippmaa et al[47] recorded chemical shift at -74.5 and -76.9ppm for synthetic rankinite. It is probable that the environment within our model ceramic glazes affects the electron density on the silicate oxygens which would give slightly different chemical shift values. When only laponite is heated to 800°C (as in previous experiments) the resulting crystalline product formed is enstatite ($MgSiO_3$). However, in this experiment the calcium oxide which is known to have a greater affinity for the silica that magnesium oxide, preferentially reacts with the SiO_2 at temperatures at and above 800°C. A calcium silicate phase is therefore more likely to result than a purely magnesium silicate phase; hence our assignment to rankinite is justified. Phase equilibrium diagrams also indicate that $Ca_3Si_2O_7$ is more likely to form at such temperatures than $MgSiO_3$ or $Mg_2Si_2O_6$.[3]

At 1000°C a variety of peaks indicates that a different equilibrium of Q^n species is present in the glaze fired at this temperature. There is no trace of rankinite but the ^{29}Si peaks are sharp and therefore due to another crystalline phase.

Phase diagrams [3] indicate that at this temperature, both calcium and magnesium may be present in a formed crystalline phase. On the basis of phase diagrams and chemical shifts reported by other workers[47,50] the sharp peak at -73.8ppm is assigned the pyrosilicate akermanite ($Ca_2MgSi_2O_7$). The two sharp peaks at -81.1ppm and -83.5ppm are assigned to enstatite ($MgSiO_3$) since the chemical shift and relative peak intensity are exactly as we would expect. The peak at -84.7ppm has a lower intensity than the other peaks and is assigned to that of the pyroxene mineral diopside ($CaMgSi_2O_6$).

At 1300°C the dominant ^{29}Si peak at -72.3ppm is assigned to akermanite ($Ca_2MgSi_2O_7$) in which all the silicons are of the Q^1 type ie three non-bridging oxygens and one bridging oxygen per SiO_4 tetrahedron. This is also in agreement
with Lippmaa's findings and with the phases predicted by the relevant phase diagrams. Of the two minor peaks (7% intensity each) the peak at -62.2ppm is assigned to the orthosilicate mineral forsterite (Mg_2SiO_4) while the peak at -66.2ppm is assigned to the orthosilicate mineral monticellite ($CaMgSiO_4$).[44]
The chemical shift values are in very good agreement with those obtained independantly by Lippmaa et al and Smith et al.

5.3.6 X-Ray Diffraction Data

The x-ray diffraction results for the model ceramic glazes fired in the temperature range 400 to 1300°C are summarised in appendix 1. For the glaze samples fired below 700°C, although a large number of X-Ray reflections are recorded none of them could be unambiguously assigned to the presence of a crystalline silicate phase. This was in agreement with NMR results which indicated a disordered structure below 700°C. Glaze samples fired above 800°C also show a large number of strong x-ray reflections, but because many peaks are either suppressed or enhanced in intensity and often strongly overlapping, unequivocal assignment is a problem. On the basis of d-spacings alone the principal lines corresponding to those of rankinite ($Ca_3Si_2O_7$) are observed for glazes fired at 800°C and 900°C.

At 1000°C evidence of a di-calcium silicate phase probably (α-Ca_2SiO_4) is found, but no clear evidence for enstatite could be found, as otherwise indicated by the NMR results. The results for the glaze fired at 1300°C show clear evidence for the presence of akermanite ($Ca_2Mg\ Si_2O_7$) as the major component. A number of reflection peaks could also be assigned to monticellite ($CaMgSiO_4$) and forsterite (Mg_2SiO_4). No reflections attributable to calcium oxide, calcite of magnesium oxide (periclase) are observed implying that all of the calcium oxide present is used in forming the mineral phases.

5.3.7 Infra-Red Data

Infra-red spectra for the glazes of composition laponite and 100 mol% calcium oxide fired at various temperatures are summarised in figs. 5.2.3 and 5.2.4 and the results summarised in table 5.2.3. For samples fired up to 700°C. the i.r. spectra are dominated by the fundamental vibrational modes of calcite (calcium carbonate). Four main i.r. active modes are identified for calcite. The very strong, broad band at 1418-22cm^{-1} is due to the ν_3 (ungerade) stretching modes of the carbonate anion CO_3^{2-} [97] and can be represented as:

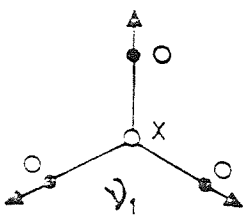

The very strong, sharp band at 875-76cm^{-1} is assigned to the ν_2 (ungerade) stretching mode of the carbonate anion represented as:

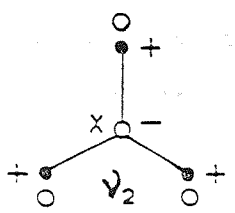

and the medium intensity band at 712cm^{-1} is assigned to the $\nu_4(u)$ stretching mode. A strong band at 312cm^{-1} is assigned to one of the E_u lattice vibrational modes of calcite. The broad strong band at 1014cm^{-1} is due to Si-O lattice

stretching modes, while Si-O$^-$ bending modes are also observed as a broad band at 475cm^{-1}. A broad absorption maximum due to hydroxyl groups involved in water-water H-bonds is seen at 3442cm^{-1} and a weak shoulder at 3662cm^{-1} is assigned to a hydroxyl stretch.

As the firing temperature is increased the ν_3, ν_2 and ν_4 stretching modes of the carbonate anion become more intense compared to the Si-O stretching band which becomes weaker in relation. Also, the Si-O stretching mode is seen to merge into the continuum as the 312cm^{-1} absorption maximum intensifies. After 800°C the calcite vibrational modes begin to disappear and the silicate stretching modes between 850cm^{-1} and 1100cm^{-1} become more intense and dominate the spectrum. At higher firing temperatures ie 900 and 1000°C the silicate band becomes split into several distinct, strong bands, implying several Si-O stretching modes. On the basis of these results we speculate that no chemical reaction occurs until after 700°C when $CaCO_3$ is decomposed to CaO and the silicate network begins to break up. This is in agreement with the NMR results which also imply that reordering of the silicate network only occurs above 700°C.

An interesting situation occurs with the water band. As the firing temperature is increased, the band due to hydroxyl H-bonding at 3442cm^{-1} becomes gradually weaker. At the same time the 3662cm^{-1} maximum becomes slightly stronger up to 700°C. This is expected since an increase in temperature is expected to break H-bond interactions. Normally at temperatures exceeding 800°C, we would expect any water in the system to be lost completely. The i.r. results show otherwise. At 800°C an intense and very sharp band appears at 3662cm^{-1}. This is therefore assigned to a strong O-H stretching mode. Although it was present in the low temperature glazes, its intensity was weak to negligible. This band is present in the glazes fired at 1000°C but disappears at a firing temperature of 1300°C.

The role of water in glassy materials has been considered by various workers[104]. It has been demonstrated that hydroxyl groups in various states of association are always present in glasses unless extreme precautions are taken

Fig. 5.2.3 F.T.I.R Spectra for a Model Ceramic Glaze Laponite + CaO Fired at Various Temperatures

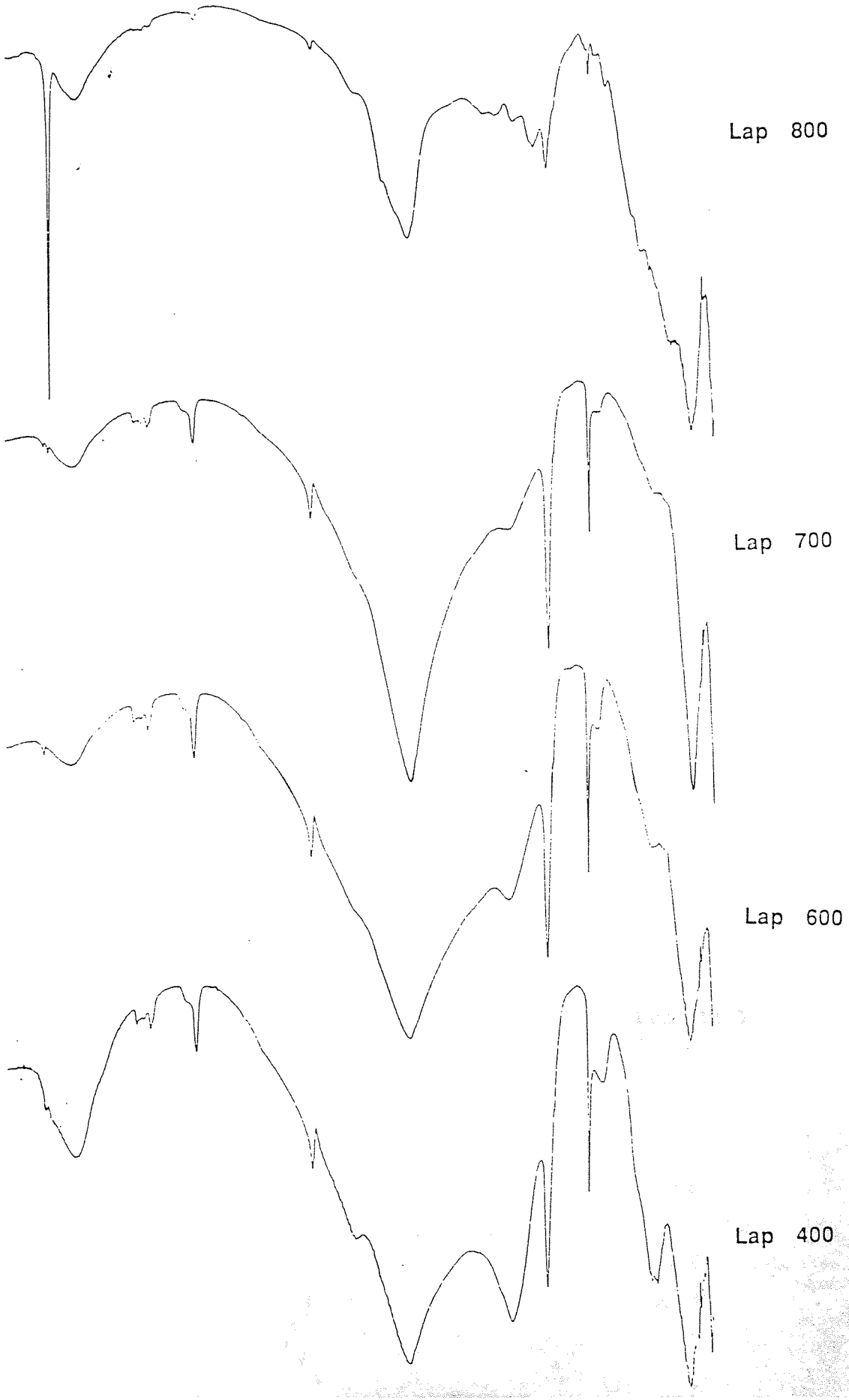

Fig. 5.2.4
F.T.I.R Spectra for a Model Glaze [Laponite + CaO] Fired at Various Temperatures

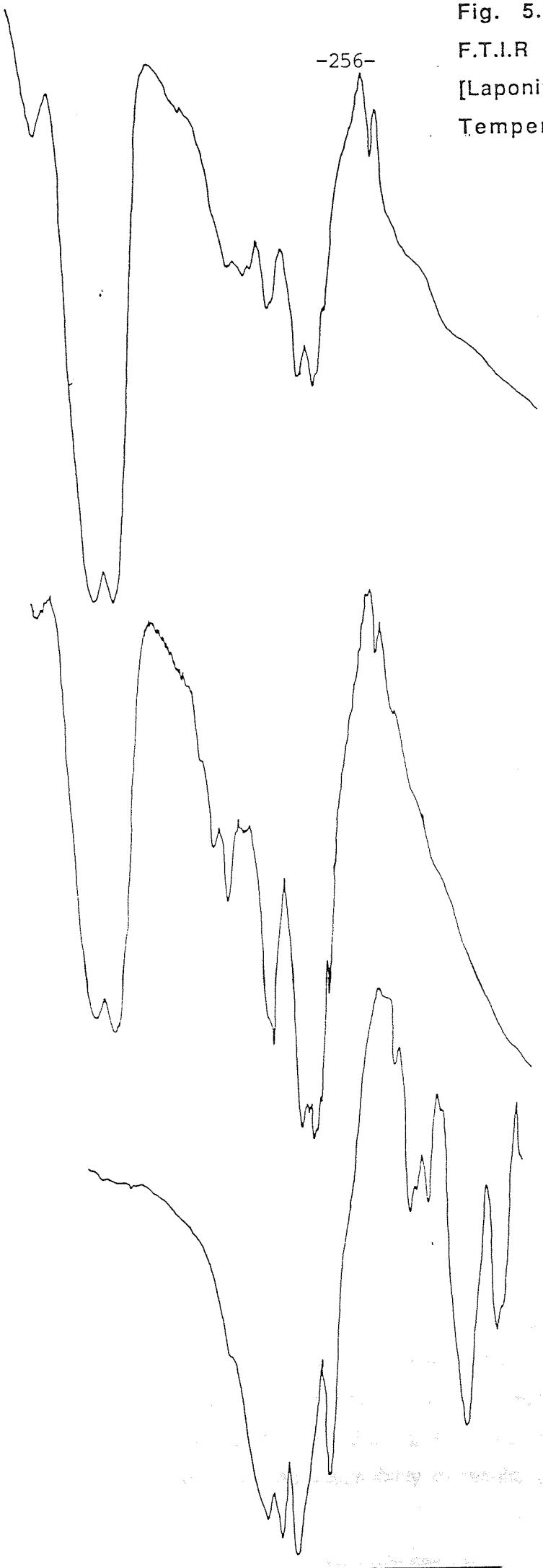

in dehydration of batch materials. We speculate that in glazes fired between 800°C and 1000°C the OH stretching mode arises from two sources. It could either be due to the perpendicular (axial) lattice OH groups on the silica sheets of laponite, or due to unassociated OH groups rather than molecules of water.

5.3.8 Conclusions

In this study, ^{29}Si (MAS) NMR, XRD and i.r. were used to study the effect of firing temperature on a model ceramic glaze of Laponite and 100 mol% CaO. The NMR spectra showed that at each firing temperature a different structural equilibrium was present throughout the glaze. The formation and distribution of different silicon environments (Q^m units) was dependent on the thermal history of the ceramic glaze. Below 700°C, the ^{29}Si spectra had very broad linewidths particularly at 600°C indicating that considerable fracturing and splintering of laponite crystal edges had occurred. The highest intensity peaks at these lower firing temperatures were the Q^3 peaks (around -93ppm) which implied that sheet structures remained more or less the dominant silicate species. Above 700°C the spectra were marked by very sharp, distinct peaks arising from crystallographically distinct silicon sites. Assignment to mineral phases was easy and agreement with literature was good. Above 700°C mainly Q^1 and Q^0 silicon sites were formed as more non-bridging oxygens were created. Rankinite was the stable phase formed between 800 and 900°C while at 1000°C a mixture of diopside and enstatite was formed. At 1300°C pyrosilicates and orthosilicates were formed namely akermanite, forsterite and monticellite. The overall effect of increasing the firing temperature was to progressively depolymerise the Q^3 silicate network until at 1300°C only pyro and orthosilicates were formed. The formation of crystalline phases did not begin until 800°C.

IR and XRD both provided complimentary evidence to the ^{29}Si NMR results. However, both of these techniques are severely limited in their usefulness and are affected by the presence of more than one mineral phase. Hence no quantitative information can be gained using XRD and i.r. The NMR technique is clearly superior in terms of reproduceability of results and in content of

information. Furthermore, NMR provides very useful information on the short-range ordering within the glaze and very precise information about changes in the topology of the silicate network.

5.4 ^{29}Si MAS NMR STUDY OF THE EFFECT OF INCREASING CaO CONTENT IN A MODEL CERAMIC GLAZE

5.4.1 Experimental

Calcium carbonate was added to samples of laponite in increasing amounts (based on the mol% of CaO to SiO_2 in laponite) in the proportions shown below. the mixtures were ground thoroughly in an agate mortar and then fired separately at 1300°C for three hours in porcelain crucibles. After firing the glazes were cooled overnight in a vacuum desiccator.

Laponite/g	$CaCo_3$/g	Mol% CaO
3	0.27	10
3	0.54	20
3	1.08	40
3	1.35	50
3	1.62	60
3	2.16	80
3	2.7	100
3	5.4	200

5.4.2 ^{29}Si NMR Data

The ^{29}Si nuclear magnetic resonance spectra of the model glazes with different CaO/SiO_2 compositions exhibit sharp, symmetrical multiple peaks implying the presence of several chemically distinct ^{29}Si sites in the glazes. The spectra are illustrated in fig. 5.3.2. The ^{29}Si chemical shifts, linewidths and relative peak intensities are summarised in table 5.3.1. The chemical shift values of the peak maxima are within the range -91.9 to -61.9ppm.

Table 5.3.1

Laponite + CaO Glaze [CaO] Increasing[SiO_2]	Q^0		Q^1		Q^2		Q^3	
	δ	I	δ	I	δ	I	δ	I
Laponite					-84.1		-93.6	
20% CaO	-61.9	18%			-84.6	(82%)		
40% CaO	-61.9	(13%)			-84.3	(70%)	-91.9	(17%)
50% CaO	-62.2	(33%)			-14.7	(67%)		
60% CaO	-61.8	(21%)	-72.0	(41%)	-84.3	(38%)		
80% CaO	-61.8 -65.9	(7%) (19%)	-72.1	(69%)	-84.5	(6%)		
100% CaO	-61.9 -65.9	(6%) (19%)	-72.1	(74%)				
200% CaO			-72.1 -73.6	(55%) (45%)				

Table 5.3.4 IR Results for a Modelled Ceramic Glaze Containing Laponite + Calcium Carbonate

mol% CaO in Glaze	20%CaO	40%CaO	60%CaO	80%CaO	100%CaO	200%CaO
Wave No. cm^{-1}	1073vs	1072vs	1070-50sh	1040sh	1110sh	1120
	1000sh	990sh	1011	1013	1040sh	1019s
	975 (b)	970vs	974vs (sp)	975	1015s	980
	924	922s	932vs	936vs(b)	976	937s
	888	890	920sh	920sh	935vs	925
	730vw	840sh	890sh	885sh	920sh	854vs
	710sh		854	852vs	853vs	710
	678	675	675	690	710	680
	637s(sp)	634	637vs	640	680	640]db
	610	610	620sh	630sh	639]db	620
	508s(sp)	514	586	588	625	590
	481	481	508	510sh	589	476vs
	422	473sh	481	480	510sh	410
	409	405	402		478vs	

The effect of introducting even a small amount of calcium oxide (in the form of calcite) into the ceramic glaze system can be seen by comparing the ^{29}Si NMR spectra of laponite heated to 1300°C, and laponite plus 20% CaO heated to 1300°C for the same length of time. The NMR spectrum for laponite + 20% CaO exhibits two sharp peaks. The most intense peak has a chemical shift of -84.6ppm (relative to TMS), a relative intensity of 82% and is assigned to Q^2 silicon sites or middle chain groups. The smaller peak at -61.9ppm has 18% relative intensity and it assigned to Q^o silicon sites or isolated island structures with four non-bridging oxygens. There is also a weak shoulder at -81.1ppm assigned to Q^1 silicon sites. The broad ^{29}Si component at about~96ppm is probably due to a residual lithium silicate phase.

The spectra of the glazes with 40% and 50% calcium oxide are similar in appearance to laponite + 20% CaO, in that a dominant Q^2 silicon peak at -84.3ppm and a smaller Q^o silicon peak at -61.9ppm are observed in both cases. The only difference is that the relative intensity of each of the peaks is significantly altered by the addition of more CaO to the glaze recipe. For 40% CaO addition, the intensity of the Q^2 peak at -84.3 is reduced to 70% and that of the Q^o peak at -61.9 is reduced to 13%. The amorphous glassy component also becomes less broad and less noticeable as CaO content increases, until at 50% CaO it is completely absent. At 50% CaO the Q^o peak intensity rises to 33% and that of the Q^2 peak falls to 67%.

As more CaO is added to the system, a different distribution of Q^m silicate units is observed. The ^{29}Si NMR spectrum for laponite and 60% CaO shows three sharp peaks each with linewidth less that 50Hz. The multiple peaks reflect chemically distinct silicon sites, most probably due to crystalline phases. The most noticeable feature is the appearance of a new ^{29}Si peak at -72.8ppm assigned to Q^1 silicons ie one silicon connected to three non-bridging oxygens and connected to another silicon atom via a bridging oxygen. The Q^2 silicon peak at -84.3ppm and a Q^o peak at -61.8ppm are also present. The Q^2 and Q^1 peaks have almost equal intensities while the Q^o is half as intense, which means that Q^2 and Q^1 sites are equally abundant but twice as abundant as Q^o sites. A further increase in the CaO content of the glaze leads to a reduction of Q^o and Q^2 silicon signals and increase in the intensity of the Q^1 signal. For

Fig. 5.3.1 ^{29}Si MAS NMR Spectra for Model Ceramic Glazes in the Composition Range Laponite + CaO (20 mol% to 60 mol%)

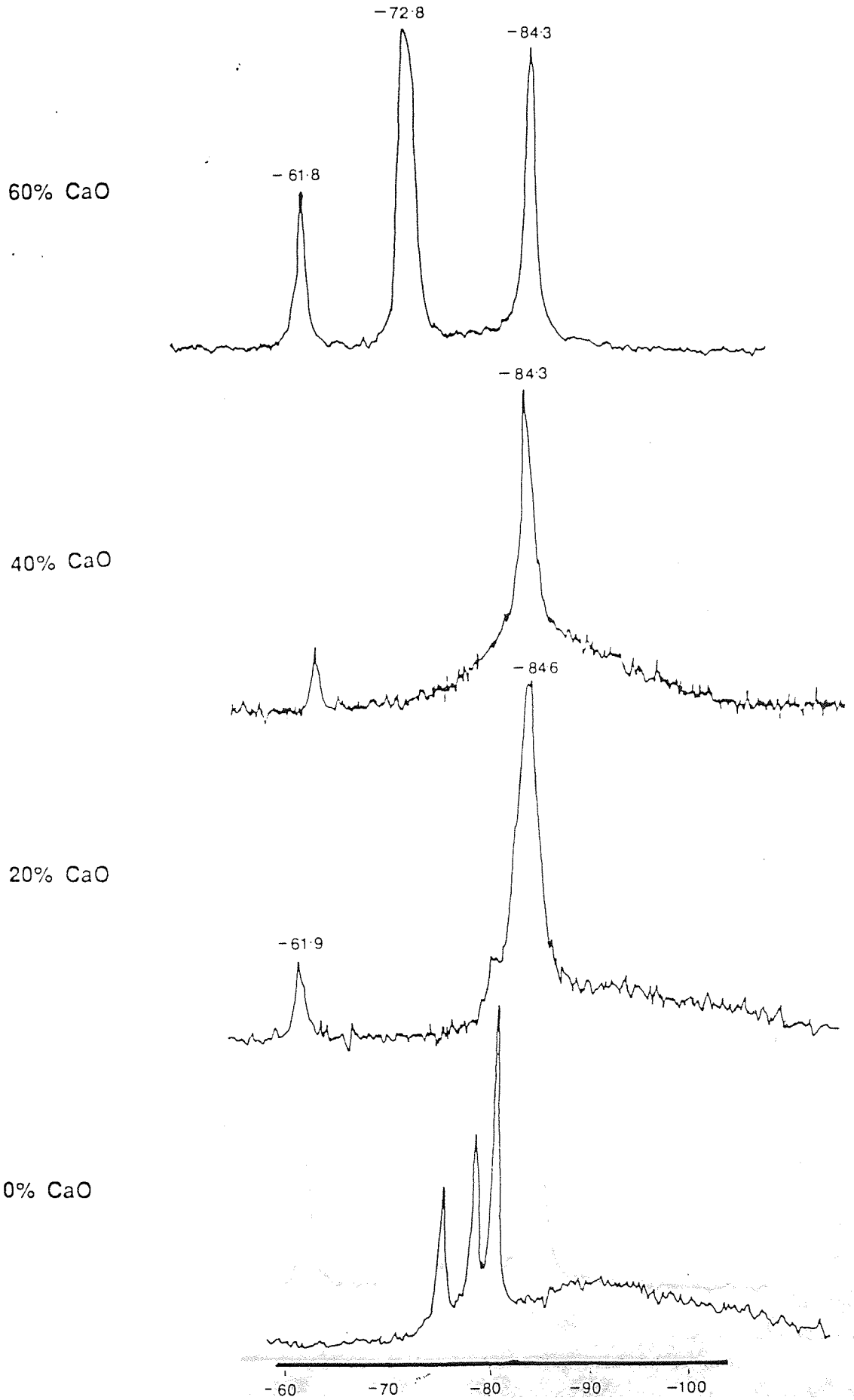

Fig. 5.3.2A ^{29}Si MAS NMR Spectra for Model Ceramic Glazes in the Composition Range Laponite + CaO (60 mol% to 200 mol%)

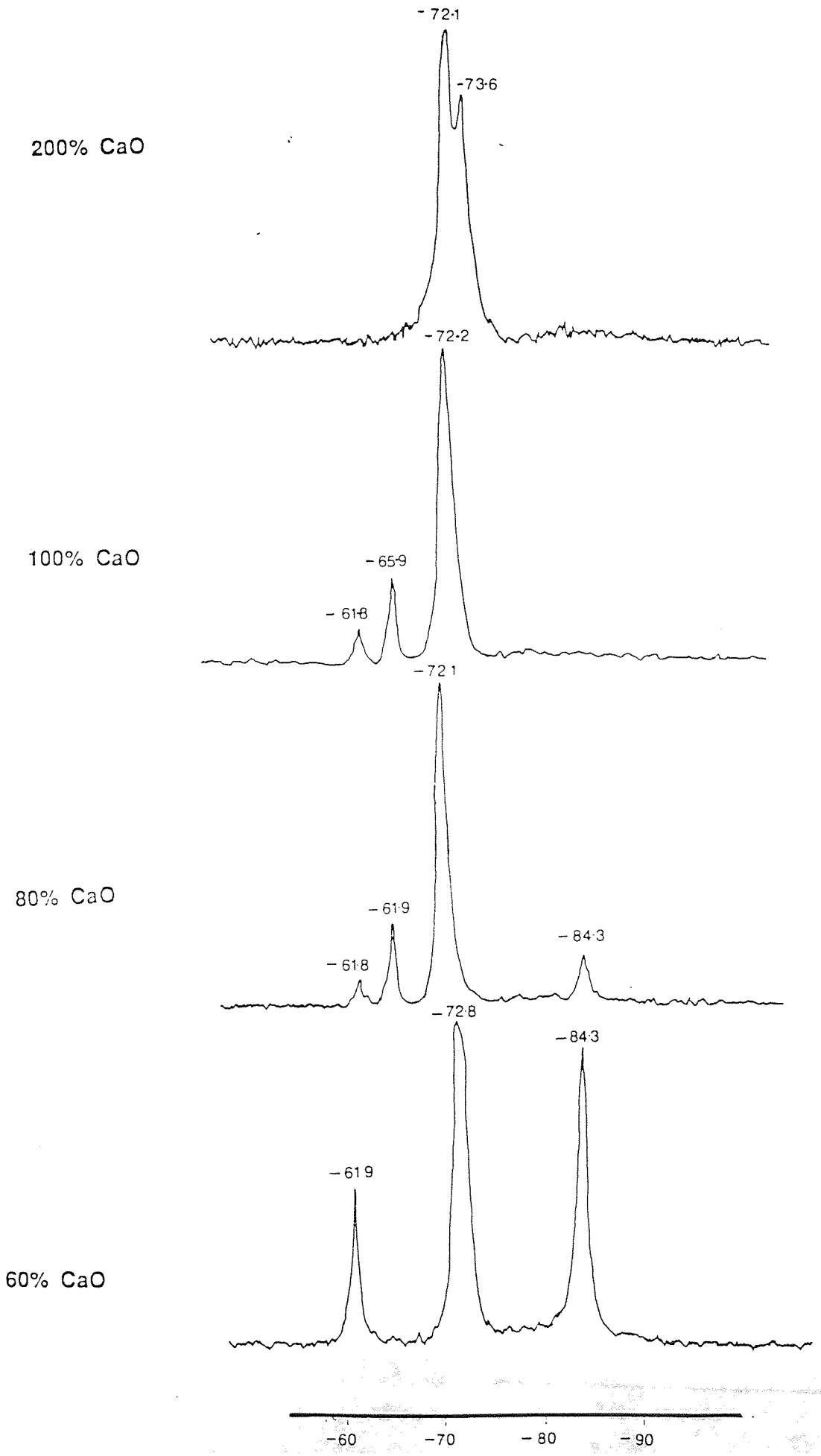

Fig. 5.3.2B ^{29}Si MAS NMR Spectrum of the Glaze [Laponite + CaO (60 mol%)] Magnified to Show the Small Linewidths (FWHH)

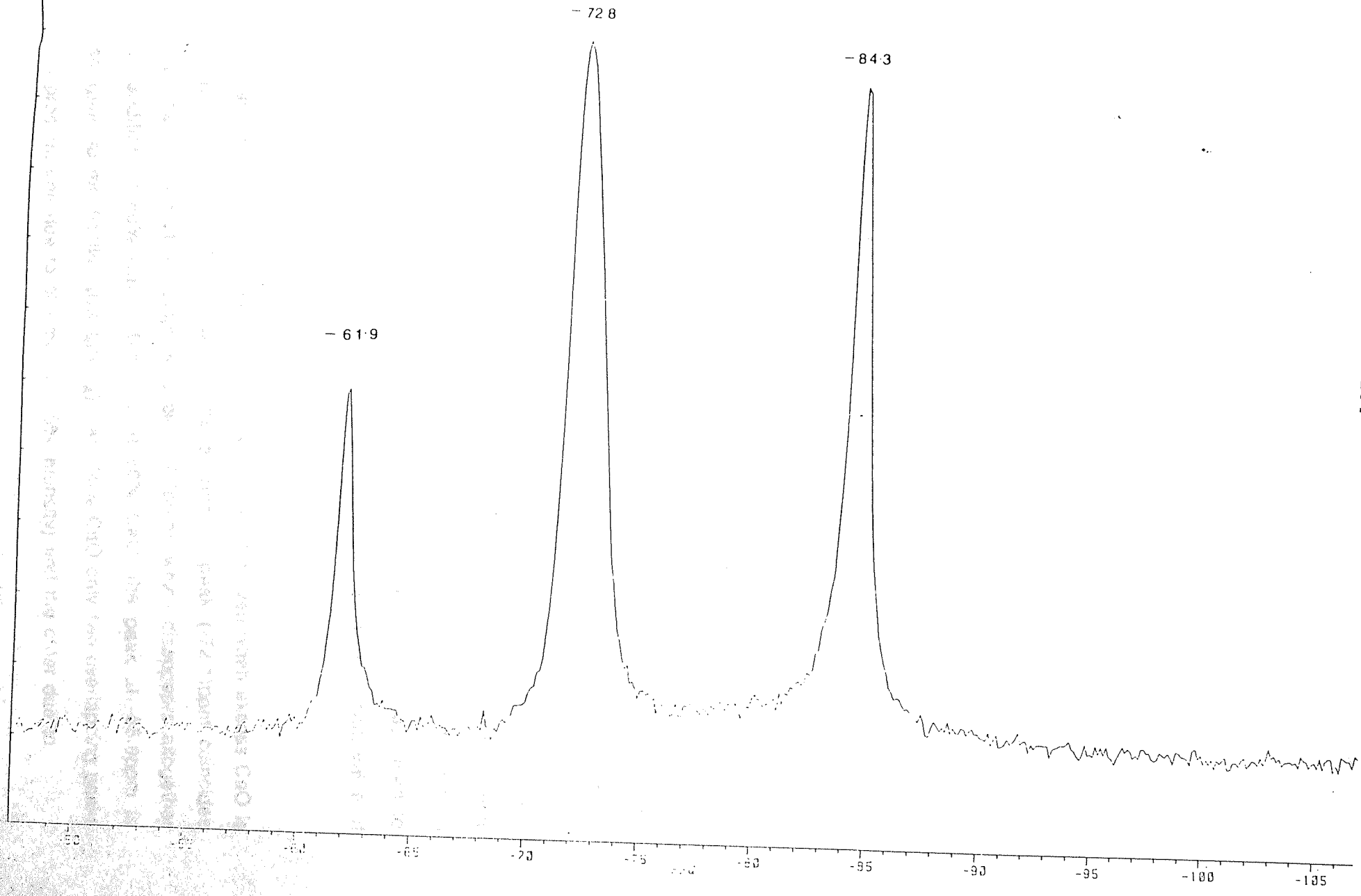

BRUKER
CA.060
DATE 24-11-8
SF 59.62
SF0 59.58
O1 47454.15
SI 8192
TD 8192
SW 29411.76
HZ/PT 7.16
PW 4.0
RD 1.00
AQ .13
RG 200
NS 6000
TE 303
FW 36800
O2 5000.00
DP 144 P0
LB 4.00
GB 0.0
CX 38.00
CY 20.00
F1 -47.52
F2 -106.93
HZ/CM 93.53
PPM/CM 1.56
SR 48301.47

fairly low CaO concentration (20 to 50%) Q^2 silicon sites are dominant but decrease continually. At higher CaO concentration (60 to 100%) a variety of different silicate species are created as more non-bridging oxygens are created. In this composition range Q^2 sites disappear altogether and are replaced by Q^1 sites. Eventually after an addition of excess CaO the silicate network is further polymerised giving Q^0 and Q^1 sites only.

5.4.4 Assignment of ^{29}Si Chemical Shifts to Crystalline Phases

A number of factors including small linewidths, multiple peaks and the reproduceable chemical shift values strongly indicate that for each composition of the ceramic glaze there are crystallographically distinct Si sites due to mineral phases formed during the cooling of the fired glaze. By looking at the spectra in fig. 5.3.1 and 5.3.2 a clear pattern emerges; it is possible to observe the progressive growth and disappearance of different silicon peaks and to attribute these to the growth and disappearance of crystalline mineral phases as the level of CaO added to the glaze is altered. For example the Q^2 silicon peak at -84.3 ppm dominates the spectra from 20% to 50% CaO addition. On the basis of work carried by Lippmaa et al[47] this peak is readily assigned to diopside ($CaMgSi_2O_6$) which consists of pyroxene type chains. The ^{29}Si chemical shift for diopside has been calculated by Oldfield[44] at -84.4ppm relative to TMS. The accompanying small peak at -61.9ppm is assigned to the mineral forsterite (Mg_2SiO_4). At 60% CaO addition the relative proportion of diopside falls, in relation to a new mineral phase observed at -72.1ppm which is assigned to akermanite ($Ca_2MgSi_2O_7$). Lippmaa et al recorded a chemical shift value of -73ppm for akermanite.

The akermanite peak is very consistent and is present even when excess CaO is present (ie200%). The growth of the akermanite peak (-72.1)ppm coincides with the demise of the diopside peak (-84.3ppm), which disappears altogether on addition of 80% CaO. Similarly at 80% CaO, the peak at -65.9ppm is assigned to monticellite ($CaMgSiO_4$). At 200% CaO only two overlapping peaks are present; one due to akermanite (45% intensity) and the other due to

γ-dicalcium silicates (γ-Ca_2SiO_4) also known as calcio-olivine, and where the calcium ions are known to be in six-coordination with oxygen atoms.

The formation of the mineral phases at each level of CaO addition to the glaze can be explained if we consider the relative portions of the glaze constituents. The composition of laponite in terms of its oxides is $(MgO)_{5.34}(Li_2O)_{0.66}(SiO_2)_{7.5}$, which provides magnesium oxide as a potential glass former. The crystalline phases observed by ^{29}Si NMR are summarised in table 5.3.2.

At low CaO levels of addition (20 to 50%) the amount of MgO present is relatively higher, and so forsterite (Mg_2SiO_4) and diopside ($CaMgSi_2O_6$) are the resultant phases. On increasing the CaO content to equal and above the MgO content ie from 60% to 100% CaO, similar quantities of the two oxides are present in the glaze mixes, but since CaO has a greater affinity for SiO_2 than MgO, mineral phases containing relatively more calcium and less magnesium are formed. For example, akermanite is formed in preference to diopside at and above 60% CaO. At 80% CaO the relative amount of forsterite drops and a similar olivine type mineral, monticellite so formed which has Ca substituted for one of the Mg atoms ($CaMgSiO_4$). At excess CaO levels the CaO content far exceeds that of MgO and so akermanite and a pure calcium silicate phase (γ-dicalcium silicate γ-Ca_2SiO_4) is formed. This sequence of events is illustrated in fig. 5.3.3 which is a plot of relative intensity of the ^{29}Si peaks for diopside (Q^2), akermanite (Q^1) and the olivine type (Q^o) minerals, versus mol% CaO. The diagram also illustrates the rise in relative proportion of the Q^1 peak (akermanite) and the synonymous fall in the intensity of the diopside (Q^2) peak. It is interesting to note that it is the overall concentration of the fluxing oxide which determines the dominant structural silicate unit formed on cooling of the fired glaze. As the concentration of CaO is increased the result is a successive depolymerisation by production of non-bridging oxygens and eventual formation of calico-olivine (γ-Ca_2SiO_4) which has four non-bridging oxygens. But even when MgO is the major fluxing oxide present such as an olivine phase is still formed (Mg_2SiO_4), implying that CaO and MgO have similar

Mineral Phase	Molecular Formula	C^1 Chemical Shift/ppm OBSD	REF	Q^m
Forsterite	Mg_2SiO_4	-61.9	-62.0	Q^o
Monticellite	$CaMgSiO_4$	-65.9	-66.0	Q^o
γ–di-calcium Silicate	γ-Ca_2SiO_4	-73.5	-73.5	Q^o
Akermanite	$Ca_2MgSi_2O_7$	-72.1	-73.7	Q^1
Diopside	$CaMgSi_2O_6$	-84.3	-84.4	Q^2
Lithium Disilicate	$Li_2Si_2O_5$	≈-92.95	-92.7	Q^3

Table 5.3.2: A List of Mineral Phases Formed in Glazes Fired at 1300°C in the Composition Range Laponite +20% Cao to Laponite + 200% CaO.

Fig. 5.3.3 Change in Relative Intensity of the ^{29}Si Peaks Due to Akermanite and Diopside with Composition of Model Ceramic Glaze

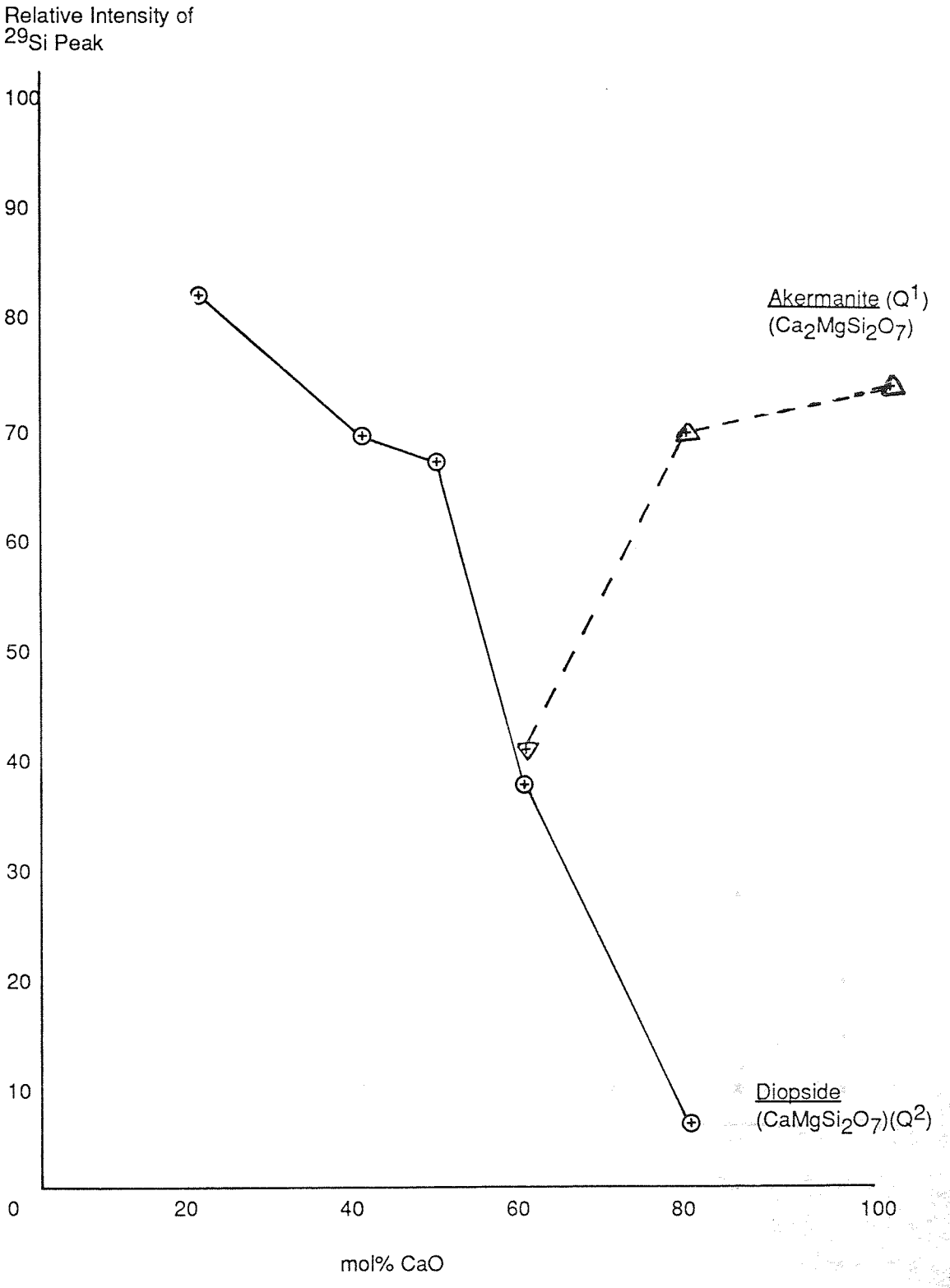

Table 5.3.3 XRD Results: Assignment to Mineral Phase for Modelled Ceramic Glazes Ca20 to Ca200

	Ca20	Ca40	Ca60	Ca80	Ca100	Ca200
Forsterite	√	√	√	√	x	x
Akermanite	x	x	x	√	√	√
Monticellite	x	x	x	√	√	x
Enstatite	√	x	x	x	x	x
Clinoenstatite	x	x	x	x	x	x
Diopside	√	√	√	√	x	x
Merwinite	x	x	x	x	x	x
Wollastonite	x	x	x	x	x	x
Tricalcium Silicate	x	x	x	x	x	x
α-Dicalcium Silicate	x	x	x	x	x	x
ß-Dicalcium Silicate	x	x	x	x	x	x
γ-Dicalcium Silicate	x	x	x	x	x	√
Rankinite	x	x	x	x	x	x
Lime(CaO)	x	x	x	x	x	√
Periclase (MgO)	x	x	x	x	x	x

depolymerisation effects on the silicate network and give rise to structurally similar phases. It is only their relative proportion which determines the exact mineral phase formed.

5.4.5 X-Ray Diffraction Data

The X-ray diffraction results are recorded in table 5.3.3 d-spacings for each of the model ceramic glazes in the composition range laponite + 200% CaO to laponite + 22% CaO. In this composition range a large number of silicate phases may be formed. Table 5 is a list of all the mineral phases that could be formed and also shows which of these phases were detected by XRD. Generally speaking the results are in agreement with the NMR data. Diopside and akermanite were only found to co-exist at 60 and 80 mol% CaO, whereas forsterite was not detected beyond 80%mol CaO. No trace of CaO was observed except at 200 mol% CaO.

5.4.6 Infra-Red Data

NMR and XRD results strongly indicated that several mineral phases are formed between the ceramic glaze composition range, laponite + 20 mol% CaO to laponite + 200 mol% CaO, including akermanite, diopside and dicalcium silicate. We therefore expect to see certain bands in the infra-red region which would support the NMR and XRD evidence. The i.r. spectra are recorded in fig. 5.3.4 and the results summarised in table 5.3.4. The spectra exhibit a variety of intense bands in the region $1100cm^{-1}$ to $400cm^{-1}$ implying the existence of a range of structural units. The most intense bands occur in the range 1100 to $850cm^{-1}$ and 500 to $400cm^{-1}$. The existence of more than one mineral phase is quite apparent because if only one phase was present, the high-frequency region would consist of one broad but intense band. Instead this region is dominated by several equally intense bands arising from several different Si-O stretching modes. The presence of more than one mineral phase also means that many absorption bands become suppressed or enhanced by others at the same frequencies.

Fig. 5.3.4 F.T.I.R Spectra for the Model Ceramic Glazes Laponite + CaO (20 mol% to 200 mol%)

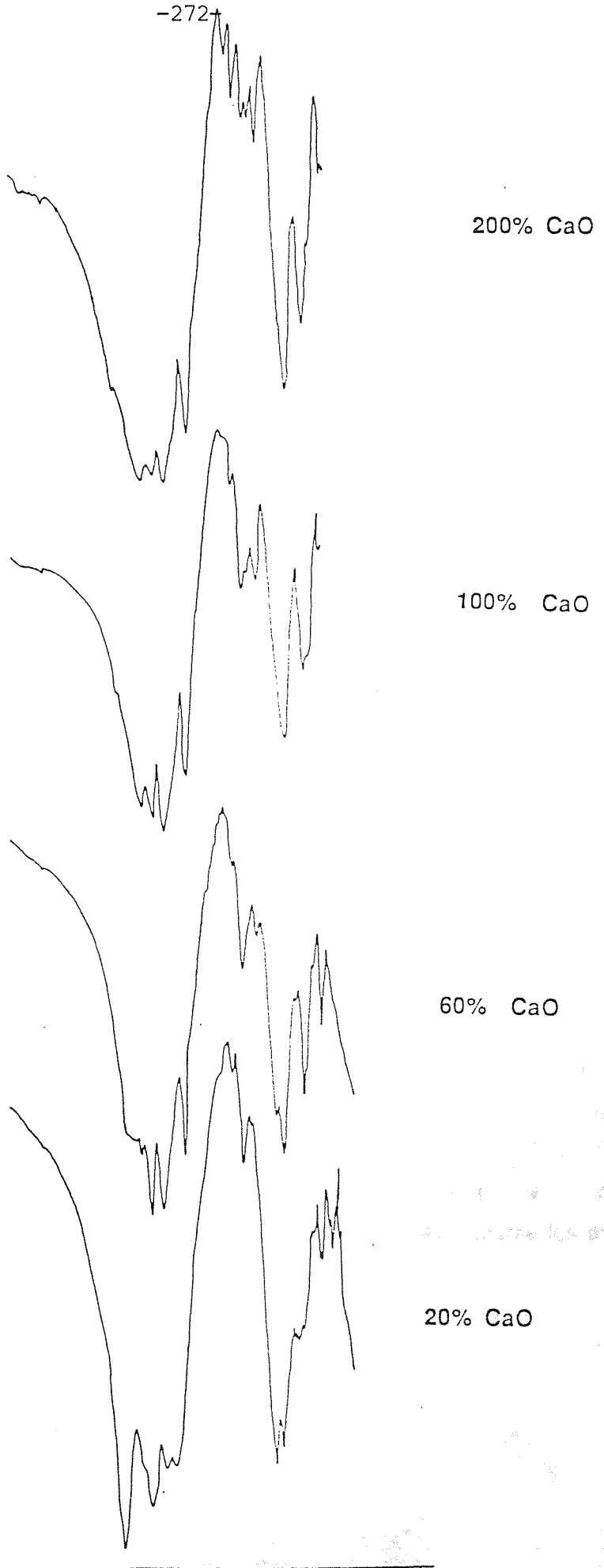

According to the ^{29}SiNMR results, the dominant mineral phases formed after firing of the ceramic glazes are diopside and akermanite, one phase being dominant over the other depending on the CaO content. The i.r. results show evidence which supports this assertion. A strong sharp band at 1011cm^{-1} and 1015cm^{-1} in glazes with 60 mol% to 200 mol% CaO, but not in glazes with 20% and 40% CaO. This band is attributed to the Si-O-Si assymmetric stretching mode in akermanite, arising from the vibrations of the bridging Si-O-Si bond. The strong band at 935cm^{-1} is attributed to terminal Si-O^{-} vibrations of akermanite. Neither the 1015-11cm^{-1} band nor the 935cm^{-1} band is seen in glazes with 20 mol% and 40 mol% CaO. The medium intensity band at 854 cm^{-1} occurring in glazes with 60% or higher CaO content is diagnostic of akermanite. According to Dowty this band is assigned to the oscillation of the O3 oxygens, that is the oxygens coordinated to magnesium, and arises from the contractions in the plane SiOMg[100]. Such a band is known to be absent in diopside[99,100].

On the other hand, glaze samples with 20 mol% and 40 mol% CaO content both exhibit strong, intense bands at 1073 and 1072 cm^{-1} respectively. The ceramic glaze at 60 mol% CaO exhibits a shoulder at 1075cm^{-1} but this band is not present at CaO above 60 mol%. Saksensa has assigned this absorption band to one of the triply degenerate (ω_3) frequency modes in diopside;[99] more specifically the motion of the silicon atoms against the oxygens along the three axes. This band is not known to be present in akermanite and is usually diagnostic of pyroxene type minerals with a silicate chain structure. The shoulder at 924-25cm^{-1} is observed over the entire glaze compostion range and is assigned to terminal Si-O^{-} stretching vibrations present in diopside and akermanite. It is important to note that the evidence provided by i.r. data is only complimentary to the NMR and XRD data and in no way supersedes them as a major physical technique.

5.5 ^{29}Si MAS NMR STUDY OF THE EFFECT OF Na_2O ON A MODEL CERAMIC GLAZE

5.5.1 Experimental

Laponite, calcium carbonate and sodium carbonate were mixed together in the molar quantities shown in the table below. The mixtures were ground in an agate mortar and pestle and fired at 1300°C for four hours in porcelain crucibles. the fired glazes were then removed from the furnace and allowed to cool overnight in a vaccum desiccator.

Laponite/g	Na_2O mol%	CaO mol%	Na_2CO_3/g	$CaCO_3$/g
3	0	100	0	2.7
3	10	90	0.17	2.43
3	20	80	0.34	2.16
3	30	70	0.51	1.89
3	40	60	0.67	1.62
3	60	40	1.05	1.08
3	80	20	1.34	0.54
3	100	0	1.67	0

5.5.2 ^{29}Si NMR Data

The model ceramic glaze under study differs from those in the previous section where calcium oxide was the only modifier oxide added to laponite in the glaze mix. In this series of experiments Na_2O has been increasingly substituted for CaO in the glaze mixes in order to determine the relative effects of the two oxides on the structure of the glaze. The ^{29}Si spectra for the glaze samples are illustrated in figs. 5.4.1 and 5.4.2. the chemical shift values and their assigneme to Q^m silicate species are recorded in table 5.4.1, along with relevant linewidths and intensity values. For the sake of simplicity each glaze sample is labelled in terms of the mol% of sodium oxide present eg NaO%, Na10%, Na20% and so on.

	Q^0		Q^1		Q^2		Q^3	
	δ	I	δ	I	δ	I	δ	I
Laponite	-	-	-	-	-84.1	(10%)	-93.6	(90%)
10%Na_2O	-66.0	(65%)	-72.2	(28%)	-90.1	(7%)	-	-
20%Na_2O	-61.9	(7.0%)	-72.2	(60%)	-85.6	(12%)	-	-
30%Na_2O	-61.8	(4.6)	-71.9	(43%)	-85.0	(17%)	-	-
40%Na_2O	-61.8	(18%)						
	-65.9	(26%)	-74.3	(24%)	-85.0	(32%)		
60%Na_2O	-	-	-78.8	(100%)	-	-	-	-
80%Na_2O	-	-	-79.8	(100%)	-	-	-	-
100%Na_2O	-	-	-80.8	(100%)	-	-	-	-

Table 5.4.1 ^{29}Si NMR Results for Model Glaze [Laponite + xCaO + (1-x)Na_2O] δ /ppm

Table 5.4.2 ^{23}Na NMR Results for Modelled Ceramic Glaze Laponite + CaO + (1-x)Na_2O

	$\delta\ ^{23}Na$/ppm	Linewidth Hz^{-1}
Na10	-8.81	2100
Na20	-14.46	2100
Na30	-8.75	2550
Na40	-14.6	2250
Na60	-10.24	2550
Na80	-11.33	2500
Na100	-12.24	2300

Table 5.4.3 IR Results for Modelled Ceramic Glaze Containing Laponite + CaO + Na_2O

Wavenumber cm^{-1}	mol% Na_2O in Glaze			
20% Na_2O	40% Na_2O	60%Na_2O	80%Na_2O	100%Na_2O
1013 s				
980 s	988vb	1001 vb	1011	1012
938 s	960	920 vb sh	980 sh	980 sh
920 sh	820-890 sh	725 vb	730	724 vs
554	718	487 vb	477 vb	471 vb
708 CJ	690			
682	594			
640	520 sh			
620	476 s			
594	440-10 sh			
525 sh	394 sh			
476 vs				
420 -394 (b)				

The most noticeable feature of the ^{29}Si spectra is the concurrent growth of a very broad silicate phase and the disappearance of sharp, discrete peaks with increase in Na_2O content. The NMR spectra of Na0% (which contains 100 mol% Ca_2O) consists of three distinct ^{29}Si peaks each with a linewidth less than 50Hz. As for a ceramic glaze of the same composition prepared in the previous study, the peak at -61.8ppm is assigned to Q^o units and to the mineral forsterite (Mg_2SiO_4); the Q^o peak at -65.9ppm is assigned to monticellite ($CaMg\ SiO_4$), and the dominant (86% intensity) Q^1 peak at -72.1ppm is assigned to akermanite ($Ca_2MgSi_2O_7$). The ^{29}Si spectrum of Na10 (ie 90 mol% CaO and 10 mol% Na_2O) shows two sharp, distinct peaks at -66.0ppm and -72.2ppm assigned to monticellite and akermanite respectively. No peak at -61.9ppm corresponding to forsterite is observed. The relative intensities of the Q^o peak is twice that of the Q^1 component. A broad phase at about -90ppm with a relative intensity of 7% was also noticed.

The ^{29}Si NMR spectrum of Na20 exhibits three distinct peaks at -61.9ppm (forsterite), -65.9ppm (monticellite) and -72.2ppm (akermanite) as well as a broad shoulder at -85.6ppm. The same mineral phases are detected in Na30 and Na40 but their relative intensities are different. Also in Na30 another distinct ^{29}Si peak at -74.4ppm is seen to emerge. As the Na20 content is increased above 40% the sharp crystalline peaks disappear to be replaced by the very broad silicate phase mentioned earlier. At 0 mol% Na_2O no such broad component is observed. As the Na_2O content is increased however, the growth of the broad component becomes quite prominent. The chemical shift of this phases varies with each addition of Na_2O, from -90ppm to -80ppm. At 30% and 40% Na_2O content, the phase practically dominates the entire spectrum. Several overlapping ^{29}Si peaks are present within the component which has a linewidth of about 1050Hz. For glaze samples Na60 to Na100 the spectra consist of a broad symmetrical peak at -78.8 to -80.8ppm are still in relatively high concentration compared to the sodium oxides and therefore determine which minerals are formed. However the equilibrium between akermanite and monticellite is altered by the presence of even small amounts of sodium oxide. This is manifested as significant changes in the relative intensities of the akermanite and monticellite peaks.

Fig. 5.4.1 ^{29}Si MAS NMR Spectrum of the Model Ceramic Glaze [Laponite + CaO + Na_2O] (10 to 40 mol% Na_2O)

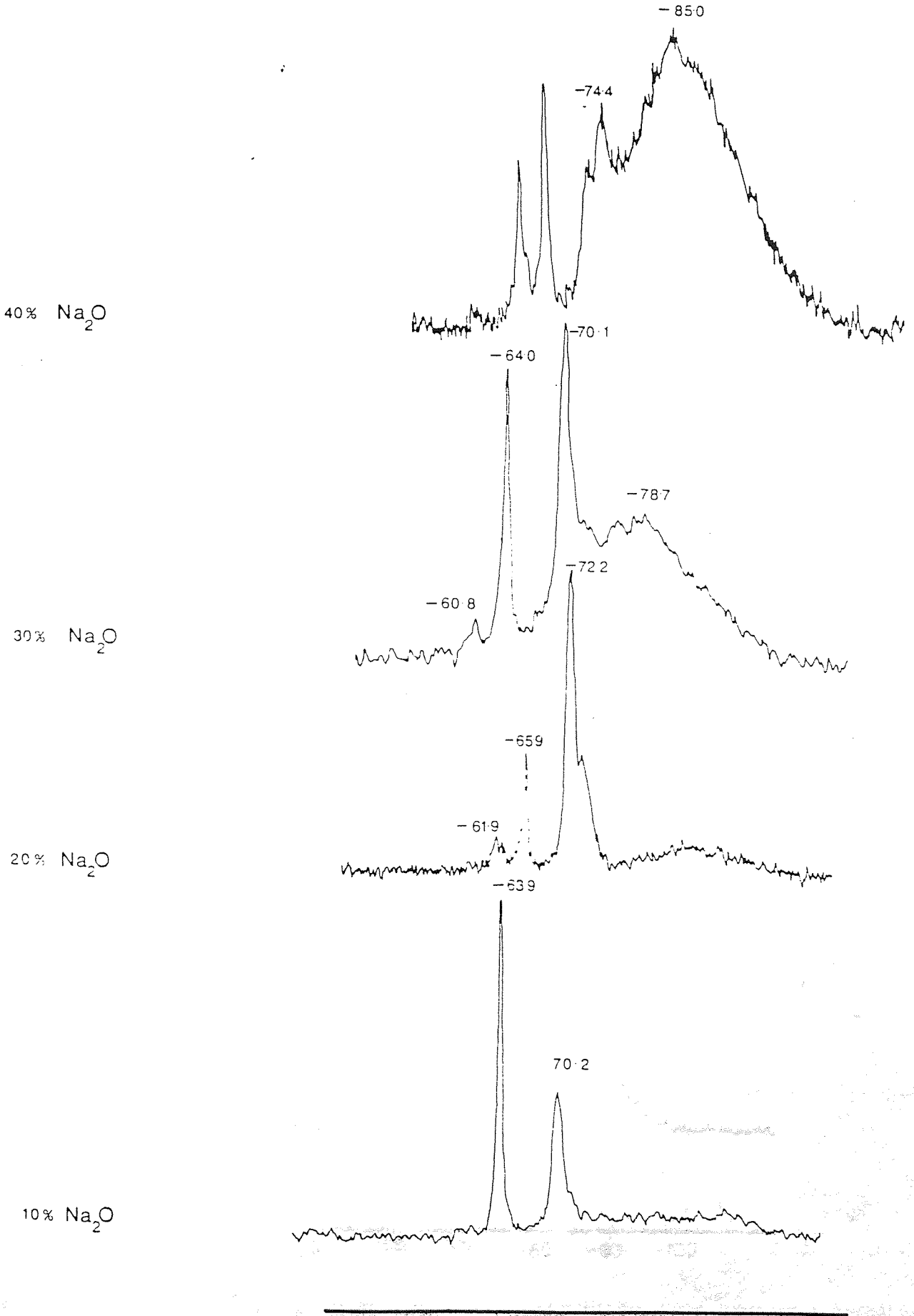

Fig. 5.4.2 ^{29}Si MAS NMR Spectrum for the Model Ceramic Glaze [Laponite + CaO + Na_2O] (60 to 100 mol% Na_2O)

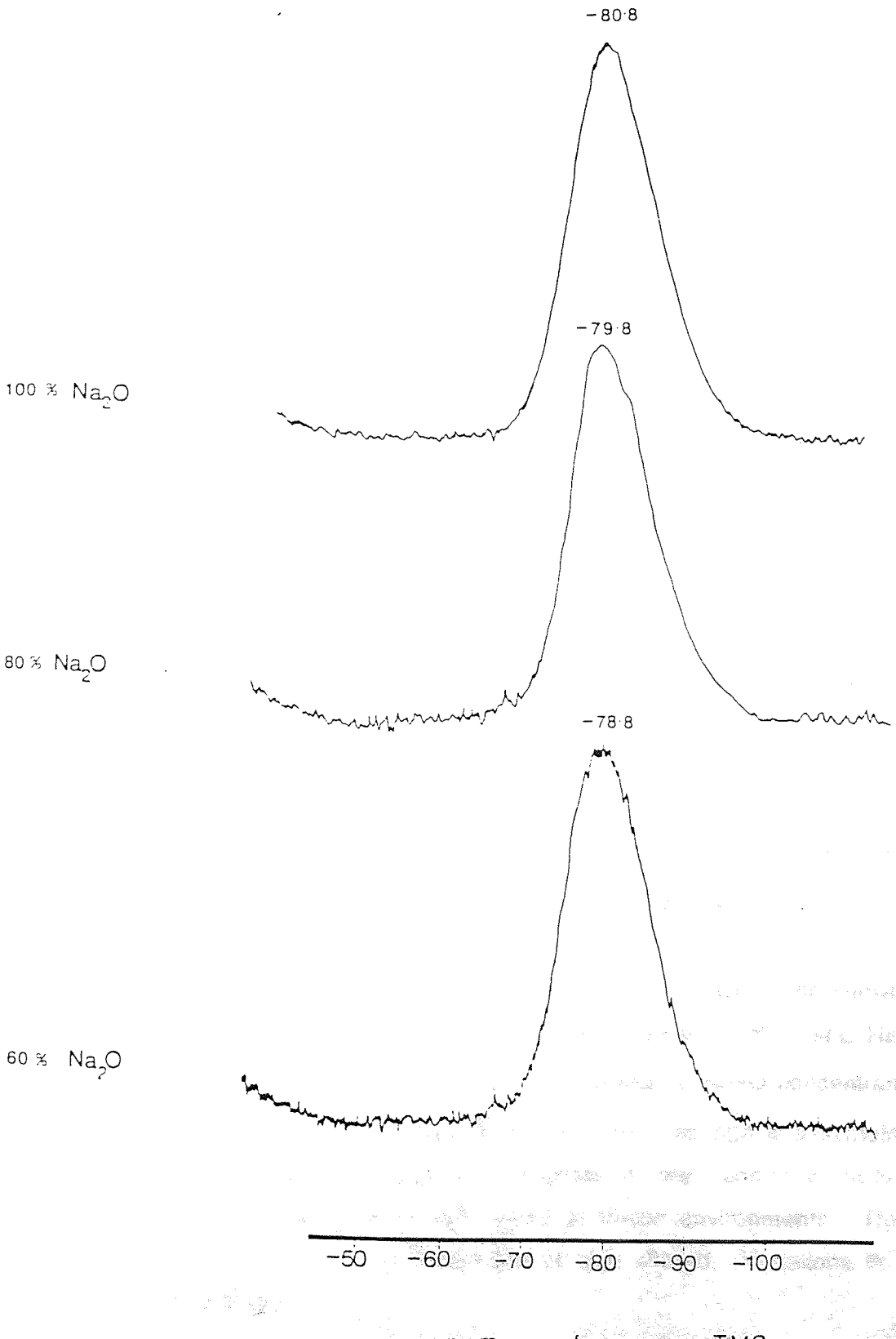

The broad silicate component can be detected as low as in Na10. There is a steady rise in the ^{29}Si signal intensity and linewidth up to 40 mol% Na_2O. We speculate that this is caused by the creation of non-bridging oxygens. Na_2O is known to break Si-O bonds in silicate network; the negatively charged non-bridging oxygens being replaced by Na^+ ions. On going from 40 to 60 mol% Na_2O there is a dramatic increase in the intensity of the broad component and the crystalline components disappear completely. This result reflects a completely different ^{29}Si local environment which is formed between 40% and 60 mol% of Na_2O. There is some similarity between this result and the results achieved by other workers. Dupree and Pettifer, and Grimmer et al found that for soda-silica glasses changes in the distribution of Q^m units occurred at 33% and 50% replacement of vitreous silica (Q^4) by sodium oxide. They showed that Na_2O is incorporated into vitreous silica by the progressive transformation of Q^4 silicons (four bridging-oxygens) into Q^3 silicons were found to be present; above this composition Q^3 were transformed into Q^2 by the progressive formation of non-bridging oxygens and sodium ion association, until at 50% Na_2O only Q^2 species were present.

In this study as the Na_2O content is increased, we observe a decrease in the chemical shift from -90ppm (Q^3 silicons) through -85ppm (Q^2 silicons), to -78ppm (Q^1 silicons). This reflects a gradual transformation of the sheet silicate Q^3 silicons into Q^2 silicons and eventually Q^1 silicons, by the continuous formation of non-bridging oxygens. The major change occurs between 40% and 60% Na_2O (probably 50 mol%). when all the crystalline phases are replaced by an amorphous, glassy phase consisting of Q^1 silicons.

By applying similar reasoning it is possible to explain the linewidth and lineshape changes of the non-crystalline phase. Between NaO and Na40, the linewidth increases by 200Hz for each 10% increase in Na_2O concentration. At Na40, the linewidth is approximately 800Hz and the lineshape is assymetrical. The change in linewidth is attributed to increase in the number of non-bridging oxygens which results in a broader range of silicon environments. The mean geometry around each silicon tetrahedron is also altered. Variations in the Si-O-Si bond angles and

Si-O bond length also contribute to the increased linewidth. In general an increasing disordered silicate structure is formed. Sharp, multiple peaks on the other hand are the result of crystalline phases where considerable long range order is present throughout the glaze.

5.5.3 Distribution of Q^m Silicate Units

The NMR results show that a different distribution of Q^m units exists at each different composition of the model ceramic glaze. As shown by the ^{29}Si spectra and the plot of ^{29}Si chemical shift versus mol% of Na_2O fig. 5.4.3, it is possible to differentiate between two completely different silicate phases present in the fired glazes; a crystalline mineral phase giving rise to sharp, distinct peaks with small linewidths, and a non-crystalline amorphous phase with a very large linewidth.

The appearance of the calcium and magnesium silicate minerals in glazes with low Na_2O content (NaO to Na40) can be explained by considering the oxide composition of each of the glazes. When no Na_2O is present, the glaze composition can be respresented as laponite + 100% CaO. Since CaO and MgO (from laponite) are the only fluxing oxides present then the formation of forsterite, monticellite and akermanite is expected. A low Na_2O content (Na10 to Na40) CaO and MgO sodium oxide concentrations above 40 mol% (Na60 to Na80) results in symmetrical but very borad peaks, reflecting a wholly disordered glass silicate environment. The chemical shift values indicate that the dominant silicate species is sodium metasilicate (Na_2SiO_3) which is a Q^1 silicate and has the structure shown below.

The symmetrical peaks imply that there is a greater uniformity in the symmetry and mean geometry of the individual SiO_4 tetrahedra. In other words most of the silicate species present are of a disilicate composition.

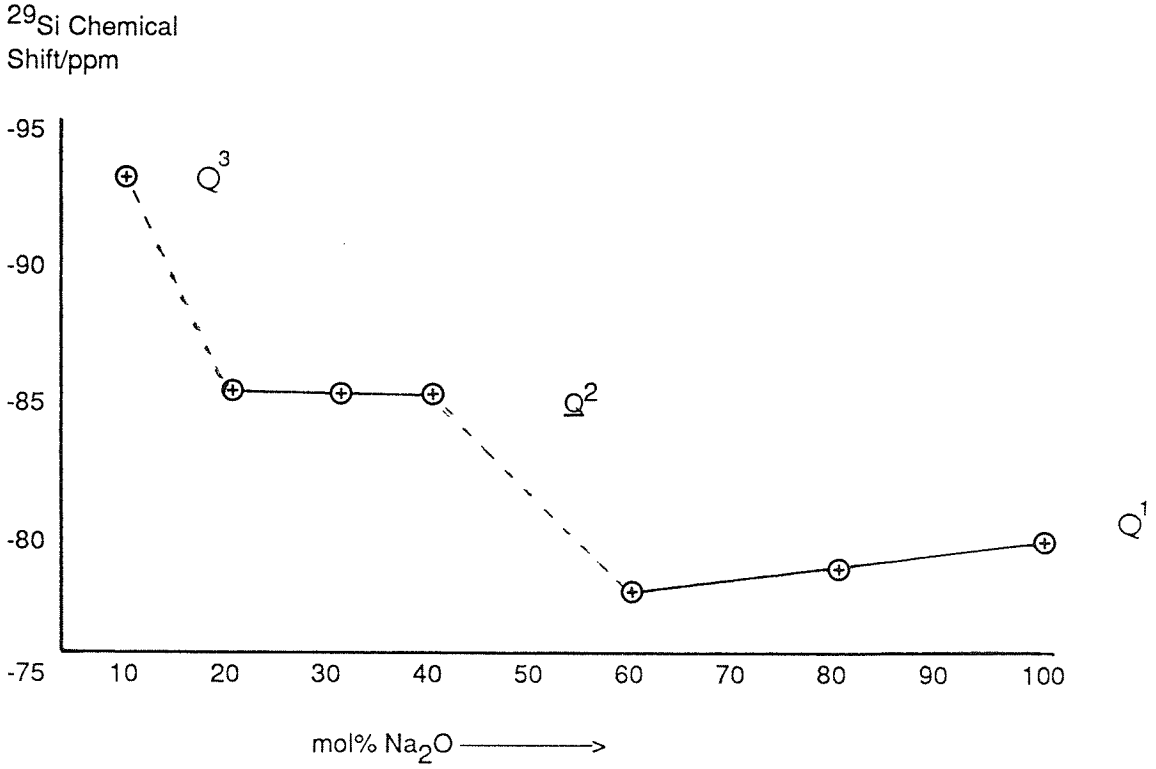
^{29}Si Chemical Shift/ppm
-95
-90
-85
-80
-75
Q^3
Q^2
Q^1
10
20
30
40
50
60
70
80
90
100
mol% Na_2O ⟶

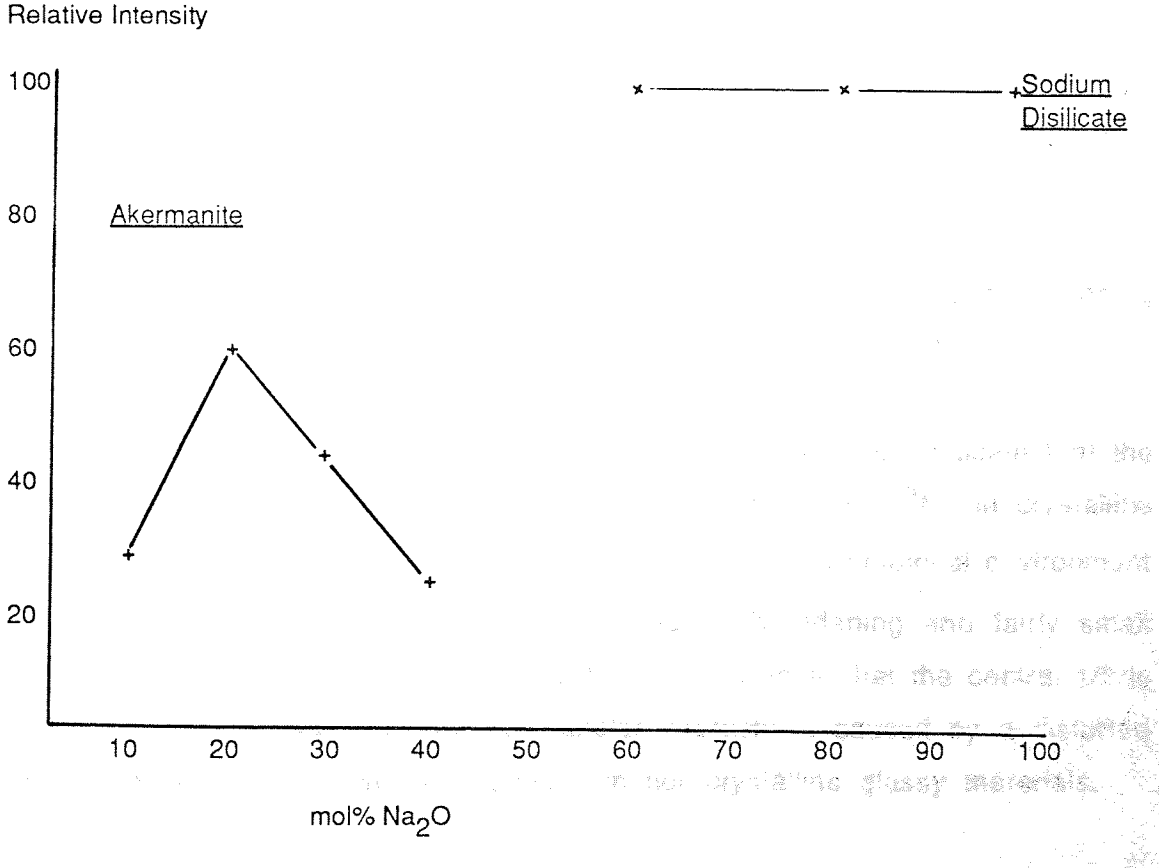
Relative Intensity
100
80
60
40
20
Akermanite
Sodium Disilicate
10
20
30
40
50
60
70
80
90
100
mol% Na_2O

5.5.4 ^{23}Na MAS NMR Data

The ^{23}Na NMR spectra of samples Na10 to Na100 are illustrated in Fig. 5.4.4, and the chemical shifts and linewidths are recorded in table 5.4.2. Because of the strong quadrupolar broadening of the ^{23}Na resonance and its smaller chemical shift variation in crystalline materials the ^{23}Na resonance is less informative than that for ^{29}Si. However, it is noteworthy that there is an apparent change in chemical shift with composition which implies a variation in the sodium environment.

The ^{23}Na spectrum for Na10 consists of a broad peak centred at -8.8ppm relative to NaBr, and a small but distinct shoulder at -10ppm. As the level of Na_2O in the ceramic glazes in increased only the broad central peak, representative of the $m_{=1/2}$ to $_{-1/2}$ transition is observed. The linewidth remains fairly constant throughout, at about 2.5 KHz. There does not appear to be any consistency to the chemical shift values which do not vary a great deal with each composition. However, it is possible to conclude that the Na^+ ions introduced into the model ceramic glaze are not associated with the crystalline mineral phases. Instead, as shown by the ^{29}Si NMR results, sodium oxide creates more non-bridging oxygens by breaking down the Q^3 silicate network. Na^+ ions become associated with the negative charge on these non-bridging oxygens, hence the relatively small variation in ^{23}Na chemical shifts.

Nevertheless, the very broad linewidths for the glaze samples indicate that the Na^+ local environment is considerably different from that of ^{23}Na in crystalline compounds, such as in Na_2O or NaBr where the highly symmetrical environment around the Na^+ ions produces little quadrupolar broadening and fairly small linewidths. The large linewidths of the fired glazes imply that the central 1/2 to -1/2 transition is broadened by quadrupolar interactions caused by a distorted structural environment which is present in non-crystalline glassy materials.

Fig. 5.4.4 ^{23}Na MAS NMR Spectra for the Model Ceramic Glaze [Laponite + CaO + Na_2O] (10 to 100 mol% Na_2O)

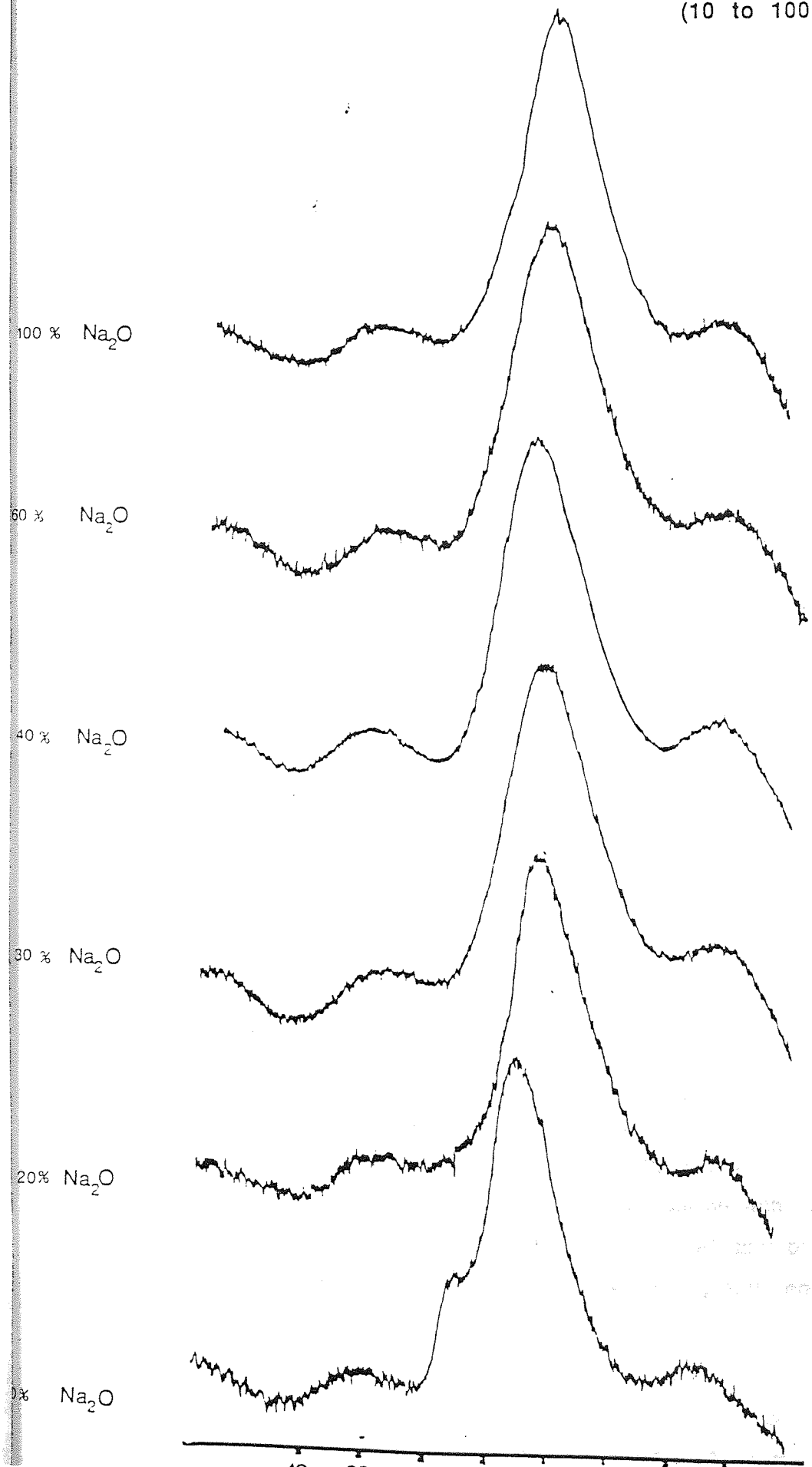

5.5.5 Infra-Red Data

Compared to the previous experiments in which calcium oxide alone was added to the glaze, the replacement of CaO by Na_2O produces marked changes in the i.r. spectra of the ceramic glazes. This is apparent from Fig.5.4.5 which shows the spectra of ceramic glazes of different compositions with increasing Na_2O content. The i.r. spectrum of Na20% is fairly similar to that of NaO% (ie 0% Na_2O/100% CaO). Little change occurs in the frequency of the absorption bands. The spectra of Na40 and Na60 however show marked changes. At 40% Na_2O there is an overall reduction in the number of absorption bands, and the emergence of new bands. For example, a series of shoulders at 1040, 1015 and 935cm^{-1} disappear and are replaced by a very broad absorption band at 988cm^{-1}, and a weaker band at 960cm^{-1}. There is quite a noticeable change in the principal Si-O stretching vibrational modes as the Na_2O content is increased.[108,109] At Na40 some of the mid-frequency bands representing bending vibrations of Si-O disappear. Another notable feature of the i.r. spectra is the growth of an absorption band at 920cm^{-1}. We speculate that this is due to the $Si\text{-}O^-$ or $^-O\text{-}Si\text{-}O^-$ bond stretching vibrations. The intensity increase of this band coincides with the fact that more non-bridging oxygens are created as the Na_2O content is increased. For ceramic glazes with a low Na_2O content there are a number of bands present below 500cm^{-1} which on addition of Na_2O are seen to merge into the continuum, resulting in a very broad, intense band at 487 -77cm^{-1}. This band is assigned to the motions of silicon atoms and also to weak Na^+ - O associations. The most notable overall feature of the i.r. spectra is the loss of virtually all sharp absorption bands above a 40% Na_2O content. This is in agreement with the ^{29}Si results which indicates a lack of long range order throughout the glaze. The i.r. spectra strongly resemble those for glassy, non-crystalline phases. The broadening is probably due to the fact that the dominant vibrational species present are silicon with two or three non-bridging oxygens. This explains the three very broad absorptions bands at 1011cm^{-1}, 980cm^{-1} and 477cm-1, due to $Si\text{-}O^-$ stretching and bending modes respectively.

Fig. 5.4.5 I.R. Spectra of M
Ceramic Glazes Laponite + Ca
Na_2O

5.6 A ^{29}Si, ^{27}Al MAS NMR STUDY OF THE EFFECT OF ALUMINIUM OXIDE (CORUNDUM) ON A MODEL CERAMIC GLAZE

5.6.1 Experimental

A model ceramic glaze composition was prepared using laponite, calcium carbonate and aluminium oxide (corundum) in the quantities expressed in the table below. The compositions were designed such that the molar percentage of CaO in the glaze is increasingly replaced by corundum (Al_2O_3). The mixtures were ground in an agate mortar and then fired at 1300°C for four hours in porcelain crucibles. The fired glazes were then removed from the furnace and allowed to cool to room temperature overnight in a vacuum desiccator.

5.6.2 ^{29}Si NMR Assignments

The model ceramic glaze under study in this section is composed of laponite, calcium-oxide and aluminium oxide, with alumina gradually replacing the calcium oxide content until the glaze mix consists of laponite and alumina in a 1:1 (SiO_2 : Al_2O_3) ratio. ^{29}Si NMR spectra are shown in Fig 5.5.1 and the chemical shift values and linewidths are recorded in table 5.5.1. For the sake of brevity each glaze sample is labelled by reference to the mol% of Al_2O_3 eg Al0%, Al20% and so on.

The ^{29}Si NMR spectra exhibit a variety of peaks in the shift range -62ppm to -95.5ppm. The different chemical shifts and lineshapes at each composition inidcate a different ^{29}Si local environment which changes significantly with composition of the glaze. At low concentrations of aluminium oxide (Al10 to Al40), the spectra consist of fairly sharp well defined peaks with a linewidth less than 50Hz, and with chemical shifts at -61.9, -66.2 and -72.2ppm for Al10; -62.0 and -72.2 ppm for Al20; and -62.0 and -72.2ppm for Al40. As well as these sharp well defined peaks a broad absorption component is also detected between -79 and -80ppm which becomes increasingly more intense and broader as the alumina content is increased.

Table 5.5A

Laponite/g	Al_2O_3(mol%)	CaO(mol%)	Al_2O_3/g	$CaCo_3$/g
3	0	100	0	2.7
3	10	90	0.46	2.43
3	20	80	0.93	2.16
3	30	70	1.39	1.89
3	40	60	1.86	1.62
3	60	40	2.79	1.08
3	80	20	3.72	0.54
3	100	0	4.55	0

Table 5.5.1 ^{29}Si NMR Results for the Modelled Ceramic Glaze Laponite + x CaO + (1-x) Al_2O_3

				Q^3			
	Q^0	Q^1	Q^2	3Al	2Al	1Al	0Al
Laponite		-84.1 10%					-9.6 90%
Al 10	-62.1 (12%) -66.2 (34%)	-72.3 (54%)					
Al 20	-62.0 (30%)	-72.2 (65%)		-79.0 (5%)			
Al 40	-61.9 (30%)	-72.1 (60%)		-80.4 (10%)			
Al 60				-80.4 100%			
Al 80	-61.9 (38%)				-84.7 (62%)		
Al 100					-84.9 (69%)		-95.5 (31%)

Table 5.5.2 ^{27}Al **Chemical Shift Assignments for the Modelled Ceramic Glaze Laponite + x CaO + (1 - x)** Al_2O_3

	Chemical Shift/ppm		Linewidth KHz^{-1}
	δ OCT	δ TET	
Al 20	0.6 - 6.5	60.2	2.1
Al 40	-	64.8	2.1
Al 60	-	55.8 - 59.6	2.2
Al 80	7.6 - 9.1	55.8 - 58.0	2.3
Al 100	10.6	68.2	2.3

Table 5.5.3 X-Ray Assignments

X-ray diffraction data for glazes Al20 to Al100 is shown in table 5.5.3. The mineral phases detected by XRD are summarised in table 5.5.3 below.

	%Al_2O_3 in Ceramic Glaze				
	Al 20	Al 40	Al 60	Al 80	Al 100
Akermanite ($Ca_2MgSi_2O_7$)	√	√	x	x	x
Forsterite (Mg_2SiO_4)	√	√	x	x	x
Monticellite ($CaMgSiO_4$)	√	√	x	x	x
Calcium Aluminate ($CaAlO_2$)	x	√	x	x	x
Spinel ($MgAl_2O_4$)	x	x	√	√	√
Corundum	x	x	x	√	√
Sillimanite (Al_2SiO_5)	x	x	x	√	√

At 60% Al_2O_3 (Al60) the sharp peaks disappear altogether and are replaced by a very broad resonance at -80.4ppm with a linewidth of almost 2000Hz and covering a chemical shift range from -40ppm to -120ppm (greater than the entire silicate shift range). At 80% Al_2O_3 (Al80) another very broad response (linewidth 1.2 KHz) is observed but there is also a sharp peak at -84.7ppm At 100% Al_2O_3 (Al100, when the alumina to silica ratio is 1:1) this sharp component appears as a single discrete ^{29}Si peak at -84.9ppm (linewidth 50Hz) implying a crystallographically distinct ^{29}Si site probably due to a mineral phase. Another very broad component is observed along with the sharp peak mentioned above. However, the broad silicate phase is shifted from the previous broad phase in A180 to -95.5ppm. This represents a diamagnetic shift of about -7.5ppm and the linewidth is considerably reduced to only 0.6 KHz.

It is apparent from the ^{29}Si results that substitution of Al_2O_3 for CaO into the ceramic glaze composition has a completely different effect from using CaO alone or Na_2O. Addition of the latter two oxides results in an overall depolymerisation of the silicate network (less negative chemical shifts). With aluminium oxide however, as CaO is replaced by alumina, the chemical shift becomes increasingly more negative. This points to a more polymerised network. It is possible to relate the ^{29}Si assignments to the relative proportions of CaO MgO and Al_2O_3 in the glaze mixes.

For the ceramic glazes Al10 and Al20 the relative concentration of CaO and MgO is greater than Al_2O_3 and thus calcium and magnesium silicate minerals can be expected to be formed. The peaks at -61.9ppm and -66.2ppm are assigned to the olivine silicates forsterite (Mg_2SiO_4) and monticellite ($CaMgSiO_4$), while the peak at -72.2ppm is assigned to the disilicate mineral akermanite ($Ca_2MgSi_2O_7$). The peak due to akermanite is more intense than the forsterite peak indicating that akermanite is the major component formed during the coolingof the fired glaze. Above 40% Al_2O_3 however these phases are not detected since the concentration of Al_2O_3 is far in excess of CaO and MgO.

Fig. 5.5.1 ^{29}Si MAS NMR Spectra for the Model Ceramic Glaz
[Laponite + CaO + Al_2O_3] (20 to 100 mol% Al_2O_3)

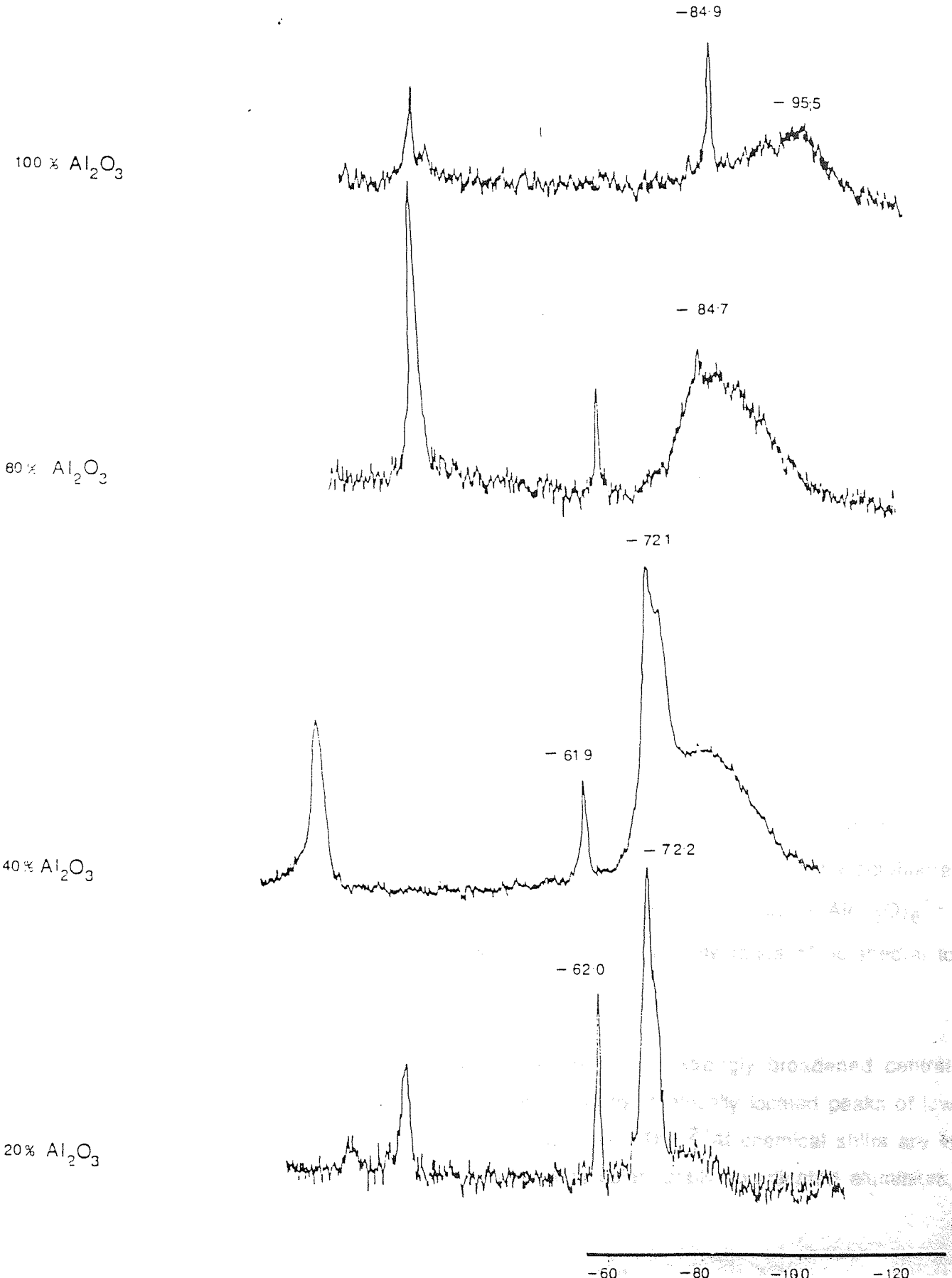

The assignment of the broad component at -80.4ppm present in glazes Na40 and Na60 is made more complicated than in purely silicate phases because of the presence of aluminium. Since aluminium has a similar charge/size ratio, aluminium atoms, when present in the correct quantity, are expected to substitute for Si atoms. Hence the Q^m units for layer silicates normally designated as Q^3 (or silicon surrounded by three SiO_4 tetrahedra) is now denoted by Q^3 (nAl), or silicon surrounded by SiO_4 tetrahedra and n (AlO_4) tetrahedra.

By adopting the mode of classification of layer silicates with substituted aluminium used by Kinsey et al[52], the broad peaks observed at -80.4ppm are assigned to Q^3(3Al) units. Similarly the ^{29}Si peaks at -84.7ppm and -84.9ppm (for Al80 and Al100) are assigned to Q^3(2Al) sites, while the broad ^{29}Si component at -95.5ppm (Al100) is assigned unequivocally to Q^3(0Al) silicon sites. Although the broad components are not attributable to crystalline phases, the sharp emerging peak at -84.7ppm (Al80) is clearly established at -84.9ppm (Al100) can be assigned to a crystalline component containing silicon atoms with Q^3(2Al) sites.

5.6.3 ^{27}Al MAS NMR Data

^{27}Al results for glazes Al10 to Al100 are summarised in table 5.5.2 and the spectra are recorded in Fig5.5.2. In table 5.5.2 the first column consists of mol% of Al_2O_3 added to the glaze mix denoted as Al10, Al20, and so on. The second and third columns respectively show the chemical shift of the octahedral and/or tetrahedral signal shifted from the reference compound $Al(H_2O)_6^{3+}$. Also recorded are the ^{27}Al linewidths and the intensity ratios of octahedral to tetrahedral signals.

In general the ^{27}Al spectra consist of one or two strongly broadened central peaks accompanied both sides by one or two symmetrically located peaks of low intensity, which represent spinning sidebands. The ^{27}Al chemical shifts are in the range from +2.7 to +10.6ppm indicating octahedrally coordinated aluminium,

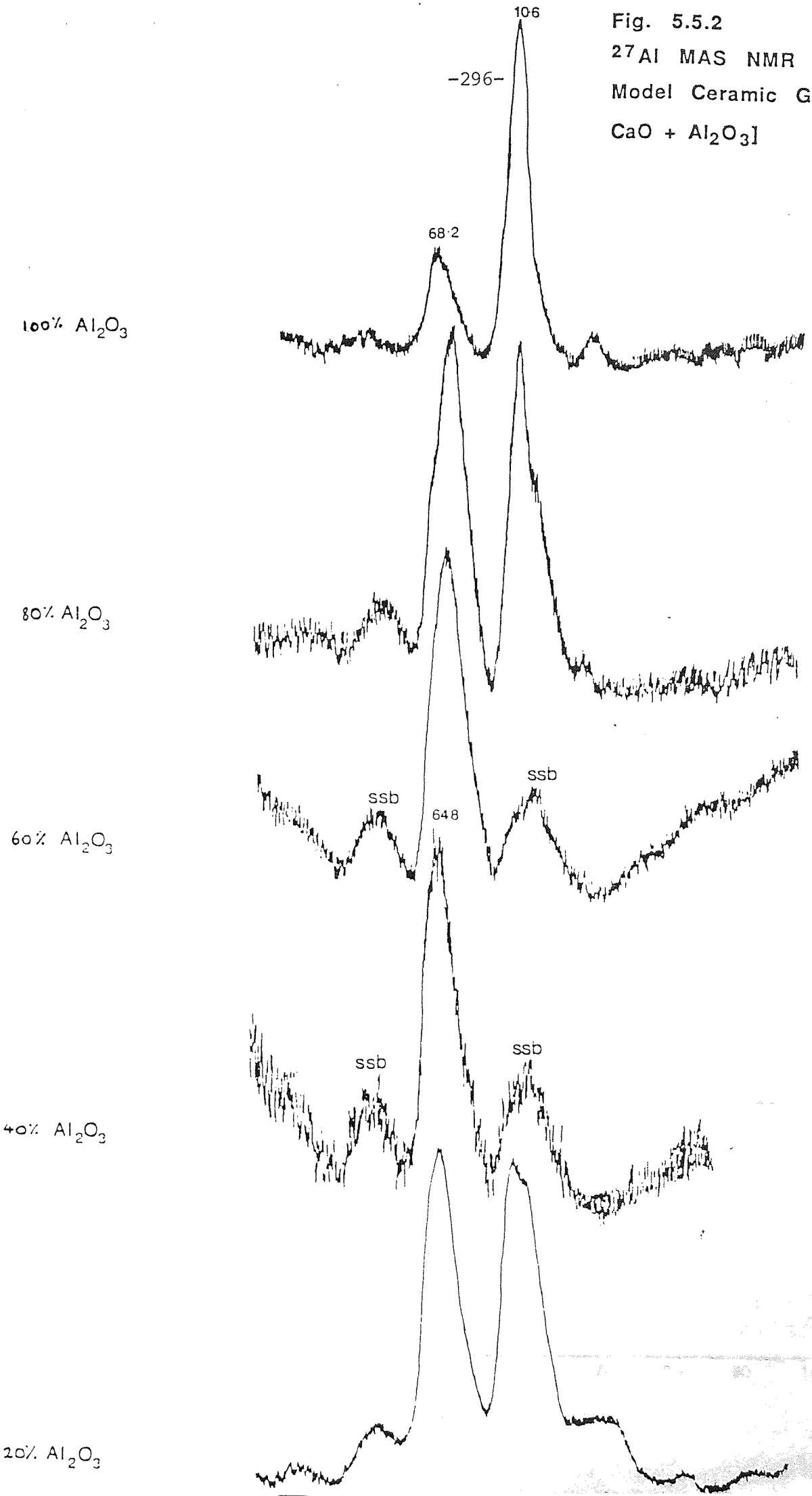

Fig. 5.5.2
^{27}Al MAS NMR Spectra for th
Model Ceramic Glaze [Laponite
CaO + Al_2O_3]

Fig. 5.5.5 Connectivity Versus Mol% of CaO and Al_2O_3. A Schematic Representation of the Effect on the Polymerisation State of the Dominant Silicate Species, of Two Different Modifier Oxides

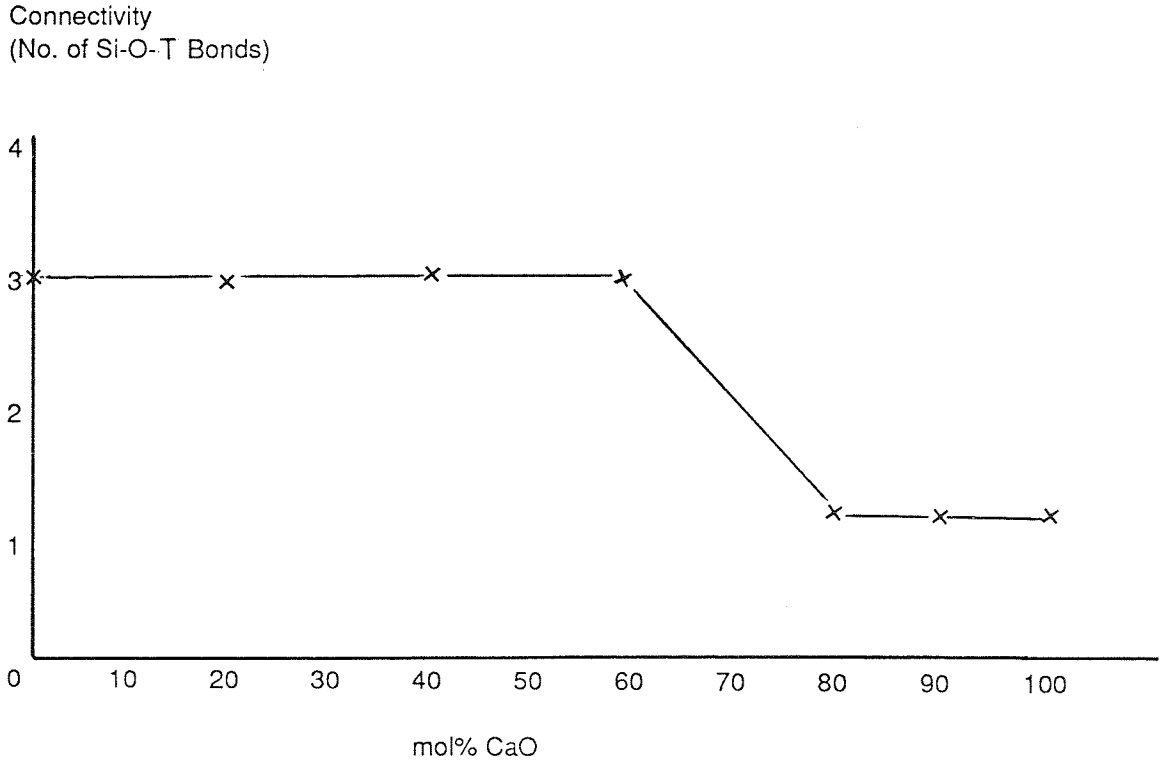

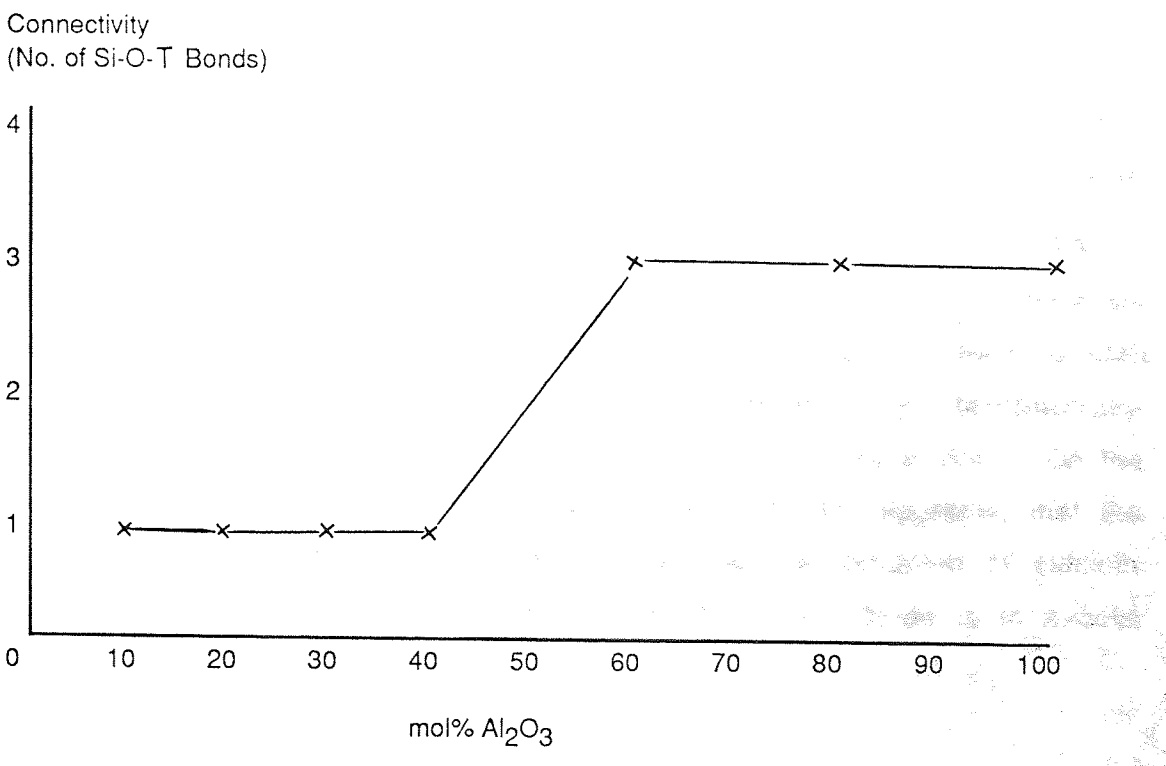

and from +55.7 to +68.2ppm indicating tetrahedrally coordinated aluminium. The size and range of chemical shifts obtained indicate that in all of the final glazes, ^{27}Al is present in sites of cubic symmetry, either octahedral or tetrahedral. No NMR signal for ^{27}Al in five coordination is observed which would be observed as a very broad resonance at around +35 to +38ppm. There does not appear to be any correlation between addition of Al_2O_3 (mol%) and either chemical shift values or octahedral and tetrahedral signal intensity ratios. the presence of tetrahedral aluminium [Al(4)] is detected in all samples with the chemical shift varying from +55.7 to +68.4ppm. Octahedral aluminium [Al(6)] detected in all samples except Al40 and Al60, and the signal becomes most prominent at high Al_2O_3 content. The [Al(6)] to [Al(4)] intensity ratios do not offer a great deal of information because each of the signals may be composed of several overlapping resonance lines due to the presence of separate ^{27}Al phases. Mueller er al found rough correlation between $^{27}Al(4)$ chemical shifts and the local Al environments, and have shown that Al(4) shift values depend on the number of aluminium next nearest neighbours. Since we also observe an Al(4) chemical shift range of about 14ppm it may be possible to comment on the environment of AlO_4^- tetrahedra.

5.6.4 Interpretation of ^{29}Si and ^{27}Al NMR Data

The structural model used for interpretation of the ^{29}Si and ^{27}Al NMR data is based on the structural units $Q^m(nAl)$, consisting of a central SiO_4 tetrahedron and its directly coordinated Si and Al atoms. When the Al_2O_3 concentration is relatively low compared to CaO and MgO, sharp peaks in the ^{29}Si spectra are readily assigned to crystalline calcium and magnesium silicates. The ^{27}Al NMR spectra show the presence of both octahedrally and tetrahedrally coordinatedaluminium in Al20 and only tetrahedral aluminium in Al40. On the basis of reported ^{29}Si NMR results and relevant phase diagrams, that the tetrahedral signals in Al20 and Al40 are due to the formation of calcium aluminate species which may be formed when calcium oxide is in excess concentration to Al_2O_3.[59]

The presence of a broad ^{29}Si NMR component is detected throughout the series of fired ceramic glazes Al10 to Al100. In Al20 the component is a weak shoulder at -79.0ppm. As the alumina content is increased, the band becomes broad and shifts to more negative chemical shift values (increased shielding of the ^{29}Si nucleus) to -80.4ppm, until at Al60 (60% Al_2O_3) the band engulfs the entire silicate shift range. With further increases in Al_2O_3 content the component undergoes a decrease in linewidth and further shifts to more negative shift value (-95.5ppm assigned to Q^3 (OAl)). We speculate that the growth in the band corresponds to Al atoms entering the silicate network. At low alumina content, Al_2O_3 acts as a network breaker and creates non-bridging oxygen sites,[67] the excess charge being neutralised by compensating cations that may be present, such as Mg^{2+}, Li^+, Al^{3+}, Ca^{2+}. The increasing linewidth up to Al60 is thus a manifestation of the disorder created in the glaze network by the increasing formation of non-bridging oxygens. Hence the geometry around each SiO_4 tetrahedron varies around the mean geometry of the network. The observed signal broadening therefore reflects the distribution of the geometry of individual SiO_4 units. Each different SiO_4 unit gives rise to a slight different resonance value for the ^{29}Si nucleus (ie varying chemical shift) which thus broadens the signal.[60]

Above 60% Al_2O_3 content however, Al enters the silicate network by substituting for silicon atoms and forming AlO_4^{5-} tetrahedra. Calcium aluminates are not expected to be formed when the Al_2O_3 content is much greater than the CaO content.[61] Thus the Al(4) signals observed are most like due to AlO_4^{5-} tetrahedra. The result is reflected as a diminution of the ^{29}Si linewidths with increasing polymerisation of the glaze network and is explained in terms of a more homogeneous distribution of SiOSi(Al) bond angles and Si-O bond distances; in other words a more relaxed structure within the glaze network.[61]

The assignment of the sharp distinct NMR signal in Al80 and Al100 (at -84.7 and -84.9ppm) to the aluminosilicate mineral sillimanite illustrates how ^{29}Si and ^{27}Al can be combined effectively to positively identify both the local structural

environment and the species present. As the Al_2O_3 to SiO_2 ratio approaches 1:1, three polymorphs with a molecular composition Al_2O_3 : SiO_2 can be envisaged, namely sillimanite, andalusite and kyanite. Our results indicate a local silicon environment for the crystalline phase of $Q^3(2Al)$, a chemical shift of -84.7ppm, and ^{27}Al present in both octahedral and tetrahedral sites.

Kyanite is discounted on the grounds that its ^{29}Si spectrum exhibits Q^o type silicon sites and the ^{27}Al is in five-coordination with oxygen atoms giving a quadrupolar broadened spectrum.[50] Andalusite is also discounted since it has only Q^o silicon sites and the ^{27}Al is in tetrahedral sites only.[50] On the other hand, sillimanite is known to exhibit $Q^3(2Al)$ silicon peaks and ^{27}Al in both octahedral and tetrahedral sites, [44] and our results fit this data very well. The structure of sillimanite is shown overleaf:

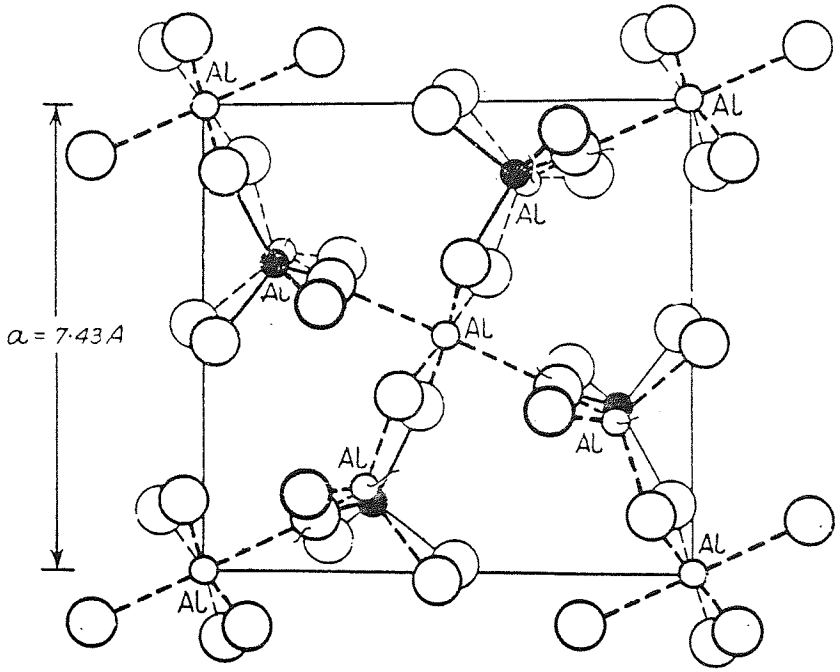

Fig. 5.5.3 The Structure of Sillimanite ($AlSi_2O_5$)

The sillimanite unit cell is orthorhombic. Aluminium atoms are at the corners and at the centre of the unit cell in the projection along the c-axis. Thus there are two different coordinations of aluminium ie Al(4) and Al(6) which give rise to corresponding ^{27}Al NMR signals. These aluminium atoms are linked to other similar atoms immediately below and above them and so there is a series of chains of aluminium oxygen linkages running parallel to the c-axis and linked

laterally by silica tetrahedra and tetrahedrally coordinated aluminium.

When chemical shift values for $^{27}Al(4)$ (tetrahedral) signals are considered a significant variation in these values is noted. The large differences in chemical shift for Al(4) may indicate a difference in Lewis acidity of the aluminium ion. This may be caused by alkali (Li^{+}) and alkaline earth ions ($Ca^{2+}Mg^{2+}$) attached to the aluminate polyhedron. Thus strong electron acceptors such as magnesium and lithium ions or protons are capable of inducing a large charge transfer from $^{1}Al(4)$, resulting in low residual electron density on the aluminium ion, and consequently a large negative chemical shift of Al(4), and hence a tendency for this ion to accept electrons. De Jong and others[59] have considered the possibility that the presence of alkali or alkaline earth ions and more probably protons, are capable of influencing the formation of certain crystalline minerals depending on exactly how the aluminium atoms are coordinated. Thus ^{27}Al NMR may provide a sensitive indicator in following such reactions.

5.6.6 Infra-Red Data

Replacement of CaO by Al_2O_3 in the modelled ceramic glaze produces significant changes in the i.r. spectra, particularly at high Al_2O_3 content. The i.r. spectra are displayed in Fig. 5.5.4. At low Al_2O_3 content (Al_2O and Al_4O) the spectra show a variety of sharp well defined absorption bands indicative of a similar glaze environment to that of the glaze composed of laponite + CaO (100 mol%), except for minor differences. The band at 1040cm^{-1} disappears into the continuum and peaks representative of Si-O lattice stretching vibrations at 1019, 980 and 936cm^{-1} are retained with similar intensities. The Si-O lattice bending modes (700 - 500cm^{-1}) are also unchanged as is the very strong, broad mode at 478cm^{-1} due to O - M association. This means that introduction of Al^{3+} into the system has little impact on this mode. One of the main changes observed however, is the emergence of weak bands at 769cm^{-1} and 710cm^{-1} which are thought to be due to AlO_4^{5-} tetrahedra. [110, 111]

The spectra for Al60 and Al80 differ markedly form the previous ones in that most of the individual i.r. bands are lost at Al60 due to broadening of the main vibrational modes. Hence at Al60 we only observe three very broad main frequency bands in the regions 1080 to 920cm^{-1}, 697cm^{-1} and 520 to 400cm^{-1}. The ^{29}Si spectrum of Al60 also shows a very broad signal thought to arise partly from AlO_4^- tetrahedra entering the first and second coordination sphere of the silicate tetrahedra. Broadening of the i.r. bands is another sign of the increasing disorder occurring in the glaze network. The appearance of a shoulder at 1080cm^{-1} is in line with the result obtained by Rindome who observed a shift of the main Si-O vibrational frequencies as Na_2O was replaced by Al_2O_3.[110]

The i.r. spectra of Al80 and Al100 show further important changes and frequency shifts. The broad band at 1080cm^{-1} (in Al60) is split into a number of distinct, sharp shoulders and the frequency of vibration shifts to 1130cm^{-1}. A variety of bands also appear in the mid-frequency region of the spectrum between 700 and 500cm^{-1}. We believe that these bands can be attributed to the

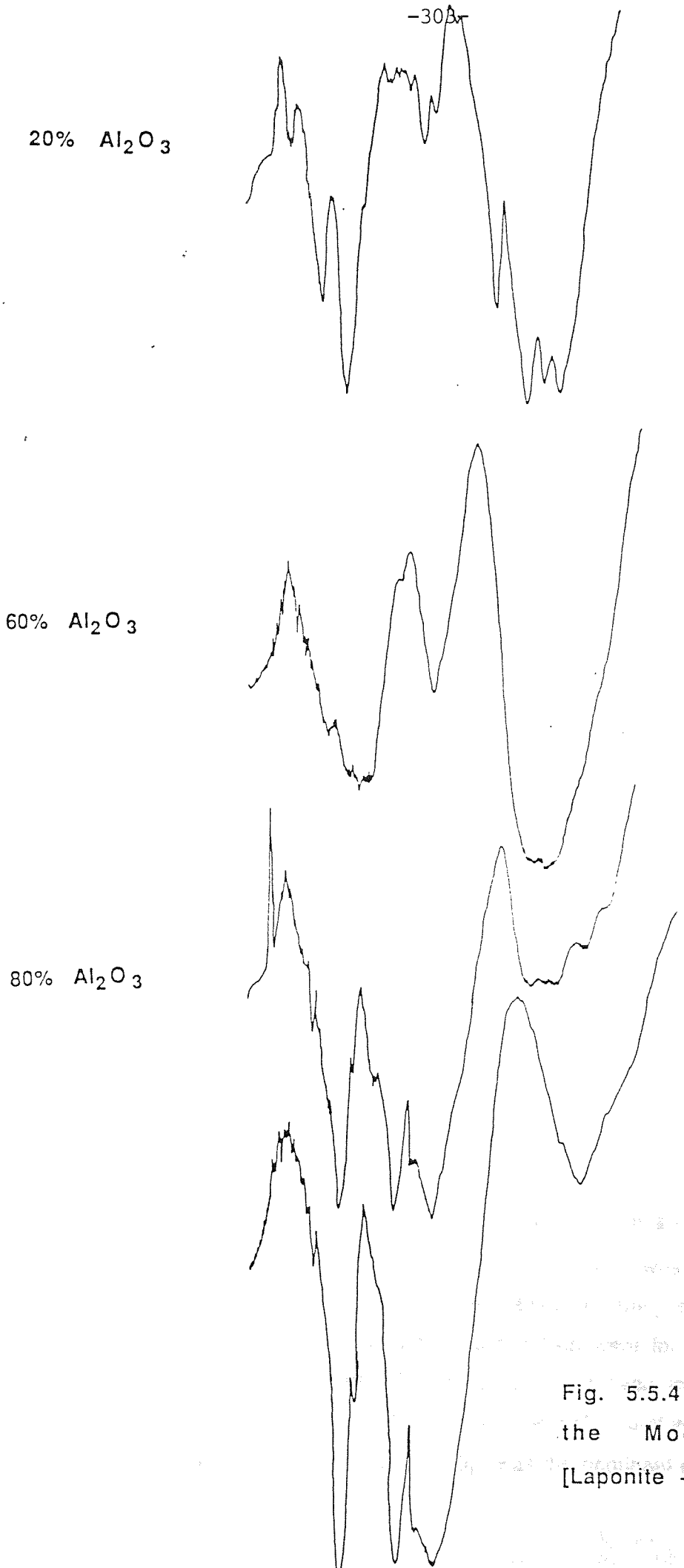

Fig. 5.5.4 F.T.I.R Spectra for the Model Ceramic Glaze [Laponite + CaO + Al_2O_3]

presence of sillimanite at A180. The i.r. spectrum of Al100 is consistent with the presence of sillimanite.[111]

In sillimanite, perturbation of the Si-O vibrations caused by four-coordinate aluminium is extraordinary. The stretching frequency observed in Al100 as shoulders at 1200 and 1185cm^{-1}, is one of the highest in the whole field of silicate spectra. The bands above 700cm^{-1} are assigned in terms of the vibrations of the ribbon anions consisting of alternating SiO_4 and AlO_4 tetrahedra. The 1200cm^{-1} band is attributed to the vibration of oxygen in the almost linear Si-O-Al bonds that link the two chains forming the ribbon. This high frequency correlates well with the abnormally short Si-O and Al-O distances in these bonds. The bands in the region 1000-900cm^{-1} are assigned to assymmetric type Al-O-Si vibrations of oxygen. The decrease in broadness of the bands in going from Al60 to Al100 is also seen in the ^{29}Si NMR spectrum and due to ordering of Al and Si tetrahedra in the formation of sillimanite.

There is also evidence for the presence of spinel ($MgAl_2O_4$) in Al80 and Al100, although some of the i.r. bands strongly overlap with those of sillimanite. Diagnostic i.r. bands for spinel are a distinct shoulder at 1080cm^{-1}, a very broad band at 1020cm^{-1} and a strong band at 690 - 85cm^{-1}, which is due to Al-O$^-$ stretching modes in AlO_4^- tetrahedra.

5.6.7 Conclusions

In the preceding studies 29Si MAS NMR X-Ray Diffraction and Infra-Red spectroscopy have been used to look at the effects of different network modifier oxides CaO, Na_2O and Al_2O_3 on the network structure of a model ceramic glaze based on laponite. In the first study calcium oxide alone was added in increasing quantities to laponite. At each glaze composition a variety of crystalline mineral phases were formed, the relative amounts of which were found to be dependent on the calcium oxide content. The proportions of each mineral formed in a particular glaze mix were calculated from the ^{29}Si relative intensity values. Below 60 mol% CaO diopside ($CaMgSi_2O_6$) was the dominant glaze component,

while akermanite ($CaMgSi_2O$) was the major component formed above 60mol% CaO. Minor quantities of forsterite (Mg_2SiO_4) and monticellite were also formed at all CaO concentrations up to 100 mol%.

In the second study the CaO content was increasingly replaced by sodium oxide. At low Na_2O content the calcium silicate minerals akermanite, forsterite and monticellite were detected by ^{29}Si NMR, whereas at relatively high Na_2O content (above 60 mol% Na_2O) the majority of the silica was converted to a sodium metasilicate (Na_2SiO_3) phase. In the last study, the CaO content was increasingly replaced by aluminium oxides in the form of corundum. At low Al_2O_3 content, calcium silicate minerals were again detected as shown in table 5.5.5, but at higher Al_2O_3 content other aluminate and aluminosilicate minerals such as spinel ($MgAl_2O_4$) and sillimanite (Al_2SiO_5) were detected by NMR and XRD.

The different effect of the three oxides CaO, Na_2O and Al_2O_3 was clearly illustrated by ^{29}Si NMR spectra and chemical shift values, particularly by the effect of each oxide on the overall polymerisation state of the glaze network. Both CaO and Na_2O produced a decrease in the polymerisation state from Q^3 to Q^o, by the increasing formation of non-bridging oxygens with oxide content. Calcium oxide produced a variety of mineral phases and the glaze network had considerable long range order, whereas Na_2O (especially in higher quantities) produced an amorphous, non-crystalline network with very little long range order. On the other hand aluminium oxide showed opposing trends to both calcium and sodium oxides. Aluminium entered the network by eliminating non-bridging oxygens and by substituting for silica tetrahedra as aluminate tetrahedra in the second coordination sphere of silicon atoms. Alumina therefore acted as a network former rather than a network breaker. The overall effect was to maintain the Q^3 polymerisation state by forming $Q^3(nAl)$ tetrahedra, although an alumino-silicate mineral sillimanite was also formed. The relative effects of the three oxides on the glaze polymerisation state can be compared by considering the connectivity of silica tetrahedra as shown in fig. 5.

Silicon -29 and aluminium -27 MAS NMR have proved to be very sensitive techniques for detecting various mineral phases in the presence of each other. Since NMR is sensitive to the local nuclear environment. each phase is manifested by discrete ^{29}Si peaks and the chemical shift values are very reproducible and do not vary greatly even if several 'impurity' phases are present. There is an added advantage in that the relative peak intensities allow us to ascertain the proportions of each mineral present in the glaze. Another advantage of the NMR technique is that amorphous, non-crystalline and aluminosilicate phases can also be detected. Hence this is a very powerful technique for following reactions in complex inorganic solids. X-ray diffraction and IR however were severely affected by presence of more than one mineral phase, giving in both techniques overlapping peaks. Only a limited amound of data could be obtained from these techniques and they are therefore merely complimentary to solid state NMR in the study of complex mixed-mineral phases.

	mol % SiO_2					mol % CaO				
SiO_2	Laponite + CaO									CaO
0	10	20	30	40	50	60	70	80	90	100
100 $Mg_2Si_2O_6$ Mg_2SiO_4 Li_4SiO_4	90	80 $Mg_2Si_2O_6$ Mg_2SiO_4 $CaMgSi_2O_6$	70	60 Mg_2SiO_4 $CaMgSi_2O_6$	50 Mg_2SiO_4 $CaMgSi_2O_6$	40 Mg_2SiO_4 $CaMgSi_2O_6$ $Ca_2MgSi_2O_7$	30	20 Mg_2SiO_4 $CaMgSiO_4$ $CaMgSi_2O_6$ $CaMgSi_2O_7$	10	0 Mg_2SiO_4 $CaMgSiO_4$ $Ca_2MgSi_2O_7$
	Laponite [CaO + Na_2O]									
		mol % CaO				mol % Na_2O				
CaO										Na_2O
0	10	20	30	40	50	60	70	80	90	100
100 Mg_2SiO_4 $CaMgSiO_4$ $Ca_2MgSi_2O_7$	90 $CaMgSiO_4$ $CaMgSi_2O_7$	80 $MgSiO_4$ $CaMgSiO_4$ $Ca_2MgSi_2O_7$	70 Mg_2SiO_4 $CaMgSiO_4$ $Ca_2MgSi_2O_7$	60 Mg_2SiO_4 $CaMgSiO_4$ Na_2SiO_3	50	40 Na_2SiO_3	30	20 Na_2SiO_3	10	0 Na_2SiO_3
	Laponite CaO + Al_2O_3									
CaO										Al_2O_3
0	10	20	30	40	50	60	70	80	90	100
100 Mg_2SiO_4 $CaMgSiO_4$ Ca_2MgSiO_6	90 Mg_2SiO_4 $CaMgSiO_4$ Ca_2MgSiO_6	80 Mg_2SiO_4 Ca_2MgSiO_6	70	60 $MgSiO_4$ Ca_2MgSiO_4	50	40 $MgAl_2O_4$	30	20 $MgAl_2O_4$ Al_2SiO_5	10	0 $MgAl_2O_4$ Al_2SiO_5

Table 5.5.5 A Summary of the Mineral Phases Detected by ^{29}Si MAS NMR in Various Glaze Compositions Based on Laponite

CHAPTER 6

A SOLID-STATE MAS NMR STUDY OF THE EFFECT OF SELECTED NETWORK MODIFYING OXIDES ON A MODEL FELDSPAR GLAZE

6.1 INTRODUCTION

In the previous chapter, the clay mineral laponite was used in the glaze mix as the only component which provided a source of silica, and the silica provided was of the Q^3 type in the form of a two dimensional sheet network. In the proceeding study a different source of silica in the form of a fully cross-linked three dimensional (Q^4) network was used. Feldspar is an ideal glaze component as it contains a Q^4 silica network. Indeed feldspathic glazes consisting of feldspar, whiting ($CaCO_3$) and sometimes a little clay are commonly used on cheap earthenware and white sanitory ware, a well-known example being Bristol glaze.

The structure of feldspars is based on a framework of SiO_2, but one which is more open than that of the other silicate minerals. There is some replacement of silicon by aluminium ions however which results in charge deficiencies, balanced by K^+, Na^+, Ba^{2+} or Ca^{2+} cations entering the lattice as follows:

$$4\ SiO_2 = Si_4O_8 = Si^{4+}\ Si_3O_8 = Si_2^{4+}\ Si_2O_8$$

$$Na{+}Al^{3+}Si_3O_8 \qquad Ca^{2+}Al_2^{3+}Si_2O_8$$

Albite (sodium feldspar, $NaAlSi_3O_8$) and anorthite (calcium feldspar, $CaAl_2Si_2O_8$) are regarded as end members of a complete series of solid solutions which are termed the plagioclase feldspars. Albite ($NaAlSi_3O_8$) was selected as the basis of the glaze composition to be studied. Natural feldspars however, contain structural iron impurities and therefore are unsuitable for NMR studies. Hence the composition of albite feldspar was mimicked by choosing the constituent oxides which made up the natural mineral. The oxide composition is written as:

$$(Na_2O)\ (Al_2O_3)\ (SiO_2)_6$$

The above composition was used as the basic glaze component throughout the following study. The nature of the glaze was altered by addition of oxides containing cations of CaO, Li_2O,SrO and BaO.

6.2. Experimental

The oxides were mixed and ground together in the compositions shown in the tables 6.A to 6.D. The oxides were added as carbonates (analar reagents). The glaze mixes were fired in porcelain crucibles for four hours at 1300°C. After firing the glaze melts were quenched by placing in a vacuum desicator immediately, and leaving to cool overnight.

6.2. GLAZE COMPOSITIONS

6.2.1 Addition of Calcium Oxide to Albite Composition

Composition Range Based on consititutent oxides	$(CaO)_{1.2}(Na_2O)(Al_2O_3)(SiO_2)_6$ to $(CaO)_6(Na_2O)(Al_2O_3)(SiO_2)$

Glaze Components

Quartz	2.23g
Silica (amorphous)	2.23g
Sodium Carbonate (analar)	0.76g
Aluminium Oxide (analar)	1.26g
Calcium Carbonate (analar)	(see table 6.A)

Calcium oxides (as the carbonate) was added to produce the albite composition based on the molar percentage of the total silica content as shown below.

Table 6A

SiO_2 (mol%)	CaO (mol%)	$CaCo_3$(g)
100	0	0
100	20	2.25
100	40	4.50
100	60	6.75
100	80	9.00
100	100	11.25

6.2.3 Addition of Lithium Oxide to Albite Composition

Composition Range Based on Consistent Oxides	$(Li_2O)_{0.3}$ (Na_2O) (Al_2O_3) $(SiO_2)_6$ to $(Li_2O)_{3.0}$ (Na_2O) (Al_2O_3) $(SiO_2)_6$
Glaze Components	
Quartz	2.23g
Silica (amorphous)	2.23g
Sodium Carbonate (A)	0.76g
Aluminium Oxide (A)	1.26g
Lithium Carbonate (A)	(table 6B)

Lithium Oxide (as carbonate) ions added to the albite composition based on the mol% of the total silica content.

Table 6B

SiO_2 mol%	Li_2O mol%	Li_2Co_3(g)
100	0	0
100	5	0.37
100	10	0.75
100	20	1.50
100	30	2.25
100	40	3.00
100	50	4.25

6.2.4 Addition of Strontium Oxide to Albite Composition

Composition Range Based on Constituent Oxides	$(SrO)_{0.6}$ (Na_2O) (Al_2O_3) $(SiO_2)_6$ to $(SrO)_6$ (Na_2O) (Al_2O_3) $(SiO_2)_6$
Glaze Components	
Quartz	2.23g
Silica (amorphous)	2.23g
Sodium Carbonate	0.76g
Aluminium Oxide	1.26g
Strontium Carbonate	(table 6c)

Table 6C

SiO_2 (mol%)	SrO (mol%)	$SrCO_3$ (g)
100	0	0
100	10	0.82
100	20	1.64
100	30	2.46
100	40	3.28
100	50	4.05
100	100	8.21

6.2.5 Addition of Barium Oxide to Albite Composition

Composition Range	$(BaO)_{0.6}$ (Na_2O) (Al_2O_3) $(SiO_2)_6$ to
Based on Constituent Oxides	$(BaO)_{6.0}$ (Na_2O) (Al_2O_3) $(SiO_2)_6$

Glaze Components

Silica (amorphous)	2.23g
Quartz	2.23g
Sodium Carbonate	0.76g
Aluminium Oxide	1.26g
Barium Carbonate	(table 6D)

Table 6D

SiO_2 (mol%)	BaO (mol%)	$BaCO_3$ (g)
100	0	0
100	10	2.22
100	20	4.45
100	30	6.69
100	40	8.91
100	50	11.14
100	100	22.30

Table 6.1 ^{29}Si MAS NMR Results for a Model Feldspar Ceramic Glaze with Increasing Mol% of Calcium Oxide

	Q^0	Q^1	Q^2	Q^3	Q^4 (4Al)	Q^4(3Al)	Q^4(2Al)	Q^4(1Al)	Q^4(0Al)
Silica									-109
Quartz									-108
0% CaO						-93.3			
20% CaO							-99.5		
40% CaO					-83.6	-89.9			
60% CaO	-69.7				-83.6				
80% CaO	-71.5				-83.8				
100% CaO	-71.5	-73.8			-83.9				

Table 6.2 ^{27}Al and ^{23}Na MAS NMR Results for a Model Feldspar Glaze Containing Increasing Mol% of Calcium Oxide

	^{27}Al Resonance		^{23}Na Resonance	
	δ (TET) (ppm)	δ (OCT) (ppm)	$\delta^{23}Na$ (ppm)	Linewidth (Hz)
0%	52.9 (16)	-	-21.5	2000
10% CaO				
20% CaO	52.7 (16)	6.2 (16)	21.1	2250
30% CaO				
40% CaO	54.2 (20)	-	-20.9	2250
60% CaO	54.9 (1)	8.1 (6)	-18.0	3000
80% CaO	81.3 (1)	4.2 (3)	-12.4	17,350
100% CaO	80.4 (2)	7.5 (1)	-10.5	2250

6.3. CALCIUM OXIDE ADDITION TO A MODEL FELDSPAR GLAZE

6.3.1 ^{29}Si MAS NMR Data

The ^{29}Si NMR spectra of the model feldspar glaze with added calcium oxide exhibit a series of broad and then sharp resonance peaks which reflect the changes in the local silica environment within the glazes. The linewidth varies with CaO content from 1270H_z for 20 mol%.CaO, to 7OHz for 60 mol% CaO. Figure 6.1 displays the ^{29}Si spectra of the glazes. The ^{29}Si chemical shifts and linewidths are summarised in table 6.1. The chemical shift values are in the range -99ppm to -71.5 ppm which is typical of SiO_4 terahedra in aluminosilicates. Distinct paramagnetic chemical shifts are observed with each addition of CaO.

The ^{29}Si NMR spectrum for pure silica and quartz show typically sharp but weak resonance signals with a noisy base line, at -109 and -108 ppm respectively. The large number of transients (FID'S) needed to display the signals reflect the very long transverse relaxation times of ^{29}Si nucleus in such environments. The chemical shift values are typical of silicon in a pure Q^4 environment ie. a three dimensional framework structure where each SiO_4 tetrahedron is linked to four other SiO_4 tetrahedra.

The model feldspar mix contains Al_2O_3, Na_2O, silica and quartz in the composition (Na_2O) (Al_2O_3) $(SiO_2)_6$ which is typical of the sodium feldspar, high albite ($NaAlSi_3O_8$). The ^{29}Si spectrum of the mimicked high albite glaze shows a broad symmetrical peak centred at -93.3 ppm (FWHM = 1300H_z), covering a shift range of -80 ppm to -110 ppm region assigned to Q^4(2Al) silica units. Addition of 20 mol% CaO to the model albite composition [giving a new oxide composition $[(CaO)_{1.2}$ (Na_2O) (Al_2O_3) $(SiO_2)_6]$ produces a similarly broad ^{29}Si peak centred at -99.0 ppm covering a shift range from -80 ppm to -110 ppm, and is assigned to Q^4(2Al) silica units. At 40 mol% CaO

[composition $(CaO)_{2.4}(Na_2O)(Al_2O_3)\ (SiO_2)_6$] a distinct sharp peak at -83.6 ppm overlapping with a broad peak at -89.9 ppm is observed. At 60 mol% CaO the previously sharp peak at -83.6 ppm develops into a broad, asymmetrical peak centred at -83.6 ppm, covering a shift range of -70 to 100 ppm. A significant change occurs in the spectrum at 80 mol % $CaCo_3$; the spectrum consists of two distinct, sharp peaks at -71.5 ppm and -73.9 ppm both of which are assigned to Q^0 silica sites. The relatively small linewidths (70Hz) for the sharp peaks imply crystallographically distinct silica sites. The most notable trend in this series of model glazes is the distinct paramagnetic shift of about 5-10 ppm with each 20 mol% addition of calcium oxide.

6.3.2. ^{27}Al and ^{23}Na MAS NMR Data

^{27}Al NMR spectra are displayed in figure 6.2 and the data recorded in table 6.2. At 0% CaO ie. for the model albite glaze $(Na_2O)\ (Al_2O_3)\ (SiO_2)_6$, the ^{27}Al signal consists of a strongly broadened, asymmetrical signal. However a strong signal from ^{27}Al in four coordination can be clearly distinguished at +52.9 ppm. On addition of CaO to the feldspar glaze, the signals become much narrower and more intense with several spinning sidebands. The chemical shifts for the peak maxima are in the range +52.7 to +81.3 ppm for tetrahedrally coordinated ^{27}Al and +0.9 to 8.1 ppm for octahedrally coordinated ^{27}Al. As the CaO content is increased occupancy of tetrahedral and octahedral Al sites varies .

^{23}Na resonance data are recorded in table 6.2 and the spectra are shown in figure 6.3. The spectra are generally very broad with linewidths (FWHH) in the range 2.2 KHz to 17 KHz. The chemical shifts are in the range -21.5 ppm to -10.5 ppm indicating a significant change in the environment of the Na^+ ions.

6.3.3. Discussion

The model ceramic glaze used in this study has a composition very close to that of the feldspar mineral high albite ($NaAlSi_3O_8$). The crystalline form of albite

INCREASING ADDITION OF Ca

TO A FELDSPAR GLAZE MIX

(^{29}Si MAS NMR)

Fig. 6.1

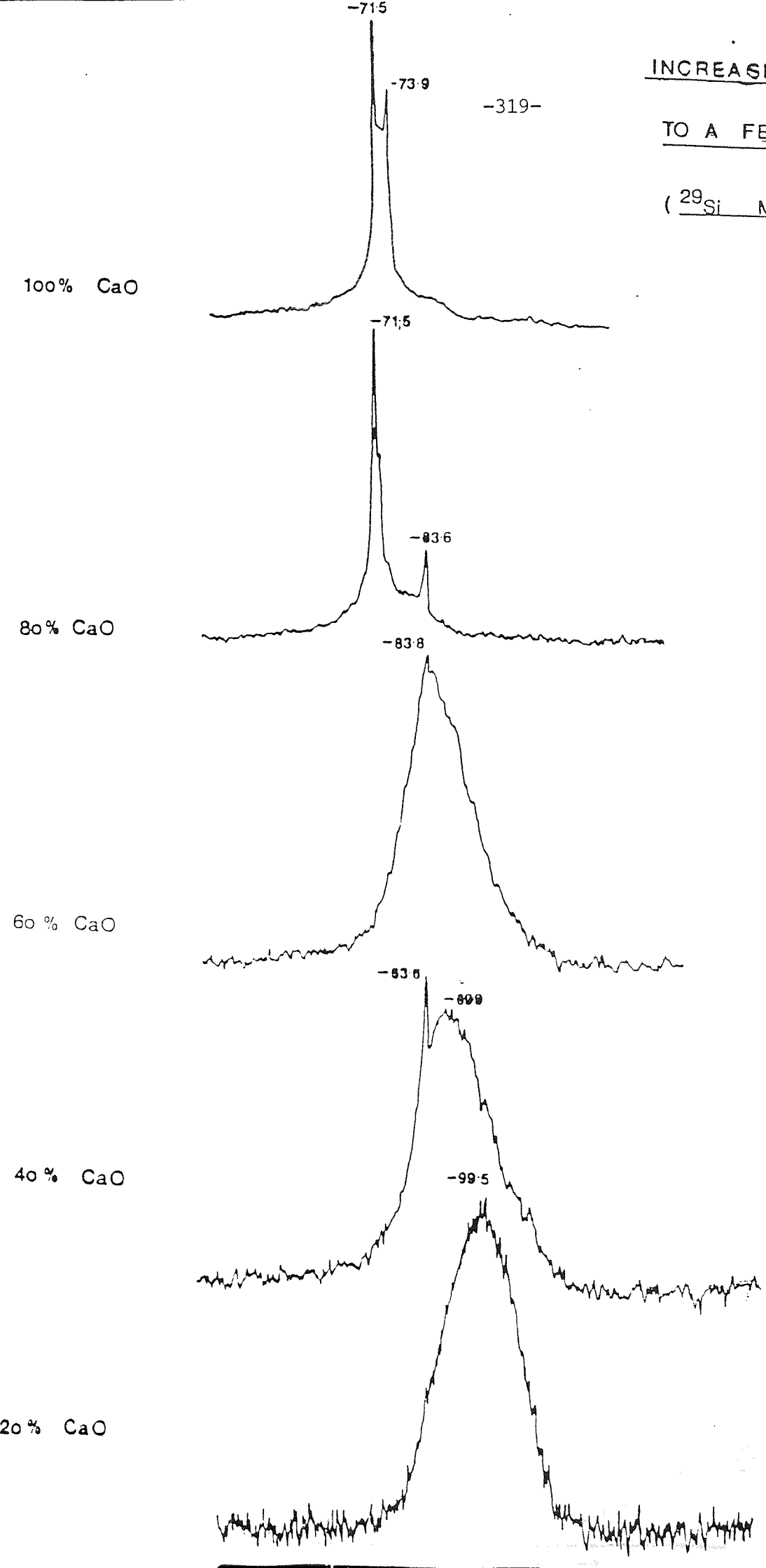

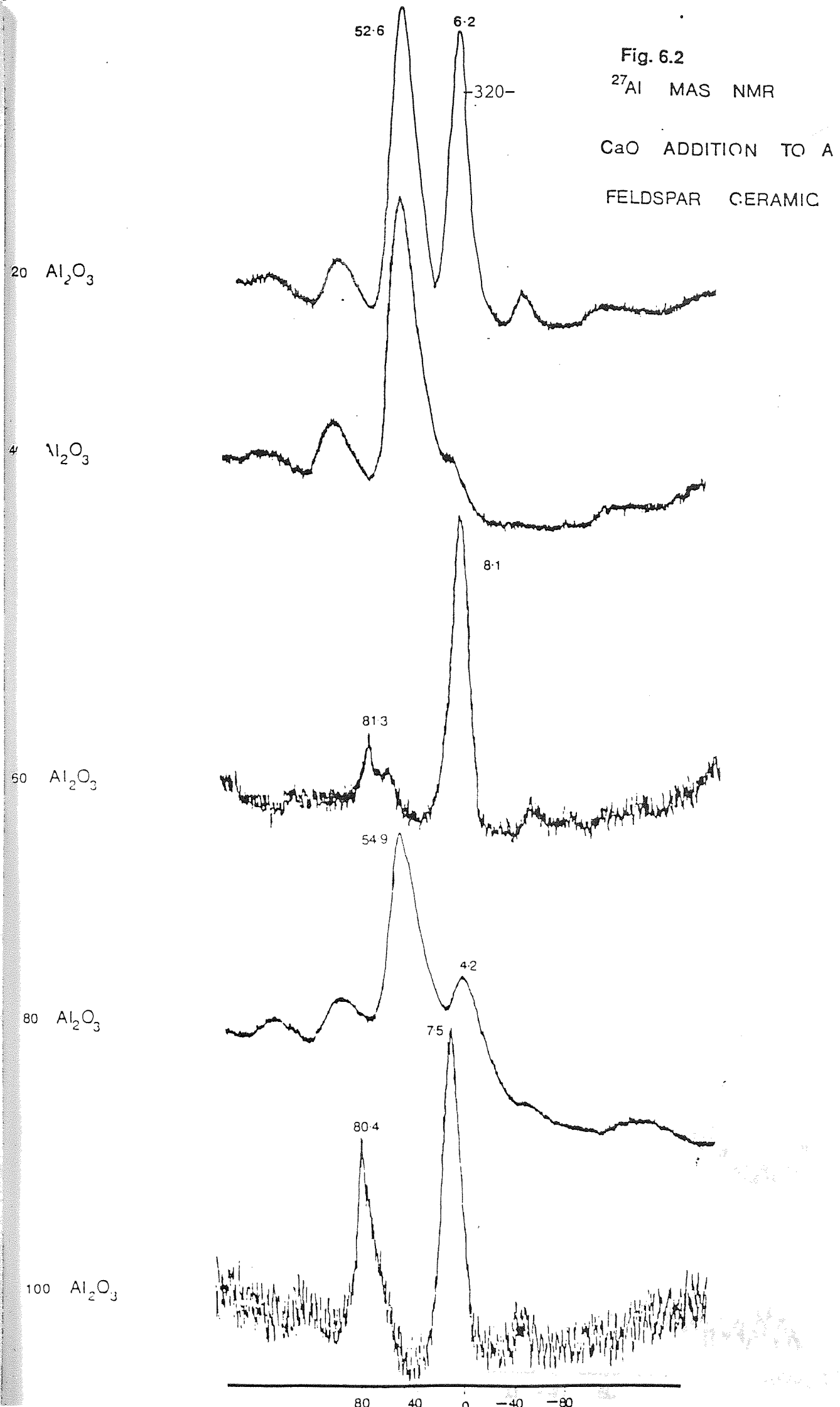

Fig. 6.2

^{27}Al MAS NMR

CaO ADDITION TO A

FELDSPAR CERAMIC

Fig. 6.3 ^{23}Na NMR Spectra of CaO Glazes

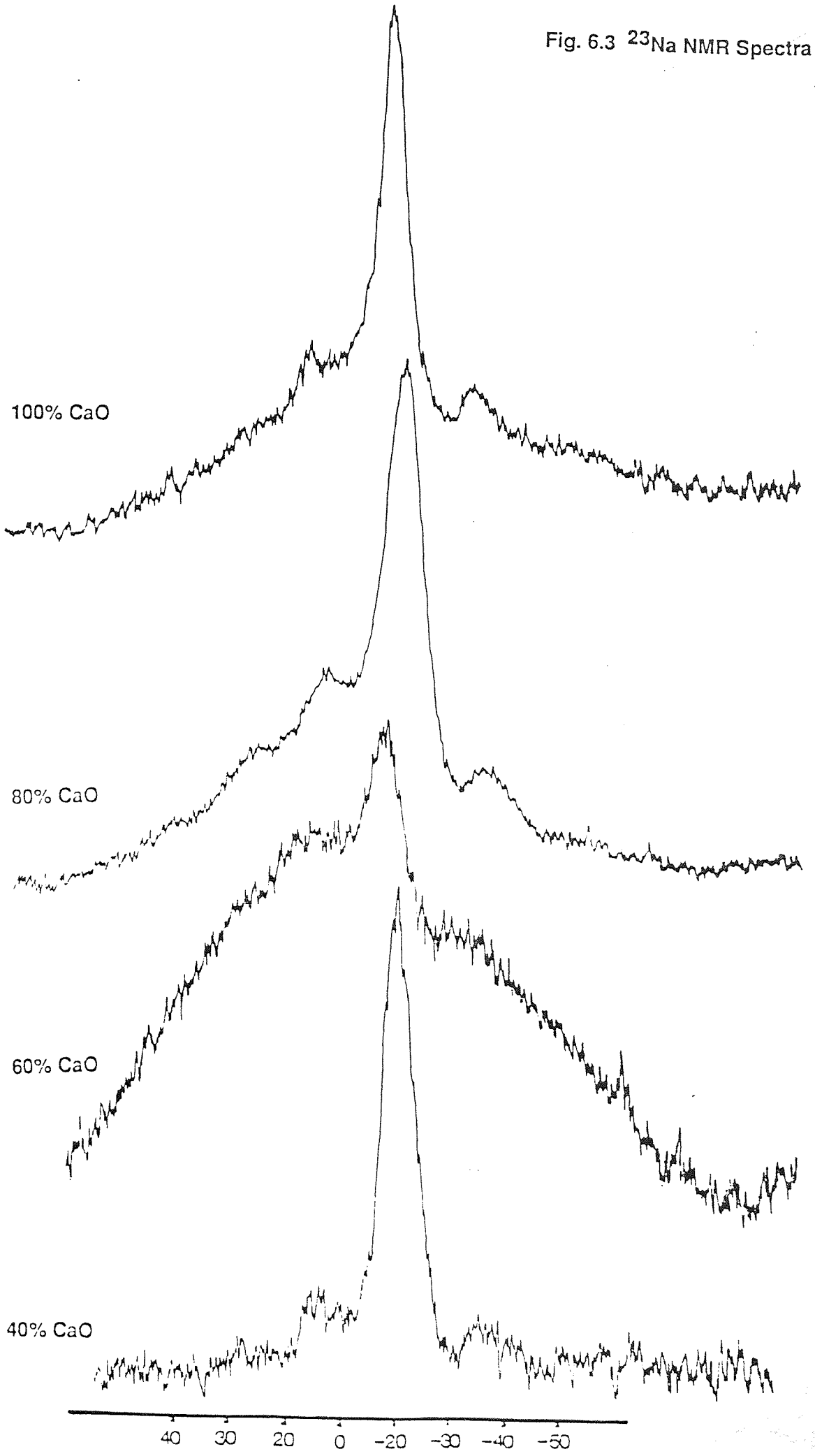

exhibits three particularly well resolved peaks at -92.2 ppm, -96.3 ppm and -104.7 ppm attributed to $Q^4(2Al)$, $Q^4(2Al)$ and $Q^4(1Al)$ silica sites[45]. In a later study Kirkpatrick et al prepared albite glass from the constituent oxides and reported a ^{29}Si spectrum which consisted of a single broad peak with a maximum at -98 ppm, covering a shift range from -85 ppm to -115ppm. This ^{29}Si peak was found to be about 12 to 15 ppm broader than the corresponding crystalline phase. In the present study, the observed ^{29}Si spectrum of the mimicked feldspar based on the albite composition (Na_2O) (Al_2O_3) $(SiO_2)_6$ consisted of a broad featureless peak centred at -93 ppm and covering a shift range from -80 to -110 ppm. The ^{27}Al results show a peak at +52.9 which is clearly assigned to aluminium in four-fold coordination. If we assume that all the aluminium in these glazes is in tetrahedral coordination (since there is no octahedral signal) the model albite glaze must have a fully polymerised framework structure. This is because the ratio of tetrahedral cations (Si + Al) to oxygen is half. All the Si sites must therefore be $Q^4(nAl)$. Because of large shift range of the ^{29}Si signal it is likely that detectable amounts of all five possible types of silica sites $Q^4(4Al)$ through to $Q^4(0Al)$ are present in the glaze; nevertheless the dominant silica site is the one corresponding to the ^{29}Si peak maxima ie. Q^4 (2Al).

The introduction of CaO into the model albite glaze produces marked changes in the overall network structure of the glaze as well as in the local silicon environments. The overall changes in distribution of $Q^m(nAl)$ units can be expressed as shown overleaf.

			Major Components
	Q^4	0% >	Q^4 (2Al)
	Q^4	20% >	Q^4 (2Al)
mol% Cao	Q^4	40% >	Q^4(3Al) + Q^4(4Al)
	Q^4	60% >	Q^4(4Al)
	Q^4	80% >	Q^4(4Al) + Q^o
	Q^4	100% >	Q^4(4Al) + 2Q^o
Local ^{29}Si Environment Silica/Quartz		x mol% CaO >	Local ^{29}Si Environments in Glaze

As the CaO concentration is increased more aluminium is seen to occupy the second coordination sphere of the silica tetrahedra. From 20 mol% CaO to 60 mol% CaO, the local ^{29}Si environment changes from silicon surrounded by two silica and two alumina tetrahedra, to silicon surrounded by four alumina tetrahedra. At 60 mol% CaO, a point is reached where most of the available aluminium is in tetrahedral coordination and perfect Si/Al ordering is attained. This in effect is a manifestation of Lowensteins rule[36] (ie. no Al-O-Al linkages). It is noteworthy however, that with further increase in the CaO content, the intensity of the Q^4(4Al) (for aluminosilicate) phase decreases in relation to the signal due to the silicate phases.

Between 20% and 60% CaO addition the ^{29}Si peaks cover a shift range from -80 to -115 ppm. The paramagnetic ^{29}Si shifts from -99 ppm to -89.6 ppm to -83.6 ppm are attributed to the well established trend of ^{27}Al moving into tetrahedral sites around the SiO_4 tetrahedra, rather than to a depolymerisation of the Q^4 network alone. An interesting point to note is the presence of the

sharp, distinct peak at -83.6 ppm which is particularly prominent at 80% CaO. The small linewidth implies a crystallographically distinct ^{29}Si site. Peaks at -83.6 ppm were also present at 40% and 60% CaO but not as the sharp peak seen at 80% CaO. The presence of this peak is tentatively assigned to the formation of an anorthite ($Ca_2Al_2Si_2O_8$) type phase. Crystalline anorthite is known to exhibit peaks at -83.0, -84.6 and -89.2 ppm. We speculate that at 40% and 60% CaO content, the ^{29}Si NMR peaks at -83.6 and -89.9 are due to $Q^4(4Al)$ and $Q^4(3Al)$ silica sites in an anorthite structure.

At 80% CaO content, the sharp, distinct ^{29}Si peak at -83.8 ppm is also attributed to $Q^4(4Al)$ sites in anorthite, but the most notable feature is the presence of a very intense sharp ^{29}Si peak at -71.5 ppm. The chemical shift value is too far down field (ie. deshielded) to be an aluminosilicate phase; such phases do not have chemical shifts beyond -80 ppm. The peak is thought to arise from a crystalline calcium silicate phase with only Q^0 silica sites. Evidence from the literature and from the corresponding phase diagrams suggests that the peak at -71.5 ppm is due to β-dicalcium silicate (β-Ca_2SiO_4) which has an olivine type silicate structure and hence gives rise to Q^0 sites.[3, 44, 47] The shoulders at -74.5 ppm and -76 ppm are thought to be due to the presence of another calcium silicate, namely rankinite ($Ca_3Si_2O_7$) giving rise to Q^2 sites[47].

At 100 mol% CaO the two sharp peaks at -71.5 and -73.8 ppm reflecting crystallographic ^{29}Si sites are attributed to the Beta and gamma polymorphs of dicalcium silicate (β and γ.Ca_2SiO_4). The very small "bump" at -83.6 is due to anorthite.[44]

The evidence obtained suggests that the exact phase formed after firing is dependent on the composition of the glaze. Between 20 mol% and 60 mol % CaO addition to the model albite composition, anorthite and a variety of other aluminosilicate phases are formed. Between 80 and 100 mol% CaO, the Q^4 silica network is fully depolymerised to form Q^0 and Q^1 silicate structures, with only a small amount of the $Q^4(4Al)$ phase remaining. At low CaO content the ^{29}Si shift range extends as far as -115 ppm which implies that the ^{29}Si peak

probably contains a component due to unreacted quartz or silica. At high CaO contents, the shift range only extends up to -95 ppm, all the ^{27}Al is present in Q^4 (4Al) sites; there is no component due to silica/quartz which implies that any unreacted silica/quartz probably reacted with CaO to form the crystalline calcium silicate phases.

The ^{27}Al chemical shifts for the model glazes with greater than 60 mol% CaO show a marked departure from low CaO content glazes. ^{27}Al chemical shift values at +80 and + 81 ppm with respect to $Al(H_2O)_6^{3+}$ are observed. For glazes with 20 mol% and 60 mol% CaO, tetrahedral Aluminium shifts of +52 to +55ppm are consistent with the values obtained by Kirkpatrick et al[55] for anorthite and albite glass at a magnetic field strength of 11.7 Tesla. According to Mueller the ^{27}Al chemical shifts around 80 ppm suggest that the tetrahedral ^{27}Al is surrounded by four AlO_4 tetrahedra in the second coordination sphere[83]. These chemical shift values are discussed in more detail later.

The ^{23}Na NMR spectra provide considerable information on the environment of Na^+ ions. The ^{23}Na spectrum of the model albite glaze (no calcium oxide) consists of a single symmetrical ^{23}Na peak with a linewidth of approximately 1950 Hz, and a chemical shift of -21.5 ppm relative to NaBr. Kirkpatrick et al., observed a quadrupolar split doublet with peaks at -13.1 and -21.9 ppm for albite glass. Their split peak was due not to the presence of two Na^+ sites in albite glass but was caused by second order quadrupolar broadening which is only partially averaged by magic-angle-spinning. No such doublet is observed for our model albite glaze implying that there is probably only one Na^+ site and that it is not severely broadened by quadrupole interactions.

With the successive addition of CaO to the glaze composition, marked changes in the lineshape and chemical shifts of the ^{23}Na peaks are observed. For 20 and 40 mol% CaO relatively little change in the chemical shift occurs and the lineshape is also unaltered by the presence of Ca^{2+} ions. ^{23}Na chemical shifts of -21.1 and -20.9 ppm reflect slight if any change in Na^+ coordination.

At 60 mol% CaO however, the linewidth increases to 3000Hz; the spectral broadening indicates a distortion of the Na^+ site symmetry indicating

Fig. 6.4 Plot of ^{23}Na Chemical Shift vs mol% CaO for a Model Feldspar Glaze

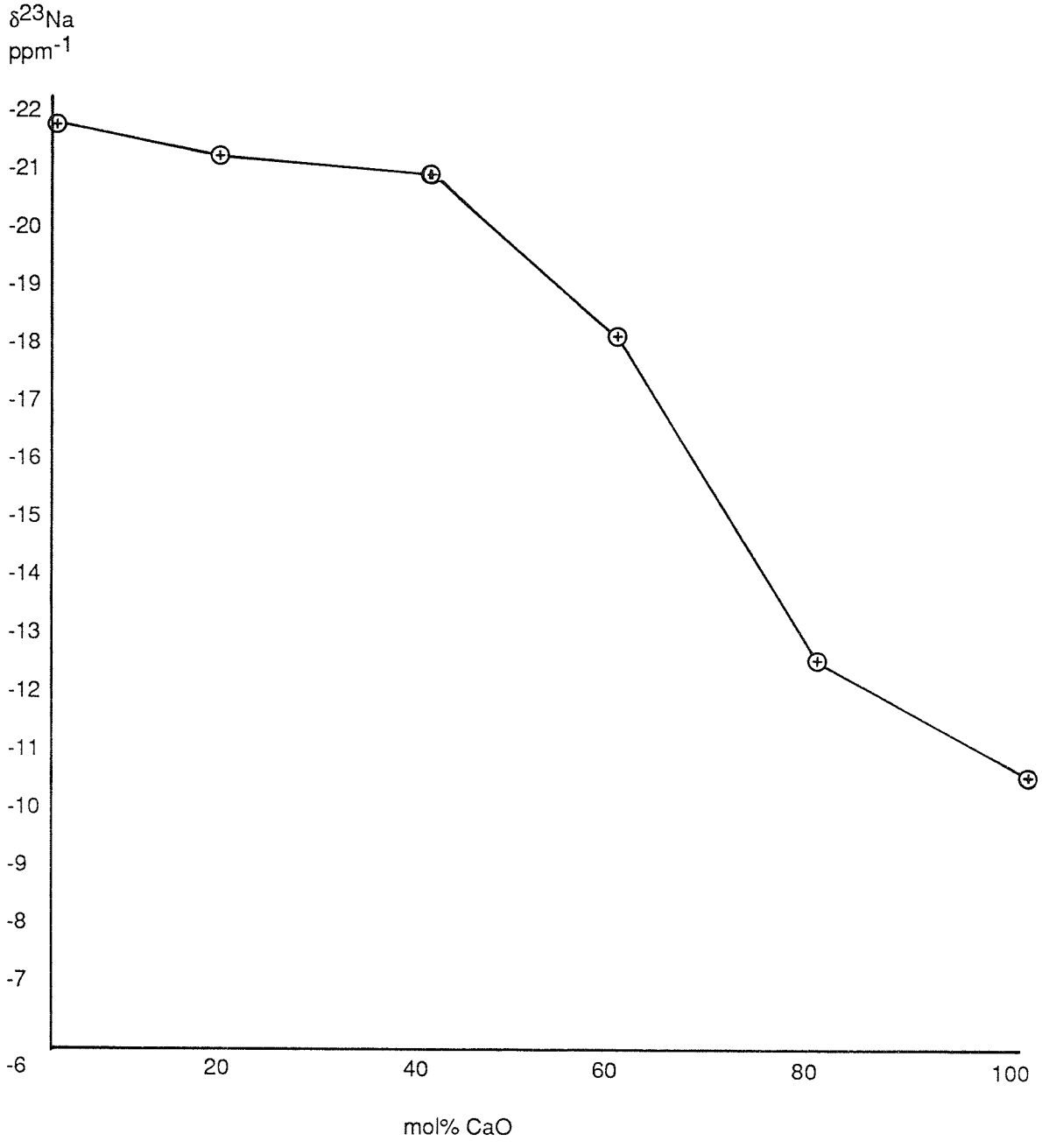

quadrupolar interactions arising from changes in the electric field gradients around the Na^+ ions. The chemical shift falls to -18 ppm which is a manifestation of a change in the electron density around the Na^+ ions. At 80% CaO a very severely quadrupolar broadened spectrum is observed with a linewidth exceeding 17,000Hz, along with several spinning sidebands. The central peak due to the m = 1/2 to -1/2 transition is engulfed by the broadening and the lineshape also indicates the presence of more than one site. It appears that there are a range of electric field gradients due to several distorted Na^+ sites within the glaze. The chemical shift falls dramatically to -12.4 ppm. With further increase in CaO content, a more stabilised spectrum is observed, as the linewidth falls to about 2,200Hz, with a chemical shift of -10.5 ppm. Figure 6.4 is a plot of ^{23}Na chemical shift (^{23}Na) versus mol% of CaO and shows that the chemical shift of Na^+ falls to less shielded values i.e. less negative values as the concentration of CaO within the glaze is increased.

6.4. A MAS NMR STUDY OF THE EFFECT OF LITHIUM OXIDE ON A MODEL FELDSPAR GLAZE

6.4.1. ^{29}MAS NMR Data

^{29}Si NMR results are displayed in table 6.3. and the spectra are shown in figure 6.5. At first sight the broad ^{29}Si peaks appear to be structureless with no distinct 'bumps' for glazes in the oxide composition range $[(Li_2O)_{0.3}(Na_2O)(Al_2O_3)(SiO_2)_6]$ to $[(Li_2O)_{3.0}(Na_2O)(Al_2O_3)(SiO_2)_6]$. After careful scrutiny however it is apparent that the individual spectra for each composition cover a discrete chemical shift range from -80 ppm to -115 ppm in 5 mol% Li_2O, to -70 ppm to -100 ppm in 50 mol% Li_2O. As the Li_2O content is increased the peaks become slightly more asymmetrical and distinct shoulders can be observed. The linewidths (FWHH) do not alter very much with composition and are between 0.9 and 1.1 KHz. The chemical shift for each peak is assigned to the central peak maximum in each case, and are in the range -83.1 ppm to -97.1 ppm. Thus although the peak maxima point to the dominant$Q^m(nAl)$ phase present at a certain glaze composition, the wide shift range covered by

Table 6.3 ^{29}Si MAS NMR Results for a Model Feldspar Glaze with an Increasing Lithium Oxide Content

							Q^4		
	Q^o	Q^1	Q^2	Q^3	Q^4 (4Al)	Q^4(3Al)	Q^4(2Al)	Q^4(1Al)	Q^4(0Al)
Silica									-109
Quartz									-108
0% Li_2O							-93.3		
5% Li_2O								-97.1	
10% Li_2O							-89.3		
20% Li_2O						-89.3			
30% Li_2O					-87.9				
40% Li_2O					-85.9				
50% Li_2O	-69.7				-83.1				

Table 6.4 ^{27}Al and ^{23}Na MASNMR Results for a Model Feldspar Glaze Containing Increasing Mol% of Lithium Oxide

	^{27}Al Resonance		^{23}Na Resonance	
	δ (TET) (ppm)	δ (OCT) (ppm)	$\delta^{23}Na$ (ppm)	Linewidth (Hz)
0% Li_2O	52.9	+0.9	-21.5	2000
5% Li_2O	53.3	-	-21.0	2500
10% Li_2O	52.4	-	-20.9	2500
20% Li_2O	56.8	-	-16.7	3400
30% Li_2O	58.8	-	-15.3	2750
40% Li_2O	57.4	-	-13.3	2700
50% Li_2O	58.4	-	-11.4	3250

the ^{29}Si peaks imply that there is significnt contribution to the ^{29}Si signal from a range of other $Q^m(nAl)$ or Q^m silica units. As the Li_2O content is increased the peak maxima display regular paramagnetic shifts.

6.4.2. ^{27}Al and ^{23}Na MAS NMR Data

^{27}Al NMR spectra for the glazes in the composition range defined above are displayed in figure 6.6. and the results are summarised in table 6.4. In general the ^{27}Al NMR spectra consist of a broad central peak (FWHH 2000Hz) flanked by several spinning sidebands. The chemical shift values are all in the range +52 to +58 ppm relative to $Al(H_2O)_6$ indicating that all the ^{27}Al present is in four-fold coordination. Significantly there is no signal around 0 ppm which would imply the presence of ^{27}Al in six-fold coordination.

The ^{23}Na NMR results are displayed in table 6.4, and the spectra displayed in figure 6.7. Again the spectra consist of a broad central peak (representing the central m = +1/2 tom = -1/2 transition) flanked by spinning sidebands. The central peaks are actually superimposed on an even broader component. For glazes with low Li_2O content (5 mol% to 20 mol%) the ^{23}Na peaks are symmetrical and the central peak is quite intense compared to the much broader basal component. At higher Li_2O content (30-50 mol%) there is considerable second-order quadrupole broadening dominating the spectrum since it is only partially averaged by MAS. The ^{23}Na chemical shifts decrease with mol% of Li_2O added and are in the range -21.5 ppm to -11.4 ppm.

6.4.3. Discussion

Bearing in mind the paramagnetic ^{29}Si shifts for the glaze spectra, the central peak maxima were assigned to discrete $Q^m(nAl)$ units. The distribution of the dominant $Q^m(nAl)$ units at each composition can be represented as follows overleaf:

Fig. 6.5

^{29}Si MAS NMR

Li_2O ADDITION TO A FELDSPAR CERAMIC

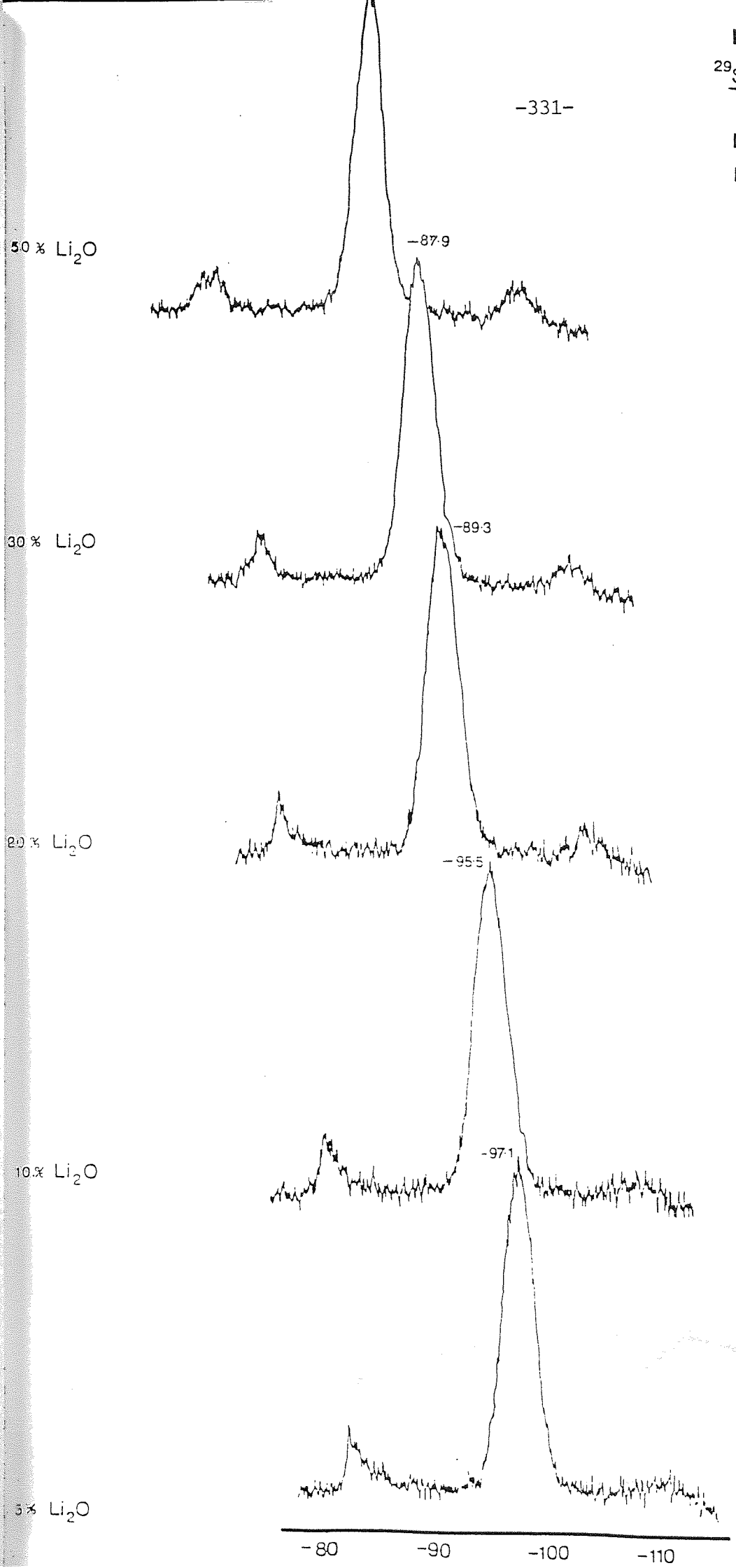

Fig. 6.6 ^{27}Al MAS NMR of Li_2O Glazes

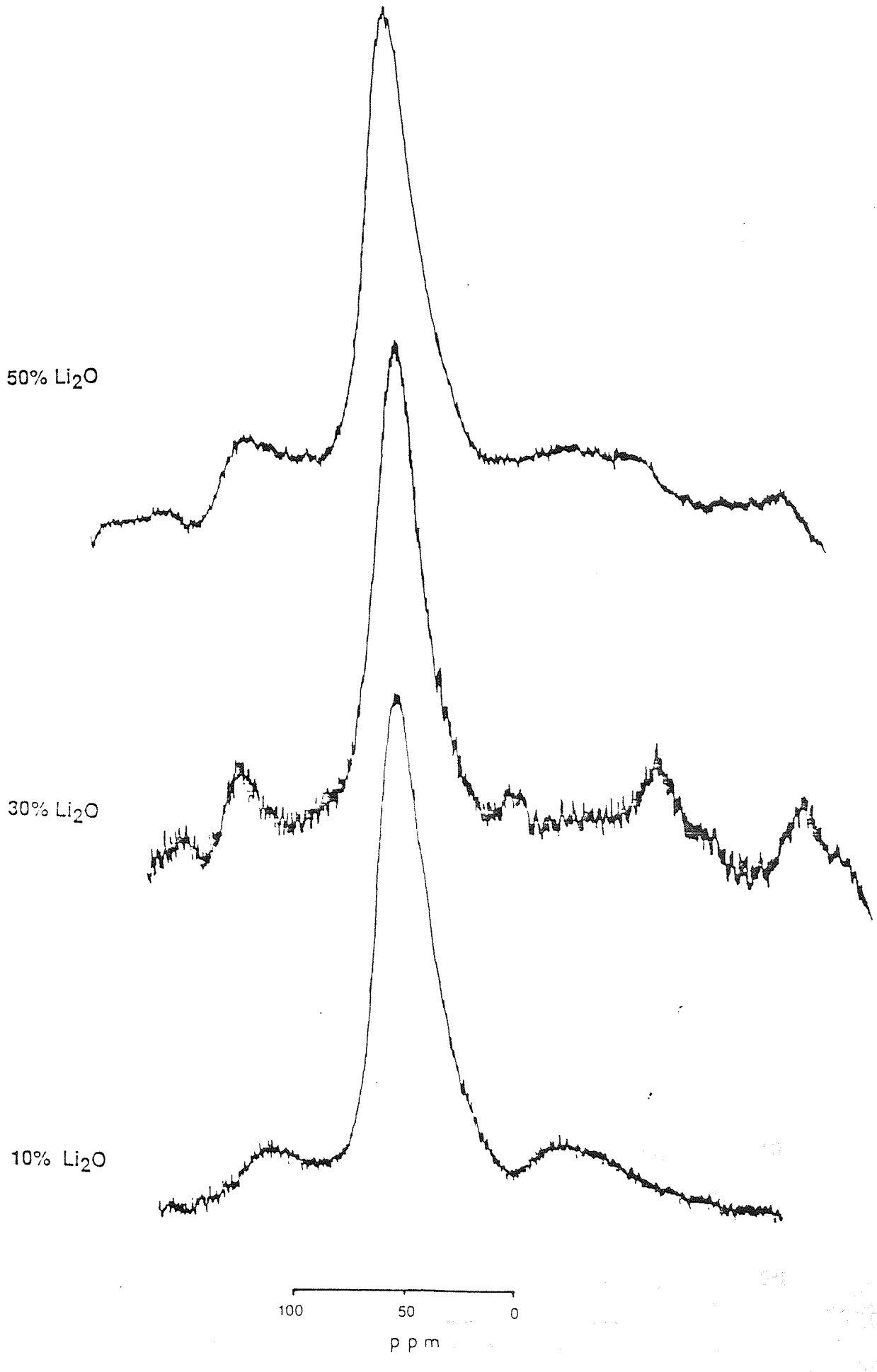

Fig. 6.7 ^{23}Na MAS NMR Spectra of Li_2O Glaze

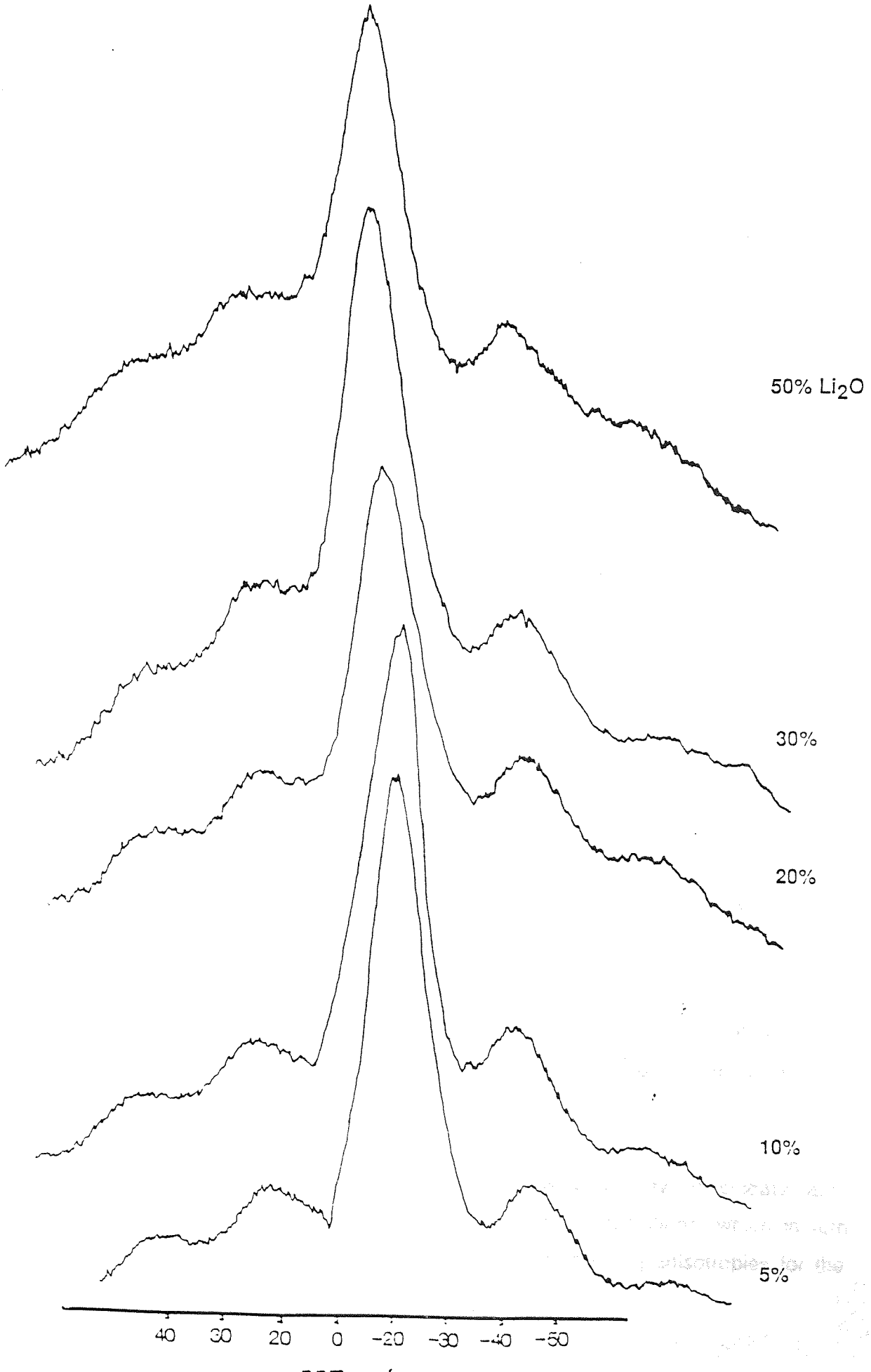

Major Components

	Q^4	5% >	Q^4 (1Al)
	Q^4	10% >	Q^4 (2Al)
mol%	Q^4	20% >	Q^4(3Al)
CaO			
	Q^4	30%- 50% >	Q^4(4Al)

As the lithium oxide content is increased, more aluminium enters the second coordination sphere of the silicate tetrahedra. From 5 mol% Li_2O to 20 mol% Li_2O the local ^{29}Si environment changes from silicon surrounded by one aluminate tetrahedron to silicon surrounded by three aluminate tetrahedra. After 30 mol% Li_2O there is perfect alternation of SiO_4 and AlO_4 tetrahedra as shown by the assignment to Q^4(4Al) units i.e. silicon surrounded by four aluminate tetrahedra and vice-versa. This is the dominant alumino silicate species present throughout the glaze network between lilthium content of 30 mol% and 50 mol%. This does not mean however, that the units assigned to the peak maxima are the only ones present. The spectra at each glaze composition cover a shift range of approximately 30 ppm. For example, at 5 mol% Li_2O there is evidence that ^{29}Si signals due to Q^2 and Q^3 silica units as well as a range of Q^4(nAl) units from Q^4(4Al) to Q^4(OAl) are also present. The presence of Q^4(OAl) is obviously to unreacted silica or quartz. Similarly at 50 mol% Li_2O the spectral shift range is from -70 ppm to -100 ppm, indicating the possible presence of Q^0, Q^1, Q^2, Q^3 silica units as well as Q^4(4Al) to Q^4(1Al) but not Q^4(OAl) units. At 50 mol% Li_2O therefore, there is no evidence for any unreacted silica or quartz.

The breadth of the ^{29}Si peaks reflects the wide variety of silicate and aluminosilicate phases present at the various glaze compositions, which in turn give rise to a large range and smooth dispersion of shielding anisotropies for the

different silicate and aluminosilicate units. In this respect the chemical shift values are in line with those for other oxides in that increasing the modifier oxide concentration increases the break-up of the Q^4 silicate network; more Si-O bonds are broken thus decreasing the overall polymerisation state of the network. Also, as more non-bridging oxygens are created, an increasing proportion of them are eliminated by aluminium atoms which form AlO_4 tetrahedra; hence the progression from $Q^4(1Al)$ to $Q^4(4Al)$ units as more Li_2O is added to the glaze. Since $Q^4(4Al)$ are the dominant units between 30 and 50 mol% Li_2O, the overall Q^4 polymerized state of the network is retained.

An alternative method of visualising the changes occuring in the glaze network is to consider connectivity. Figure 6.8. shows the connectivity of the dominant aluminosilicate phases as a function of Li_2O content[63]. By connectivity is meant the number of Si-O-Si bonds per silica tetrahedron. This number can vary between zero i.e. no Si-O-Si bond per tetrahedron, and four i.e. four Si-O-Si bonds per tetrahedron. Alternatively stated the number of Al-O-Si bonds can vary between zero and four per tetrahedron. The plot clearly shows that as the mol% of Li_2O is increased the connectivity of the dominant ^{29}Si component (i.e. number of Si-O-Si bonds per tetrahedron) decreases.

The ^{27}Al NMR spectra show that when Li_2O is added to the glaze composition, all the ^{27}Al is present in tetrahedral sites and no octahedral signal is detected for any one of these glazes. The chemical shift values do not vary greatly (+52 to +58 ppm) implying that the ^{27}Al signals probably arise from similar aluminate species. Also the central ^{27}Al peaks are very intense and there is virtually no evidence of any major quadrupolar interactions due to either a large number of different four-coordinate aluminium sites or distorted tetrahedral aluminium sites. This appears to show that the tetrahedral aluminium is present in the network as any one of $Q^4(4Al)$, $Q^4(3Al)$ $Q^4(2Al)$ or $Q^4(1Al)$ sites. The expected variation in tetrahedral aluminium chemical shift value is from +55 to +80 ppm relative to $Al(H_2O)_6^{3+}$. However this shift range is inclusive of aluminate species in tetrahedral coordination (i) with aluminium in the second coordination sphere and (ii) without aluminium in the second coordination sphere. Aluminates

Fig. 6.8 Connectivity vs mol% Li_2O

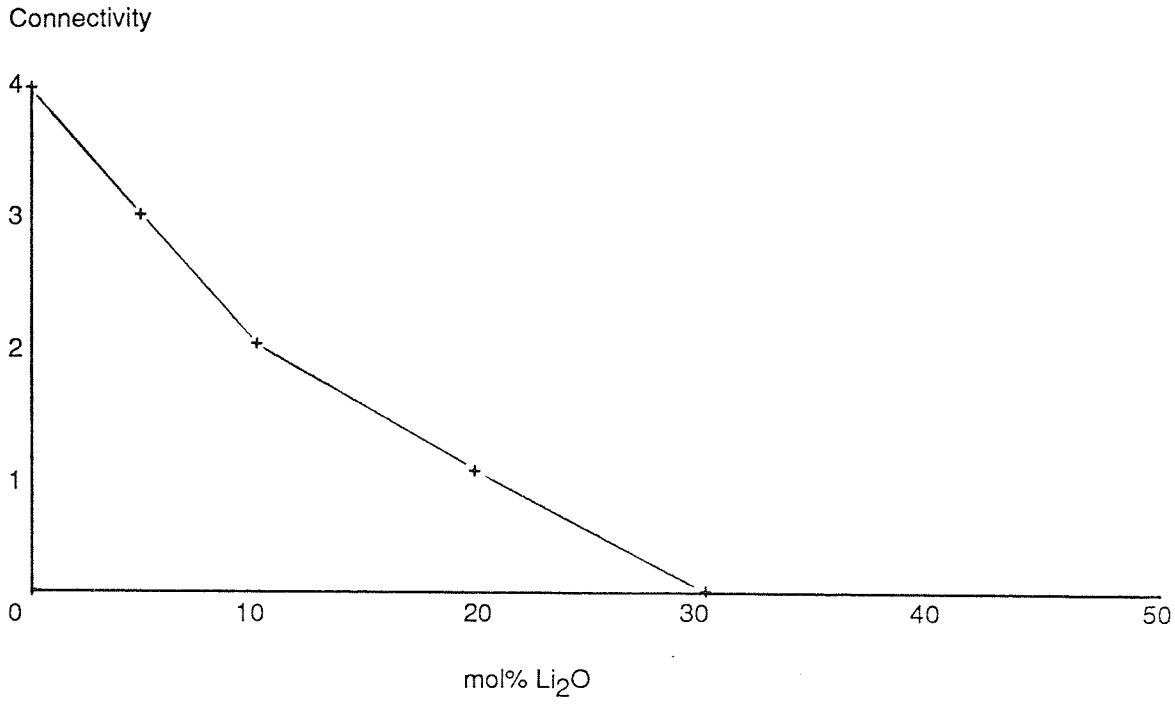

with Al-O-Al linkages i.e. aluminium in the second coordination sphere are known to have ^{27}Al chemical shifts between +65 and +80 ppm, while aluminates with only silicon in the second coordination sphere have a narrower range, recorded below +60 ppm. Our interprectation and assignment to a range of $Q^4(4Al)$ to $Q^4(1Al)$ sites is therefore probably correct. It is possible that any available octachedral sites are preferrably occupied by Li^+ cations which are known to be more mobile than Al^{3+} cations. Li^+ cations can adopt either four or six fold coordination. It is likely that Li^+ cations may be leaching out Al^{3+} from octahedral sites. Consider the ionic radii of the two cations for different coordination numbers:

	Pauling Radius (Å)	Goldschmidt Radius (Å)
Li^+ (C.N.= 4)	0.60	0.71
Al^{3+} (C.N. = 4)	0.45	0.55
Li^+ (C.N. = 6)	0.85	0.88
Al^{3+} (C.N. = 6)	0.68	0.68

It is clear that for a higher coordination number the ionic radius of each cation is significantly larger, and that for both 4- and 6- coordination, Li^+ has a slightly larger ionic radius than Al^{3+}. Bearing this in mind we can see why Li^+ cations prefer an octahedral environment rather than a tetrahedral one, and conversely why Al^{3+} prefer only a tetrahedral environment (no octahedral ^{27}Al signal observed). The eventual environment chosen by the cation must be the one which is energetically more favourable and in the case of the ceramic glazes under consideration this is determined primarily by the relative sizes of the two cations.

The ^{29}Si and ^{27}Al data suggest a glaze structure which can be envisaged as follows. The dominant ^{29}Si component and therefore the most abundant phase is the $Q^4(nAl)$ unit, the connectivity of which depends on the Li_2O content of the

glaze. Other aluminosilicate and silicate phases are also present in the glaze network, including Q^o, Q^1, Q^2 and Q^3 silica units, the relative intensity of which again is dependent on the Li_2O concentration.

The silicate units present are expected to be formed by actual depolymerisation of the Q^4 network with a concommitant formation of non-bridging oxygens which are expected to be neutralized by Li^+ cations. Unfortunately from the present data we are unable to comment on the exact distribution and relative intensities of the Q^n units formed as the spectra exhibit a smooth dispersion of chemical shifts. However, in qualitative terms we can say that the relative abundance of Q^n units apparently follows the order $Q^3>Q^2>Q^1>Q^o$.

The diagram below shows some definitions of the possible local silicon environments (for Q^n units):[63]

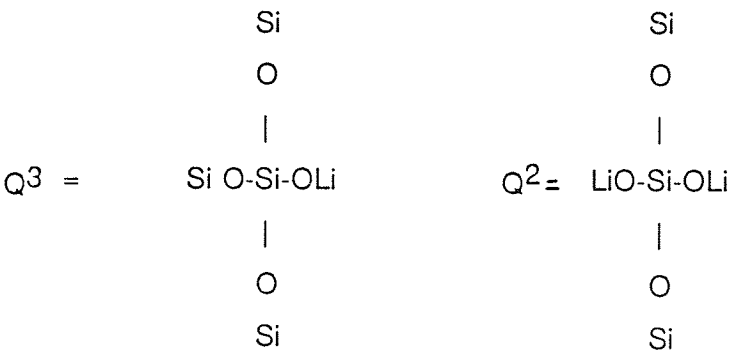

Table 6.4.A. Definitions of Some Possible Q^n Species in the Glaze Network.

As in the previous study (addition of CaO) the ^{23}Na NMR spectra provide very useful information on the environment of the Na^+ ions and how it is affected by the presence of Li_2O. As shown in figure 6.9. the ^{23}Na chemical shifts show a similar trend to those in the previous study where CaO was the modifier oxide. From O to 10% Li_2O the ^{23}Na chemical shift values change only slightly from -21.5 ppm to -20.9 ppm implying that the Na^+ ions are in a similar environment to that in the original albite glaze. At 20 mol% Li_2O, the ^{23}Na chemical shift drops sharply to -16.7 ppm; with further increase in Li_2O content the chemical

Fig. 6.9 Plot of ^{23}Na Chemical Shifts vs mol% Li_2O for a Model Feldspar Glaze $(Li_2O)_2(Na_2O)(Al_2O_3)(SiO_2)_6$

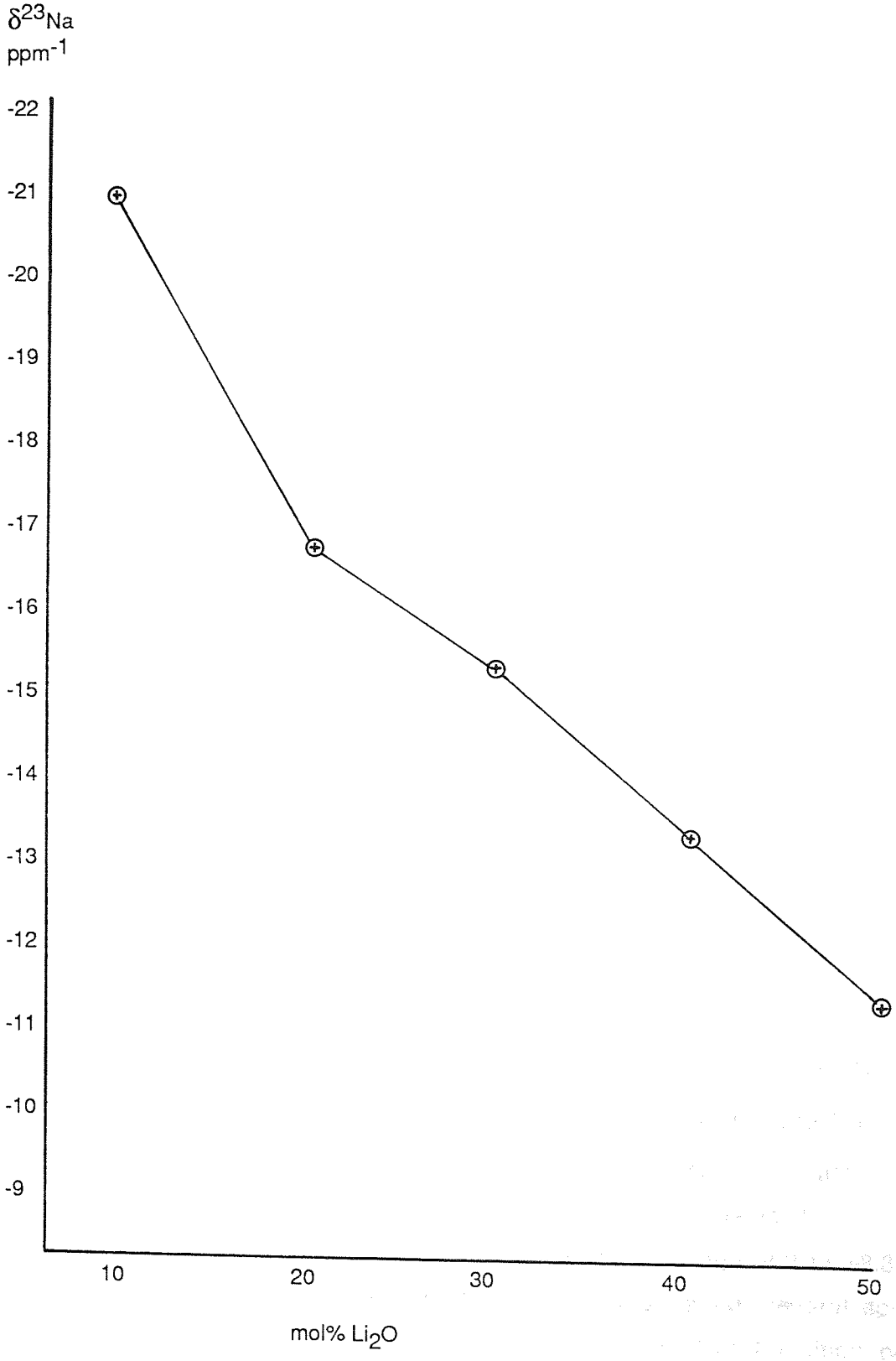

shift falls to less negative values.

Again we observe a point on the ^{23}Na vs mol% Li_2O plot when the Na^+ coordination is markedly changed from that in albite glaze. For lithium oxide this point occurs at 20 mol% Li_2O. For calcium oxide the same change in Na^+ coordination occurred at 60-80 mol% calcium oxide.

6.5. STRONTIUM OXIDE ADDITION TO A MODEL FELDSPAR GLAZE

6.5.1. ^{29}Si MAS NMR Data

^{29}Si NMR spectra (figure 6.10) are generally broad and show some important changes from the ^{29}Si spectrum of the mimicked albite glaze. At 10% SrO addition, the ^{29}Si signal centred at -86.1 ppm (linewidth 990Hz) covers a shift range from -72 ppm to -107 ppm. Several shoulders can be observed at -77 ppm, -80 ppm and -107 ppm. For 20% SrO addition, the ^{29}Si peak is considerably sharper (linewidth = 920Hz) but is asymmetrical and a distinct shoulder is observed at -103 ppm. The peak is centred at -85.1 ppm and covers a shift range from -75 ppm to 105 ppm. For the remaining glaze samples the shift range covered decreases to -95 ppm, the peaks become sharper still and the linewidth decreases. At 100 mol% SrO two distinct ^{29}Si peaks are observed; a broad peak at -80.6 ppm and a much smaller one at -69.7 ppm.

6.5.2. ^{27}Al and ^{23}Na MAS NMR Data

Throughout the oxide composition range $[(SrO)_{0.6}(Na_2O)(Al_2O_3)(SiO_2)_6]$ to $[(SrO)_6(Na_2O)(Al_2O_3)(SiO_2)_6]$ the ^{27}Al NMR spectra exhibit broad lineshapes. Signals from both four-coordinate Al sites [Al(4)] and six-coordinate Al sites [Al(6)] are detected for each glaze. Al(4) chemical shifts are in the range +52 ppm to +65.3 ppm while Al(6) chemical shifts are in the range -4.2 to +8.3 ppm. Although the central resonances are not severely broadened, several spinning sidebands appear on either side of the ^{27}Al (1/2 $\leftrightarrow$ -1/2) transition peaks. The positions of certain sidebands appeared to coincide with the Al(6) chemical

Table 6.5 ^{29}Si MAS NMR Results for a Model Feldspar Ceramic Glaze with Increasing Strontium Oxide Content

							Q^4		
	Q^0	Q^1	Q^2	Q^3	Q^4 (4Al)	Q^4(3Al)	Q^4(2Al)	Q^4(1Al)	Q^4(0Al)
Silica									-109
Quartz									-108
0% SrO							-93.3		
10% SrO					-86.1				
20% SrO					-85.9				
30% SrO					-84.5				
40% SrO					-85.0				
50% SrO					-84.6				
100% SrO	-69.7				-80.6				

Table 6.6 ^{27}Al + ^{23}Na MAS NMR Results for a Model Feldspar Glaze Containing Increasing Mol% of Strontium Oxide

	^{27}Al Resonance		^{23}Na Resonance	
	δ (TET) (ppm)	δ (OCT) (ppm)	$\delta^{23}Na$ (ppm)	Linewidth (Hz)
0% SrO	52.9	+0.9	-21.5	2000
10% SrO	52.3	-4.2	-21.1	1800
20% SrO	61.4	+4.5	-20.9	2400
30% SrO	61.9	+6.2	-20.7	2800
40% SrO	59.9	+3.2	-13.8	2500
50% SrO	62.3	+4.5	-14.3	2750
100% SrO	65.3	+8.3	-10.5	230

Fig. 6.10 ^{29}Si MAS NMR Spectra of SrO Glazes

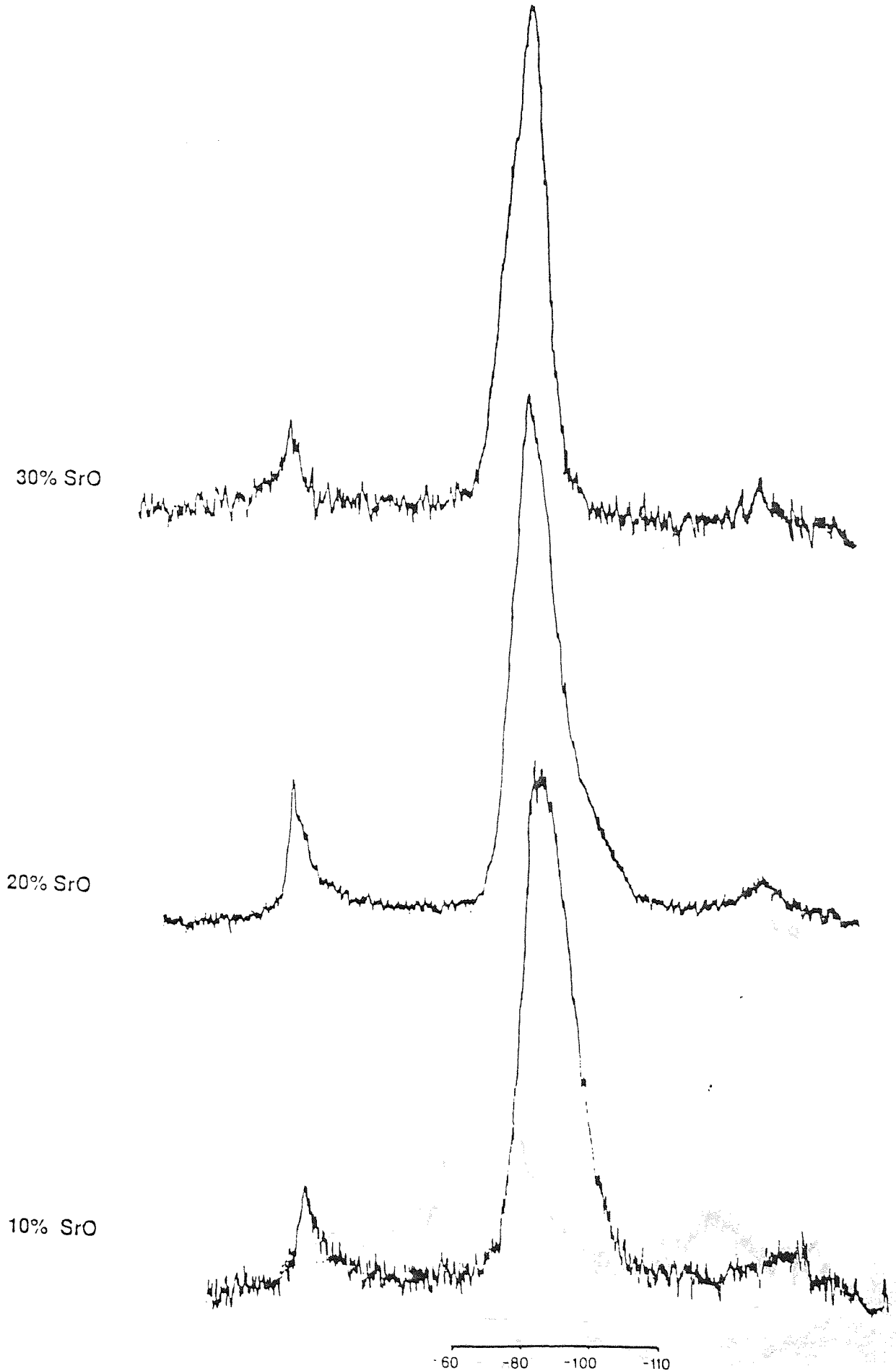

Fig. 6.11 ^{29}Si MAS NMR Spectra of SrO Gla

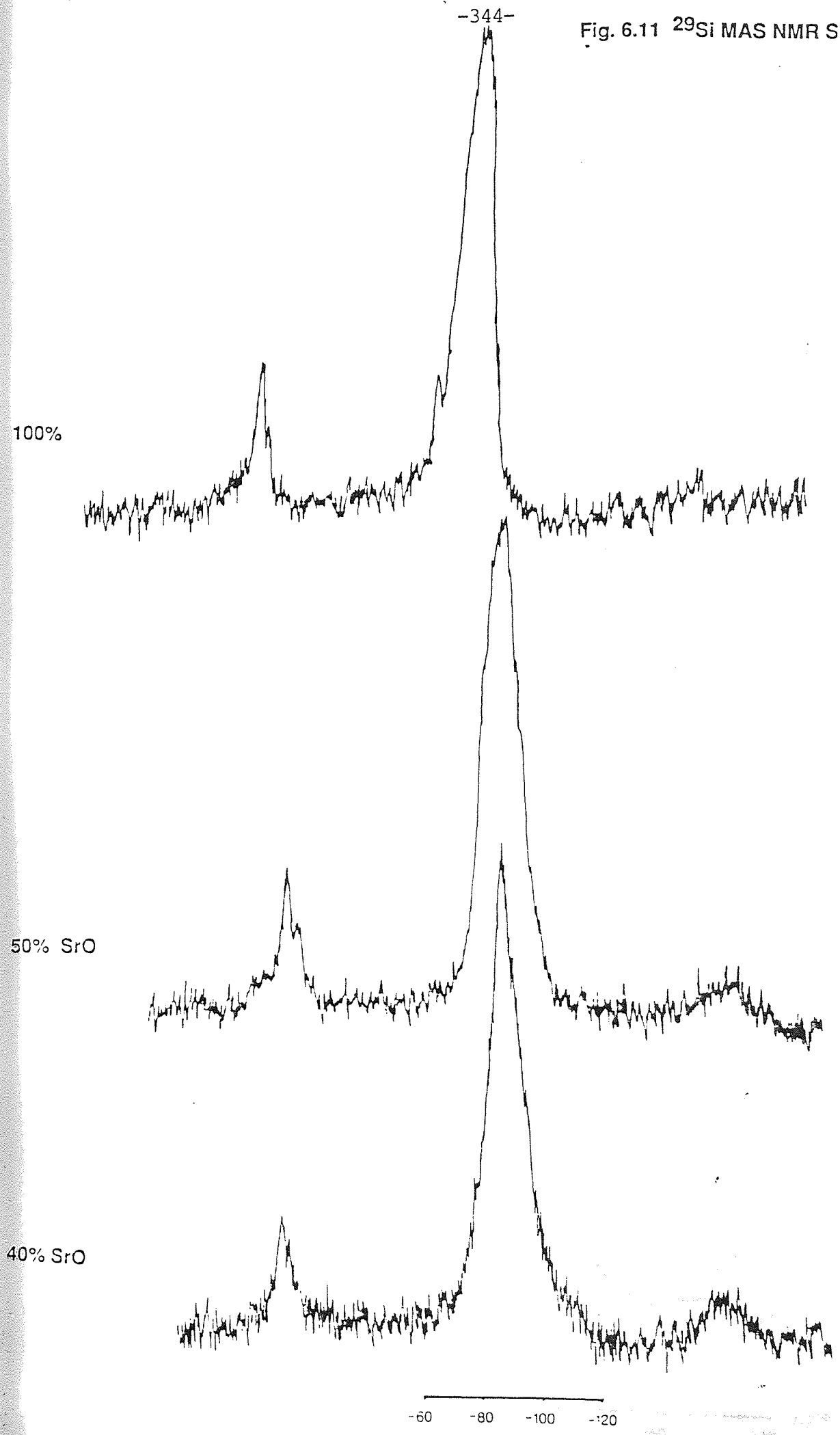

Fig. 6.13 ^{27}Al MAS NMR Spectra of SrO Glazes

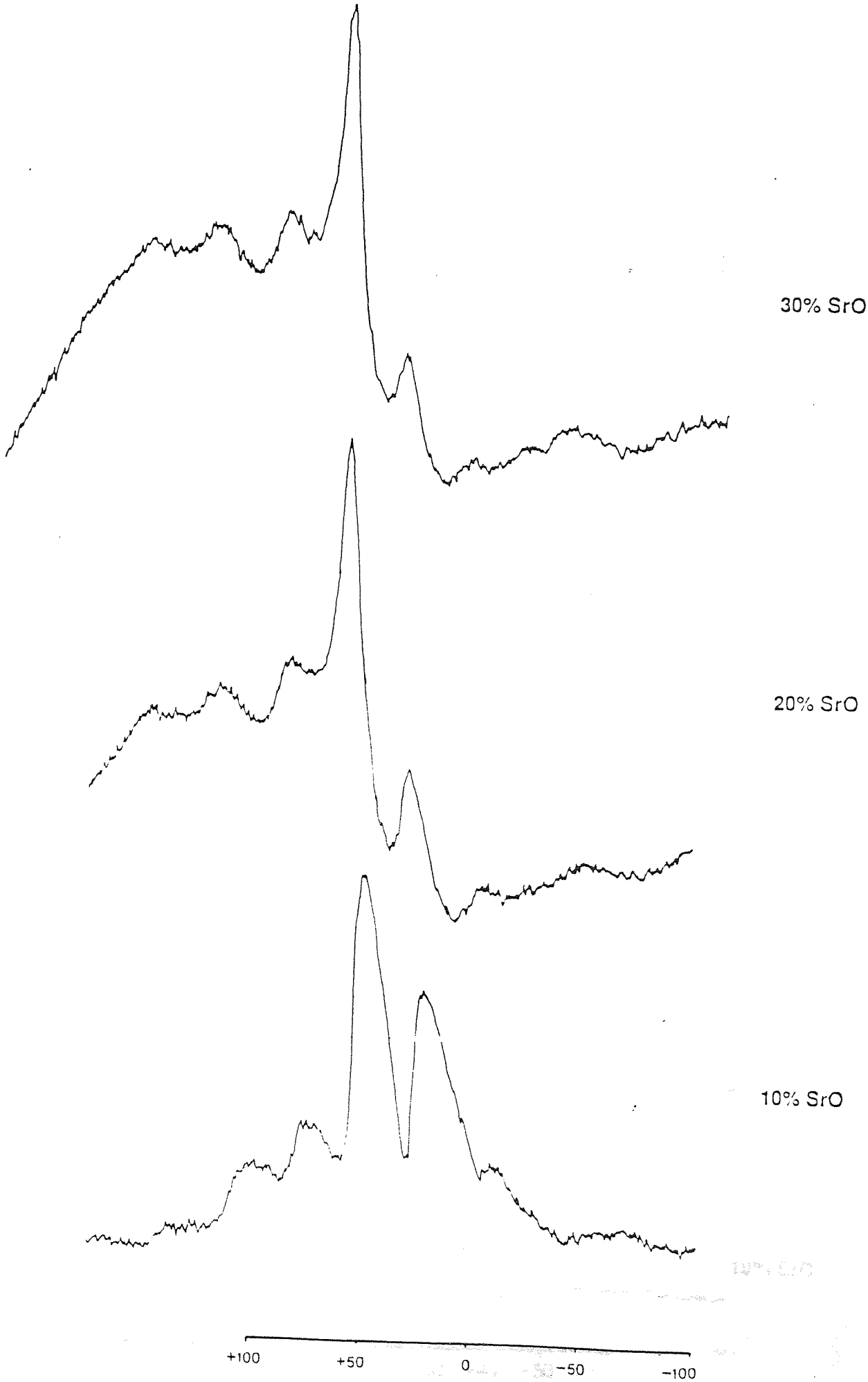

Fig. 6.14 ^{23}Na MAS NMR Spectra of SrO Glazes

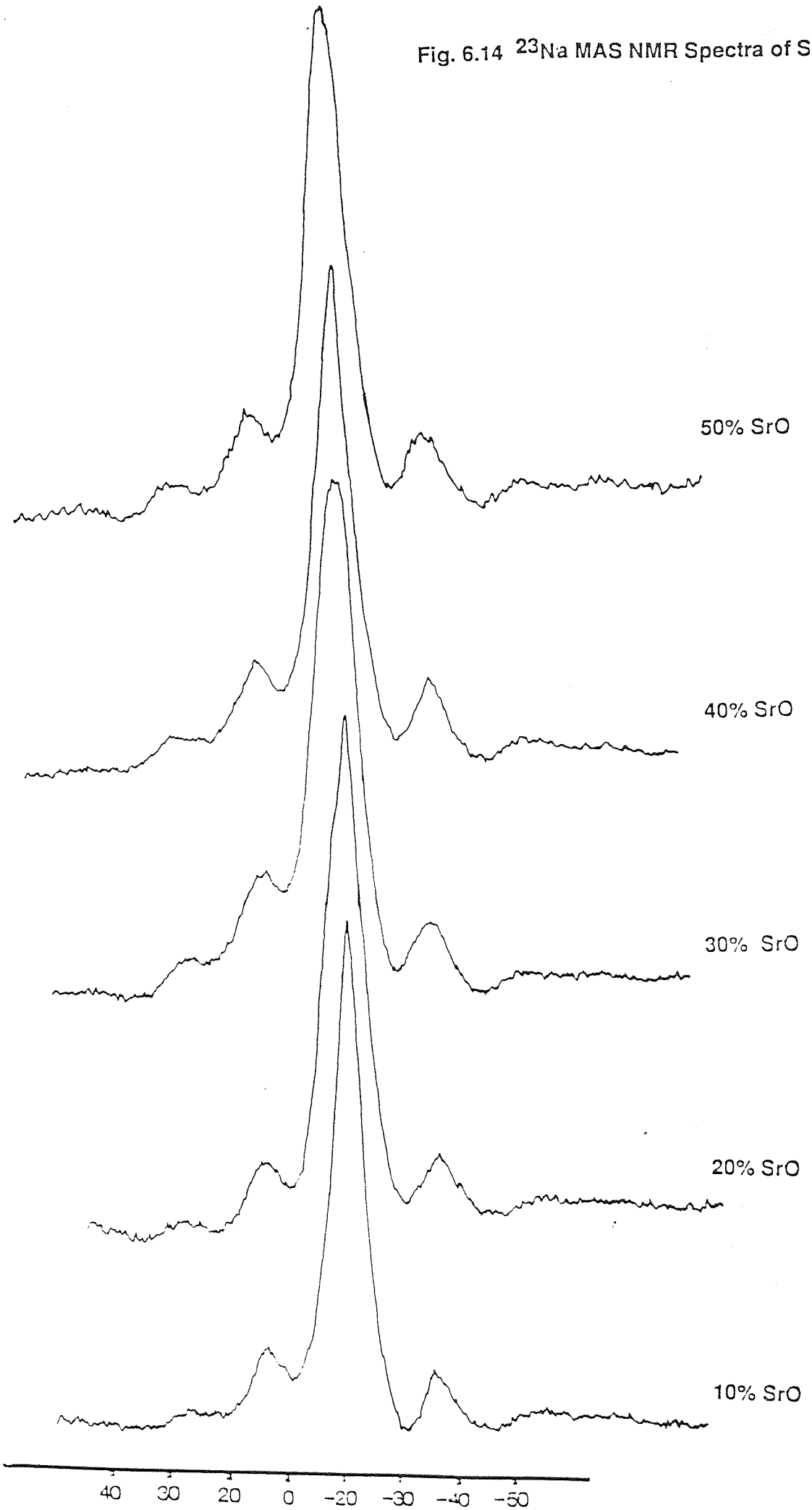

shift range, and at first it was difficult to establish whether the peaks were due to octahedrally coordinated Al or to sidebands. This problem was easily resolved by applying a different spinning frequency. When the samples were spun at a higher frequency, the sidebands accordingly moved further away from the central resonance peaks. However there was apparently no effect on the disputed octahedral ^{27}Al signal implying that this was a real peak. In the spectra shown all sidebands are labelled S.S.B. in order to avoid confusion.

The basal components of the ^{27}Al spectra are severely broadened. The exact cause of the broadening and any quantitative evaluation of the ^{27}Al spectra is difficult to establish.[59] Other workers have speculated that the broadening could arise from a range of ^{27}Al environments and/or distorted Al(4) and Al(6) sites present in the disordered or amorphous regions of the glaze network.[55,81] We speculate that the broadening is due mostly to the larger quadrupole coupling constants which are created in disordered or amorphous solids. In such cases additional structure appears on the normally sharp central line (in crystalline compounds) due to the higher order effects which arise when the quadrupole interaction is a significant fraction of the actual resonance frequency. The larger quadrupole interactions are in turn due to highly distorted sites (or in crystal defects) which give rise to higher electric field gradients. If the broadening was due to a range of ^{27}Al environments alone, then we should observe pure homogeneously broadened resonance lineshape, which is not the case.

The ^{23}Na spectra (figure 6.12) show similar lineshapes and linewidths over the entire composition range. Although several sidebands appear in each spectrum there is no clear evidence of second order quadrupole broadening which should arise from highly distored Na^+ sites. The Na^+ lineshapes are homogenously broadened and are relatively sharp (linewidth -- 2.0 KHz), indicating a range of undistorted (small efg's) environments in each case. The chemical shift however, does vary with composition but shows a very similar trend to previous spectra. ^{23}Na chemical shifts are in the range -21.1 to -10.5 ppm relative to NaBr.]

6.5.3. Discussion

The most notable feature of the ^{29}Si spectra is that even at low SrO contents, the dominant silica phase detected is assigned to $Q^4(4Al)$ units. In fact from 10 mol% to 50 mol% SrO both the ^{29}Si shift of the peak maxima and the chemical shift range covered (-75 to -105 ppm) vary only slightly with increase in SrO content of the feldspar glaze. Only at 100 mol% SrO is there a significant shift to -80.6 ppm (still assignable to $Q^4(4Al)$, and a small peak at -69.7 ppm assigned to a Q^o silicate phase. It appears that the concentration of SrO does not affect the glaze network, as the dominant silica phase formed is $Q^4(4Al)$.

The shift range covered (-75 to -105 ppm) implies that $Q^4(4Al)$ units are by no means the only species formed. In fact a wide variety of silicate and aluminosilicate species are formed in turn giving rise to a large variety of Si-O-Si or Si-0-T bond lengths and bond angles.[65] This results in a smooth dispersion of ^{29}Si shielding anisotropies and hence the broad, featureless ^{29}Si peaks. The only silica units unlikely to exist in a shift range -75 to -105 ppm are $Q^4(OAl)$ or Q^4 units, and possibly Q^o and Q^1 units. ^{27}Al NMR data support the assertion that the dominant units formed in the glaze are $Q^4(4Al)$, by the fact that a strong Al(4) signal is present at each glaze composition. The fairly wide range of aluminium (4) and (6) chemical shifts suggest that a variety of ^{27}Al resonances are present in both four and six fold coordination.

The overall picture of the glaze network is one in which the main structural phase present is a fully polymerised lattice with regularly alternating SiO_4 and AlO_4 tetrahedra. Other silica phases including Q^2, Q^3, $Q^4(3Al)$, $Q^4(2Al)$ and Q^41Al are also present although in smaller quantity.

At this stage it is only fair to say that if the ^{29}Si chemical shifts alone are relied upon for assignment, than a certain amount of ambiguity can and does arise, particularly in the absence of x-ray differaction data. The problem stems from the fact that in the case of the SrO glazes, assignment cannot unequivocally be made to $Q^4(nAl)$ or Q^m silica units alone. There is a possibility that these signals may be attributed to the presence of strontium disilicate ($SrSi_2O_7$) or

strontium metasilicate ($SrSiO_3$) units in the glaze. The disilicate has a recorded ^{29}Si chemical shift of -80.3 ppm while the metasilicate has a shift of -92.1 ppm in the glassy state.[84] The presence of disilicate is disregarded on grounds that the observed chemical shift range in our study only extends to about -90 ppm (at 100 mol% SrO addition) and there is no detectable component beyond -90 ppm. If we assign the ^{29}Si peaks as due to the metasilicate this would mean that this phase is formed at all levels of SrO addition. In view of the evidence from phase equilibrium diagrams $SrSiO_3$ is not likely to be formed at low concentrations of SrO (e.g. 10-30%). Also the chemical shift observed is around -85 ppm which is too shielded even for $SrSiO_3$ in a glassy state. However the ^{29}Si chemical shift of -80.6 ppm observed at 100 mol% SrO does suggest the presence of $SrSiO_3$ units. A more plausible assignment is to the coexistence of both Q^1 units ($SrSiO_3$) and $Q^4(4Al)$ units due to feldspar like rings.

The ^{23}Na NMR results are broadly in line with those in the two previous studies in particular with respect to chemical shifts. In all cases the lineshape consists of relatively narrow central resonance (m = 1/2 to -1/2 transition) accompanied on either side by spinning sidebands. Unlike previous spectra (for CaO and Li_2O glazes) the basal component of the spectra is not broadened showing a lack of second order quadrupole broadening. However there is a possibility that Na^+ ions exist in more than one site. For example for 10% SrO addition the ^{23}Na peak is very sharp (comparatively) and symmetrical. At 20% SrO the peak is still sharp but there is a distinct shoulder or inflexion in the lineshape at about -13 ppm. At higher SrO contents the peaks become rounded but split into two components. Kirkpatrick et al have attributed this splitting of the ^{23}Na peaks not to two Na^+ sites but to quadrupolar splitting. These workers however had the advangtage of using variable - angle sample spinning as opposed to magic angle spinning and were thus able to show that at a different angle of inclination to the external magnetic field e.g. 75^o for ^{23}Na, it is possible to remove second order broadening effects and observe the quadrupolar split doublet.

The chemical shift values of the ^{23}Na peak maxima show a similar trend to that observed previously, in that with increased SrO addition the ^{23}Na value drops

Fig. 6.15

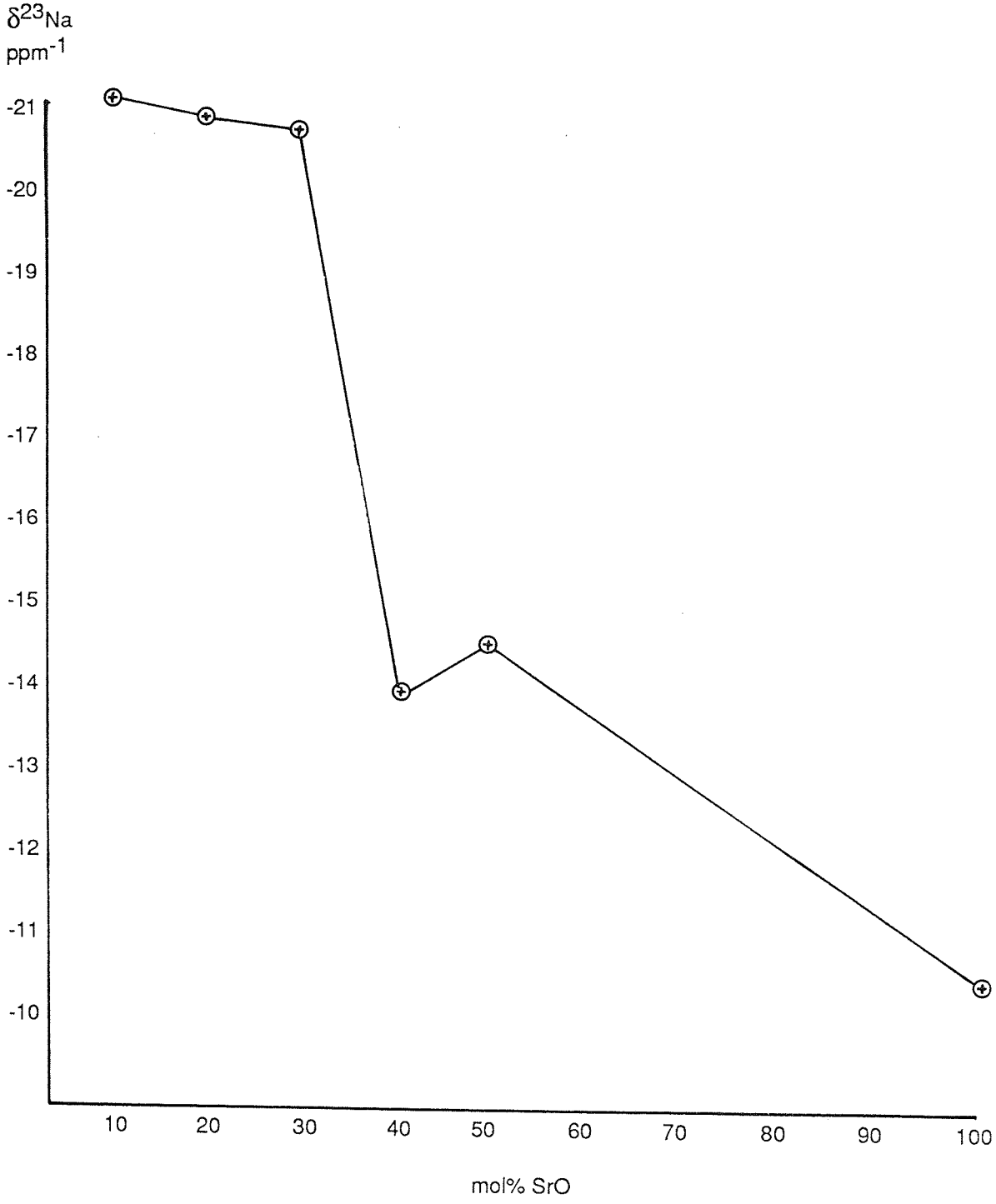
$\delta^{23}Na$
ppm^{-1}
-21
-20
-19
-18
-17
-16
-15
-14
-13
-12
-11
-10
10
20
30
40
50
60
70
80
90
100
mol% SrO

speculate that the change in chemical shift with increasing SrO content is due to Na^+ ions becoming associated with a different coordination environment within the glaze network, and is discussed in detail later.

6.6 BARIUM OXIDE ADDITION TO A MODEL FELDSPAR GLAZE

6.6.1 ^{23}Si MAS NMR Data

The ^{29}Si NMR spectra displayed in figure 6.16. are similar to those for the SrO glazes, and consist of broad symmetrical peaks. The ^{29}Si shift range covered is slightly smaller than for the SrO glazes (-70 ppm to -90 ppm). The ^{29}Si chemical shifts (table 6.7) also show similar trends to the SrO glazes. At 10 mol% BaO the ^{29}Si peak with a maximum at -86.0 ppm is assigned to $Q^4(3Al)$ silicon sites. For the glazes with between 20 mol% and 50 mol%. BaO, the ^{29}Si peaks are all in the region -81.1 ppm to -81.5 ppm and are assigned to $Q^4(4Al)$ units. At 100 mol% BaO, two peaks are observed; a dominant peak centred at -81.4 ppm ($Q^4(4Al)$ and a much smaller one at -70.5 ppm assigned to Q^o silicon sites.

6.6.2. ^{27}Al and ^{23}Na MAS NMR Data

^{27} Al NMR spectra generally show distinct resonances due to Al(4) and Al(6) with Al(4) dominating the other for all levels of BaO addition. The chemical shifts show considerable variation from +52.9 ppm for Ba Omol% to +69.6 ppm for Ba 50 mol%. Octahedral Al is detected but is in very small proportion compared to tetrahedral Al.

The ^{23}Na NMR spectra displayed in figure 6.18 show different lineshapes and chemical shift values as the BaO content is increased. Chemical shifts are in the range -21.5 ppm to -0.4 ppm indicating considerable difference in the ^{23}Na environment as BaO content is altered. Linewidths are also found to be dependent on the glaze composition and are particularly broad at higher BaO concentration.

Table 6.7 ^{29}Si MAS NMR Results for a Model Feldspar Glaze with Increasing Mol% of Barium Oxide

					Q^4				
	Q^0	Q^1	Q^2	Q^3	Q^4 (4Al)	Q^4(3Al)	Q^4(2Al)	Q^4(1Al)	Q^4(0Al)
Silica									-109
Quartz									-108
0% BaO							-93.3		
10% BaO						-88.0			
20% BaO					-81.1				
30% BaO					-81.2				
40% BaO					-81.5				
50% BaO					-81.4				
100% BaO	-70.5				-81.4				

Table 6.8 ^{27}Al + ^{23} Na MAS NMR Results for a Model Feldspar Glaze Containing Increasing mol% of Barium Oxide

	^{27}Al Resonance		^{23}Na Resonance	
	δ (TET) (ppm)	δ (OCT) (ppm)	$\delta^{23}Na$ (ppm)	Linewidth (Hz)
0% BaO	52.9	0.9	-21.5	2000
10% BaO	59.2	1.8	-15.9	2500
20% BaO	62.9	7.0	-8.5	3800
30% BaO	61.8	5.4	-0.4	11,100
40% BaO	70.2	8.7	-12.9	4750
50% BaO	69.6	8.7	-12.9	4250
100% BaO	67.7	8.3	-13.1	4050

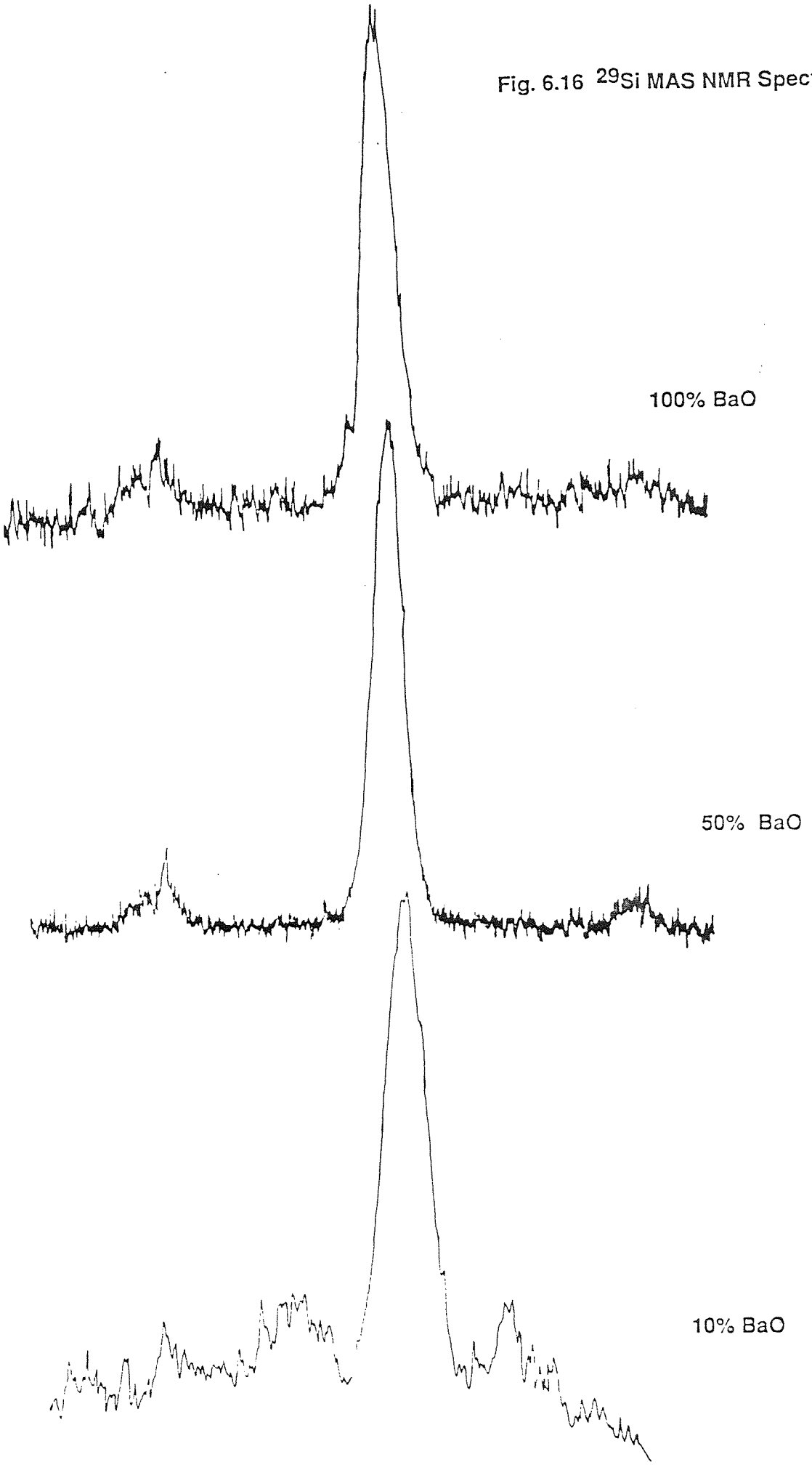

Fig. 6.16 ^{29}Si MAS NMR Spectra of BaO Glaze

Fig. 6.17 ^{27}Al MAS NMR Spectra of BaO Glazes

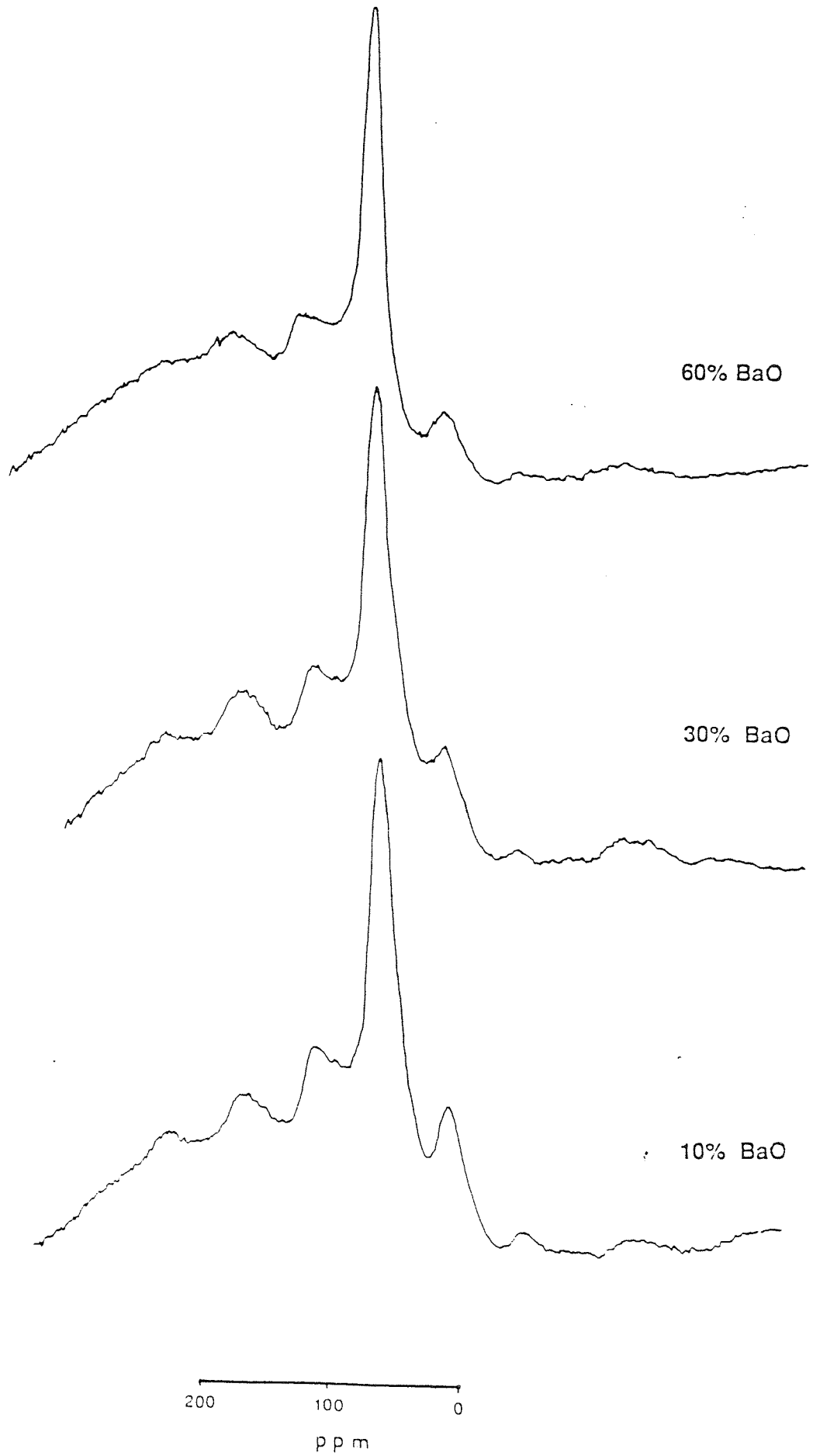

Figure 6.18
^{23}Na NMR spectra

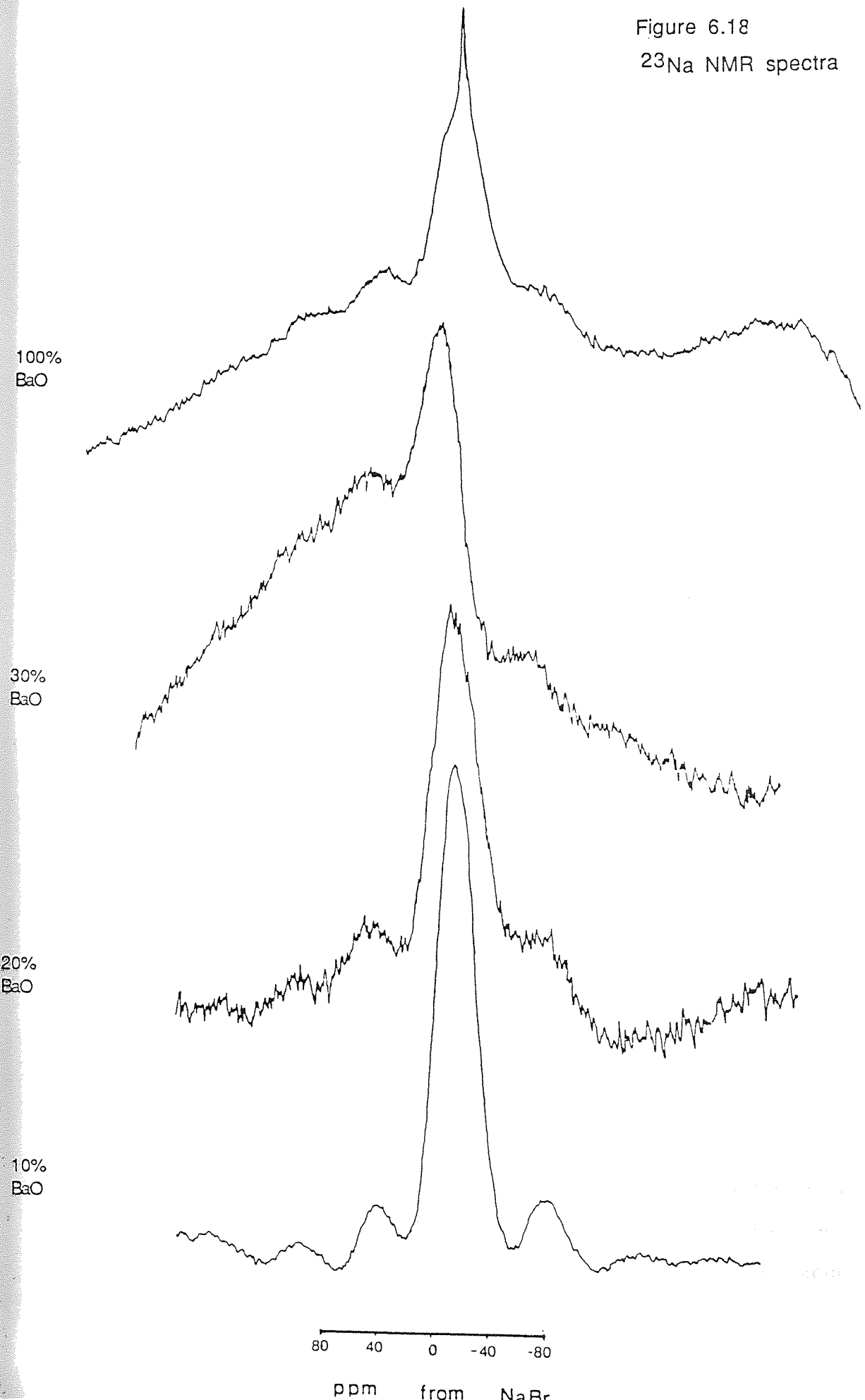

6.6.3. Discussion

The ^{29}Si NMR results show that at relatively low BaO concentrations (10% mol%) the dominant aluminosilicate unit present within the glaze is $Q^4(3Al)$. Above 10 mol% BaO the major component of the ^{29}Si spectra is assigned to $Q^4(4Al)$ units. As in the previous section (SrO glazes) there may be some initial confusion in assigning the ^{29}Si chemical shifts to Q^m (silicate) or $Q^m(nAl)$ (aluminosilicate) units. However the ^{27}Al NMR results show that virtually all the ^{27}Al is present as four-coordinate Al which means that we must have a fully polymerised network. At high BaO content (100 mol%) fully polymerised Q^o units are also produced.

The fact that $Q^4(4Al)$ is the major component of the glaze network does not exclude the co-existence of other $Q^m(nAl)$ or Q^m units. In fact the large ^{29}Si linewidths are thought to arise from the superposition of signals arising from a whole range of $Q^m(nAl)$ and Q^m sub-units. The ^{29}Si shift range covered does not appear to vary a great deal with BaO content and remains between -75 ppm and -90 ppm. This implies that there are no $Q^4(2Al)$, $Q^4(1Al)$ or $Q^4(OAl)$ units present within the glaze. The possibility of the existence of $Q^3(nAl)$ and $Q^2(nAl)$ units is considered to be relatively small in comparison to the fully polymerised $Q^4(nAl)$ components. This follows from the fact that tetrahedral Al is known to occupy the most polymerized network possible. The large ^{29}Si linewidths also indicate that there is a range of Si-O-T bond angles and bond lengths throughout the glaze. Each of the different speices with differing bond angles and bond lengths throughout the glaze. Each of the different species with differing bond angles and bond lengths would give rise to slightly different ^{29}Si resonances (and hence chemical shifts) which in turn leads to a inhomogeneously broadened lineshape. Chemical shift anisotropy is another probable cause of inhomogeneous line broadening.

^{27}Al NMR spectra exhibit strong quadrupolar broadening of the peaks and are thus less informative than ^{29}Si spectra. However there is a significant shift of the ^{27}Al resonance to low field (more positive values) as more BaO is added to the glaze. For Li_2O glazes the observed ^{27}Al chemical shift values were in the range +52 to +55 ppm, whereas for SrO glazes the shift range was from +52 to

+65 ppm. BaO glazes exhibit an ^{27}Al shift range (for tetrahedral Al) of between +59 and +70 ppm. This suggests that for BaO and SrO glazes the Al(4) signals arise from extra-network aluminate species although ^{27}Al shifts cannot be relied upon to identify the exact species.

The ^{23}Na data shows a slightly different trend to the previous three studies. At only 10 mol% BaO the chemical shift value of the ^{23}Na falls from -21.5 ppm to -15.9 ppm and with further addition of BaO falls to -0.4 ppm. At higher BaO the ^{23}Na chemical shift rises to about -12 ppm and thereafter appears to have reached a stable value at -13.1 ppm. The large variation in chemical shift suggests that BaO has a significant effect on the ^{23}Na resonances. The Na^+ ions appears to have changed its environment from one where the electron density around the nucleus was relatively high (-21.2 ppm) to one where the electron density is a lot less (-0.4 ppm, deshielded). It should be noted however that the ^{23}Na spectra show strong quadrupolar broadening particularly at high BaO contant. The ^{23}Na linewidth shows a similar variance to chemical shift values as the BaO content is changed. The spectrum for 40 mol% BaO is particularly interesting. Apart from the quadrupolar broadened basal region of the spectrum, the main +1/2 <--> -1/2 resonance (central peak) is highly asymmetrical and shows a distinct shoulder at about -5 ppm. Although this appears to suggest the presence of two distinct Na^+ sites, some authors have suggested that because of the large amount of quadrupolar broadening, the angle at which the sample is spun (54^o 44' i.e. the magic angle) does not allow an averaging of the signal due to the m = +1/2 to -1/2 transition. This has been termed as a quadrupolar-split peak. When quadrupolar interactions (which may result from distorted Na^+ sites) are high it is necessary to spin at a different angle than the magic-angle since the quadrupolar interaction is not dependent on the ($3\cos^2$ -1) term. In comparison the ^{23}Na spectrum for 10 mol BaO shows a relative undistorted spectrum indicating an undistorted environment for ^{23}Na.

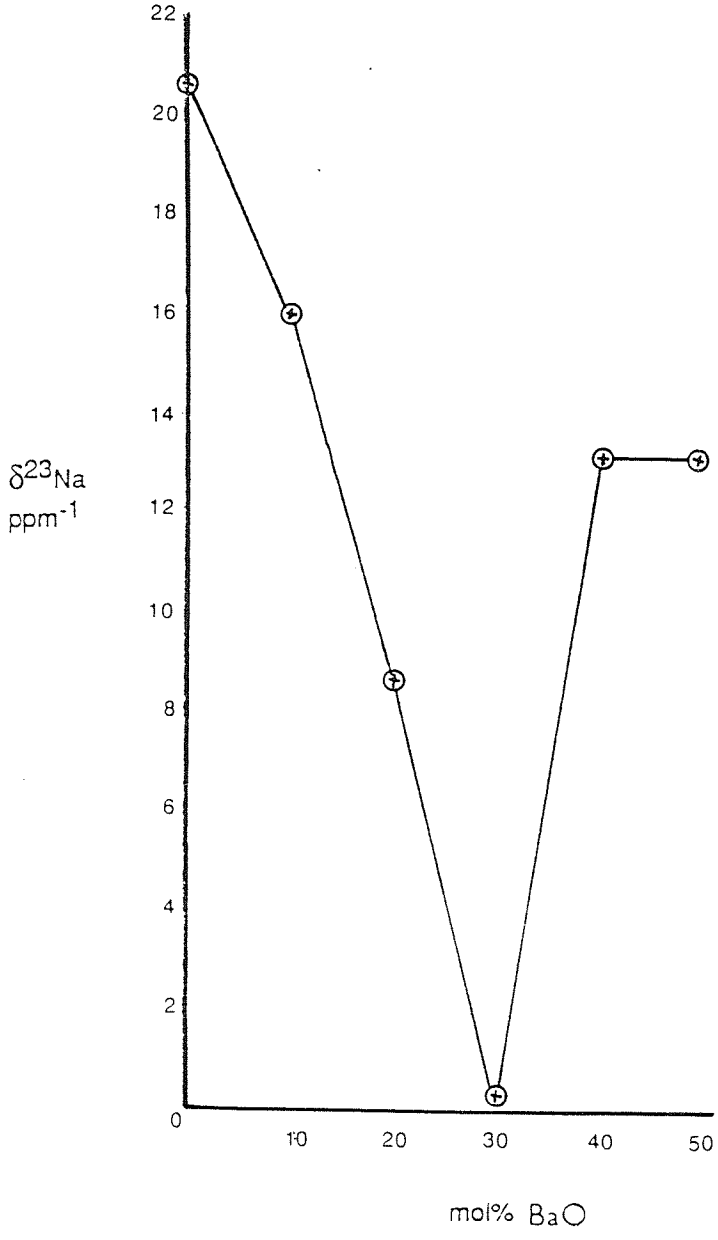

Fig. 6.19 A Plot of ^{23}Na Chemical Shift Versus mol% BaO

6.7. STRUCTURAL IMPLICATIONS OF 29Si, 27Al + 23Na MAS NMR DATA FOR THE MODEL FELDSPAR GLAZES

Crystalline feldspar structures are based on a framework of vertex-linked SiO_4 and AlO_4 tetrahedra. The ratio of aluminium to silicon ranges from 1:3 to 1:1. Feldspar frameworks have inherent monoclinic symmetry. Because AlO_4 tetrahedra are slightly larger than SiO_4 tetrahedra, some patterns of Al/Si distribution give monoclinic frameworks whereas others cause slight distortions and triclinic symmetry. The framework structure of crystalline feldspars is based on condensed rings of four tetrahedra. A type of chain structure results which is linked to simfilar formations on all sides, thus forming a three-dimensional framework. The resulting structure contains voids large enough to hold extra-cations which electrically balance the lattice. The alkaline or alkaline-earth ions dictate the type of structure in that they are the units around which the Al/Si framework is constructed.[132] Potassium and barium cations, being of large size confer a different structural arrangement from the smaller cations, Na^+ and Ca^{2+}.

The most widely accepted view of the structure of feldspar glasses is that proposed by Taylor and Brown on the basis of their x-ray radial distribution analysis results.[57] Taylor and Brown proposed that albite (Na Al Si_3O_8) and anorthite (Ca $Al_2Si_2O_8$) feldspar glasses have essentially different structures. For albite in both crystalline and glassy state, their results suggested a close correspondence i.e. a structure composed of tetrahedrally coordinated silicon and aluminium atoms sharing all four comers with other tetrahedra in the first coordination sphere; but there were fundamental differences in the way in which tetrahedral groups formed rings. The structural model that they proposed for albite glass suggested a trydymite-like structure based on a three-dimensional framework of six-membered tetrahedral rings. Aluminium would substitute for silicon in some of the tetrahedral sites. If the rings were fairly regular, such a structure would naturally have void spaces or interstices between the rings (one for every two tetrahedral atoms) to accommodate the alkali cations in approximately twelve-fold coordination.

For the anorthite glasses however, their results indicated that calcium occupies seven-fold coordination sites in the glass, very similar to crystalline anorthite, and a larger number of four-membered feldspar rings plus very little long range order. This model envisioned a glass structure based on feldspar like four-membered rings of SiO_4 and AlO_4 tetrahedra, connected to other four membered rings in a more or less random fashion. For example some of the rings may be connected through only one T-O-T bridge whereas others may be joined through adjacent tetrahedra producing a so called crankshaft arrangement.

The ^{29}Si NMR results obtained for the mimicked feldspar glaze mix based on the composition $(Na_2O)(Al_2O_3)(SiO_2)_6$ indicated the presence of $Q^4(2Al)$ aluminosilicate units as the dominant ^{29}Si sites in the glaze. Combined ^{27}Al, ^{23}Na and ^{29}Si NMR results suggested that we had obtained a similar glaze environment to that obtained for the albite glasses in Kirkpatrick's work, whose results also pointed to the dominance of $Q^4(2Al)$ units, as well as a ^{23}Na peak at -18.3 ppm. In our study we added to the albite glass composition increasing amounts of different oxides in the series CaO, Li_2O, BaO and SrO. The ^{29}Si NMR results showed that the broad peaks could be attributed to a variety of $Q^4(nAl)$ silica units depending on the exact composition of the glaze. It is found that after a certain mol% of the modifier oxide is added to the glaze mix, a point is reached when the dominant ^{29}Si is due to $Q^4(4Al)$ units. With CaO ^{29}Si peak maxima indicating $Q^4(4Al)$ units appear after the addition of 60 mol% CaO, whereas for Li_2O, SrO and BaO peak maxima for $Q^4(4Al)$ units appear at much lower oxide contents i.e. 10-20 mol%. Hence a glaze structure is envisaged consisting in the main part of a fully polymerised aluminosilicate network of SiO_4 tetrahedra surrounded by four AlO_4 tetrahedra and vice-versa in an alternating arrangement. However the chemical shift ranges covered by the ^{29}Si peaks strongly suggest the coexistence within the glaze of a variety of other $Q^m(nAl)$ and Q^m phases.

At this point an important question which arises is how well can we differentiate between $Q^m(nAl)$ and Q^m components? In other words to what extent does an overlap of chemical shift ranges for two different components affect our final

assignment. The strongest evidence for assignment of the major components of a spectrum to $Q^m n(Al)$ units rather than Q^m units comes from the ^{27}Al NMR spectra. The spectra show that in the majority of the glazes there is only a signal due to four coordinate aluminium and the octahedral Al component, if present is very small. This implies that most of the Al is present in tetrahedral coordination in a fully polymerised network and consist of $Q^4(nAl)$ type units. Raman studies by Mysen et al [169] and Sharma et al[168] have shown that aluminium enters the network by substituting in the most polymerised sites. Furthermore glasses with an albite type composition (particularly natural composition glasses obtained from Fe-poor silicia lavas) consist predominately of Q^4 type units i.e. a fully polymerised network system.[55] Nevertheless we cannot rule out the existence of $Q^2(nAl)$ or $Q^3(nAl)$ units.

Given the oxide composition range that was used, we speculate that the major component $Q^4(4Al)$ silica sites arise from feldspar-like four membered rings in a similar arrangement to that in anorthite type glasses. The four-rings are probably linked randomly to each other. A variety of Si-O-T bond angles would therefore be created which would give rise to discrete ^{29}Si chemical shifts (but which have not been resolved individually with the apparatus at our disposal) leading to an overall broadening of the spectrum.

It is also apparent from the ^{29}Si chemical shift data that the exact composition of the glaze in terms of the mol% of the oxide and the nature of the cation both have an effect on the overall glaze structure. For example at low CaO/Li_2O content the major component of the ^{29}Si spectrum is the $Q^4(2Al)$ unit. This result agrees with the findings of Kirkpatrick et al who found that for albite glass the major component was also $Q^4(2Al)$ unit. Using Taylor and Brown's model for albite glass,[57] the $Q^4(2Al)$ units arise from tridymite-like six membered rings with alkali cations (usually Na^+) closely associated with the ring voids. The ring sizes are actually determined by the size of the alkali cations (as proposed by Ribbe and Smith)[170]. Therefore at low CaO/Li_2O content, Na^+ ions predominate in the ring voids in twelve-coordination sites, and are not displaced by the Ca^{2+} or Li^+ cations[56].

When the CaO/Li_2O content is increased however, the major ^{29}Si component is due to $Q^4(4Al)$ units, indicating a greater alternation of Si/Al in the network. The presence of mainly $Q^4(4Al)$ units means that the network is dominated by mainly four-membered feldspar rings, rather than the six-membered tridymite like rings.[56, 168] The switch to smaller four-membered feldspar rings is obviously due to the higher concentration of Ca^{2+} and Li^+ ions which are now thought to determine the ring sizes. At higher CaO contents an anorthite type structure is expected.[57] Na^+ ions are thought to be displaced from their tweleve coordinate sites and are replaced by Ca^{2+} (or Li^+) ions which are known to take up seven (or six) coordinate sites in the voids between the feldspar rings which are randomly distributed throughout the glaze network.[57, 132]

The observed trends in ^{23}Na chemical shift also appear to support the above hypothesis. Recalling the ^{23}Na NMR data from table 6.2, it appears that ^{23}Na chemical shift undergoes a distinct shift to more positive (less shielded) chemical shifts as the oxide (CaO/Li_2O) content in increased. At relatively low oxide content (< 40 mol%) the ^{23}Na chemical shifts are fairly consistent at -21.5 to -20.9 ppm (relative to NaBr). Above 40 mol% CaO there is a distinct shift to less shielded values eventually ending up at -10.5 ppm. According to the hypothesis above the Na^+ ions are in a tweleve-fold coordination closely associated with (or even inside as some authors suggest)[56] the six-membered rings at low Ca_2O content in an albite type glaze structure, and the ^{23}Na chemical shifts of around -21 ppm correspond to this environment. At high CaO content there is an apparent deshielding of the ^{23}Na nuclei which indicates that there is less electron density at the ^{23}Na nuclei than previously. In other words, in going from a $Q^4(2Al)$ to $Q^4(4Al)$ environment, ^{23}Na experience a decrease in electron density. Dupree et al[67] have suggested that a chemical shift of around -21.1 ppm in aluminosilicates is representative of Na^+ ions associated with aluminate tetrahedra e.g. Na^+ AlO_4^- type association. Our results are consistent with the view that at low CaO/Li_2O content Na^+ reside in an albite type $Q^4(2Al)$ glaze within six-membered tridymite rings in close association with the aluminate tetrahedra. At high CaO contents there is evidence from ^{27}Al of the formation of calcium aluminate species. Na^+ are no longer associated with six-membered rings but are now part of a more random

glaze structure and are associated with less electron density. Some authors have suggested that ^{23}Na chemical shifts of about -10 ppm suggest a more mobile ^{23}Na ion associated with a number of possible sites. The increased linewidth of the ^{23}Na spectra at higher CaO/Li_2O content also suggests a range of ^{23}Na chemical shifts arising from Na^+ in a number of different sites as well as a larger quadrupole coupling constant and asymmetry parameter.

The effect of cation size on the glaze network is demonstrated by the ^{29}Si spectra for glazes containing SrO and BaO. The ^{29}Si peaks are assigned to $Q^4(4Al)$ units irrespective of the concentration of BaO or SrO. A glaze structure composed mainly of four-membered rings is envisaged. We can consider this by considering the relative sizes of the cations. Pauling and Goldschmidt[171] both present values for ionic radii which are consistent with the order

Ba > Sr > Ca > Li

	Ba	Sr	Ca	Li
Pauling	1.35	1.13	0.99	0.6
Goldschmidt	1.43	1.27	1.06	0.78

Table 6.9 Ionic Radii (in Å)

Obviously Ba^{2+} and Sr^{2+} cations would be too large to support an albite type structure consisting of six-membered rings. Therefore considerable distortion of the feldspar rings is expected leading to larger interstices to accomodate Ba^{2+} and Sr^+ cations.

The ^{23}Na chemical shift data are also in line with the above view. At 0% BaO (albite glaze composition), the chemical shift is -21.5 ppm; in the above discussion this chemical shift value was attributed to Na^+ associated with alumina tetrahedra ($Na^+AlO_4^-$) in the six-membered ring voids. Addition of a relatively small amount of BaO (10%) produces in shift to a more positive (less

Table 6.11 ^{29}Si Linewidths (ppm) for Model Feldspar Glazes Containing Various Oxides

	Modifier Oxide Added to Glazed Recipe			
mol% Oxide	CaO	Li_2O	SrO	BaO
0	21.2	21.2	21.2	21.2
5	-	15.3	-	-
10	-	19.2	16.5	15.4
20	20.0	19.2	15.6	10.8
30	-	17.6	13.5	10.8
40	19.6	16.5	11.9	10.8
50	-	15.7	14.6	-
60	17.0	-	-	10.8
80	3.60	-	-	-
100	1.20	-	12.7	10.8

silicate species and giving rise to more variety in the number of aluminate neighbours around different silicon atoms[56].

This trend is indeed apparent when the linewidths (FWHH) for the model feldspar glazes are considered. In general (table 6.11) the ^{29}Si NMR peaks grow broader in the order

$$CaO > Li_2O > SrO > BaO$$

The increasing linewidth reflects a widening distribution of Q^4 Si-O-T bond angles and bond lengths (where T = Si or Al). We can relate the ^{29}Si linewidths to the cation polarising power of the oxide added to each feldspar glaze. Cation polarising power is also known as cationic potential which is expressed as charge divided by the ionic radius. Taking both Pauling and Goldschmidt ionic radii[171] the cationic potentials are:

	Ca^{2+}	Sr^{2+}	Li^+	Ba^{2+}
Pauling	2.02	1.77	1.66	1.48
Goldschmidt	1.88	1.57	1.39	1.28

Table 6.10 Cationic Potentials Based on Pauling and Goldschmidt Ionic Radii

Thus cationic potential decreases in the order $Ca^{2+} > Sr^{2+}$ $Li^+ > Ba^{2+}$. It is noteworthy that with the exception of SrO and Li_2O , the order of increasing ^{29}Si linewidth is the same as order of cationic potentials. Calcium has a much higher cationic potential than Li^+, Sr^{2+} or Ba^{2+} and therefore depolymerisation of the Q^4 silica network occurs at a much lower CaO concentration. In fact, above 60 mol% CaO, the Q^4 network is completely broken down to Q^1/Q^o network. On the other hand, Barium, lithium and strontium oxides have lower cationic potentials and thus the Q^4 polymerised network is maintained as the major component, although the existence of a wide variety of silicate species is not discounted.

Another important piece of information which can be gained from ^{29}Si linewidths is the linewidth dependence on the Si/Al ratio of the dominant $Q^m(nAl)$ alumino silicate phase. It appears that when examined as a function of Si/Al ratio, the linewidths of the glazes in the series CaO to BaO are consistent with substantial adherence to Lowenstein's aluminium avoidance principle. In lithium, strontium and barium oxide glazes the $Q^4(4Al)$ assignment means that Si and Al alternate in the tetrahedral framework i.e. each Si is surrounded by four Al and vice versa. This alternation of Al and Si appears in itself to be a manifestation of Lowensteins rule which states that Al-O-Al linkages are energetically unfavourable. However in the case of calcium oxide containing glasses some workers have argued that Ca^{2+} inspires a breakdown in aluminium avoidance because of its greater cationic potential (polarising power) compared to Li^+, Sr^{2+} or Ba^{2+}. Evidence for what at first appeared to be a possible breakdown of Lowenstein's rule for glazes containing high CaO content was provided by ^{27}Al NMR data.

For glazes with high CaO content (80 mol% and 100 mol% CaO) the tetrahedral aluminium -27 chemical shifts were found to occur at +80 and +81 ppm relative to $Al(H_2O)_6^{3+}$. Normally, for four-coordinate Al aluminium [Al(4)] in albite glass chemical shifts in the region of +52 to +54 ppm are expected at 78.2 MH resonance frequency. Such chemical shift values are typical for aluminosilicates where the tetrahedral aluminium atoms are surrounded by four SiO_4 tetrahedra. Mueller et al correlated increases in Al(4) chemical shifts with the increasing number of AlO_4 tetrahedra in the second coordination sphere for various aluminates / aluminosilicates [83]. According to Mueller's results as the number of aluminium increases from zero to four there is an increase in Al(4) chemical shift. The ^{27}Al chemical shift for a $Q^4(OAl)$ unit (or alternatively Q^o4 Si) or R^o is expected at about +55 ppm relative to $Al(H_2O)_6^{3+}$ where Q^o is a four coordinated Al atom.

R^4	R^3	R^2	R^1	R^o
Q^o	$Q^o(1Si)$	$Q^o(2Si)$	$Q^o(3Si)$	$Q^o(4Si)$
79.5	74.3	69.5	64.2	55(ppm)

Thus the ^{27}Al chemical shift for an R^4 Al atom i.e. coordinated to four other AlO_4 tetrahedra is around +79.5 ppm. The ^{27}Al chemical shift values obtained in the present study for 80 mol% and 100 mol% CaO addition of 80 + 81 ppm are somewhat tentatively assigned to a four coordinate aluminium, possibly a calcium aluminate. At this point it should be pointed out that in a MAS NMR study of Ca Al silicate glasses Engelhardt et al[61] found ^{27}Al shifts as high as +76 ppm (relative to $Al(H_2O)_6^{3+}$ when the proportion of Al_2O_3 and CaO were much higher than that of SiO_2. The ^{27}Al shifts were attributed to neutral aluminium 'triclusters' such as $Al^{3+}(AlO_2^-)_3$ as well as to tetrahedrally coordinated calcium aluminate ($CaAl_2O_4$).

De Jong et al[59] related the formation of calcium aluminates with a breakdown in Lowenstein's rule. Their reasoning was as follows. de Jong and Schramm[59] argue that although the overall electron density on the bridging oxygen in $^{IV}Al\text{-}O\text{-}Al^{IV}$ and $^{IV}Si\text{-}O\text{-}Si^{IV}$ linkages is similar (6.76 and 6.73 electrons) the non-bonded electron density on the bridging oxygen Obr) varies substantially from about 2 electron pairs on O(br) in silicon linkages to about 2 1/4 electron pairs in the aluminium linkage. Also this non-bonded valence electron density on O(br) is less tightly held in the aluminium linkage than in the silicon linkage, hence forming a strong Lewis base (electron donor) in the Aluminium Linkage. Due to the fact that the overal electron density on O(br) in AlO_2^- and SiO_2 is similar an excess electron density still must reside on the aluminium atoms in AlO_2^-. Reduction and stabilisation of this excess electron density and hence stabilization of higher Al(4) condensates becomes possible by attachment of alkaline or alkaline earth cations (Lewis acids). The presence of such cations results in charge transfer from aluminium atoms and therefore a depopulation of the aluminium valence states. Calcium ions can function well as Lewis acids and hence may stabilise R_4 or lower condensates of Al(4) In other words Al-O-Al linkages, which would be forbidden in normal silicate and aluminosilicate systems due to their instability, could exist if they are stabilized. If we are to follow this argument, then judging from the ^{27}Al data for the glazes containing Li^+, Sr^{2+} and Ba^{2+} ions the following conclusions can be made. For the Li glazes, all the Al (4) chemical shifts are in the range +52 to +58 ppm, indicating only R^o type

[Q^4(OAl)] aluminate tetrahedra. Sr and Ba glazes however give ^{IV}Al chemical shifts as high as +69 ppm suggesting R^2 and R^1 type aluminates, i.e. ^{IV}Al surrounded by two and one AlO_4 tetrahedra, but no sign of R^4 type aluminates. Hence Sr^{2+} and Ba^{2+} ions have less stabilising effect than Ca^{2+}; in other words they are weaker Lewis acids. This conclusion is in line with ^{29}Si linewidth data which suggests that ^{29}Si linewidths are related to the cationic potential. As we saw previously the cations were placed in order of their polarising power as follows:

$$Ca^{2+} > Sr^{2+} > Li^{+} > Ba^{2+}$$

which was in good agreement with ^{29}Si linewidth data which suggested the order

$$Ca^{2+} > (Sr = Li^{+}) > Ba^{2+}$$

In terms of their ability to stabilize aluminate tetrahedra (i.e. Lewis acidity) the cations can be arranged in a slightly different order:

$$Ca^{2+} >> (Ba^{2+} = Sr^{2+}) > Li^{+} \ (^{27}\text{Al chemical shift data})$$

The only anomalous result here is the position of lithium which on the basis of its cationic potential would be expected to be a stronger Lewis acid than Ba^{2+}.

Inspite of the apparent strength of Ca^{2+} as a Lewis acid and the consequent formation of R^1 to R^4 aluminate tetrahedra, in our view there is not enough evidence for a breakdown in the Lowenstein rule. Instead we argue that by considering the glaze structure in terms of a homogeneous silicate phase then the Lowenstein rule is actually adhered to. The only time that an apparent breakdown is suggested is at very high oxide content (particularly 80 mol% and 100 mol% CaO). The ^{29}Si results still suggest a Q^4(4Al) i.e. strictly alternating aluminosilicate network implying adherence to Lowenstein's rule. It is possible that at very high CaO levels the existence of calcium within the homogeneous aluminosilicate phase is energetically unfavourable. In other words the free energy of the system is considerably altered at high Ca^{2+} content (and to a lesser extent Li^{+} and Sr^{2+}), such that there is one value for the free energy of

formation of the homogeneous aluminosilicate/silicate phase i.e. the overall glaze network, and a lower free energy for the formation of calcium aluminates. In order for calcium to be incorporated into the homogeneous silica glaze network, a higher free energy of formation would be necessary. Therefore the more energetically favourable route is followed which means that calcium aluminates are precipitated out of the glaze network and become extra-network species, not part of the overall glaze network. This explanation is in part substantiated by the previously discussed concept of Lewis acidity of the cations involved, since the stronger the Lewis acidity of the cation the more it will stabilize the corresponding R^1 to R^4 aluminates, which can therefore precipitate out of the overall glaze structure.

6.9. CONCLUSION AND FURTHER POSSIBILITIES FOR SOLID-STATE NMR IN THE STUDY OF CERAMIC GLAZES

In this study ^{29}Si, ^{27}Al and ^{23}Na MAS NMR spectroscopy were combined in order to determine the effects of different modifying cations on the overall structure of a model feldspar glaze with an oxide composition $(Na_2O)(Al_2O_3)(SiO_2)_6$. A qualitative correlation between ^{29}Si NMR linewidths and the cationic potential (cation polarising power) of the modifier oxide cations was found; ^{27}Al chemical shifts for tetrahedrally coordinated aluminium were found to correlate with the Lewis acidity of the modifying cations. ^{29}Si chemical shifts showed that a definite distinction between Ca^{2+} and Li^+ on one hand, and Sr^{2+} and Ba^{2+} on the other hand could be made. Model glazes containing relatively low amounts of CaO (o to 40 mol%) exhibited broad ^{29}Si peaks which were assigned to $Q^4(nAl)$ local silicon environments, pointing to a glaze structure based on four and six-membered feldspar like rings. At high CaO content ^{29}Si results implied that crystalline calcium silicates were formed in preference to a feldspar like structure. Also, ^{27}Al NMR results suggested that the presence of large amounts of Ca^{2+} inspired a possible breakdown in the aluminium avoidance principle, leading to the formation of R^4 type aluminate structures.

For model glazes containing strontium and barium oxides, ^{29}Si and ^{27}Al results

indicated that irrepsective of the proportion of Ba^{2+} and Sr^{2+} in the glaze composition, tetrahedral aluminium showed a preference for the most polymerised network, giving rise to a predominance of $Q^4(4Al)$ silica sites; a glaze structure based upon feldspar-like four-membered rings linked in a random fashion was envisaged. The NMR results for glazes containing lithium oxide showed that there was a chaning distribution of Al/Si in the most polymerised network with increase in Li^+ content, and that aluminium atoms only occuppied tetrahedral sites.

Relatively little information was available on the long range order or disorder in the glaze, although the large range of chemical shifts covered by ^{29}Si peaks implied a highly disordered network structure with a wide variety of Si-O-T bond angles and bond lengths. The study of non-crystalline systems such as ceramic glazes clearly reveals some of the limitations of the NMR techniques. NMR is only sensitive to the local nuclear environment and at most can detect influences due to the third or fourth coordination environment. X-ray techniques on the other hand would be able to reveal more information on the overall long range order (or lack of it) in such systems, but even these techniques are of limited use because of the similar diffractive powers of aluminium and silicon atoms.

Many of the Si peaks displayed splittings and shoulders. The failure to resolve the realtively broad peaks into their components is due partly to the multitude of Si-O-T bond angles and bond lenths which give rise to individual ^{29}Si resonances, and partly due to a dispersion of chemical shift anisotropy (CSA) interactions. Although an optimisation of the NMR parameters such as magnetic field strength, number of FIDs etc, would help to resolve some of the shoulders and peak splittings, CSA interactions would still leave a broad NMR spectrum. Regardless of this fact, it is still possible to distinguish between long and short range order in the glaze environment by utilising differences in the longitudinal and transverse relaxation time of silicon in different evironments.[68] The arguments is as follows.

In a randomly oriented solid such as a ceramic glaze the nmr spectrum consists in general of a convolution of the spectra associated with a number of inherently

anisotropic interactions[173]. The major line broadening influence on ^{29}Si in a Si-Al-O glaze is the shielding anisotropy. Magic angle spinning averages the shielding anisotropy to its average value[40,174]. In systems which are highly ordered both microscopically and macroscopically, and in which CSA is the only cause of broadening in a randomly orientated sample, sharp, liquid-like lines are expected for spectra under MAS. On the other hand, in an aluminosilicate glaze where the local environment of the majority of the Si atoms is tetrahedral, but where there is disorder in the second and further coordination spheres, there will be a dispersion of shielding anisotropics of ^{29}Si and the residual NMR linewidth will reflect this dispersion. A system which is a mixture of highly ordered, and relatively disordered regions would be expected to give an NMR spectrum which is a superposition of relatively sharp and broader lines under MAS. The NMR spectra of nuclei in the disordered regions will be inhomogenously broadened due to a smooth dispersion of shielding environments, and will exhibit lines characterised by a larger linewidth ie a shorter effective transvers relaxation time, $T_{2e}H$, than those in the crystalline regions. In addition, the disordered regions would be expected to be more loosely bound on average, than the crystalline regions. Because of the increased mobility in the disordered compared to the "crystalline" regions, it may be possible to distinguish the two on the basis of their longitudinal relaxation times, T_1. One method of making such a distinction would be to signal average in the pulse mode using recycle time short, and then long compared to the value of T_1 of the rigid region. In the first case, the signal from the rigid region would be expected to be attenuated in the spectrum. In the latter, the signal from both the rigid and mobile regions is found.

Relaxation studies would be just as useful in shedding light on the environments of Na^+ ions and Li^+ ions in the glaze. For the quadrupolar nuclei, ^{27}Al and ^{23}Na further improvements to the spectra could be made by using variable angle sample spinning rather than magic angle spinning.[41,41,43] ^{27}Al and ^{23}Na in glassy environments exists in a large variety of sites, some of which are distorted, giving rise to high local electric-field-gradients, which are manifested as second order quadrupolar broadening in the NMR spectra. MAS only partially removes this second order broadening but in cases of high efgs

even MAS is useless. VASS technique, however, gives much better results as shown by Ganapathy and coworkers.[41] It may be possible to distinguish between Na^+ + Al^{3+} in a variety of different sites.

REFERENCES

REFERENCES

1) Grim, R.E. : Clay Mineralogy, McGraw-Hill, New York, 1953

2) Grimshaw, R.W. : The Chemistry and Physics of Clays and Other Ceramic Materials, 4th Edition, Benn, 1971

3) West, A. : Solid State Chemistry, Wiley, London, 1984

4) van Olphen, H. : An Introduction to Clay Colloid Chemistry, Interscience, London, 1963

5) Thang, B.K.G. : The Chemistry of Clay-Organic Reactions, Adam Hilger, London, 1974

6) Newman, A.C.D. : The Chemistry of Clay Minerals, The Mineralogical Society, London, 1986

7) Brindley, G.W. : The X-Ray Identification of Clay Minerals, Longman, 1981

8) Pinnavaia, T.J. : Intercalation of Molecular Catalysts in Layered Silicates, 1982, ACS Symp. Ser., 192, 242-53

9) Siedle, A.R. : Copper and Gold Metallotetrathiafulvalenes , Inorganic Chemistry, 1981, 20, 2635

10) Torrance, J.B. : Optical Properties of the Radical Cation TTF+ in its Mixed Valence And Monovalence Halide Salts, Physical Review B, 1979, 19, 731

11) Wudl, F. : Chemistry and Physics of One-Dimensional Metals, Keller, H.J. (ed), Plenum Press, New York, 1977

12) Wudl, F. : A Systematic Study of an Isomorphous Series of Organic Solid State Conductors Based on TTF, J. Chem. Phy. 1977, 66, 377

13) McBride, M.B. : Surface Reactions of 3,3', 5-5'- tetramethyl benzidine on Hectorite, Clays and Clay Minerals, 1983, 33, 510

14) Siadle, A.R. : Metallotetrathiaethylenes , Ann, N.Y. Aca. Sci. p377

15) Son, S., Maeda, T., : Synthesis of Cu II TCNQ Complex on the Interlayer Surface of Montmorillonite, J. Inorg. Nucl. Chem. 1979, 42, 367

16) UEYAMA, GEN-ETSU, TANAKA : Preparation and Electrical Resistivities of TTF and TSF Salts, Polyhedron 1985,4,1783

17) Schoonheydt, R.A. : Spectroscopy of Proflavine Adsorbed on Clays, J. Chem. Soc. Faraday Transactions, 1986, 82,281

18) Wudl, F. : Unsymmetrical Dimethyltetrathiafulvalenes, J. Org. Chem., 1977, 42,768

19) Wudl, F. : Electrical Conductivity of the bis-1, 3-dithiole-bis-1,3-dithiolium System, J. Am. Chem. Soc., 1972, 94, 670

20) Wudl, F. : A New Approach to the Preparation of TTF Salts, J. Am. Chem. Soc., 1975, 97, 1962

21) Thomas, J.M., Tennakoon, D.T.B., Tricker, M.J., : J. Chem. Soc. Dalton Transactions, 1974 p2207 Part I

22) Pinnavaia, T. J. : Intercalation of Metal Cluster Complexes in Smectites, Inorganic Chemistry, 1985, 24, 3602

23) Vogel, A. I. : A Textbook of Quantitative Inorganic Analysis, London, 1962

24) Van Damme, H., Obrect, F., Letellier, M. : Intercalation of Tetrathiafulvalene in Smectite Clays: Evidence for Charge Transfer Interactions, Nouv, J. Chim. 1984, 8, 681

25) Bancroft, G. M. : Mossbauer Spectroscopy, An Introduction for Inorganic Chemists and Geochemists, McGraw-Hill, Maidenhead, UK, pp122

26) Cardile, C. M., Johnson, J. H. : Clays and Clay Minerals, 1986, 34, 307

27) Singh, H. B., McWhinnie, W.R., Ziolo, R.F. and Jones, C.H.W. : J. Chem. Soc., Dalton Transactions, 1984, p1267

28) Rozenson, I., Heller-Kallai, L. : Clays and Clay Minerals, 1977, 94, 25

29) Monsef-Mirzai, P. : Unpublished results (1983)

30) Poole, C., Monsef-Mirzai, P. : (Unpublished Results)

31) Bryce, M.R., Murchy, L. : Nature, 1984, 309, 119

32) McBride, M.B., Pinnavaia, T.J., Mortland, M.M. : Electron Spin Resonance Studies of Cation Orientation in Restricted Water Layers on Phyllosilicate Surfaces, J. Phys. Chem., 1975, 79, 2430

33) Mandair, A.S. : (Unpublished results)

34) Mandair, A.S., Monsef-Mirzai, P., McWhinnie, W.R. : Inorg. Chim. Acta. 1987

35) Gillard and Mitchel : Inorganic Synthesis, 1971, 14, 159

36) Lowenstein, W. : Am. Mineral. 1954, 39, 92

37) Clayden, J., Dobson, C.M., Hayes, C.J., Rodger, S.A. : J. Chem. Soc. Chem. Comm. , 1984, p1396

38) Gillespie, P. : The Goechemistry of Waste Disposal, PhD Thesis, The University of Aston in Birmingham, 1980

39) Ali, N. : The Chemistry of Ceramic Glazes, PhD Thesis, The University of Aston in Birmingham, 1983

40) Maricq, M., Waugh J.S. : NMR in Rotating Solids, J. Phys. Chem. 1979, 70, 330

41) Ganapathy, S., Schramm, S., Oldfield, E. : Variable-angle Samples Spinning High Resolution NMR of Solids, J. Phys. Chem. 1982, 77, 4360

42) Meadows, M.D., Smith, K.A., Kinsey, R.A., Oldfield, E. : High Resolution Solid State NMR of Quadrupolar Nuclei, Proc. Natl. Acad. Sci. U.S.A. : 1982, 79,1351

43) Lippmaa, E., Samoson, A., Kundla, E. : High Resolution MAS NMR of Quadrupolar Nuclei in Powders, J. Magn. Res. 1982, 49, 350

44) Oldfield, E., Janes, N. : Prediction of Silicon-za NMR Chemical Shifts Using a Group Electronegativity Approach, J. Am. Chem. Soc. 1985, 107, 6769

45) Lippmaa, E., Magi, M., Samoson, A., Engelhardt, G., Grimmer, A.R. : Structural Studies of Silicates by Solid-State High Resolution ^{29}Si NMR, J. Am. Chem. Soc., 1980, 102, 4889

46) Lippmaa, E., Alla, M.A., Pehk, T.J., Engelhardt, G. : J. Am. Chem. Soc., 1978,100, 1929

47) Lippmaa, E., Magi, M., Samoson, A., Engelhardt, G., Grimmer, A.R. : Solid-State High Resolution ^{29}Si NMR Chemical Shifts in Silicates, J. Phys. Chem., 1984, 88, 1518

48) Thomas, J.M., Klinowski, J. : The Magic Angle and All That : Probing the Structure of Solids Using NMR, Endeavor, 1986, 10, 1.

49) Kirkpatrick, R.J., Smith, K.A., Schramm, S., Turner, G., Yang, W.: Solid-Sate NMR Spectroscopy of Minerals, Ann. Rev. Earth. Planet. Sci. 1985, 13, 29

50) Smith, K.A., Kirkpatrick, R.J., Oldfield, E., Henderson, D.M. : High Resolution ^{29}Si NMR Spectroscopic Study of Rock Forming Silicates, Am. Mineral, 1983, 68, 1206

51) Sanz, J., Serratosa, J.M. : ^{29}Si and ^{27}Al High-Resolution MAS NMR Spectra of Phyllosilicates, J. Am. Chem. Soc. 1984, 106, 4790

52) Kinsey, R.A., Kirkpatrick, R.J., Hower, J., Smith, K.A., Oldfield, E. : High-ResolutionAluminium-27 and Silicon-29 NMR Spectrospin Study of Layer Silicates Including Clay Minerals, Am. Mineral. 1985, 70, 537

53) Hayashi, S., Kikuko, H., Yamamoto, O. : Multinuclear Solid-State NMR Study of Dehydration of Na-Y Type Zeolites, Bull. Chem. Soc. Jpn., 1987, 60, 105

54) Grimmer, A.R., Fechner, R.P., Molgedey, G. : High-Resolution ^{29}Si NMR in Solid Silicates, Chem. Phys. Lett. 1981, 77, 331

55) Kirkpatrick, R.J., Smith, K.A., Kinsey, R.A., Oldfield, E., Henderson, D.M. : High-Resolution Solid-State Sodium-23, Silicon-29 and Aluminium-27 NMR Spectroscopic Reconnaissance of Alkali and Plagioclase Feldspars, Am. Mineral. 1985, 70, 106

56) Murdoch, J.B., Stebbins J.F., Carmichael, I.S.E. : High Resolution ^{29}Si NMR Study of Silicate And Aluminosilicate Glasses: The Effect of Network Modifying Cations, Am. Mineral. 1985, 70, 332

57) Taylor, M., Brown, G.E. : Structure of Mineral Glass I, Geochimica et Cosmochimica Acta. 1979, 3, 61

58) de Jong, B.H.W.S., Keefer, K.D., Brown, G.E., Taylor, C.M. : Polymerisation of Silicate and Aluminate Tetrahedra in Glasses, Melts and Aqueous Solutions III, Geochimica et Cosmoschimica Acta, 1981, 45, 1291

59) de Jong, B.H.W.S., Schramm, C.M., Parziale, V.E. : Polymerisation of Silicate and Aluminate Tetrahedra in Glasses and Aqueous Solutions IV Geochimica et Cosmoschimica Acta, 1983, 47, 1223

60) Grimmer, A.R., Magi, M., Hahnert, M., Stade, H., Samoson, A., Lippmaa, E. : High Resolution Solid-State Silicon-29 NMR Studies of Binary Alkali Silicate Galsses, Phys. Chem. Glasses, 1984, 25, 105

61) Englehardt, G., Nofz, M., Forkal, K., Wihsmann, F.G., Magi, M., Samoson, A., Lippmaa, E.: Structural Studies of Calcium Aluminosilicate Glasses by Solid State Silicon-29 and Aluminium-27 Magic Angle Spinning NMR. Phys. Chem. Glasses, 1985, 26, 157

62) Dupree, R., Holland, D., McMillan, P.W., Pettifer, R.F. : The Structure of Soda Silica Glasses: A MAS NMR Study, J. Non-Cryst Solids, 1984, 68, 399

63) Schramm, C.M., de Jong B.H.W.S, Parziale, V.E. : ^{29}Si MAS NMR Study on Local Silicon Environments in Amorphous and Crystalline Lithium Silicates, J.Am. Soc., 1984, 106, 4396

64) Kirkpatrick, R.J., Oestrike, R., Weiss, C.A., Smith, K.A., Oldfield, E. : High Resolution Aluminium-27 And Silicon-29 NMR Spectroscopy of Glasses and Crystals Along the Join $CaMgSi_2O_6$ - $CaAl_2SiO_6$, Am. Miner. 1986,71, 705

65) Greaves, G.N., Lagarde, P., Raoux, D., Gurman, S.J. : Local Structrue of Silicate Glasses, Nature, 1981, 293, 611

66) Stebbins, J.F., Murdoch, J.B., Schneider, E., Carmichael, I.S.E., Pines, A. : A High Temperature High-Resolution NMR Study of Sodium-23, Aluminium-27 and Silicon-29 in Molten Silicates, Nature, 1985, 314, 250

67) Dupree, R., Holland, D.H., Williams, D.S. : A MAS NMR Study of the Effect of Modifier and Intermediate Oxides on the Local Structure in Vitreous Silicates, Journal de Physique, 1985, 46, 119

68) Gerstein, B.C., Nicol, A.T. : Crystallinity and Local Chemical Environments of Silicon in a Silicon-Aluminium -Oxygen Glass Ceramic, J.Non-cryst. Solids, 1985, 75, 423

69) Ramdas, S., Klinowski, J. : A Simple Correlation Between Isotropic Silicon -29NMR Chemical Shifts and T-O-T Angles in Zeolite Frameworks, Nature, 1984, 308, 521

70) Thompson, J.G. : Interpretation of Solid-State ^{13}C and ^{29}Si NMR Spectra of Kaolinite Intercalates, Clays and Clay Minerals, 1985, 33, 173

71) Thompson, J.G., Barron, P.F., Raupach, M.: Clays and Clay Minerals, 1987, 35, 208

72) Oldfield, E., Janes, N. : Oxygen-17 NMR Study of Bonding in Silicates, J. Am. Chem. Soc. 1986, 108, 5747

73) Plee, D., Borg, F., Gatineau, L., Fripint, J.J. : High Resolution Solid-State Aluminium-27 and Silicon-29 NMR Study of Pillared Clays, J.Am. Chem. Soc., 1985, 107, 2362

74) Barron, P.F., Frost, R.L., Skjemstad, J.O., Koppi, A.J. : Detection of Two Silicon Environments in Kaolins by Solid-State ^{29}Si NMR, Nature, 1983, 302, 49

75) Klinowski, J.: NMR Studies of Zeolites, Progress in NMR Spectroscopy, 1984, 16, 237

76) Fyfe, C.A., Thomas, J.M., Klinowski, J., Gabbi, G.C. : MAS NMR Spectroscopy and the Structure of Zeolites,Angew Chemie, 1983, 22, 259

77) Grobet, P.J., Geerts, H., Martens, J.A., Jacobs, P.A. : Correct Determination of Aluminium in Y Zeolites by MAS NMR Spectroscopy, J. Chem. Soc. Chem. Comm. 1987, p.1688

78) Sulikowski, B., Rakoczy, J., Hamdan, H., Klinowsky, J.: J. Chem. Soc. Chem. Comm. 1987, p1542

79) Fyfe, C.A., Gobbi, G.C., Murphy, W.J., Ozubko, R.S., Slack, D.A. : J. Am. Chem. Soc. 1984, 106, 4435

80) Jarman, R.H., Jacobson, A.J., Melchior, M.T., J. Phys. Chem., 1984, 88, 5748

81) Lippmaa, E., Magi, M., Samoson, A., Tarmak, M., Engelhardt, G. : J. Am. Chem. Soc., 1981, 103, 4992

82) Fyfe, C.A., Gobbi, G.C., Klinowski, J., Thomas, J.M., Ramdas, S. : Resolving Crystallographically Distinct Sites in Silicalite ans ZSM-5 by Solid-State NMR, Nature, 1982, 296, 530

83) Muller, D., Gessner, W., Behrens, H.J., Scheler, F.A. : Chem. Phys. Lett. 1981, 79, 59

84) Smith J. V., Blackwell, C.S. : NMR of Silica Polymorphs, Nature, 1983, p223

85) Fyfe, C.A. : Solid State NMR for Chemists, 1985, CEC Press, Guelph, Ontario

86) Fukushima, E., Roeder, S.B.W. : Experimental Pulse NMR, Addison-Wesley, 1981, Massachusetts

87) Saunders, J., Hunter, B.: Modern NMR Spectroscopy, Oxford, 1987

88) Derome, J. : Modern NMR Techniques for Chemistry Research, Pergammon, 1987

89) Becker, E.D., Farrar, T.C. : Pulse and Fourier Transform NMR : Introduction to Theory and Methods, Academic Press, New York, 1971

90) Weiss, C.A., Altaner, S.P., Kirkpatrick, R.J.: High-Resolution Silicaon ZA NMR of 2:1 Layer Silicates , Am. Mineral. 1987, 72, 935

91) Fyfe, C.A., Strobl, H., Kokotailo, G.T., Kennedy, G.J., Barlow, G.E.: Ultra-high Resolution Silicon-29 Solid State MAS NMR Investigation of Sorbate and Temperature-Induced Changes in the Lattice Structure of Zeolite ZSM-5, J. Am. Chem. Soc. 1988, 110, 3373

92) Akitt, J.W. : NMR and Chemistry, Chapman and Hall, 2nd Edition, London, 1983.

93) Engelhardt, G., Zeigan, D., Jancke, H., Hoebbel, D., Wicker, W. : Z. Anorg. Allg. Chem., 1975, 418, 17

94) Engelhardt, G., Radeglia, R.: Chem. Phys Lett., 1984, 108, 271

95) Lowe, I.J. : Phys. Rev. Lett., 1959, 2, 285

96) Tennakoon, D.T.B., Thomas, J.M., Jones, W., Carpenter, T.A., Ramdas, S.: J. Chem. Soc. Faraday Trans., 1986, 82, 545

97) Gadsdon, J.A. : Infra-red Spectra of Minerals and Related Inorganic Compounds, Butterworths, London, 1975

98) Tarte, P., Pottier, M.J., Process, A.M.: Spectrochim. Acta., 1973, 29A, 1017

99) Saksena, B.D. : Trans. Faraday Soc., 1961, 57, 242

100) Dowty, E.: Vibrational Interactions of Tetrahedra in Silicate Glasses and Crystals I, Phys. Chem. Minerals, 1987, 14, 80

101) Dowty, E.: Vibrational Interactions of Tetrahedra in Silicate Glasses and Crystals II Phys. Chem. Minerals 1987, 14, 122

102) Tarte, P., Spectrochim. Acta. 1962, 18, 467

103) Clark, R.J., Hester, R.E. (Eds): Spectroscopy of Inorganic Based Materials, Wiley, 1987

104) Mackenzie, J.D.: Modern Aspects of the Vitreous State, 1962, Butterworths

) Bodenhausen, G., Carvatti, P., Ernst, R.R.: J. Mag. Res., 1982, 48, 143

106) Turner, G.L., Kirkpatrick, R.J., Risbud, S.H., Oldfield, E. : Am. Ceram. Soc. Bull. 1987, 66, 656

107) Nakamota, K.: Infrared Spectroscopy of Inorganic and Coordination Compounds, 2nd Ed., New York, Wiley Interscience, 1970

124) Chatakondu, K., Green, M.L.H., Thompson, M.E., Suslick, K.S.: The Enhancement of Intercalation Reactions by Ultrasound, J. Chem. Soc. Chem. Commun., 1987, p.900

125) Nicholson, R.S., Shain, I.: Anal. Chem. 1964, 36, 706

126) Vlcek, A.A. : Nature, 1957, 180, 753

127) Waind, G.M., Martin, B.: J. Inorg. Nucl. Chem. 1958, 8, 551

128) Tanaka, N., Sato, Y.: Bull. Chem. Soc. Jpn., 1968, 41, 2059

129) Morinaga, N.: Rev. in Polarg., 1967, 14, 25

130) Vass, B.H., Ewing, G.W.: Electroanalytical Chemistry, Wiley Interscience, New York, 1983

131) Hughes, M.C., Macero, D.J.: Electrochemical Evidence for Reversible Five membered Electron Transfer Chains in Octahedral Chromium Complexes, Inorg. Chem. 1976, 15, 2041

132) Wells, Structural Inorganic Chemistry

133) Jenny, H.: Simple Kinetic Theory of Ion Exchange, J. Phys. Chem., 1936, 40, 501

134) Davis, L.E.: Simple Kinetic Theory of Ionic Exchange for Ions of Unequal Charge, J. Phys. Chem. 1945, 49, 473

135) Grimshaw, R.W., Harland, C.E.: Ion-Exchange : An Introduction to Theory and Practice, The Chemical Society, Monographs for Teachers, No. 29, 1975, 73

136) Vageler, P., Wolterdorf, J.: Z. Pflansenernahr. Dungung U. Bodenk 1930, 15, 329

137) Olmstead, L.B.: J. Agric. Res., 1931, 18, 47

138) Kiezel, L., Liszka, M., Rutkowski, M., Gryta, M.: J. Chem. Soc. Chem. Commun. 1977, 34

139) Laponite : Its Properties and Uses, Laporte Industries Ltd., 1984

140) Solomon, D.H., Hawthorne, D.G.: Chemistry of Pigments and Fillers, Wiley, 1983

141) Adams, J.M., Bylina, A., Graham, S.H., Clays and Clay Minerals, 1981, 16, 325

142) Fripiat, J.J. (Ed): Advanced Techniques for Clay Mineral Analysis, Developments in Sedimentology, Vol. 34

143) Bissada, K.K., Johns, W.D., Cheng, F.S.: Clay Minerals, 1967, 7, 155

144) Schoonheydt, R., De Pallw P., Vliero, D.: J. Phys. Chem.,1984, 88, 5113

145) Traynor, M.F., Mortland, M.M., Pinnavaia, T.J.: Ion-Exchange and Intersalation Reactions of Hectorite with Tris-bipyridyl Complexes, Clays Clay Miner, 1978, 26, 318

146) Mortland, M.M., Pinnavaia, T.J.: Formation of Copper II Arene Complexes on the Interlamellar Surfaces of Monmorillonite, Nature, 1971, 229, 75

147) Solomon, D.H., Loft, B.C., Swift, J.D.: Clay Minerals, 1958, 7, 399

148) McBride, M.B., Clays and Clay Minerals, 1979, 27, 224

149) McBride, M.B.: Surface Reactions of 3,3', 5,5'-TMB on Hectorite, Clays and Clay Minerals, 1985, 33, 510

150) McBride, M.B.: Advanced Chemical Methods for Soils and Clay Minerals Research, Ch. 9, 1980

151) Clementz, D.M., Mortland, M.M., Pinnavaia, T.J.: J. Phys. Chem. Ithaca. 1973, 77, 196

152) Pinnavaia, T.J., Welty, P.K., Hoffmann, J.F.: J. Am. Chem. Soc., 1975, 97, 3819

153) Pinnavaia, T.J., Giannelis, E.P.: Intercalation of Metal Cluster Complexes in Smectite Clay Inorg. Chem. 1985, 24, 3602

154) Monsef-Mirzai, P., McWhinnie, W.R.: Clay Supported Catalysts: An Extension of Phase Transfer Catalysis, Inorg. Chim. Acta. 1981, 52, 211

155) Barrer, R.M., MacLeod, D.N.: Activation of Montmorillonite by Ion-Exchange and Sorption Complexes of Tetraalkylammonium Montmorillonites, Trans. Farad. Soc., 1955, 51, 1290

156) Yamahaka, S., Brindley, G.W.: High Surface Area Solids Obtained by Reaction of Montmorillonite with Zirconyl Chloride, Clays and Clay Minerals, 1978, 26, 119

157) Brindley, G.W., Sempels, R.E.: Preparation of Properties of Some Hydroxy Aluminium Heidellites, Clays and Clay Minerals, 1977, 12, 229

158) Lahar, N., Shani, U., Shabtai, J.: Clays and Clay Minerals, 1978, 26, 107

159) Vaughan, D.E.W., Lussier, R.J., Magee, J.S.: Pillared Interlayered Clay Products, 1981b, US Patent, 4, 271, 043

160) Bottero, J.Y., Caeses, J.M., Poirer, J.E.: J. Phys. Chem. Ithaca., 1980, 84, 2933

161) Weis, A.: Angew. Chem. Int. Ed. Engl. 1981, 20, 850

162) Pinnavaia, T.J.: Intercalated Clay Catalysts, Science, 1983, 220, 365

163) Pinnavaia, T.J.: New Chromia Pillared Clay Catalysts, J. Am. Chem. Soc.: 1985, 107, 4783

164) Zachariason, W.H.: J. Am. Chem. Soc., 1932, 54, 3841

165) Steinberg, Y.G., Strontium Glazes, 1967, 2nd Edn. Stroiizdat, Leningrad, Moscow, p.344

166) Lippmaa, E., Samoson, A., Magi, M., Teear, R., Schraml, J., Gote, J.: Phys. Chem. Glasses, 1982, 50, 205

167) Akitt, J.W., Greenwood, N.N., Khandelwal, B.L. and Lester, G.D.: J. Chem. Soc. Dalton Trans. 1972, 604

168) Sharma, S.K., Simons, B., Yoder, H.S.: Am. Miner. 1983a, 68, 1113

169) Myser, B.O., Virgo, D., Kushiro, I.: Am. Miner, 1981, 66, 678

170) Ribbe, P.H.: Feldspar Mineralogy, 1983, Vol.2, Reviews in Mineralogy, Mineralogical Society of America

171) Cotton, F., Wilkinson, G.: Advanced Inorganic Chemistry, Third Edition, Interscience

172) McMillan, P.W., Piriou, B.: Bull. Mineral. 1983, 106, 57

173) Gerstein, B.C.: Analytical Chemistry, 1983, 55, 781

174) Andrew, E.R.: Int. Rev. Phys. Chem., 1981, 1, 195

APPENDICES

X-Ray Diffraction Data for Laponite Heated at Various Temperatures

Laponite 400°C

2θ	d-spacing(A°)
32.2	3.227
41.96	2.500
46.05	2.269
50.55	2.096
55.20	1.932
55.75	1.916
56.90	1.879
67.8	1.604

Laponite 1300°C

2θ	d-spacing
18.45	5.586
24.35	4.246
26.31	3.934
26.63	3.881
27.75	3.734
28.41	3.649
29.41	3.527
33.0	3.159
32.8	3.169
33.65	3.093
34.9	2.978
36.35	2.875
37.8	2.764
39.2	2.668
41.44	2.531
42.25	2.484
43.25	2.467
43.9	2.429
45.4	2.394
46.6	2.319
48.1	2.886
52.0	2.265
54.2	2.041
56.1	2.965
57.85	1.903
60.51	1.851
61.01	1.776
72.85	1.763
71.1	1.508

Laponite 600°C

2θ	d-spacing (A°)
20.75	4.968
31.2	3.328
32.75	3.174
33.30	3.124
34.71	3.007
35.25	2.957
36.05	2.892
39.70	2.636
41.11	2.550
41.80	2.509
42.25	2.484
50.00	2.118
55.25	1.930
59.61	1.801
64.01	1.689
74.00	1.487

XRD Data for Caramic Glaze Laponite + CaO (20 mol% to 200 mol%)

Ca 20	Ca 40	Ca 60	Ca 80
d-spacing/A^{o}	d-spacing/A^{o}	d-spacing/A^{o}	d-spacing/A^{o}
3.806	4.463	5.498	5.556
3.766	3.911	5.104	4.246
3.251	3.370	4.517	4.178
3.142	3.263	4.212	3.994
3.088	3.027	3.891	3.862
2.925	3.007	3.705	3.734
2.865	2.920	3.499	3.644
2.828	2.777	3.224	3.527
2.784	2.532	3.133	3.179
2.518	2.473	2.990	3.106
2.418	2.337	2.944	3.061
2.464	2.279	2.888	2.936
2.431	2.162	2.865	2.878
2.359	2.158	2.763	2.784
2.098	2.140	2.503	2.661
2.007	2.114	2.458	2.582
1.729	2.049	2.420	2.532
1.627	2.022	2.405	2.486
	2.006	2.369	2.431
	1.975	2.334	2.405
	1.833	2.269	2.394
	1.710	2.252	2.322
	1.678	2.222	2.290
	1.661	2.205	2.267
	1.638	2.173	2.041
	1.634	2.110	1.997
	1.626	2.093	1.963
	1.617	2.067	1.906
	1.554	2.036	1.861
	1.526	2.013	1.851
	1.502	1.958	1.813
	1.485	1.899	1.809
	1.423	1.856	1.778
	1.410	1.846	1.763
	1.331	1.812	1.758
		1.775	1.753
		1.755	1.735
		1.750	1.715
		1.670	1.671
		1.642	1.639
		1.526	1.592
		1.505	1.586
		1.499	1.541
		1.482	1.509
			1.505
			1.489

XRD Data

Ceramic Glazes Laponite + CaO (100 to 200 mol%)

Ca 100	Ca 200
d-spacing/A^{o}	d-spacing/A^{o}
4.287	3.133
3.774	2.920
3.227	2.497
3.115	2.051
2.912	1.832
2.901	1.768
2.698	1.512
2.677	
2.484	
2.437	
2.403	
2.314	
2.295	
2.045	
1.958	
1.843	
1.766	
1.749	
1.541	
1.510	

XRD Data Ceramic Glazes

Laponite + xCaO + (1-x) Al_2O_3

Al 20	Al 40	Al 60
d-spacing/A°	d-spacing/A°	d-spacing/A°
5.509	3,720	4.712
3.713	3.084	2.862
3.084	2.865	2.442
2.865	2.506	2.025
2.464	2.467	1.558
2.243	2.442	1.431
2.038	2.408	
1.758	2.394	
	2.038	
	1.941	
	1.885	
	1.840	

XRD Data for Ceramic Glazes

[Laponite + x CaO + (1-x) Al_2O_3]

Al 80	Al 100
d-spacing/A^o	d-spacing/A^o
4.703	4.682
4.055	3.492
3.504	2.870
3.214	2.562
2.870	2.445
2.562	2.384
2.520	2.090
2.447	2.023
2.089	1.740
2.026	1.607
1.750	1.518
1.654	1.431
1.604	
1.559	
1.431	